DEVELOPMENT OF NEW ELECTROCHEMICAL SENSORS FOR DETERMINATION OF BIOLOGICAL INDICATORS FOR DISEASES

KANTIMA KAEWJUA

Graduate School Srinakharinwirot University

2023

การพัฒนาตัวรับรู้ใหม่ทางเคมีไฟฟ้าสำหรับการตรวจวิเคราะห์สารชี้วัดทางชีวภาพที่ก่อโรค

กานติมา แก้วเจือ

ปริญญานิพนธ์นี้เป็นส่วนหนึ่งของการศึกษาตามหลักสูตร
ปรัชญาดุษฎีบัณฑิต สาขาวิชาเคมีประยุกต์
คณะวิทยาศาสตร์ มหาวิทยาลัยศรีนครินทรวิโรฒ
ปีการศึกษา 2566

DEVELOPMENT OF NEW ELECTROCHEMICAL SENSORS FOR DETERMINATION OF BIOLOGICAL INDICATORS FOR DISEASES

KANTIMA KAEWJUA

A Dissertation Submitted in Partial Fulfillment of the Requirements

for the Degree of DOCTOR OF PHILOSOPHY

(Applied Chemistry)

Faculty of Science, Srinakharinwirot University

2023

THE DISSERTATION TITLED

DEVELOPMENT OF NEW ELECTROCHEMICAL SENSORS FOR DETERMINATION OF BIOLOGICAL INDICATORS FOR DISEASES

BY

KANTIMA KAEWJUA

HAS BEEN APPROVED BY THE GRADUATE SCHOOL IN PARTIAL FULFILLMENT
OF THE REQUIREMENTS FOR THE DOCTOR OF PHILOSOPHY
IN APPLIED CHEMISTRY AT SRINAKHARINWIROT UNIVERSITY

(Assoc. Prof. Dr. Chatchai Ekpanyaskul, MD.)
Dean of Graduate School

ORAL DEFENSE COMMITTEE

..... Major-advisor
(Assoc. Prof. Dr.Weena Siangproh)

..... Chair
(Prof. Dr.Orawon Chailapakul)

..... Committee
(Assoc. Prof. Dr.Apinya Chaivisuthangkura)

..... Committee
(Assoc. Prof. Dr.Panarat Arunrattiyakorn)

..... Committee
(Assoc. Prof. Dr.Kriangsak Songsrirote)

Title	DEVELOPMENT OF NEW ELECTROCHEMICAL SENSORS FOR DETERMINATION OF BIOLOGICAL INDICATORS FOR DISEASES
Author	KANTIMA KAEWJUA
Degree	DOCTOR OF PHILOSOPHY
Academic Year	2023
Thesis Advisor	Associate Professor Dr. Weena Siangproh

This dissertation aims to develop new electrochemical sensing platforms using modified screen-printed graphene electrodes (SPGEs) for the determination of significant biological indicators. This research was divided into two sections. The first section is split into two subprojects: the first deals with the electrochemical sensors for tyramine detection and the other with the simultaneous detection of levodopa (L-DOPA) and L-Tyrosine (L-Tyr), respectively. The first subproject focused on the use of poly(histidine)-based SPGE electrocatalytic activity towards tyramine oxidation, yielding greater sensitivity than bare SPGEs. This developed platform showed two wide linear ranges of 0.5–20 μM and 50–300 μM with a limit of detection (LOD) of 0.065 μM. The next subproject reports on a new electrochemical platform using poly(L-proline)-linked nanodiamonds on SPGEs. To be highlighted, this platform can unlock interfering substances from printing ink components and improve L-DOPA and L-Tyr signals. Broad working ranges of 0.075–50 μM with a low LOD of 0.021 μM for L-DOPA and 2.5–120 μM with a LOD of 0.74 μM for L-Tyr were obtained. The as-prepared sensor demonstrated good reproducibility and long-term stability, lasting up to five weeks. The second section focused on the modification of SPGEs with biocatalyst materials based on a hemin matrix assembled on carbonaceous material for measuring hydrogen peroxide (H_2O_2) levels by amperometry. The combination of these modifiers produced synergistic effects that provided for a wide detection range of 1–10 μM and 30–1000 μM with a LOD of 0.11 μM. This non-enzymatic sensor offers the capacity to function as an even more effective electrocatalyst for H_2O_2 reduction, which opens up its potential uses in exhaled breath analysis. Therefore, it is possible to draw the conclusion that the key results of all the sensing platforms developed for this dissertation were user-friendliness, practicality, and the ability to provide sufficient analytical performance in practical applications.

Keyword : Electrochemical sensor, Poly (amino acids), Nanomaterials, Hemin, Biological markers

ACKNOWLEDGEMENTS

First and foremost, I would like to extend my heartfelt appreciation to my advisor, Associate Professor Dr. Weena Siangproh for generously sharing her extensive expertise and playing a pivotal role in pushing me to establish myself in this academic field. Her unwavering support, guidance, and encouragement have been invaluable throughout my Ph.D. journey. She not only guides me in defeating challenges but also provides valuable advice and constructive feedback. These have pushed me to grow both personally and academically. I am grateful for the opportunity to pursue my Ph.D. under her supervision; without her professional direction, my dissertation would not have been achievable.

I would also like to acknowledge Associate Professor Dr. Elena Ferapontova from Interdisciplinary Nanoscience Center (iNANO), Aarhus University, for giving me an opportunity to participate and work over the year in Denmark. Her guidance, motivation, and suggestions have greatly enhanced my learning experience in this journey. I am also grateful to the members of the Electrochemical Biosensors & Bioelectrocatalysis group for their backing and words of encouragement throughout difficult times. Specially to Dr. Suchanat Boonkaew for providing me with intelligent ideas to figure out all challenges there. Thank you for making my visit there a genuinely memorable and fulfilling experience.

I would like to extend my gratitude to Associate Professor Dr. Takeshi Kondo for providing me the opportunity to take part in the Sakura Science Project at Tokyo University of Science in 2019. During my three-week stay there, I gained significant knowledge of both research methodologies as well as Japanese culture.

I would like to express my appreciation to all members of the Electroanalytical and Imaging Sensor Research Group (EISRG), and my colleagues who have been a part of my academic journey. Your collaboration, shared passion, and ideas for the research, and friendship have enriched my experience and made this journey even more rewarding. A special thanks extend to Professor Dr. Orawon Chailapakul and the members of the Electrochemistry and Optical Spectroscopy Center of Excellence (EOSCE), Chulalongkorn University for their guidance and support with chemical and real samples resources during

this dissertation.

I am also grateful to the National Research Council of Thailand (NRCT) for the financial support of my Ph.D. study through the Royal Golden Jubilee (RGJ) Ph.D. Program. I would like to express my gratitude to the dissertation committee, Professor Dr. Orawon Chailapakul, Associate Professor Dr. Apinya Chaivisuthangkura, Associate Professor Dr. Panarat Arunrattiyakorn, and Associate Professor Dr. Kriangsak Songsrirote, for their insightful feedback and suggestions.

Last but not least, I would like to sincerely thank my parents, younger brother, and my relatives for their unwavering love, support, and encouragement. You all have been a source of strength, comfort, and motivation for me, and I am grateful for their unwavering belief in me even when I doubted myself. To my incredible friends, your willingness to listen, offer emotional support, and respect my point of view have helped me navigate challenging periods of my life with ease and reason. I cannot thank you enough.

Thank you all again for being a part of this milestone in my Ph.D. journey.

KANTIMA KAEWJUA

TABLE OF CONTENTS

Page

LIST OF TABLES

Page

LIST OF FIGURES

Page

CHAPTER 1
INTRODUCTION

1.1 Background

Over the past few decades, the development of analytical methods for determining biological and chemical markers in the quality and safety of food and healthcare applications has gained attention. The impact of these markers is critical to ensuring that their amounts do not affect human health. As a result, the requirement to develop and establish sensitive and practical analytical methods is always mentioned to obtain a new option for quantitative analysis. Several analytical techniques including high performance liquid chromatography (HPLC), gas chromatography (GC), spectrometric methods, quantitative real time polymerase chain reaction (qPCR) and enzyme-linked immunosorbent assay (ELISA) have been generally developed to fulfill those requirements. Even though their fascinating properties have enabled high sensitivity and selectivity, these approaches are inconvenient for routine and field analysis because of the large instrumentation, costly equipment, time-consuming, and complicated sample pretreatment. To overcome the aforementioned limitations, the development of a reliable and efficient analytical method for the detection of important biological and chemical markers is necessitated.

Biogenic amines (BAs) are one of the most important chemical markers of freshness index for protein-rich foods, microbial contamination, and quality of food products. BAs not only act as food quality markers for microbial contamination and processing conditions but also play a crucial role in physiological and toxicological effects. Tyramine is the most relevant biogenic amine which is found in cheeses (Özogul & Özogul, 2019) and is also commonly presented in other fermented products, dairy products, and beverages (McCabe-Sellers et al., 2006; Santos, 1996). The formation of tyramine is derived from the microbic decarboxylation of tyrosine. While this BA is normally present in small amounts, it was readily detoxified by the action of monoamine oxidase (MAO) in the human intestines and liver. However, large quantities of tyramine have been implicated as intoxication results for humans.

High consumption of tyramine-containing food can indirectly stimulate the increase of high blood pressure and heart rate through the release of noradrenaline from the sympathetic nerve endings (Rand & Trinker, 1968). Therefore, the potentially toxic effects of excessive amounts of tyramine may cause the adverse health risks such as severe headaches, migraine, brain hemorrhage, and heart failure (Smith, 1981). Especially, the patients who intake MAO inhibitor (MAOI) drugs can suffer a hypertensive crisis or cheese reaction (Ladero et al., 2010; Yigit & Ersoy, 2003), since the inhibition activity of these drugs may reduce the metabolism of tyramine leading to vasopressor effect. As mentioned, tyramine needs to be controlled in order to ensure the level of food quality and safety for consumers.

The other important biological markers that have a high potential for diagnostic and prognostic monitoring of cancer status will be focused on as sequence. As we know, cancer is caused by the biomarkers that are most commonly released by gene mutations and cell division. Normally, each cell type has its unique molecules and identifiable characteristics, such as gene activity, gene products, DNA, RNA, protein, enzymes, hormones, molecules and specific cells (Hasan et al., 2021). Therefore, the presence of these biomarkers at different levels from normality can be used as a marker for early detection of cancer status. The samples of detection can come from various human body fluids such as blood, urine, serum, and plasma depending on the progress of cancer. For example, the ratio of levodopa (L-DOPA) and L-tyrosine (L-Tyr) serves as an index of tyrosinase activity which is a key factor in melanogenesis since it catalyzes the rate-limiting step in melanin biosynthesis (Letellier et al., 1997). Hence, the L-DOPA/L-Tyr concentration ratio is one of the important biomarkers for the stage of melanoma in human serum and plasma. A few literature reviews addressed the development of simultaneous detection of L-DOPA and L-Tyr using the HPLC method (Letellier et al., 1999; Stoitchkov et al., 2003) and electrochemical technique (Hassanvand & Jalali, 2019; Revin & John, 2013). However, the development of electrochemical sensing for point-of-care testing of melanoma biomarkers detection,

which provides reliable diagnostics, significantly enhances sensitivity and specificity, is still needed.

Real-time tracking of oxidative metabolic substances is also crucial in clinical analysis due to their significance related to biological processes in living organism settings. Hydrogen peroxide (H_2O_2) is a signaling biomarker, that plays a key role in regulating metabolite operative processes in biological systems, such as cellular damage, aging, and cancer growth (Halliwell et al., 2000; Sies, 2017). Moderate intracellular level of H_2O_2 ranges from 10 nM to 1 μM (Stone & Yang, 2006). Additionally, elevated H_2O_2 levels in exhaled breath have been considered as a potential biomarker of inflammation and oxidative stress in the airways. It is a reliable and accurate indicator of lung-related illnesses such as chronic obstructive pulmonary disease (COPD) and asthma (Lases et al., 2000). The exhaled breath condensate (EBC) analysis serves as a non-invasive sampling tool for collecting biological samples without causing any physical injury to the body. Hence, measuring H_2O_2 in EBC samples has led to its potential monitoring and diagnosing pulmonary pathologies in humans. Nevertheless, the hydrogen peroxide content in the condensate tends to be low, typically ranging from nano-molar to micro-molar levels. Therefore, reliable and precise methods for real-time H_2O_2 monitoring in living cells remain challenging.

Accordingly, sensitive, selective, and inexpensive methods for the determination of biological indicators have been developed to evaluate their level for practical applications. Electrochemical technique has gained widespread acceptance as an alternative tool because of its simplicity, portability for on-site analysis, cost-effectiveness, fast response time, ability to analyze small volumes of samples, high sensitivity, and selectivity (Jadon et al., 2016). However, the major problem for the electrochemical detection of these mentioned biomarkers is poor sensitivity at bare electrodes without any modification. Hence, exploring new materials for electrode modification could be beneficial for remarkable improvement of the sensitivity of electrochemical sensing platforms. Recently, various materials have been used for the development of electrochemical sensors such as functionalized multi-wall carbon

nanotubes (Baghayeri & Namadchian, 2013), graphene (Zhang et al., 2016), enzyme-immobilization on various materials (Calvo-Pérez et al., 2013), nanocomposites between conducting polymer and nanomaterials (Dalkıran et al., 2019) ,and molecularly imprinted polymers (MIPs). Among these, the modified electrode via conducting polymers (CPs), has been achieving attention as a new trend in the electroanalytical field to solve the mentioned drawbacks because of their outstanding properties such as a wide range of electrical conductivities, ease of fabrication, corrosive resistance as well as high environmental stability.

Taking into account the aforementioned incentives, this dissertation has been split into two sections that focus on the development of new electrochemical sensing platforms to effectively and precisely determine biomarker levels. These platforms are constructed using either solely poly (amino acid) or in combination with nanomaterials and biocatalyst-linked carbonaceous materials-modified electrodes.

The first section of this dissertation is divided into two subprojects, which figure out the development of electrochemical sensing platforms for tyramine detecting and the simultaneous detection of L-DOPA and L-Tyr. The first subproject proposed the development of a novel electrochemical sensor based on poly(histidine) coated on printed graphene electrodes for tyramine detection. A poly(histidine) was prepared by electropolymerization directly at a screen-printed graphene electrode (poly(His)/SPGE). Moreover, this poly(His)/SPGE not only increases the electrochemical response of tyramine, but also possesses many significant advantages such as non-toxicity, biocompatibility, and ease of single modification step. After the systematic investigation and optimization of all parameters, this proposed sensor is expected to show a good linear range, reproducibility, and selectivity for the determination of tyramine. Furthermore, it will be successfully applied to the analysis of tyramine in real samples such as food samples and biological fluids.

The second subproject described the development of a new electrochemical platform for the simultaneous determination of L-DOPA and L-Tyr using layer-by-layer assembled poly(L-proline) decorated nanodiamonds on printed graphene. Generally,

the simultaneous detection of multiple analytes in electrochemical technique still suffers from similar redox potentials of analytes of interest. Hence, chemically modified electrodes fabricated from this research will be proposed to overcome the previous limitations by changing the redox reaction kinetics leading to the distinction between target analytes and co-existing substances. The as-modified electrode was fabricated via layer-by-layer electrodeposition of poly(L-proline) (poly(L-Pro)) and nanodiamond (ND) onto screen-printed graphene electrode. The use of poly(L-Pro) and ND-based electrodes paves a feasible way to unlock the coexisting interfering substances from ink composition and improve electrochemical response. Under optimal conditions, the developed sensor provided a wider linear concentration range with sufficient low limit of detection, making it suitable for real sample analysis. Ultimately, this sensor was utilized to prove a concept by using it to measure the amounts of L-DOPA and L-Tyr in human urine and serum samples. The precision and reliability of the as-proposed sensing platform were confirmed through the recovery and relative standard deviation, which matches the AOAC guidelines. As a result, this poly(L-Pro)/ND/SPGE can be a promising analytical platform for the prognosis and metastatic monitoring of melanoma as well as the other abnormalities related to these biomarkers.

The second section of this dissertation focused on the development of an electrochemical sensing platform using biocatalyst-linked carbon-based materials coated with SPGE for H_2O_2 detection in EBC samples. A non-enzymatic sensing platform was fabricated through a step-by-step drop-casting approach. First, short-thin multi-walled carbon nanotubes (ST-MWCNTs) was assembled on screen-printed graphene electrode (SPGE). Then, hemin-entrapped polyethyleneimine was drop-casted on ST-MWCNTs/SPGE, resulting in hemin-PEI/ST-MWCNTs/SPGE. Hemin-PEI/ST-MWCNTs/SPGE is a more efficient electrocatalyst towards H_2O_2 reduction due to its hemin-entrapped PEI characteristics and roughness features of ST-MWCNTs. The quantification of H_2O_2 was performed by chronoamperometry technique which provided good analytical performance. Such a sensor possesses excellent selectivity; it was successfully used to measure H_2O_2 in exhaled breath samples from healthy

subjects, yielding acceptable recovery ranges. Therefore, this proposed sensing platform has potential clinical significance as an alternative diagnostic tool for lung diseases.

1.2 Objectives of the research

The aim of this research consisted of three major goals as listed below:

1. To develop a novel electrochemical sensor for tyramine monitoring in cheese and biological samples for food safety and clinical monitoring.

2. To fabricate a new electrochemical platform for the simultaneous determination of L-DOPA and L-Tyr in urine and serum samples for evaluating the abnormalities related to these biomarkers.

3. To propose a non-enzymatic electrochemical sensing platform for amperometric detection of H_2O_2 for use as a potential alternative device for breath biopsy.

1.3 Significance of the research

1. New electrochemical sensors based on conducting polymers, nanomaterials, and biocatalyst modifiers can be used to determine the concentration of selected important biological and chemical markers, including tyramine, L-DOPA, L-Tyr, and H_2O_2.

2. All catalyst materials used in this research can be easily produced through straightforward techniques, thus boosting their electrochemical sensing capabilities.

3. The proposed electrochemical sensing platforms possess the potential to serve as promising alternative tools in practical applications such as food quality and safety control and clinical diagnosis.

1.4 Scope of the research

This research focuses on the development of new electrochemical sensors for the determination of tyramine, L-DOPA, L-Tyr, and H_2O_2. Chemically modified SPGEs based on amino acid-based polymers and biocatalyst materials were used to fabricate

electrochemical sensing platforms. All modifiers feature cost-effective materials, facile fabrication, and user-friendly while maintaining high sensitivity and selectivity. All parameters concerning modification processes, pH of supporting electrolytes, and electrochemical technique conditions were systematically investigated to obtain the optimal conditions. Analytical performances such as linear working range, the limit of detection, the effect of potential interfering substances, accuracy, precision, and long-term stability were studied. Subsequently, these developed sensing platforms were eventually applied to determine target analytes in real samples, with the goal of advancing them as alternative analytical tools for practical applications.

CHAPTER 2
THEORY AND LITERATURE REVIEWS

2.1. Electroanalytical chemistry

Electrochemistry is the subdiscipline of chemistry that is concerned with the relationship between electrical properties and chemical changes. The study of chemical changes generated by electricity in terms of a flow of electrons carried by an electric current and the electrical energy produced by chemical reactions (Bard & Faulkner, 2001). Therefore, the produced quantity of electrical properties, including current, potential, resistance, conductance, and capacitance, is an essential part that can be applied for field analysis, medical applications, environmental prevention, food safety & quality control, and other related areas (Zhu & Shi, 2019). Likewise, in field analysis, the electroanalytical technique encompasses a quantitative analytical approach based on the electrical properties of target analyte solution in the electrochemical cell.

Electroanalytical technique has been developed for qualitative and/or quantitative analysis of target analyte through measuring an electrical signal that is related to the concentration of the target analyte. This means that the measured electrical value is directly proportional to the target analyte concentration (quantitative analysis) or the characteristic potential (peak potential and half-wave potential) value can easily and unambiguously be determined (qualitative analysis) (Scholz, 2010). Depending on which characteristics of the cell are controlled and measured, this technique can be divided into 4 categories including potentiometry, coulometry, voltammetry, and electrochemical impedance spectroscopy (EIS). Here in, voltammetry and EIS techniques were employed as promising tools for quantitative analysis as well as electrochemical characterization of electrode interfaces in this research due to their sensitivity and wide dynamic range in field analysis.

2.1.1 Voltammetry

Voltammetry is a category of electroanalytical technique which is performed by applying potential to a working electrode versus a reference electrode and measuring the current (Kissinger & Heineman, 2018). The current obtained is the result from reduction or oxidation reaction of electroactive species at the working electrode. When the working electrode is applied potential to negative direction, electroactive species can be reduced (oxidizing agent) and resulting in reduction reaction. On the other hand, when the working electrode is applied potential to positive direction, electroactive species can be oxidized (reducing agent) and resulting in oxidation reaction.

A typical arrangement for a voltammetric electrochemical cell is shown in Figure 1. It consists of a three-electrode system, supporting electrolyte, and a potentiostat.

1. Three-electrode system, including a working electrode, counter electrode, and reference electrode, is an important part of this voltammetric electrochemical system.

1.1 Working electrode is a critical factor in the electrochemical reaction which corresponds to the concentration of the target analyte. The most important aspect of the working electrode is its different materials in the potential range of interest. The working electrode must be stable and may be modified by chemical surface modification to improve sensitivity.

1.2 Counter electrode is an electrode which is adjusted to balance the reaction occurring at the working electrode. It is usually made of inert materials such as platinum, gold, graphite, and glassy carbon. The surface area of this electrode must be higher than the area of the working electrode because of the reduction of the kinetic factor in the electrochemical process.

1.3 Reference electrode is used as a reference value against which the potential of a working electrode is measured in an electrochemical cell. This electrode is made in such a way that its potential is constant without any current

passing through it. The common reference electrode was used in voltammetry such as saturated calomel electrode (SCE) and silver/silver chloride electrode (Ag/AgCl).

2. Supporting electrolyte is a substance that is dissolved in the solvent to decrease the resistance. The characteristics of supporting electrolyte have a good conductivity, highly soluble, chemically and electrochemically inert, and pureness. Moreover, a proper supporting electrolyte concentration is also necessary to limit the migration current.

3. Potentiostat is used to control the applied potential of the working electrode as a function of the reference electrode potential.

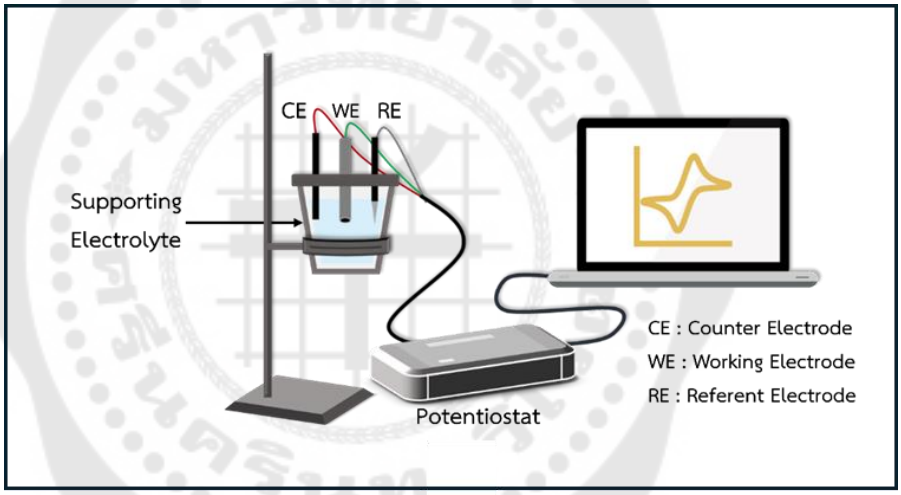

Figure 1 Illustration of a voltammetric electrochemical cell

Voltammetry includes linear sweep voltammetry (LSV), cyclic voltammetry (CV), normal pulse voltammetry (NPV), differential pulse voltammetry (DPV), square-wave voltammetry (SWV), stripping voltammetry, and amperometry. These techniques are effective for the quantitation of low levels and have a wide dynamic range that depends on the potential waveform which is scanned to a working electrode. In this research, cyclic voltammetry, differential pulse voltammetry, and chronoamperometry were used for electrode modification, characterization, and electrochemical detection, respectively.

2.1.1.1 Cyclic voltammetry

Cyclic voltammetry is a powerful and popular electrochemical technique employed as a first investigation of the electrochemical properties of electroactive species. In addition, it also offers a rapid location of the redox potentials of the electroactive species as well as the evaluation of the effect of media on the redox process.

In the CV experiment, the stationary working electrode is performed by scanning linearly the potential versus time as a potential waveform, as shown in Figure 2. The current that occurs at the electrode-solution interface from the electron transfer process is measured by the potentiostat during the potential scan. This obtained current is proportional to the concentration of electroactive species.

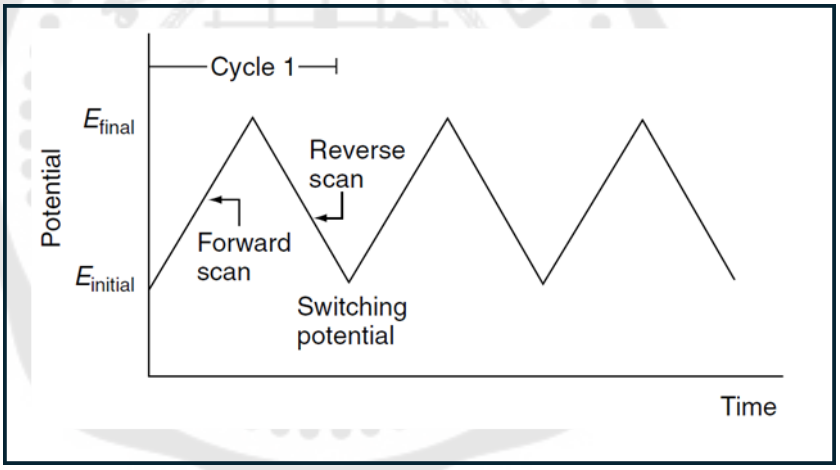

Figure 2 Potential waveform in a cyclic voltammetric experiment

Source: Wang, J. (2006). Study of Electrode Reactions and Interfacial Properties. Analytical Electrochemistry, 29-66.

The resulting plot of current versus potential is termed a cyclic voltammogram. The cyclic voltammogram for a reversible redox process in a single potential cycle is exhibited in Figure 3. The first half-cycle is performed by scanning potential to a more negative direction resulting in the only oxidized form (O) that initially

occurred. As the applied potential continually reaches the characteristic potentials (E°) of the redox process, a cathodic peak current ($I_{p,c}$) appears and the resulting potential is termed a cathodic peak potential ($E_{p,c}$). Whereas the applied potential is scanned in a positive direction, the reduced form (R) is re-oxidized back to O, resulting in an anodic peak current ($I_{p,a}$), and the resulting potential is termed an anodic peak potential ($E_{p,a}$) (Wang, 2006).

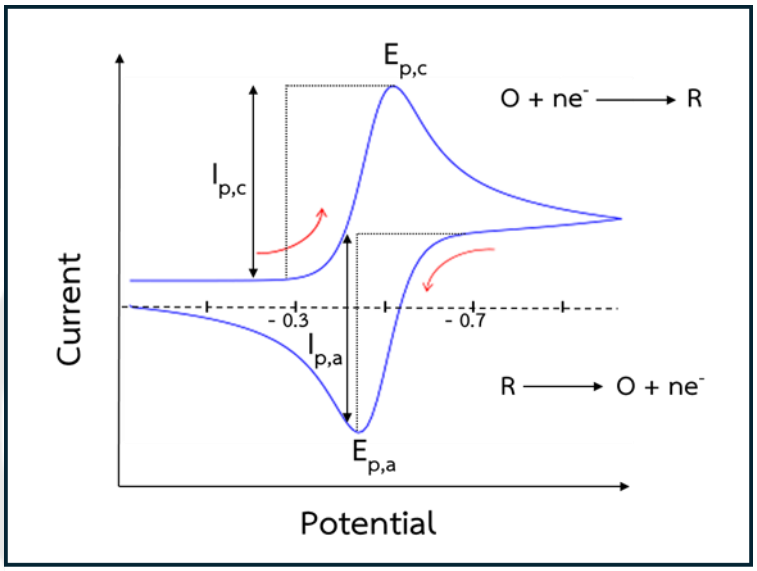

Figure 3 Cyclic voltammogram for a reversible redox process

Adapted from: Dickinson, E. (2013). Modeling Electroanalysis: Cyclic Voltammetry. Retrieved from https://www.comsol.com/blogs/modeling-electroanalysis-cyclic-voltammetry/

The cyclic voltammogram is characterized by several important parameters that influence the difference of the cyclic voltammetric response. The rate of electron transfer is a significant factor that affects CV response. It should be obvious that the CV response is related to the speed of electron transfer. If the electron transfer occurs quickly without thermodynamic barriers, it is called as a reversible process.

On the other hand, if the electron transfer is sluggish due to its complication, irreversible and quasi-reversible processes arise.

According to a reversible process, the expression for peak current is given by the Randles-Sevcik equation at 25°C, as:

$$I_p = (2.69 \times 10^5)\, n^{3/2} A C D^{1/2} \nu^{1/2} \quad \text{..... equation 1}$$

Where:

I_p is the peak current

n is the number of electrons involved in the redox reaction

A is the area of electrode in cm^2

C is the bulk concentration of the electroactive species in mol cm^{-3}

D is the diffusion coefficient in $cm^2\ s^{-1}$

ν is the scan rate in $V\ s^{-1}$

From the above equation, all parameters including the number of electrons, area of electrode, diffusion coefficient, and concentration of the electroactive species are constantly controlled. Thus, the increase of peak current depends on the square root of the scan rate. This means that the relationship between peak current and the square root of the scan rate is considerably useful for the study of controlled electrode processes at the electrode surface.

For an irreversible process, which is of the sluggish electron transfer process. The individual peaks are smaller and more widely separated (Figure 4, curve A). Since, an irreversible process is characterized by a shift of the peak potential with the scan rate. Thus, the peak current, given by:

$$I_p = (2.99 \times 10^5)\, n\, (\alpha\, n_a)^{1/2} A C D^{1/2} \nu^{1/2} \quad \text{..... equation 2}$$

Where:

I_p is the peak current

α is the electron transfer coefficient

n_a is the number of electrons involved in the redox reaction

A is the area of electrode in cm^2

C is the bulk concentration of the electroactive species in mol cm^{-3}

D is the diffusion coefficient in $cm^2\ s^{-1}$

ν is the scan rate in $V\ s^{-1}$

While a quasi-reversible process is controlled by both electron transfer and mass transport. The voltammogram of a quasi-reversible process (Figure 4, curve B) is extended, which leads to a larger separation in peak potentials compared to a reversible process.

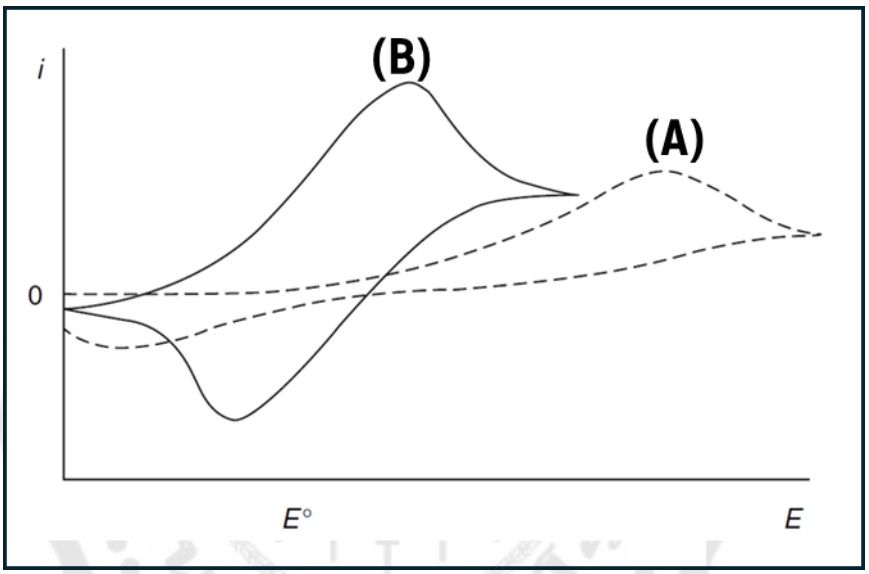

Figure 4 Cyclic voltammogram of (A) an irreversible and (B) a quasi-reversible process

Source: Wang, J. (2006). Study of Electrode Reactions and Interfacial Properties. Analytical Electrochemistry, 29-66.

For obtaining the characterization and qualitative information of target analytes, cyclic voltammetry is the most extensively used technique. Because of its capacity to rapidly provide significant information on the redox process and the kinetics of electron transfer reaction. However, this technique is not suitable for quantitative analysis due to its sensitivity and its complexity in peak identification of target analyte. Therefore, differential pulse voltammetry and chronoamperometry were selected for quantitative analysis of the target analyte.

2.1.1.2 Differential pulse voltammetry

Differential pulse voltammetry is one of the popular voltammetric techniques that is used for quantitative analysis of organic and inorganic substances. The power of this technique in field analysis is based on its superior elimination of the background current. Moreover, its sensitivity is achieved by the twice current sampling. The first current sampling is before the pulse application (t_1) and the second current sampling is at the end of the pulse application (t_2). A potential waveform for differential pulse voltammetry is shown in Figure 5. The voltammogram output is equal to the difference in the two current values ($\Delta i = i_1 - i_2$). The twice current sampling not only allows to detection of the target analyte solution at a concentration as low as 0.05 μM, but it also ensures that the differential pulse voltammogram has a symmetrical peak-shape. The obtained differential pulse voltammogram consists of a current peak which is directly proportional to the concentration of the target analyte.

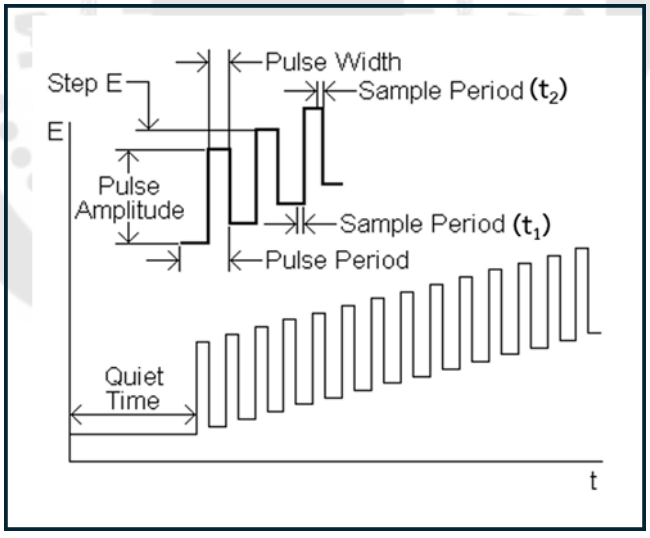

Figure 5 Differential pulse voltammetry waveform

Source: Bioanalytical Systems, Inc. Pulse Voltammetric Techniques. Retrieved from https://www.basinc.com/manuals/EC_epsilon/Techniques/Pulse/pulse.

2.1.1.3 Chronoamperometry

Chronoamperometry is a highly used detection method in the field of bioanalysis. In this mode, the working electrode is held at a constant potential, which is sufficient to either oxidize or reduce the target analytes at the electrode interface and the resulting current is monitored over time (Patel, 2020). The typical waveform is shown in the Figure. 6A. The voltage is initially held at a resting potential (E_1), at which no electron-transfer reaction occurs. Subsequently, the working electrode is stepped to E_2 beyond the E° of the redox species, allowing complete oxidation or reduction of the target analytes. Thus, the current is limited by diffusion and gradually decreases over time (Núñez-Bajo & Fernández Abedul, 2020). The current–time response signal (Figure 6B) for the forward potential step (E_1 to E_2) is described as a linear diffusion by Cottrell equation:

$$i = \frac{nFACD^{1/2}}{\pi^{1/2}t^{1/2}} \quad \text{..... equation 3}$$

where i is the current, t is time (s), n is the number of electrons (eq mol^{-1}), F is the Faraday's constant, A is the electrode area (cm^2), C is the concentration of target analytes (mol cm^{-3}), and D is the diffusion coefficient of target analyte (cm^2 s^{-1}).

Chronoamperometry offers greater selectivity in comparison to alternative pulse techniques. This is due to the fixed applied potential at a specific potential, which is based on the well-established essential reference subjected to the oxidation/reduction processes of target analytes. Thus, this approach has greater possibilities for practical applications.

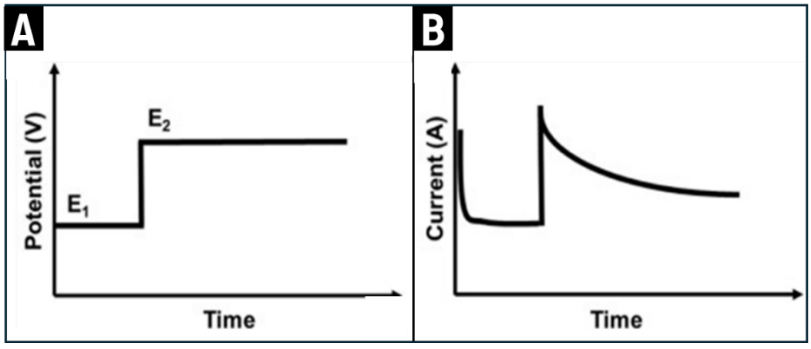

Figure 6 (A) Chronoamperometry waveform and (B) response signal for single step chronoamperometry

Source: Patel, B. A. (2020). Chapter 2 - Amperometry and potential step. Electrochemistry for Bioanalysis (pp. 9-26).

2.1.2 Electrochemical impedance spectroscopy

EIS is an interfacial technique utilized to monitor the impedance response to the applied current (voltage) as a function of frequency. Initially applied to the determination of the double-layer capacitance and in AC polarography, it is now used to characterize electrode processes and complex interfaces. Thus, it has grown in popularity owing to its ease of implementation and wide range of applications, including corrosion, batteries, coatings, semiconductors, fuel cells, electrocatalytic reactions, chemical reactions combined with faradaic processes, and so on. EIS measurement involves applying the small signal sinusoidal voltage (V) with varying frequency to the system. The resultant current (I) is subsequently measured (Lasia, 2002).

The impedance (Z) related to the system can be described through the Ohm's law as:

$$Z = \frac{V}{I} \quad \text{..... equation 4}$$

The Nyquist Plot (Figure 7A) displays the imaginary part ($Z_{Im}=i\,|Z|\sin\Phi$) over the real part ($Z_{Re}=|Z|\cos\Phi$) of the impedance. On the other hand, the Bode plot (Figure 7B), illustrates the absolute magnitude of the impedance IZI, and the phase shift Φ at two different Y-axes over the $\log_{10}$ of the applied frequencies. To describe this relationship for a sinusoidal signal over time, Z represents a complex function and therefore, consists of a real part (Z_{Re}) and an imaginary part (Z_{Im}) described by i =1 or i_2=–1

$$Z = Z_{Re} - iZ_{Im} \quad \text{..... equation 5}$$

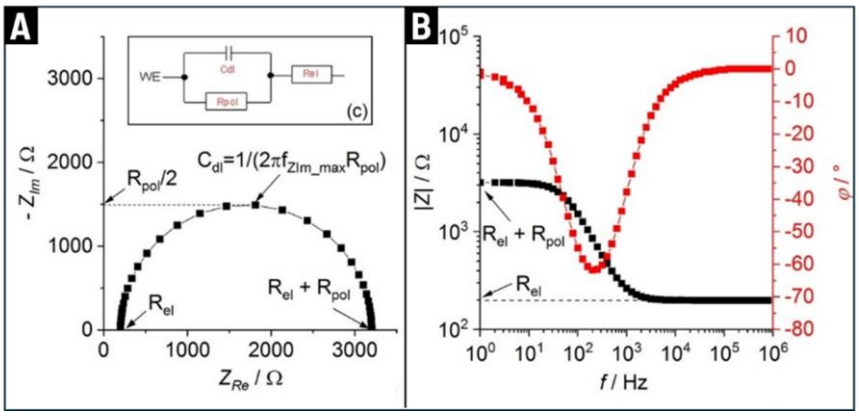

Figure 7 EIS data of an electrode immersed into an electrolyte with (A) Nyquist plot and (B) Bode plot

Source: Kretzschmar, J., & Harnisch, F. (2021). Electrochemical impedance spectroscopy on biofilm electrodes – conclusive or euphonious? Current Opinion in Electrochemistry, 29, 100757.

2.2 Screen-printed electrode

According to the voltammetric electrochemical cell, the conventional three-electrode system is complicated for on-site analysis and point-of-care testing. In order to achieve and comply with rapid testing and better traceability, the transition from conventional benchtop to miniaturized platform has attracted considerable attention. Therefore, screen-printed electrodes (SPEs) are a well-established platform for use as cost-effective and disposable sensors for target analyte detection.

SPE is a miniaturized electrochemical measurement device that consists of working, counter, and reference electrodes on an all-in-one substrate (Figure 8). The device can be manufactured on various substrates, such as transparency sheets, paper, and poly(vinyl) chloride, for suitable applications. As a result, this electrode has gained popularity in electrochemical sensors due to its inexpensive material, the possibility of production in different designs and materials depending on applications, the ease and speed of mass production, and its portability for on-site analysis.

Moreover, the electrode surface can be easily modified to improve the sensitivity and selectivity of measurement in electroanalytical applications.

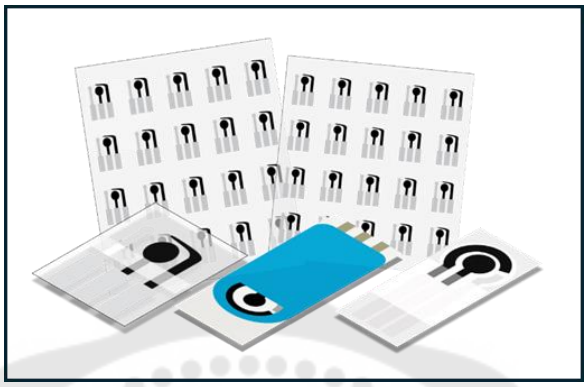

Figure 8 Schematic representation of screen-printed electrodes

2.2.1 Chemical modification of electrode surface

Chemically modified electrodes have been widely implemented as an efficient method for improving conductive properties, leading to sensitive and selective performances in the electroanalytical field. This method has been utilized for various applications because of its potential, such as ease of fabrication and the possibility of an in-situ approach. Modification of the electrode surface improves the electron transfer process while also acting as a catalytic phenomenon and causing a little change in surface characteristics. Regardless of the benefits of chemically modified electrodes, the appropriate modifier is a crucial factor, which in turn allows for better sensitivity and selectivity. Among the modifiers commonly used for electrode modification are metal nanomaterials, carbon-based nanomaterials, and conducting electroactive polymers (Jadon et al., 2016). Therefore, this research focuses on new poly (amino acids), biocatalyst materials, and carbon-based nanomaterials to improve sensitivity of the proposed sensors for target biological and chemical marker detection.

2.2.1.1 Poly (amino acids)

Amino acids are the building blocks of peptides and proteins, which are essential components found in living organisms. Their molecular structure, which

contains two functional groups (the carboxyl and the amine groups) and distinct side chains, makes them crucial for a wide range of physiological processes. Amino acids-based polymers have attracted significant interest for practical use due to their unique characteristics, such as biocompatibility, non-toxicity, aqueous solubility, stimuli-responsive capabilities, high stability, and self-assembly nature (Gohil et al., 2017). In addition, the presence of distinctive side chains in poly (amino acids) offers the potential for attaching cross-links with other substrates, which can be used to modify a physio-mechanical characteristic and detect a wide range of biomarkers, and important substances (Bauri et al., 2018). The electropolymerization procedure is a beneficial method for facile polymerization that is crucial for producing biocompatible polymer materials. Therefore, poly (amino acids) has great potential in the field of sensing. These materials are extremely effective in immobilizing biological receptors, attaching directly to target analytes, and accelerating electron transfer.

Based on their different effective side chains, L-histidine and L-proline were used as monomers for creating conductive polymers in as-synthesized sensing platforms in this research. Histidine is an essential amino acid that is comprised of a positively charged imidazole side chain. While proline is a non-essential amino acid, which contains a secondary amino group on the alpha position of the carboxyl group. Three techniques, electropolymerization, radical polymerization, and self-polymerization, have been employed to fabricate poly (His)- and poly(L-Pro)- based sensors. To improve sensitive and selective sensors, these conductive polymers need to be functionalized with additional materials, including metal nanoparticles, carbon-based materials, nanocomposites, and magnetic mesoporous materials (Dalmasso et al., 2015; Hasanzadeh et al., 2018; Hasanzadeh et al., 2017; Mavrogiorgis et al., 2014).

Considering the complicated and multi-step architecture of the fabrication process, it is essential to figure out a more straightforward method for creating poly(amino acids)-based sensors. Furthermore, there are no previously published studies on the detection of target analytes using both of these materials. In this dissertation, poly (His) and poly(L-Pro) were produced using a simple

electropolymerization method under mild conditions. These polymers were developed to enable efficient detection of tyramine and simultaneous detection of L-DOPA and L-Tyr, respectively.

2.2.1.2 Nanomaterials

Significant advances in nanotechnology have opened the road for the invention of a wide range of new materials and devices with attractive characteristics for a variety of applications. Nanomaterials are substances that have at least one dimension in the nanoscale range, which is between 1 and 100 nm (Datta et al., 2022). They have garnered significant interest due to their exceptional physicochemical features, such as high mechanical resistance, good electrical and thermal conductivity, biocompatibility, and ease of surface modification through chemical processes. The classification of nanomaterials consists of three distinct categories: discrete nanomaterials are either zero-dimensional (particles) and/or one-dimensional (fibers), nanoscale device materials (two-dimensional (thin films)), and bulk nanomaterials (three-dimensional). Discrete nanomaterials, such as nanodiamonds and multi-walled carbon nanotubes, were the primary focus of this dissertation.

2.2.1.2.1 Nanodiamond

Nanodiamond (ND) refers to the broad category of nanocarbons, which encompasses various nanosized structures such as amorphous carbon, fullerenes, diamondoids, tubes, rods, cones, whiskers, platelets, and foam. The structure consists of a core based on tetrahedral sp^3 carbon. It has attracted interest due to its low-cost, large-scale synthesis using carbon-containing explosives, small core particle size (about 4 to 5 nm) with narrow size distribution, simple surface functionalization, and high biocompatibility. Furthermore, the existence of delocalized π-bonds and oxygenated functional groups on ND's surface improves its electrical conductivity (Holt et al., 2008). Being a nanomaterial, the ND surface chemistry dominates the electrochemical behavior of these nanoparticles. It has the capability to produce homogeneous mixtures in aqueous solutions, which is a fascinating feature for

creating modified electrodes for electroanalytical purposes (Schrand et al., 2009). Hence, ND is a highly promising material for developing new electrochemical sensors with remarkable analytical performance.

2.2.1.2.2 Multi-walled carbon nanotubes

Multi-walled carbon nanotubes (MWCNTs) are elongated, hollow, cylindrical nanostructures composed of sp^2 carbon atoms. They extend several centimeters in length and range in diameter from 3 to 30 nanometers. Their numerous concentric tubes composed of rolled-up graphene show remarkable characteristics such as a large active surface area, mechanical strength, and low charge-transfer resistance in both aqueous and non-aqueous conditions (Kukovecz et al., 2013). MWCNTs offer a range of capabilities to enhance the performance of electrochemical- and bio- sensors, turning them into highly effective devices for analytical applications. Herein, this material was used for enlarging the active surface area on printed graphene electrodes in the second section of this dissertation.

2.2.1.3 Biocatalyst materials

Biocatalyst materials can be produced from the use of enzymes as biological catalyst-based substrates to produce a range of important metabolites. They have been positioned as an area of wide interest because of their low toxicity and environmentally friendly catalysts, as well as their excellent selectivity (Melgarejo-Torres et al., 2019; Simoska et al., 2023). Hemin, a well-known natural iron protoporphyrin (IX), is one of the most popular biocatalyst materials in the field of sensor technology. It is the main active center for the hemeprotein family, which includes b-type cytochromes, peroxidase, myoglobin, and hemoglobin (Guo et al., 2011; Kolpin & Swofford, 1978). It possesses peroxidase-like activity, with the porphyrin ring composed of 4 pyrrole rings and the nitrogen atom on the pyrrole rings coupled with a ferrous ion ligand (Zhang & Dasgupta, 1992). Hemin offers an effective catalytic activity for H_2O_2 reduction due to its unique redox characteristics, which arise from the electron-conjugated system with π bond and changes in the valence state of iron ions (Fe^{3+}/Fe^{2+}) (Xue et al., 2012).

Applying hemin as a catalyst is still an ongoing challenge due to its ability to form inactive catalyst dimers in aqueous solutions and suffer oxidative self-destruction in oxidizing environments, both of which limit its catalytic activity. Hence, the use of supporting materials such as polymers can enhance stability while improving the direct electron transfer characteristics of hemin, thus boosting the efficacy of sensing performance. As a result, hemin-stabilized polyethyleneimine was used as a biomimetic catalytic material for H_2O_2 sensing platform in this research.

2.2.1.4 Polyethyleneimine

Polyethyleneimine (PEI) is a positively charged polymer that has been found to improve both the activity and stability of enzymes. Generally, PEI can be classified into two categories: linear and branching (Bahulekar et al., 1991). Linear polyethyleneimine is a solid powder that consists mainly of secondary amines. Conversely, branched PEI is a colorless liquid with a dense consistency that contains a combination of primary, secondary, and tertiary amines. The ratios of primary, secondary, and tertiary amino groups in PEI structures can vary according to the synthesis process used. PEI is utilized for the precipitation of nucleic acids and as a flocculating agent to remove cell debris during the purification of proteins from raw materials. The polymer's abundant amine groups enable it to efficiently immobilize biocatalysts onto solid substrates via adsorption, which facilitates the covalent binding of enzymes (Chen et al., 2020). Herein, branched PEI was employed as a stabilizing agent for the hemin matrix, enabling the assembly of effective biomimetic systems.

2.3 Tyramine

2.3.1 Significant roles of tyramine

Biogenic amines (BAs) are low-molecular-weight nitrogenous compounds that can be formed mainly by decarboxylation of amino acids through enzymatic activity or decarboxylase activity of bacteria. The level of these BAs presents normally in the body with biological activity influencing important physiological functions (Biji et al., 2016). However, the excessive ingestion of BAs is associated with adverse health effects on consumers. Thus, the quantitative risk assessment of BAs is critical to ensure that the consumed food is not contaminated with high levels of these potentially harmful substances. In order to their quantities and toxicological effects, the most important BAs with serious effects for human health are histamine and tyramine. This research focuses on tyramine due to its high cytotoxicity at concentrations commonly found in BA-rich food (Linares et al., 2016).

Tyramine (p-hydroxyphenethylamine) is an aromatic biogenic amine (Figure 9) that is produced by the microbic decarboxylation of tyrosine. It is commonly found in a variety of fermented food, beverages, and dairy products, including aged meat, sausage, soy sauces, fish, beer, wine, and yoghurt, especially cheese. Tyramine is normally metabolized by the monoamine oxidase (MAO) enzyme leading to inactive activity. Nevertheless, high amounts of this BA can be hazardous to human health because it can trigger intoxication processes and severe symptoms, such as hypertensive crises, severe migraines, and even brain hemorrhages. Moreover, it associates with individuals on monoamine oxidase inhibiting drugs after the consumption of cheeses with high levels of tyramine, is known as “cheese reaction” (Shalaby, 1996). Tyramine exerts vasopressor effect as it is an indirectly acting sympathomimetic amine. This phenomenon will be available for the uptake of tyramine into the sympathetic nervous system, induces the release of noradrenaline (Figure 10) which causes an increase of the blood pressure and cardiac output (Youdim et al., 2006).

Tyramine’s toxicological level is extremely difficult to establish. The European Food Safety Authority (EFSA) concluded that exposure to 600

mg/person/meal of tyramine in food had no adverse health effects on healthy people who did not take monoamine oxidase inhibitor drugs. However, individuals who took third-generation and classic MAOI drugs had safe limits of 50 and 6 mg, respectively (Hazards, 2011). The maximum tolerable tyramine contents of food products in Austria were found to be 1000 mg kg^{-1}, 2000 mg kg^{-1}, 950 mg kg^{-1}, and 800 mg kg^{-1} for cheese, fermented sausage, fish products, and sauerkraut, respectively (Paulsen et al., 2012). Similarly, the acceptable levels of tyramine in cheese is also reported in the range of 100–800 mg kg^{-1} (Benkerroum, 2016). Furthermore, intravenous injections of tyramine at dosage of 30 μg kg^{-1} were observed to cause a considerable vasopressor effect, probably related to the plasma noradrenaline concentration (Bianchetti et al., 1982).

The measuring of tyramine levels in biological fluids and even food is vital to acquire a better knowledge of the biological functions and to avoid the risk of tyramine. Consequently, a simple and highly sensitive analytical method for tyramine detection is required for healthcare applications and food safety & quality controls.

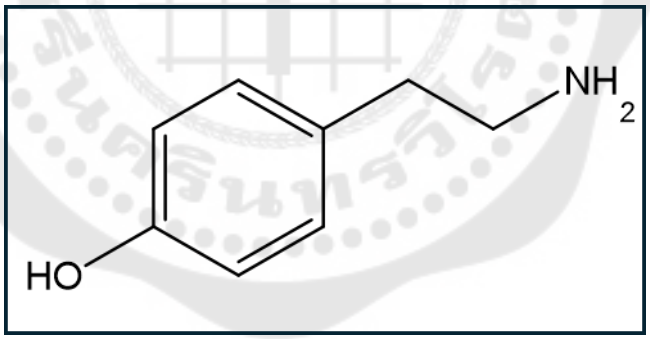

Figure 9 The chemical structure of tyramine

2.3.2 Literature reviews

According to the potential impact of dietary tyramine on human health, researchers have attempted to develop and propose analytical methods for tyramine detection, including high performance liquid chromatography, gas chromatography, ion chromatography, spectrometric methods, quantitative real time polymerase chain reaction, enzyme-linked immunosorbent assay, and capillary electrophoresis. However,

the methods mentioned above required time-consuming, several sample preparation procedures, specialized operators, and expensive instruments, which have been limited to routine and on-site monitoring. Therefore, the electroanalytical method is a great alternative for measuring tyramine. Because of its benefits, such as portability for on-site analysis, ease of operation, cost-effectiveness, rapid analysis time, and sample volume reduction while maintaining high sensitivity and selectivity. Hence, these literature reviews focus on the working electrode materials and the different modifiers used for electrochemical detection of tyramine.

In 2013, Calvo-Pérez et al. proposed a disposable amperometric biosensor for selective detection of tyramine in complex matrices. This proposed biosensor was fabricated by immobilization of plasma amine oxidase (PAO) enzyme on screen-printed carbon electrodes (SPCEs). The PAO enzyme was immobilized via a cross-linking process using a mixture of glutaraldehyde (GA) and bovine serum albumin (BSA), which made its catalytic sites more accessible for redox reactions. In addition, hydroxymethyl ferrocene (HOMeFc) was employed as a redox mediator that generated the enzyme-catalytic tyramine oxidation at potentials of +0.26 V. This lower potential decreased the possibility of interfering effect in the electrochemical detection of the target analyte. Therefore, the PAO/SPCE biosensor provided high sensitivity, selectivity, good reproducibility, and repeatability for tyramine determination. Moreover, it was successfully applied to the determination of tyramine in cheese samples (Calvo-Pérez et al., 2013).

In 2016, Zhang's group developed a simple electrochemical sensor for octopamine and tyramine measurements. The developed sensor was fabricated based on electrochemically reduced graphene oxide (ERGO) nanosheets modified on the glassy carbon electrode (GCE). The oxidation responses of target analytes at the ERGO/GCE were considerably increased and shifted to negative potentials when compared with the bare GCE. As a result, the use of ERGO modified GCE possessed a large surface area and good electrocatalytic activity towards octopamine and tyramine oxidations. In addition, this developed sensor exhibited highly sensitive detection of

octopamine and tyramine with detection limits of 0.1 μM and 0.03 μM, respectively (Zhang et al., 2016).

In 2017, Li et al. proposed a sensitive electrochemical sensing platform coupled with molecularly imprinted polymer (MIP) for tyramine quantification. The proposed sensing was achieved by constructing a conductive polymer on a screen-printed carbon electrode, followed by electrodeposition with gold nanoparticles (AuNPs) for linking with positively charged 1-methyl-4-mercaptopyridine (1-m-4-MP) through Au-S bond. In addition, this approach is performed by controlling the negatively charged tyramines under alkaline conditions which selectively interact with positively charged electrode surfaces, leading to highly sensitive detection. Therefore, the developed electrochemical sensing that coupled with sample pre-treatment showed an excellent analytical performance for tyramine detection and is also applied for practical application (Li et al., 2017).

The indium tin oxide (ITO) electrode modified with electrochemically reduced graphene oxide (ErGO) through 3-aminopropyltriethoxysilane (APTES) monolayer (ITO/APTES/ErGO) was developed by Liu's group in 2018. The modified electrode provided a sensitive and selective behavior towards electrooxidation of tyramine in the presence of other interferences due to its potential of ErGO which increased the active electrochemical surface and conductivity. In addition, this modifier exhibited the electrocatalytic activity towards the oxidation of tyramine, leading to a clearly well-defined peak of tyramine in the presence of high concentrations of interfering substances. The resulting sensor presented a good analytical performance via the concentration range of 1–100 nM with LOD of 0.1 nM. Moreover, the obtained recovery data in real sample detection suggested that this proposed sensor was reliable in food and clinical applications (Khan et al., 2018).

Kucukkolbas's group proposed a new non-enzymatic sensor based on TiO_2-Ag/PPy nanocomposite modified glassy carbon electrode (GCE). In this work, the utilization of metallic nanoparticles coupled with conductive polymers possessed high conductivity and increased the surface area of electrodes resulting in the excellent

capacity of the electron transfer process. The linear concentration range of tyramine was found to be 41.0 nM to 3.06 μM with a limit of detection of 20 nM. Furthermore, the proposed sensor offered good sensitivity, repeatability, anti-interference ability, and suitable for real food sample analysis (Erdogan et al., 2018).

A novel amperometric biosensor for the determination of tyramine was developed by Brett's group. This developed sensor was fabricated with the nanocomposites between gold nanoparticles and poly-(8-anilino-1-napthalene sulphonic acid) modified on glassy carbon working electrodes. To enhance the specific detection of target analyte, this fabricated electrode was immobilized with tyrosinase enzyme. For electrochemical detection, it was performed by fixing the potential at –0.3 V using amperometry technique. Under the optimal conditions, the calibration curve showed a good linear concentration in the ranges of 10–120 μM with LOD 0.71 μM. Hence, it was found that this biosensor had good selectivity and stability, and that it has been potentially used to quantify tyramine for food safety purposes (da Silva et al., 2019b).

Recently, Ayerdurai et al. presented a molecularly imprinted polymer (MIP) film-based electrochemical sensor for the selective determination of tyramine. For the specific recognition, tyramine was imprinted in a derivatized polythiophene conductive film. The electrochemical detection of tyramine is performed by using potassium hexacyanoferrate as a redox probe. The concept of this sensor is that a high concentration of tyramine accumulated into the MIP film cavity, which blocked the flow of the redox probe to the electrode surface, resulting in a decreased current signal. Therefore, this developed sensor provided enough selectivity for tyramine detection in food samples (Ayerdurai et al., 2021). Moreover, the other enzymatic sensors and non-enzymatic sensors for determination of tyramine were summarized as shown in Table 1

Table 1 Comparison of the various modified electrodes-based sensors for tyramine detection.

Modification electrode	Technique	Linear range (μM)	LOD (μM)	References
MWCNT-AuNP/chitosan/MIP	Amp	0.1 -10	0.057	(Huang et al., 2011)
Modified MWCNT/GCE	DPV	1–17 and 17-85	0.8	(Raoof, Ojani, Baghayeri, et al., 2012)
Pea seedling amine oxidase MnO_2/SPCE	Amp	10–300	3.0	(Telsnig et al., 2013)
Polypirrole/Pt	Amp	4–80	0.547	(Apetrei & Apetrei, 2013)
Tyr_{ase}/TiO_2/CMK-3/PDDA/Nafion/GE	CV	6–130	1.5	(Kochana et al., 2016)
P3MT/Pt	DPV	4.4 - 14000	1.32	(Küçük & Torul, 2018)
OPOAP/GCE	SWV	0.1-200	0.054	(Zhao et al., 2018)
AuNP-PANSA/AuE	EIS	0.8–80	0.04	(da Silva et al., 2019a)
PCGE	DPV	0.6–100	0.5	(Gonçalves da Silva et al., 2021)

AuNP = gold nanoparticle; MWCNT = multi-walled carbon nanotube; MAO = monoamine oxidase A; GCE = glassy carbon electrode; Tyr_{ase}= Tyrosinase; SPCE = screen-printed carbon electrode; TiO_2 = titania dioxide sol; PDDA = poly-(diallyl dimethyl ammonium chloride); GE = graphite electrode; P3MT = poly(3-methylthiophene); Pt = Platinum electrode; OPOAP = Overoxidized Poly(o-aminophenol); PANSA= poly-(8-anilino-1-napthalene sulphonic acid); AuE= gold electrode; PCGE = pencil carbon graphite electrode; Amp= Amperometry; CV= Cyclic voltammetry; DPV= Differential pulse voltammetry; EIS = Electrochemical impedance spectroscopy.

According to the literature reviews, the previously modified electrodes are limited by multiple modification steps and the use of complicated materials which became the inability for on-site and real-time analysis. They are challenging problems to improve these limitations while maintaining high sensitivity and selectivity for the detection of the target analyte. Hence, this research demonstrated the use of a modified electrode based- conducting polymer by using histidine as a monomer. A facile and simple electropolymerization procedure was utilized for generating the poly (His) film onto the electrode surface. In addition, these generated films become a new biocompatible material for electroanalytical applications. Moreover, the benefits in terms of excellent electrical properties, ease of synthesis onto electrode surfaces by environmentally-friendly processes, and good electrocatalytic materials were obtained (Kordasht et al., 2021).

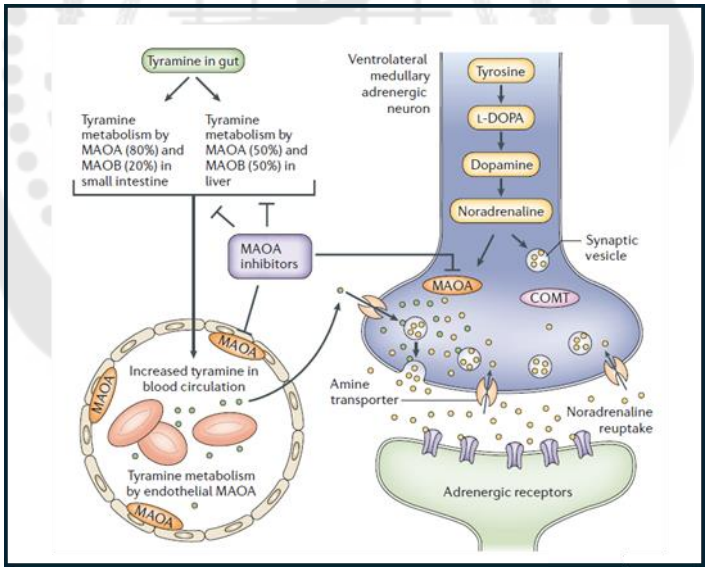

Figure 10 The mechanism of potentiation of vasopressor effects of tyramine

Source: Youdim, M. B., Edmondson, D., & Tipton, K. F. (2006). The therapeutic potential of monoamine oxidase inhibitors. Nature reviews neuroscience, 7(4), 295-309.

2.4 Significant roles of L-DOPA and L-Tyr

L-DOPA is the naturally occurring via biosynthesis from the amino acid L-tyrosine through tyrosine hydroxylase. It is easily converted to dopamine in dopaminergic cells by DOPA decarboxylase, which regulates dopamine levels and alleviates Parkinson's disease symptoms. Hence, L-DOPA is the major drug used in the treatment of patients with Parkinson's disease (Chaudhuri et al., 2006; Sveinbjornsdottir, 2016). Nevertheless, long-term use of L-DOPA might result in adverse effects such as low blood pressure, nausea, cognitive impairment, and disruptions in sleep cycles (Hadjiconstantinou & Neff, 2008; Pourhajghanbar et al., 2023). Significantly, there have been research studies suggesting a potential cause-and-effect association between levodopa treatment and an increased risk of malignant melanoma.

L-Tyr is a non-essential amino acid and can be synthesized in the body by hydroxylation of phenylalanine. It plays a crucial role in controlling protein synthesis and maintaining an appropriate nitrogen balance (Weber & Reiser, 1982). Additionally, it serves as a precursor to several neurotransmitters, including adrenaline, norepinephrine, and dopamine. Excessive accumulation of L-Tyr and its byproducts in living organisms might result in significant negative health effects. High levels of tyrosine can lead to hyperthyroidism and Parkinson's disease, whereas low levels can result in hypothyroidism, dementia, depression, and albinism (Chitravathi et al., 2012).

Interestingly, L-DOPA and L-Tyr serve as initial materials for melanin biosynthesis, and the ratio of both chemicals defines the index of tyrosinase activity. In addition, tyrosinase has an essential part in melanogenesis as its abnormality boosts the rate-limiting process in the melanogenic pathway by converting L-Tyr to L-DOPA via hydroxylation. Then, L-DOPA is oxidized to dopaquinone, which is further oxidized to dopachrome, yielding 5,6-dihydroxyindoles. These derivative indoles are finally oxidized to produce eumelanin (black/brown pigments). Conversely, if dopaquinone conjugates with cysteine or glutathione, pheomelanin (red/yellow pigments) is produced (Figure 11) (Hushcha et al., 2021; Slominski et al., 2012). The typical blood serum levels of L-DOPA and L-Tyr concentrations, as well as the L-DOPA/L-Tyr ratio in healthy

persons, are approximately 6.48 nM, 60.0 μM, and 16.0×10^{-5}, respectively. Melanoma patients can be detected by monitoring the ratio of L-DOPA to L-Tyr in their blood serum, which should be over 20×10^{-5}(Garnier et al., 2007; Stoitchkov et al., 2003). Hence, the L-DOPA/L-Tyr ratio in human plasma and serum samples can be considered a crucial biomarker for determining the stage of melanoma, predicting disease progression, and mortality in individuals with metastatic melanoma (Stoitchkov et al., 2002). Apart from the benefits pointed out, the abnormal levels of these biomolecules are significant for diagnosing further clinical conditions, including progressive neurological illnesses, neuropsychiatric disorders, and eating disorders (Capuron et al., 2011).

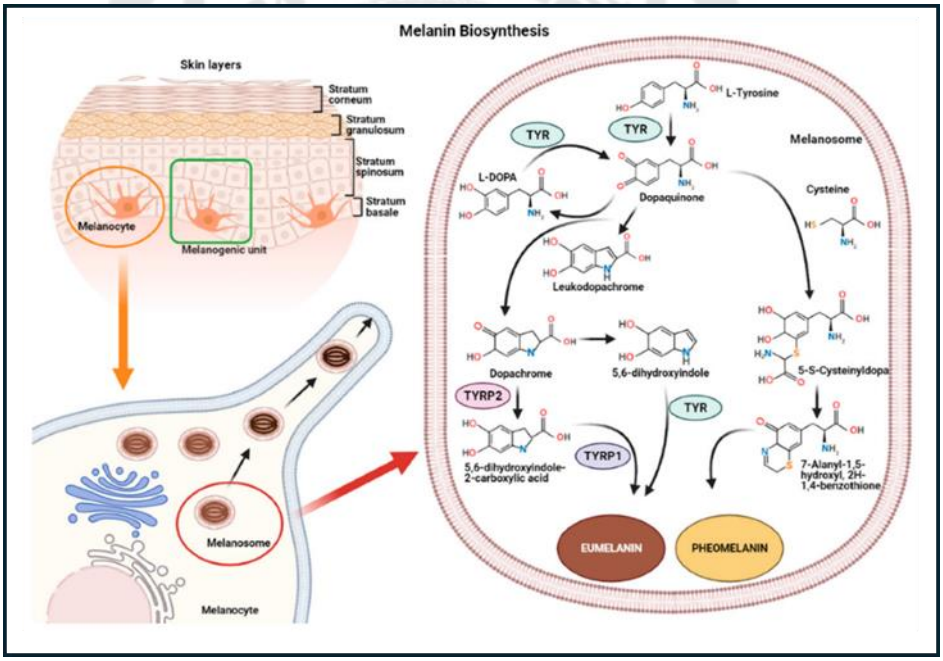

Figure 11 Representation of the melanogenic unit and melanin biosynthesis

Source: Hushcha et al., 2021 microRNAs in the Regulation of Melanogenesis. International journal of molecular sciences, *22*(11), 6104.

2.4.1 Literature reviews

The incidence of malignant melanoma has significantly increased in recent years. Therefore, the development of an analytical platform that features a simple, sensitive, selective, and fast method for analyzing specific biochemical markers is crucial for supporting medical professionals in diagnosing and tracking these diseases. Only a few techniques, such as high-performance liquid chromatograph, and capillary electrophoresis coupled with different detectors, have been developed to simultaneously determine L-DOPA and L-Tyr. Nevertheless, most of those techniques are tedious and rely on sophisticated technology, costly equipment, sizable instruments, and the requirement for sample preparation. Alternative methods, including electroanalytical techniques, have been proposed to detect both target analytes simultaneously. The molecular structures of both target analytes (Figure 12) are similar, except for the presence of a more hydroxyl group on L-DOPA. Due to their structural similarity and susceptibility to oxidation at slightly distinct potentials, thus, simultaneous detection of both target analytes is challenging.

In 2013, Revin, SB, and John, SA have proposed an electrochemical platforms for the malignant melanoma by determining L-DOPA and L-Tyr ratio using poly(3-amino-5-mercapto-1,2,4-triazole on glassy carbon electrode (p-AMTa/GCE) (Revin & John, 2013). The use of p-AMTa film-based electrodes successfully distinguished the signals of L-DOPA and L-Tyr in a mixture. Under the optimized conditions, the sensor demonstrates a linear range from 1×10^{-8} to1×10^{-4} M, with a limit of detection of 5.78×10^{-11}M (S/N = 3) for L-DOPA, while Tyr concentration in the linear range of 5.0×10^{-8}–1×10^{-4} M with the limit of detection of 1.9×10^{-10}M. Moreover, the researchers have successfully determined the concentrations of L-DOPA and L-Tyr in human blood plasma samples.

Yang, JH et al presented an electrochemical sensing approach for monitoring L-DOPA and L-Tyr (Yang et al., 2014). The use of various cyclodextrin (CD) possesses physically unique molecular structures to target analytes, which enhance the selectivity towards L-DOPA and L-Tyr oxidations. The developed sensing platform has

successfully detected two distinct analytes, in the absence of ascorbic acid, with α-CDs and γ-CDs exhibiting a stronger response to L-Tyr, while β-CDs showed a greater sensitivity to L-DOPA. Using amperometry as a quantitative method, the current obtained demonstrated a linear relationship with increasing concentrations ranging from 0.005 to 10 mM when plotted on a logarithmic scale.

In 2018, the simultaneous detection of L-DOPA and L-Tyr using gold–cobalt binary composites on screen-printed carbon electrodes (Au-Co/SPCEs) (Shaidarova et al., 2018) was proposed. The as-proposed sensor was successfully fabricated through the electrodeposition of the bimetallic Au–Co system. These modifiers offer a significant increase in oxidation current, as well as a lower oxidation potential of both analytes at the modified electrode, allowing better sensitivity and a low limit of detection. Moreover, amperometry measurement coupled with a flow-injection system was used to determine L-DOPA and L-Tyr. The linear dependence of the current signal on the concentration of L-DOPA and L-Tyr is observed in the ranges from 1×10^{-9} to 1×10^{-4} M and from 5×10^{-8} to 5×10^{-4} M, respectively.

Crown ether - modified poly(hydroquinone) / carbon nanotubes - based electrochemical sensor was developed by Atta's group in 2020 (Atta et al., 2020). This CE/PHQ/CNT/GCE sensor was used to detect L-DOPA, uric acid, L-Tyr, and ascorbic acid levels in biological fluids. The developed exhibited good responses towards simultaneous determination of L-DOPA, uric acid, L-Tyr, and ascorbic acid in the concentration ranges of (0.005–20 μM), (0.005–25 μM), (0.03–170 μM), and (0.1–50 μM) with low detection limits of 0.221 nM, 0.769 nM, 1.31 nM, and 3.32 nM, respectively. The practical application was proved in the detection of target analytes in human serum samples with excellent recovery results.

Recently, poly (para toluene sulphonic acid) modified glassy carbon electrode (pPTSA/ GCE) was reported by Kumar's group to detect L-DOPA and L-Tyr simultaneously. pPTSA-based GCE has an efficient electrocatalyst for the oxidation of L-Dopa and L-Tyr, allowing their simultaneous determination. Combining effective modified electrodes with sensitive square wave voltammetry provides electrochemical

signals that rapidly determine target analytes. The calibration curve was obtained within two dynamic ranges from 9 × 10^{-5} M to 2 × 10^{-5} M and from1 × 10^{-5} to 1 × 10^{-6} M for L-DOPA and from 7 × 10^{-5} M to 2 × 10^{-5} M and from1 × 10^{-5} to 1 × 10^{-6} M for L-Tyr. The pPTSA/GCE was applied to quantify both analytes in artificial blood serum and urine samples as well.

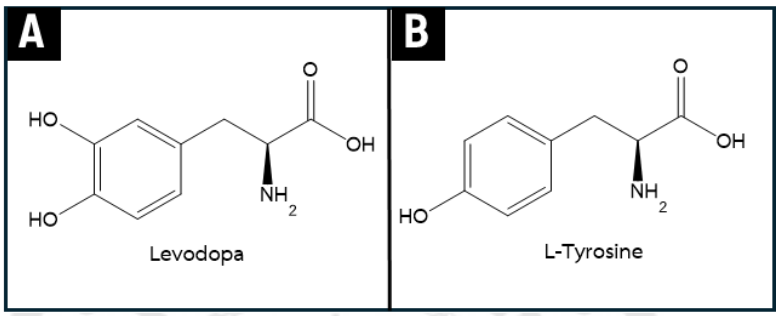

Figure 12 The chemical structures of (A) L-DOPA and (B) L-Tyr

As mentioned in the literature reviews, the previous reports proposed various modifiers-based sensing platforms. All of the aforementioned modified electrodes exhibited poor long-term stability and required time-consuming modification operations, making them unsuitable for practical point-of-need applications. Improving sensitivity and selectivity for the detection of both analytes while overcoming these limitations are challenging issues to resolve. In this dissertation, a straightforward and sensitive electrochemical sensor-based layer-by-layer poly(L-Pro)/ND/SPGE was developed to simultaneously detect L-DOPA and L-Tyr to unlock the bottleneck issues. The fabrication process of modified electrodes takes just 8 min., accomplished by the electrodeposition of poly(L-Pro) and ND. The coupling between the good conductivity of poly(L-Pro) and the high surface area of ND offers fast electron transfer and shows excellent electrocatalytic properties for L-DOPA and L-Tyr oxidation. Under optimized conditions, the proposed strategy offered a wide working concentration range, which is sufficient for practical applications.

2.5 Hydrogen peroxide

Hydrogen peroxide (H_2O_2) is a significant reactive oxygen species (ROS) in biological processes, and excess levels can lead to cellular and tissue damage. It is a byproduct of respiration, a metabolic end product, including peroxisomal oxidation pathways, and potentially a transmitter of cellular signals (Veal et al., 2007). Moreover, it is worth mentioning that H_2O_2 is the only reactive oxygen species generated by various specific enzymatic systems (Figure 13). These enzymes include phagocytic oxidases (PHOX) and NADP/H oxidases (NOX) in the plasma membrane, superoxide dismutase (SOD2), mitochondrial p^{66}Shc (p66), and amine oxidase (AO) in mitochondria, peroxisomal oxidases (POX) in peroxisomes, sulfhydryl oxidase (SOX) in the endoplasmic reticulum (ER), and amino-acid oxidases (AAO), cyclooxygenase (COX), lipid oxygenase (LOX), xanthine oxidase (XO), and superoxide dismutase (SOD1) in the cytosol (Xin et al., 2022). This indicates that the amount of H_2O_2 inside cells is well controlled and could play unique roles in cellular processes. Being such a crucial molecule in both biological and industrial processes, H_2O_2 can be found in human body fluids, the environment, and food. The typical range of H_2O_2 levels is from micromolar to nanomolar for live organisms, residual levels in food and drinking water to tens of millimolar for bleaching applications, and molar for waste treatment applications (Evans et al., 2002). Thus, it is crucial to monitor the H_2O_2 concentration within the permissible safeguard human well-being, ensure safety, and preserve the environment.

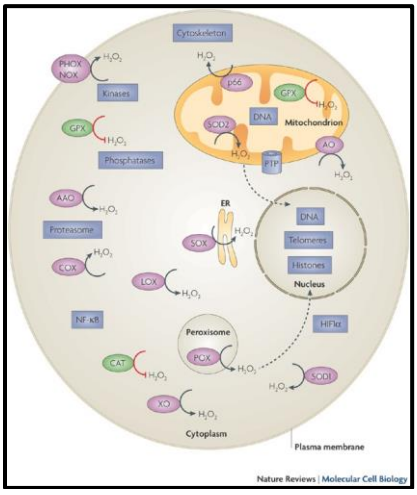

Figure 13 Illustrates the key function of H_2O_2 within the cell

Source: Xin, X., Gong, T., & Hong, Y. (2022). Hydrogen peroxide initiates oxidative stress and proteomic alterations in meningothelial cells. Scientific Reports, 12(1), 14519.

2.5.1 Hydrogen peroxide in breath

Reactive oxygen species, such as superoxide radical ($O_2^{\bullet-}$), H_2O_2, are produced rapidly by white blood cells such as neutrophils, eosinophils, and macrophages during inflammation (Figure 14) (Kim et al., 2023; MacNee, 2001; Wittmann et al., 2012). This leads to elevated levels of oxidative stress. H_2O_2 serves as a mediator of oxidative stress, which is linked to chronic respiratory illnesses and respiratory infections (Emelyanov et al., 2001). H_2O_2 is generated through the enzymatic conversion of its precursor superoxide anions ($O^{\bullet-}_2$) by the enzyme superoxide dismutase in several cell types. The release of H_2O_2 is also linked to the respiratory burst, a process that triggers inflammation by neutrophils to enable the killing of bacteria (Figure 15). Moreover, it has been reported that elevated H_2O_2 in exhaled breath could potentially be utilized as a non-invasive biomarker for oxidative stress, airway inflammation, and lung diseases (Holguin, 2013; Nagaraja et al., 2012). Exhaled breath condensate is an approach to collecting airway samples that does not require intrusive procedures. The concentration of H_2O_2 in exhaled breath condensate rises in association with the severity of lung disorders such as asthma, chronic obstructive pulmonary disease (COPD), adult respiratory distress syndrome (ARDS), bronchial asthma, and cystic fibrosis (CF). The concentration of H_2O_2 in EBC of individuals without any health conditions typically falls within the range of 0 to 0.8 μM (Ho et al., 1999). Consequently, the analysis of H_2O_2 in EBC samples offers potential clinical significance in monitoring and diagnosing lung diseases in humans.

.

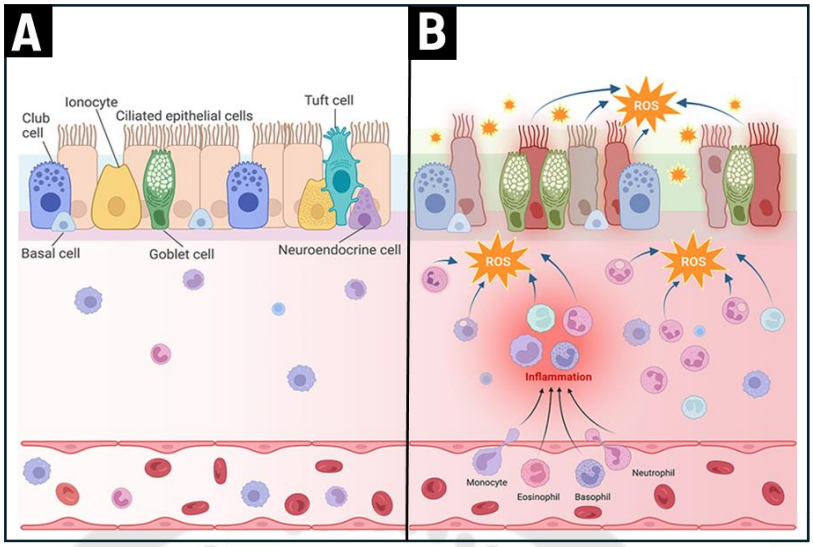

Figure 14 Airway epithelium in (A) healthy subjects and (B) lung diseases patients

Source: Kim, H. R., Ingram, J. L., & Que, L. G. (2023). Effects of oxidative stress on airway epithelium permeability in asthma and potential implications for patients with comorbid obesity. Journal of asthma and allergy, 481-499.

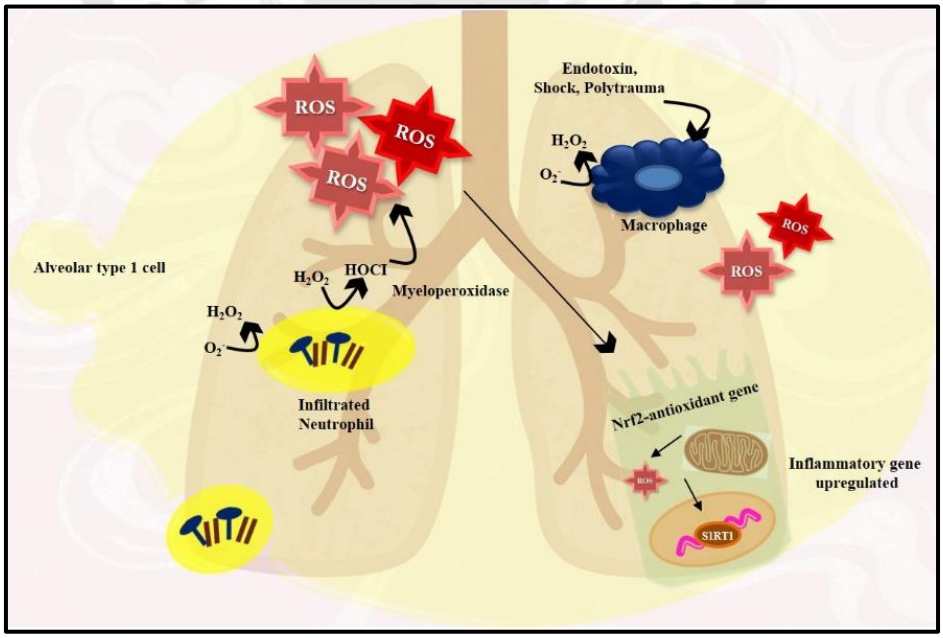

Figure 15 Pathways in which the human body releases hydrogen peroxide

Source: Banga, I., Paul, A., Muthukumar, S., & Prasad, S. (2022). HELP (Hydrogen peroxide electrochemical profiling): A novel biosensor for measuring hydrogen peroxide levels expressed in breath for monitoring airway inflammation using electrochemical methods. Biosensors and Bioelectronics: X, 10, 100139.

2.5.2 Literature reviews

Conventional analytical techniques used for the detection of H_2O_2 include chemiluminescence, titrimetry, spectrophotometry, fluorometry, and chromatography. These methods have several drawbacks, such as the need for prolonged sample pre-treatments, and in many cases, these methods require the utilization of large amounts of reagents. Electrochemical techniques using cost-effective redox proteins, enzymes, and catalyst materials-modified electrodes, can overcome the above limitations to measure H_2O_2 due to their facile approach, remarkable selectivity, and high sensitivity.

Yang's group proposed a protein thin film-modified electrode sensor for determination of H_2O_2. For the electrode architectures, nanocomposite of myoglobin (Mb) and zirconium ion (Zr (iv))-adenosine monophosphate dianion (AMP) particles, was fabricated on a glassy carbon surface using self-assembly technique, forming monolayer adsorption of protein. By using a proper electrode configuration, it can be achieved to lower the overpotential of H_2O_2 reduction, leading to improved kinetics and increased activity of the immobilized protein. The primary benefit of electrode construction is in the ability to create a noncovalently linked nanocomposite that is robust to being washed off in water and can be easily cleaned. For measuring H_2O_2, this designed sensor had a dynamic range of up to 148.47 μM and a detection limit as low as 0.06 μM. After a month, the sensor assay can maintain its initial activity at 91.7%, suggesting that long-term stable Mb-Zr$(AMP)_2$/GCE (Qiao et al., 2009).

Another redox protein, hemoglobin (Hb), is commonly used in direct electron transfer (DET) processes. Chen et al, have proposed the modified electrode configurations based on nanohybrid film of multi-wall carbon nanotubes (MWNT) and gold colloidal nanoparticles (GNPs) by using Hb as a linker. First, negatively charged

MWNT that had been acid-treated was modified on the surface of the glassy carbon electrode. Subsequently, positively charged Hb was absorbed onto MWNT sheets by electrostatic interaction. Ultimately, layer-by-layer assembly of the Hb/GNPs multilayer films was performed onto Hb/MWNT film to obtain Hb/GNPs/Hb/MWNT/GCE. This sensor showed excellent electrocatalytic activity for the reduction of H_2O_2 to construct a third-generation mediator-free H_2O_2 biosensor. Amperometric response current increases with increasing concentration of H_2O_2 in the range from 2.1×10^{-7} to 3.0×10^{-3} M with a detection limit of 8.0×10^{-8} M (Chen et al., 2007).

The DET of immobilized horseradish peroxidase (HRP) on silica–hydroxyapatite (HAp) hybrid film-modified glassy carbon electrode (GCE) was reported by Wang's group (Wang et al., 2009). The development of this H_2O_2 sensor involved using HAp nanoparticles as a matrix to immobilize HRP, while silica served as an attached reagent to improve the sensor's stability. As for silica/HRP–HAp/GCE, the obtained current was linear with the H_2O_2 concentration in the range of 1.0–100 μM with a limit of detection of 0.35 μM. After being stored in a 0.1 M pH 7.0 PBS solution at 4 °C for a duration of 2 weeks, the modified electrode maintained 95% of its initial peak current.

A stable monoenzymatic amperometric biosensor using co-immobilized the single - walled carbon nanotubes (SWCNTs) and methylene blue (MB) into metal oxide (SnO_2) derived organically modified sol-gel glasses (ormosil) was developed for the determination of H_2O_2. To enhance the sensitivity of the proposed sensor, nafion (NAF) was dispersed in the ormosil matrix. Finally, the surface of the Indium tin oxide (ITO) electrode was modified by SWNT/ormosil and Horseradish peroxidase, respectively. This HRP/NAF/SWNT-MB-SnO_2/ITO electrode showed a rapid H_2O_2 response in less than 5 s, along with a good linear concentration range of $5x10^{-7}$ to $1x10^{-4}$ M with a detection limit of 0.3 μM (Upadhyay et al., 2011).

An enzyme-free H_2O_2 sensor using the doping of ionic liquid (IL) into Prussian blue-multiwalled carbon nanotubes (PB-MWCNTs) modified screen-printed carbon electrodes, was developed by Zhu and colleagues. This sensor was prepared

by home-printing carbon electrodes using 1-butyl-3-methylimidazolium tetrafluoroborate ([Bmim]BF_4)- doped commercial graphite-based ink, followed by drop-casting the synthesized cubic PB-MWCNTs hybrid and Nafion onto the sensing surface. The findings showed that doping [Bmim]BF_4 can greatly enhance the performance of the sensing platform towards H_2O_2 detection by improving the electron transfer kinetics. Under optimized all parameters, the constructed sensor exhibits linear amperometric responses for H_2O_2 in the concentration range of 5 to 1645 μM, with a LOD of 0.35 μM. This Nafion-PB-MWCNTs/SPCE-IL was successfully applied to detect H_2O_2 in real samples (Zhu et al., 2014).

A new sensor of $Ni(OH)_2$/electroreduced graphene oxide (ERGO)–multiwalled carbon nanotube (MWCNT) has been fabricated by electrodepositing $Ni(OH)_2$ nanoparticles onto ERGO–MWCNT hybrid film modified glass carbon electrode (GlCE) from Liu's group. The well-designed nanocomposites display remarkable sensing capabilities towards H_2O_2 by using the benefits of ERGO and MWCNTs, together with the electrocatalytic properties of $Ni(OH)_2$ nanoparticles. This $Ni(OH)_2$/ERGO–MWCNT/GlCE revealed good linearity (R^2= 0.997) within the range from 10 μM to 9050 μM. The detection limit is thus estimated to be 4.0 μM (signal-to-noise ratio = 3). This developed sensing platform had a wide linear range, a low detection limit, sufficient sensitivity, good selectivity as well as remarkable reproducibility and stability (Gao et al., 2014).

Recently, AuNP-nafion@[BMIM]BF_4 modified printed carbon electrode was proposed by Banga and colleagues. This as-proposed sensor possesses an electrochemical sensor platform for assessing airway inflammation by monitoring H_2O_2 levels. Computational and chemical modeling were used to study the interaction between the modified electrode and the target analyte. Amperometric detection of H_2O_2 vapors was performed in the range of 50 to 800 ppb (1.5 – 20 μM) (Banga et al., 2022). Furthermore, the other enzymatic sensors and non-enzymatic sensors for the determination of H_2O_2 were summarized as shown in Table 2

Table 2 Analytical performance compared with various configurations for H_2O_2 sensing platforms

Electrode configurations	Technique	E_{app} (V vs. Ag/AgCl)	Linear range (μM)	LOD (μM)	References
Co_3O_4/MWCNTs/CPE	Amp	-0.19	20–430	2.46	(Heli & Pishahang, 2014)
GN–Pt/GCE	Amp	0.0	2–710	0.5	(Xu et al., 2011)
HRP-MoS_2-Gr/	Amp	-0.08	0.2 – 1,103	0.049	(Song et al., 2014)
[Co(pbda)(4,4-bpy)($2H_2O$)]n/GCE	Amp	-0.40	50–9000	3.76	(Yang et al., 2015)
HRP/C-Dots/Co-Fe LDHs/GCE	Amp	-0.35	0.1–23.1	0.04	(Wang et al., 2015)
3D rGO foam-hemin/GCE	DPV	-0.7 to -0.1 V (vs.SCE)	0.005–5000	0.003	(Li et al., 2020)
NH_2-MIL-53(Fe)/HRP/ MWCNTs/GCE	Amp	-0.40	0.1–1 and 1–600	0.028	(Jiang et al., 2020)
2D-Zn/Co-ZIF(HRP)|ZnCoO|Ti	Amp	-0.3	0.2–10 and 10–1100	0.082	(Jin et al., 2023)
nano-PANI/PB/SPE	Amp	0.2	0–1000	2.52	(Cao et al., 2023)
HRP/PBS-SPE	Amp	-0.6	0–100 and 100–5000	1.8	(Luo et al., 2024)

Co_3O_4= Cobalt (II) dicobalt (III) oxide nanoparticles; MWCNTs= multiwalled carbon nanotubes; CPE= carbon paste electrode; GN–Pt= graphene–platinum nanocomposite; GCE = glassy carbon

electrode;HRP=horseradish peroxidase; MoS_2-Gr = self-assembly of layered molybdenum disulfide–graphene; $[Co(pbda)(4,4\text{-bpy})(2H_2O)]_n$ = cobalt metal-organic framework; bpy = 4,4-bipyridine; H_2pbda = 3-(pyridine-3-yloxy)benzene-1,2-dicarboxylic acid; C-dots = Carbon nanodots; LDH = layered double hydroxide; rGO = reduced graphene oxide; [NH_2-MIL-53(Fe)] = the hybrid of metal organic framework; 2D-Zn/Co-ZIF = 2D zinc–cobalt bimetallic zeolite imidazole framework; ZnCoO|Ti = ZnCoO nanowire array on a Ti support; PANI = polyaniline; PB = Prussian blue; PBS = phosphate buffer saline ;SPE = Screen-printed electrode; Amp= Amperometry; DPV = Differential pulse voltammetry; SCE = saturated calomel reference electrode

Based on literature reviews, previous studies proposed different kinds of electrochemical sensors for H_2O_2 determination, encompassing both enzymatic and nonenzymatic systems. Enzymatic H_2O_2 sensors have limited consideration due to their low stability and recycling concerns. Being naturally produced, most enzymes are quite sensitive to environmental factors including pH, temperature, and humidity. Conversely, non-enzymatic sensors offer desirable features such as long-term stability and low costs. Nevertheless, most of the previous sensing platforms have been constructed using multiple modifier materials and performing several modification processes, resulting in a time-consuming fabrication process. Thus, an innovative strategy was proposed to develop a non-enzymatic sensing platform for the detection of H_2O_2. This platform is based on the combination of layer-by-layer hemin-entrapped polyethyleneimine and short-thin multi-walled carbon nanotubes. The as-developed sensor was created by a straightforward process of depositing ST-MWCNTs and hemin matrix onto a disposable printed graphene electrode through drop-casting. The hemin-PEI/ST-MWCNTs/SPGE exhibits greater electrocatalytic activity for H_2O_2 reduction, resulting in improved sensitivity and anti-interference properties.

CHAPTER 3
METHODOLOGY

This chapter describes the experiments that were performed to develop electrochemical sensing platforms using electrodes modified with poly (amino acids) and biocatalyst materials for biomarkers detections. The methodology has been divided into two sections based on the category of modifying materials. The first section is divided into two subprojects, focusing on the development of electrochemical sensing platforms using poly (amino acids)-based electrodes for tyramine detecting and the simultaneous detection of L-DOPA and L-Tyr. The first subproject involves developing a novel tyramine sensor using poly (histidine) assembled on a screen-printed graphene electrode. The second subproject focuses on developing a new electrochemical platform using poly(L-proline)-linked nanodiamonds on a screen-printed graphene electrode. This platform aims to enable the simultaneous detection of L-DOPA and L-Tyr. The second section of this research involves the development of an amperometric sensor for measuring H_2O_2 levels. This sensor is based on a combination of hemin-entrapped polyethyleneimine and short-thin multi-walled carbon nanotubes, which are deposited onto a screen-printed graphene electrode. Each project includes detailed information on chemicals, materials and equipment, fabrication processes, electrochemical measurements, and real sample preparation.

3.1 The development of a novel tyramine sensor using poly (histidine) assembled on a screen-printed graphene electrode

The details provided in this section are extracted from the original research article; see Appendix 1 for the full text.

3.1.1 Chemicals, materials, and equipment

Tyramine hydrochloride, L-histidine monohydrochloride monohydrate, cadaverine dihydrochloride, histamine dihydrochloride, 1,4-diaminobutane dihydrochloride, L-ascorbic acid, dopamine hydrochloride, uric acid, bovine serum

albumin, creatinine, potassium ferricyanide $K_3[Fe(CN)_6]$, and hexaammine ruthenium(III) chloride $[Ru(NH_3)_6]Cl_3$ were purchased from Sigma-Aldrich (St. Louis, MO, USA). 0.1 M Phosphate buffer solution (PBS) was prepared by mixing sodium dihydrogen orthophosphate ($NaH_2PO_4.2H_2O$) and disodium hydrogen orthophosphate ($Na_2HPO_4.2H_2O$), which were obtained from Ajax (Australia). All aqueous solutions were prepared in deionized (DI) water produced by the Milli-Q system (R = 18.2 MΩ cm at 25°C).

The morphology and chemical composition of the electrode materials were examined using a scanning electron microscope (SEM, SU3500) (Hitachi High-Tech., Japan) and a SEM and energy-dispersive X-ray spectrometer (IT300) (JEOL Ltd., Japan), respectively. The electrochemical measurements, via cyclic voltammetry and differential pulse voltammetry, were performed at room temperature on a CHI 1200C potentiostat (Austin, TX, USA). Electrochemical impedance spectroscopy measurements were performed using Sensit smart (Houten, the Netherlands).

3.1.2 Fabrication of poly(histidine)-modified screen-printed graphene electrode

The patterned SPGE was designed using Adobe Illustrator CC, and the template block screen was constructed using the designed pattern by Chaiyaboon Brothers Co., Ltd. (Bangkok, Thailand). The SPGE, consisting of a working electrode, counter electrode, and reference electrode, was fabricated onto the transparency film substrate using an in-house screen-printing technique. First, the WE and CE were manually screened onto the substrate using graphene ink from Serve Science Co., Ltd. (product code: SSG-1760A, Bangkok, Thailand) and placed into a hot air oven at a temperature of 55°C for 30 min. Then, the RE and conducting pad were screened onto the same substrate using Ag/AgCl ink obtained from Sun Chemical (product code: C2130809D5, Slough, United Kingdom) for the complement of an electrochemical cell and heated again at 55°C for 30 min for solvent drying. Before use, the prepared SPGE was attached with adhesive tape to each electrode strip under the detection area for the confinement of the electrode surface area.

A single step electropolymerization was employed for electrode modification. Electropolymerization of L-histidine was directly performed onto the prepared SPGE surface using the CV technique. This procedure was accomplished by dropping 100 µL of 40 mM L-histidine monomer in 0.1 M PBS (pH 7.4) onto the electrode surface area and applying the potential from –0.6 to +2.0 V for 20 cycles at a scan rate of 0.2 V s^{-1}. The electropolymerization of L-histidine can be explained by the anodic peak of L-histidine, which was first observed around +1.5 V (Figure 16), which is the oxidized form of the imidazole ring on the side chain. As observed in the second cycle of scans at a potential of +1.2 V, the His radicals were then coupled to form poly(His). Interestingly, as the number of cycles scans increased, this defined-peak current gradually decreased, indicating the formation of a polymer coating at the electrode surface. After the modification step, the modified electrode was rinsed with DI water and allowed to dry at room temperature. Finally, poly(His)/SPGE was obtained and kept in a zip lock bag in a dark and dry location. The overall fabrication and electrochemical measurement processes of the proposed sensor are presented in Figure 17.

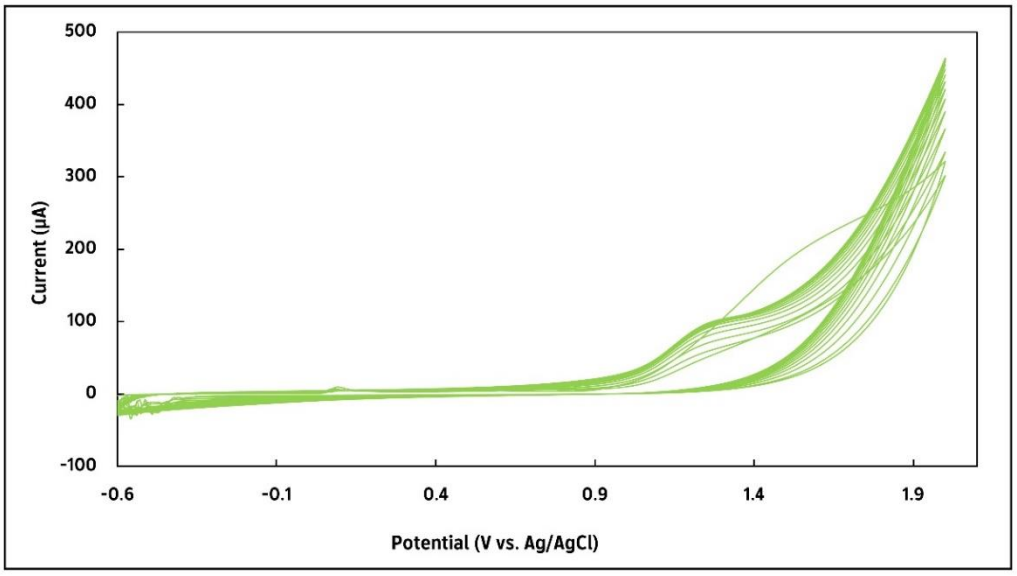

Figure 16 Cyclic voltammogram of electropolymerization of 40 mM L-histidine in 0.1 M PBS at pH 7.4 (potential ranges from –0.6 to +2.0 V for 20 cycles, scan rate at 0.2 V s^{-1})

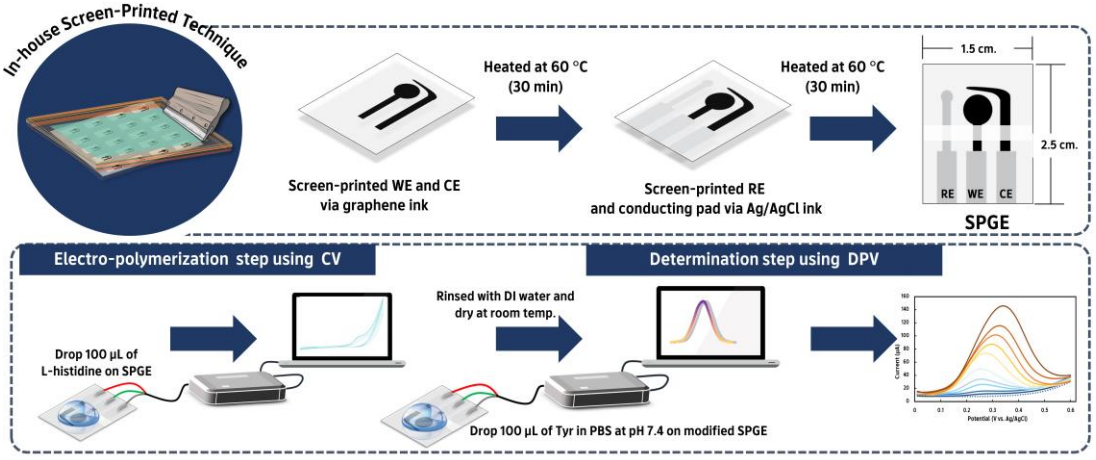

Figure 17 Schematic representation of the fabrication and electrochemical detection procedures for the tyramine quantification using poly(His)/SPGE

3.1.3 Electrochemical measurement

All measurements were performed using a three-electrode system with poly(His)/SPGE as the WE, graphene ink as the CE, and Ag/AgCl as the RE and were repeated at least three times at room temperature. For the electrochemical measurement, 100 µL of standard tyramine solution in 0.1 M PBS (pH 7.4) was dropped onto the electrode surface area. CV was employed for the study of the electrochemical behavior of tyramine. The potential range of 0.0 to +1.2 V vs. Ag/AgCl at a scan rate of 0.075 Vs^{-1} was set. DPV was optimized and used for the determination of tyramine. All parameters of DPV were successfully achieved by scanning the potential in the range of 0.0 to +0.6 V vs Ag/AgCl with a pulse width of 0.025 s, an amplitude of 0.2 V, an increment of 0.01 V, and a pulse period of 0.5 s.

The EIS measurements were performed in 5 mM $K_3[Fe(CN)_6]$ with a potential range of 0.0–0.1 V, a frequency range of 0.01 Hz to100 kHz, and an amplitude of 0.1 V, as well as 5 mM $[Ru(NH_3)_6]Cl_3$ in 0.1 M KCl with a potential range from –0.1 to 0.1 V, a frequency range of 0.01 Hz to 100 kHz, and an amplitude of 0.1 V.

3.1.4 Real sample preparation

The practical applications of the proposed poly(His)/SPGE were investigated using three different types of real samples, namely, urine, serum, and cheese samples. All biological samples were well received by volunteers who gave their consent to participate in the trial. Urine samples were obtained from healthy human volunteers in the laboratory, and serum samples were obtained from healthy patients. To eliminate particulates, urine sample solutions were filtered through a 0.45-μm Millipore membrane. On the other hand, serum sample was utilized without any purification process. Different concentrations of standard tyramine with an appropriate calibration curve were separately spiked into biological samples and then diluted 50 and 100 times (1000 μL) with supporting electrolyte (0.1 M PBS, pH 7.4) for the urine and serum samples, respectively.

Cheese samples (candy cheese pain, mozzarella cheese, and cheddar cheese) were obtained from local supermarkets in Thailand. Cheese samples were performed according to the published literature (Carelli et al., 2007). The aliquots of each homogenized sample (2.5 g) were transferred into 15 mL plastic centrifuge tubes, and 5 mL of PBS (0.1 M, pH 7.4) was added and mixed for 2 min using a vortex. The mixture was placed in an ultrasonic bath for 20 min and centrifuged for 10 min at 3000 rpm. The supernatant was collected, and the process was performed two more times. Finally, the extracts were collected and made up to volume in a 25 mL volumetric flask with PBS. Before analysis, different concentrations of standard tyramine with an appropriate calibration curve were spiked into 100 μL cheese sample solution and diluted to 1000 μL with supporting electrolyte (0.1 M PBS, pH 7.4).

3.2 The development of a new electrochemical platform using poly(L-proline)-linked nanodiamonds on a screen-printed graphene electrode for simultaneous detection of L-DOPA and L-Tyr

The details provided in this section are extracted from the original research article; see Appendix 2 for the full text.

3.2.1 Chemicals, materials, and equipment

All reagents were of analytical grade and used without further purification. 1% ND dispersions in water (10 nM) were obtained from Adámas Technologies (Raleigh, NC). L-DOPA and L-Tyr were purchased from Merck (Darmstadt, Germany). L-Pro, D-alanine, L-ascorbic acid, dopamine hydrochloride, uric acid, L-histidine, creatinine, homocysteine, L-cysteine, and potassium ferricyanide ($K_3[Fe(CN)_6]$) were supplied by Sigma-Aldrich (St. Louis, MO, USA). The 0.1 M phosphate buffer solution (PBS) was prepared by mixing sodium dihydrogen orthophosphate ($NaH_2PO_4.2H_2O$) and disodium hydrogen orthophosphate ($Na_2HPO_4.2H_2O$), which were obtained from Ajax (Australia). Deionized water, produced by the Milli-Q system (R = 18.2 MΩ cm at 25°C), was used throughout the experiments.

The morphology and element composition of the electrode surface were investigated using a scanning electron microscope and an energy-dispersive X-ray spectrometer (JSM-IT500HR) (JEOL Ltd., Japan). The bare and modified electrodes were analyzed utilizing Fourier transform Raman spectroscopy (Perkin Elmer model Spectrum GX) (Shelton, Connecticut, USA). The Raman results identified the existence of chemical bindings after each step of electrode functionalization at the excitation wavelength of 532 nm. Electrochemical measurements, via cyclic voltammetry and differential pulse voltammetry, were performed using a laptop controlled by a CHI 1200C potentiostat (Austin, TX, USA), and electrochemical impedance spectroscopy was performed using Sensit Smart (Houten, the Netherlands).

3.2.2 Fabrication of poly(L-proline)-linked nanodiamonds on screen-printed graphene electrode

Homemade SPGE was fabricated onto polyvinyl chloride (PVC) paper by stepwise ink deposition using screen-printing technology , as previously reported (Kaewjua & Siangproh, 2022). The templates for homemade SPGE were designed using Adobe Illustrator CC. The template patterns were constructed by Chaiyaboon Brothers Co., Ltd. (Bangkok, Thailand). The SPGE device consists typically of three electrodes: the counter electrode, the working electrode, and the reference electrode.

Layer-by-layer poly(L-Pro)/ND/SPGE was fabricated in two simple steps: electrodeposition of ND and electropolymerization of L-Pro. The overall fabrication steps of homemade SPGE and poly(L-Pro)/ND/SPGE are presented in Figure 18. Initially, the PVC paper substrate was cleaned with ethanol before use. Then, the template of the SPGE was attached on top of the PVC paper substrate. Graphene ink from Serve Science Co., Ltd. (product code: SSG-1760A, Bangkok, Thailand) was applied onto the template of the SPGE and then screened with a rubber squeegee. This step was repeated twice to obtain a homogeneous surface of WE and CE and placed into a hot air oven at a temperature of 60°C for 30 min. Next, Ag/AgCl ink obtained from Sun Chemical (product code: C2130809D5, Slough, United Kingdom) was applied to form the RE and conducting pad onto the same substrate and heated again at 60 °C for 30 min for solvent drying to obtain good adhesion between the ink and the PVC substrate. Finally, insulator ink was then screened on top of the homemade SPGE to fix the area of the electrode surface.

Layer-by-layer poly(L-Pro)/ND/SPGE was fabricated as follows: First, 100 µL of 0.1% w/v ND suspension was dropped on the surface of a graphene-based substrate and then deposited by sweeping a potential window from –0.8 V to +0.8 V for 10 repetitive cycles at a scan rate of 0.1 V s^{-1} (Figure 19A). The obtained ND/SPGE was carefully washed with DI water and left for about 10 sec to dry in the air. In the second step, a poly(L-Pro) layer was polymerized over ND/SPGE surface from 1 mM L-proline in 0.1 M PBS pH 7.4 by cycling in a potential window from –0.6 to +2.0 V for 15 cycles at a scan rate of 0.1 V s^{-1}. During the electropolymerization process, the adsorption of L-proline monomer on the ND/SPGE surface occurs in the first cycle at the potential of +1.31 V vs. Ag/AgCl. The irreversible second anodic peak corresponding to free cation-radical species was observed at +1.25 V. The peak current of coupling radical slightly decreased with the increase in the number of cyclic scans and then maintained constant at the fifteenth cycle (Figure 19B). This confirms that a polymeric L- proline film was completely formed on the ND-deposited SPGE surface. The different electrodes,

ND/SPGE, poly(L-Pro)/SPGE and ND/poly(L-Pro)/SPGE, and ND-(L-Pro)/SPGE, were performed as it is described above.

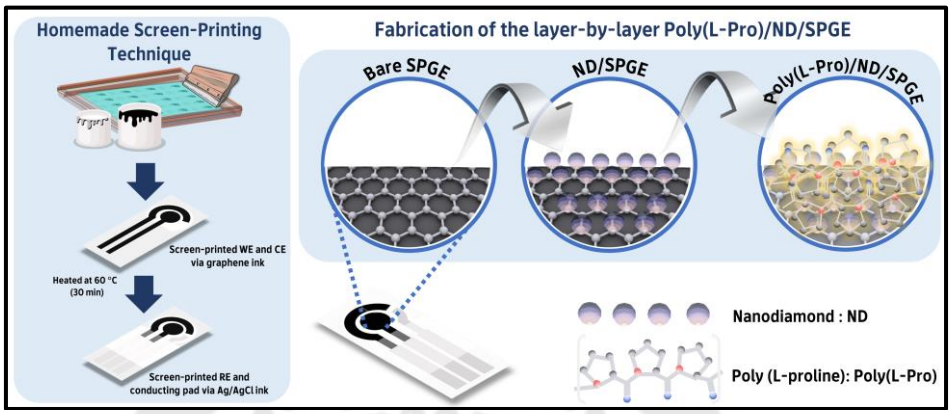

Figure 18 Schematic representation of the fabrication processes for the poly(L-Pro)/ND/SPGE

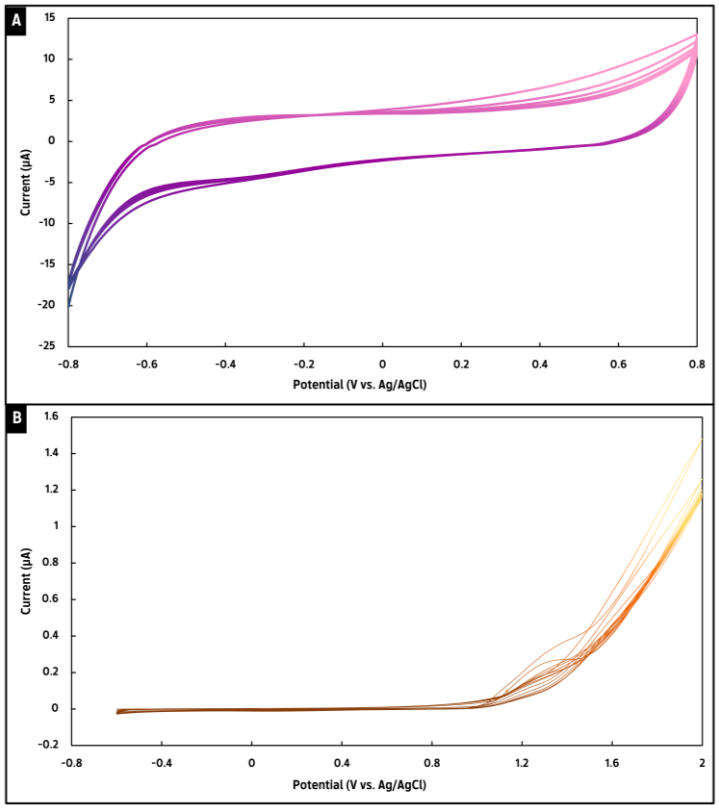

Figure 19 (A) The signals of electrodeposition of 0.1% w/v ND (potential ranges from –0.8 to +0.8 V for 10 cycles, scan rate at 0.1 V s^{-1}) and (B) cyclic voltammogram of

electropolymerization of 1 mM L-proline in 0.1 M PBS at pH 7.4 (potential ranges from –0.6 to +2.0 V for 15 cycles, scan rate at 0.1 V s^{-1})

3.2.3 Electrochemical measurement

All measurements were performed using a three-electrode system with poly(L-Pro)/ND/SPGE as the WE, graphene ink as the CE, and Ag/AgCl as the RE, and were carried out at least three times at room temperature. For the electrochemical measurement, 100 µL of a mixture of L-DOPA and L-Tyr solution in 0.1 M PBS (pH 7.4) was dropped onto the electrode surface area. CV was employed for the study of the electrochemical behaviors of both L-DOPA and L-Tyr. The potential range of –0.4 to +1.0 V vs. Ag/AgCl at a scan rate of 0.075 V s^{-1} was set. Differential pulse voltammetry (DPV) was optimized and used for the determination of L-DOPA and L-Tyr. All DPV parameters were successfully achieved by scanning the potential in the range of –0.5 to +0.7 V vs. Ag/AgCl with a pulse width of 0.025 s, an amplitude of 0.2 V, a pulse period of 0.5 s, and an increment of 0.007 V. The EIS measurements were performed in a solution of 5 mM $Fe(CN)_6^{3-/4-}$ in 0.1 M KNO_3 with a potential range of 0.0–0.1 V, a frequency range of 0.01 Hz–100 kHz, and an amplitude of 0.1 V.

3.2.4 Real sample preparation

Biological fluids have been utilized to evaluate the applicability of the proposed sensor for monitoring the target analytes in real samples. All biological samples were well received by healthy volunteers in the laboratory, and serum samples were obtained from healthy patients. Informed consent was obtained from all human subjects, and they already knew what would happen to the human subjects in a trial. There was no purification process used on any of the samples. Different concentrations of the standard mixture L-DOPA and L-Tyr with an adequate standard calibration were spiked into biological samples and then diluted 50 and 100 times (1000 µL) with supporting electrolyte (0.1 M PBS, pH 7.4) for the serum and urine samples, respectively. The electrochemical measurement was performed via DPV under

optimized conditions. Lastly, accuracy and precision were subsequently evaluated and compared to spiked values.

3.3 The development of an amperometric sensor based on hemin-entrapped polyethyleneimine assembled short-thin multi-walled carbon nanotubes on screen-printed graphene electrode for measuring H_2O_2 levels

3.3.1 Chemicals, materials, and equipment

Hemin (chloroprotoporphyrin IX iron (III)), polyethyleneimine (PEI, 50 % (w/v), Mw 1,300) , 35 wt.% H_2O_2 solutions, D (+)glucose, L-ascorbic acid, dopamine hydrochloride, uric acid, sodium chloride (NaCl), urea, glycine, calcium chloride ($CaCl_2$), ammonium sulfate ($(NH_4)_2SO_4$), sodium sulfite (Na_2SO_3), dimethyl sulfoxide (DMSO), dimethyl formamide (DMF), sodium dihydrogen orthophosphate, and disodium hydrogen orthophosphate, were obtained from Sigma-Aldrich (Broendby, Denmark). Short-thin multi-walled carbon nanotubes (ST-MWCNTs, 95+% C purity & COOH, product code: 3151) were from Nanocyl (Belgium). All reagents were of analytical grade and utilized without additional purification. Stock solution of hemin was prepared by dissolving 10 mg of hemin with 1 mL of 99.9% DMSO. Stock solution of 11%w/v of PEI was prepared by mixing 220 µL of 50 % w/v PEI with 780 µL of DI water. 1 mg mL^{-1} hemin in 10% PEI was freshly prepared by mixing 10 µL of 10 mg mL^{-1} hemin (99.9% DMSO) with 90 µL of 11%w/v of PEI. The preparation of all aqueous solutions was carried out using deionized water produced by the Milli-Q system, which possessed a resistivity of 18.2 M Ω cm at 25 °C.

3.3.2 Fabrication of hemin-entrapped polyethyleneimine assembled short-thin multi-walled carbon nanotubes on screen-printed graphene electrode

The in-house SPGE was produced using screen-printing technology on polyvinyl chloride paper described in previous work (Kaewjua & Siangproh, 2023). The template patterns for in-house SPGE were designed using Adobe Illustrator CC. The template block screens were fabricated by Chaiyaboon Brothers Co., Ltd. (Bangkok,

Thailand). Before using the PVC paper substrate, it was thoroughly cleaned with ethanol. The template block screen for WE and CE was subsequently placed on top of the PVC paper substrate. Graphene ink from Serve Science Co., Ltd. (product code: SSG-1760A, Bangkok, Thailand) was applied to the template and screened three times using a rubber squeegee. Subsequently, the obtained WE and CE on PVC substrate was placed in a hot air oven set at a temperature of 60 °C for a duration of 30 min. The template block screen for the RE and conducting pad was then placed on top of the obtained substrate. Finally, Ag/AgCl ink, sourced from Sun Chemical (product code: C2130809D5, Slough, United Kingdom), was screened three times and then heated at 60 °C for 30 min. to evaporate the solvent.

Before use, nail varnish was applied to the space between each electrode to confine the working electrode area, allowing precise electrode modification. Hemin-PEI/ST-MWCNTs/SPGE was fabricated as follow: 5 µL of 10 mg mL^{-1} ST-MWCNT in DMF was placed on the WE area of SPGE, and left to dry at room temperature for 45 min. Next, 5 µL of 1 mg mL^{-1} Hemin in 10% PEI was placed on the ST-MWCNTs/SPGE, left to dry at room temperature under a plastic lid. Finally, the hemin-PEI/ST-MWCNTs/SPGE was rinsed with PBS three times before use. The overall fabrication procedure of hemin-PEI/ST-MWCNTs/SPGE is presented in Figure 20.

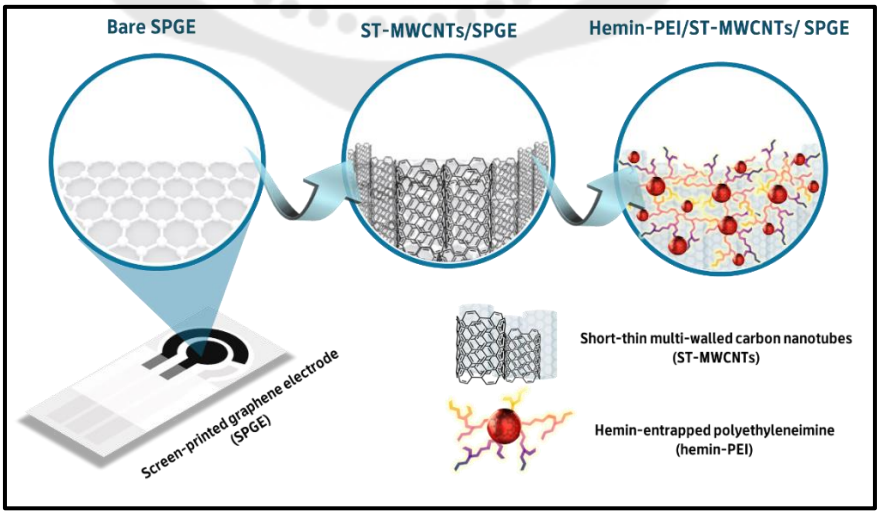

Figure 20 Schematic representation of the fabrication processes for the hemin-PEI/ST-MWCNTs/SPGE

3.3.3 Electrochemical measurement

All electrochemical measurements were performed in a three-electrode system with hemin-PEI/ST-MWCNTs/SPGE as the WE, graphene as the CE, and Ag/AgCl as the RE connected with a μAutolab potentiostat (Type III, Metrohm, Utrecht, Netherlands) equipped with GPES software (version 4.9.007), inside a faradaic cage. All measurements were carried out at room temperature using at least three equivalently prepared electrodes. Chronoamperometry analysis of H_2O_2 was performed at –0.2 V by spiking the working solution with increasing concentrations of analytes, the current response to each concentration being recorded for 50 s, followed by the next concentration added.

3.3.4 Real sample preparation

The EBC samples were obtained from healthy volunteers in the laboratory with their informed consent. During collector analysis, exhaled breath samples were collected by breathing in through the nose and blowing out through a mouthpiece connected to a REDI EBC device. (REDI. Bio., London, United Kingdom) for 5 min to obtain ~250 μL of EBC samples. For all of the samples, there was no need for a purification procedure. The obtained EBC samples were immediately diluted twice (total 500 μL) with 40 mM PBS, pH 7 to obtain the real samples in the effective supporting electrolyte environment. When not in use, they were stored in the freezer at –20 °C.

CHAPTER 4
RESULTS AND DISCUSSION

This chapter presents the results and discussion related to the development of electrochemical sensing platforms using electrodes modified with poly (amino acids) and biocatalyst materials for biomarker detection. The chapter is structured into three projects, with each project according to the proposed methodology outlined in Chapter 3.

4.1 The development of a novel tyramine sensor using poly (histidine) assembled on a screen-printed graphene electrode

The details provided in this section are extracted from the original research article; see Appendix 1 for the full text.

4.1.1 Characterization of bare SPGE and poly(His)/SPGE

As illustrated in Figure 21, the surface morphologies of bare SPGE and poly(His)/SPGE were investigated using a SEM. The SEM images of bare SPGE, as presented in Figure 21A and C (at 5,000X and 10,000X magnification, respectively), exhibited a rough and wrinkled surface, uniformly distributed particles, and a stack of graphene layers. After the modification of poly(His) onto SPGE, the electrode surface (Figure. 21B and D at 5,000X and 10,000X magnification, respectively) displayed a relatively smooth surface and a more film-like texture than the bare SPGE surface. This phenomenon indicated that the bare SPGE surface is completely covered by the polymeric thin film of poly(His).

Scanning electron microscopy and energy-dispersive X-ray spectrometry (SEM-EDS) as well as Raman spectroscopy were employed to confirm the presence of poly(His) on the SPGE surface, as presented in Figure 22. The constituent elements of bare SPGE and poly(His)/SPGE were identified using the SEM-EDS technique, as presented in Figure 22A and B, respectively. The C, O, and Cl elements, which are related to the composition of graphene ink, were present in the bare SPGE. Meanwhile,

the SEM-EDS analysis of modified poly(His) onto SPGE was similar to that of bare SPGE, with the exception that the distinguishing peak due to the N atom significantly increased when the histidine molecule was used as a monomer. This indicated that a poly(His) layer had indeed been applied to the SPGE surface. Furthermore, the Raman spectra in Figure 22C indicated the characteristic G (~1582.39 cm^{-1}) and 2D (~2718.76 cm^{-1}) bands and a D peak at 1350 cm^{-1} for bare SPGE (blue line). The appearance of the D band could be due to the low defect content of the graphene layers during the manufacturing process of graphene ink (Johra et al., 2014; Krishnamoorthy et al., 2012). Interestingly, poly(His)-modified SPGE (orange line) revealed not only increased intensities of two characteristic bands but also a sharp, intense peak at 1579.44 cm^{-1}, corresponding to the C=C stretching vibration of the imidazole ring at pH ~7 (Liu et al., 2012; Mesu et al., 2005). The disordered level of the graphene structure was calculated using the intensity ratio of D and G bands (I_D/I_G). The intensity ratio value was found to increase from 0.63 to 0.74 after modification with poly(His), indicating the higher disorder level of modified graphene (Liu et al., 2018). The results clearly indicated that the electropolymerization of L-histidine was successfully modified on the SPGE surface.

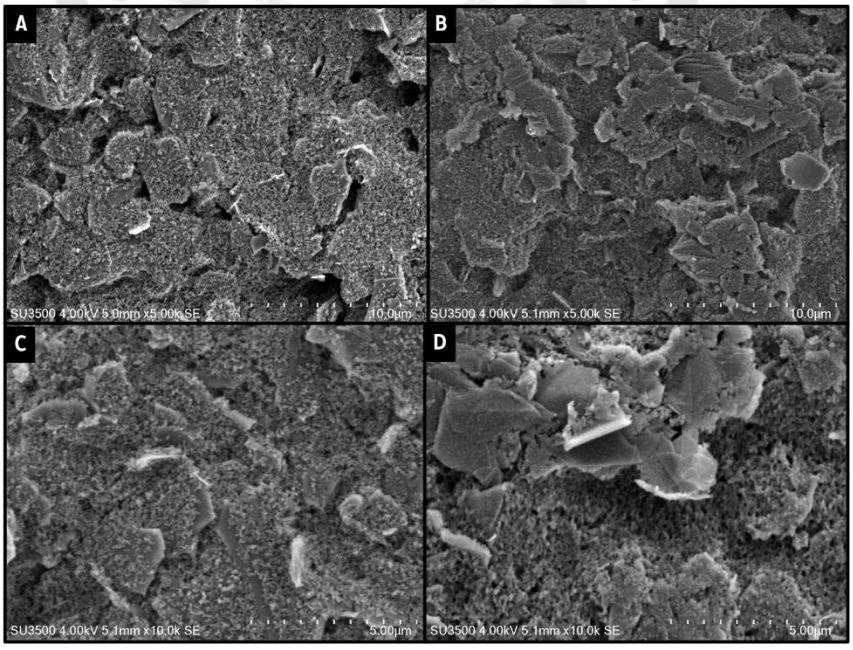

Figure 21 SEM images of (A and C) bare SPGE and (B and D) poly(His)/SPGE at 5,000X (A, B), and 10,000X (C, D)

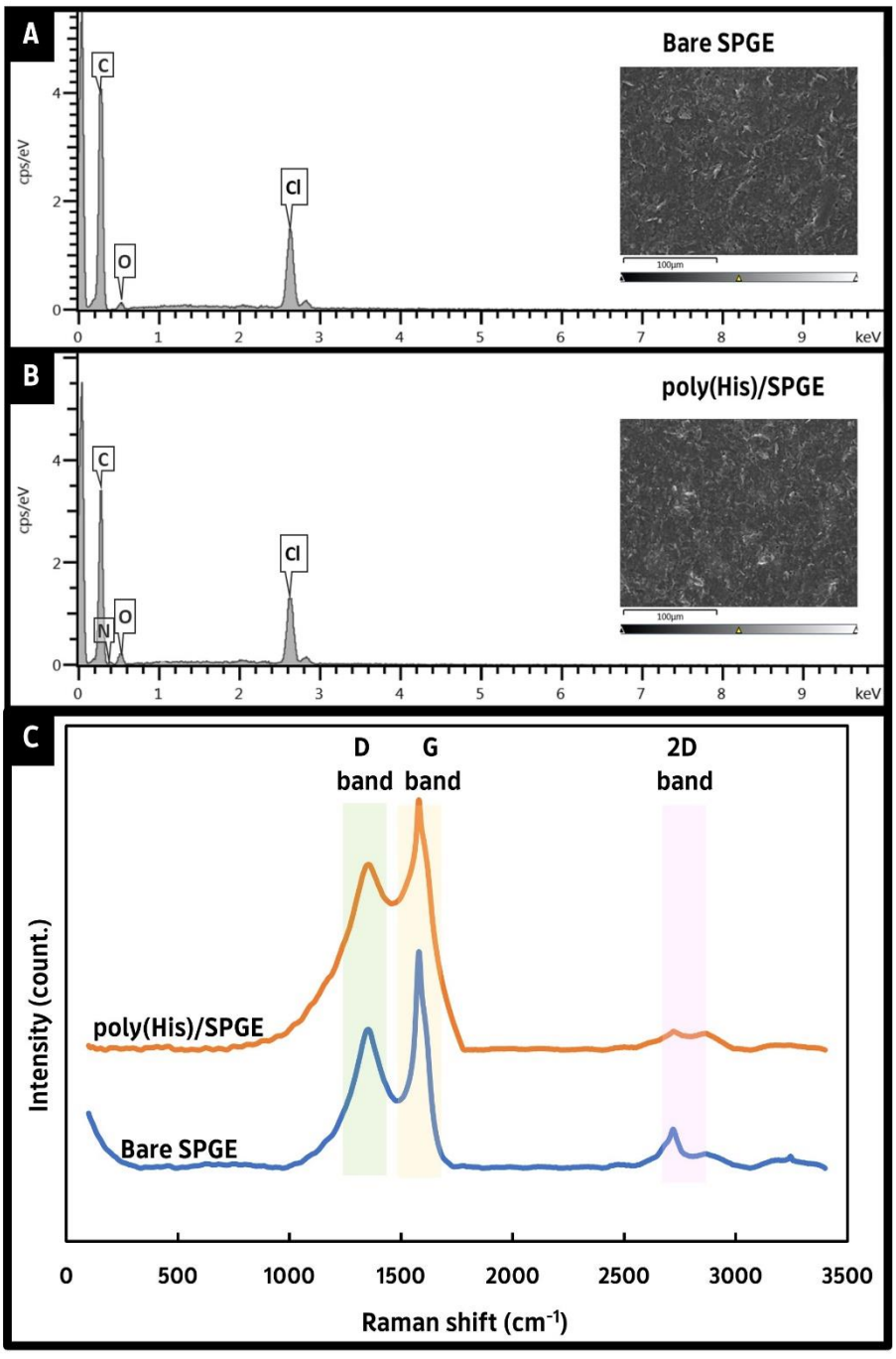

Figure 22 The SEM-EDS analysis of (A) bare SPGE, (B) poly(His)/SPGE, and (C) Raman spectra of both unmodified and modified SPGE

In addition, various amino acid-based polymers were investigated to develop highly sensitive and selective detection of tyramine. Based on the variable functional group on the side chain, some amino acids in each category: non-polar side chain, sulfur-containing side chain, polar side chain, and electrically charged side chain were chosen to modify the SPGE. As shown in Figure 23, the SPGE modified with poly(histidine) was found to provide the highest current compared to the other amino acid-based polymer modified electrodes. As a result, the histidine monomer is a potential amino acid for fabricating the polymer in order to improve the sensitivity and selectivity of tyramine detection.

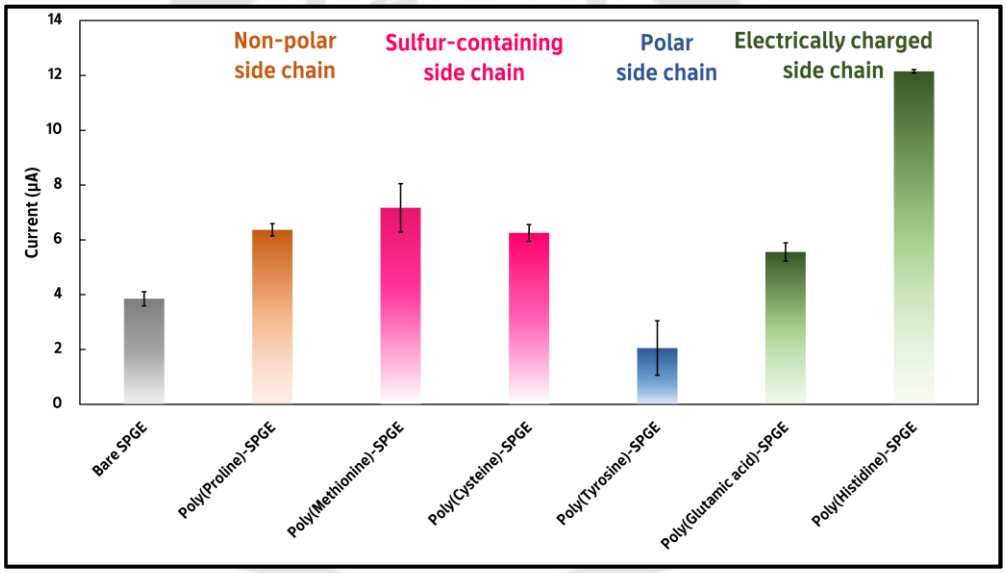

Figure 23 Preliminary results of DPV signals for 100 μM of tyramine in 0.1 M PBS (pH 7.4) at different amino acids-based polymers modified SPGE (n=3)

4.1.2 Electrochemical characterization of poly(His)/SPGE

To investigate the electrochemical performance of bare SPGE and poly(His)-modified SPGE, the CV and EIS measurements were performed by using both an anionic ($Fe(CN)_6^{3-/4-}$) redox probe and a cationic ($Ru(NH_3)_6^{3+}$) redox probe. The cyclic voltammogram of 5 mM $Fe(CN)_6^{3-/4-}$ in 0.1 M KCl exhibited two well-defined peaks at potentials of +0.280 and +0.004 V at bare electrode, as presented in Figure 24A (dash line). On the other hand, the redox behaviors of $Fe(CN)_6^{3-/4-}$ were significantly

reduced and broadened after the modification of electropolymerization of L-histidine on the SPGE surface. In addition, the peak currents decreased while the peak potential increased up to +0.357 V (straight line). This poor electrochemical response of $Fe(CN)_6^{3-/4-}$ derived from poly(His)/SPGE suggested that an electrostatic repulsion force existed between the negatively charged carboxylic group in the poly(His) thin film and the anionic redox probe. Meanwhile, a cyclic voltammogram of bare and modified SPGE using 5 mM $Ru(NH_3)_6^{3+}$ in 0.1 M KCl provided a pair of redox peaks at potentials of –0.327 and –0.125 V, correlating with the redox reaction of this electroactive probe. When the electrochemical properties of the bare (dash line) and modified electrodes (straight line) were compared, the poly(His)/SPGE electrode demonstrated minor changes in the peak current and an ΔE shift to a more positive potential (from +0.202 to +0.256 V), as presented in Figure 24B. This phenomenon can be explained by the electrostatic interaction between negatively charged carboxyl groups on the surface of the poly(His) film and the cationic redox probe. The anionic behavior of L-histidine polymeric film may be attributed to the most abundant carboxyl groups on the polymer backbone, which are derived from both the L-histidine monomer's characteristics and the overoxidized imidazole side chain (Liu et al., 2014). As a result, the electrochemical behavior of $Ru(NH_3)_6^{3+}$ on poly(His)/SPGE improved the electron-transfer process at the electrode–solution interface.

To gain a better understanding of electron-transfer processes, EIS was employed to characterize unmodified and modified poly(His) on SPGE using both $Fe(CN)_6^{3-/4-}$ and $Ru(NH_3)_6^{3+}$ as electroactive probes. In the Nyquist plot, the length of the semicircle diameter corresponds to the electron-transfer resistance (R_{ct}) at the electrode–solution interface. The calculated R_{ct} values for bare SPGE and poly(His)/SPGE using 5 mM $Fe(CN)_6^{3-/4-}$ as a redox probe were 1.60 and 11.5 kΩ, respectively. On the other hand, the calculated R_{ct} values of 5 mM $Ru(NH_3)_6^{3+}$ at the bare electrode and modified electrode were found to be 1.85 and 1.15 kΩ, respectively. As presented in Figure 24C, the bare SPGE when using anion (curve a) and cation (curve c) redox probes exhibited a similar behavior as a small length of

semicircle diameter, indicating good graphene conductivity. When comparing the bare electrode with the modified polymer of L-histidine on SPGE, the length of the semicircle diameter of $Fe(CN)_6^{3-/4-}$ was significantly increased (curve b), whereas the semicircle diameter of $Ru(NH_3)_6^{3+}$ was slightly decreased (curve d). The increased impedance at the modified electrode when using $Fe(CN)_6^{3-/4-}$ arises from the electron-transfer process at the interface was hindered. This was attributed to the strong electrostatic repulsion between the carboxyl groups of the poly(His) film and the negatively charged redox indicator ferricyanide, which was in good agreement with the CV data presented in Figure 24A. On the other hand, the R_{ct} value when using the cationic electroactive probe at the modified electrode was smaller than that of a bare SPGE, indicating that the polymeric film of L-histidine has a higher electroactive surface coverage and excellent electrocatalytic activities, which improves the electron-transfer process at the electrode interface. As a result, $Ru(NH_3)_6^{3+}$ was selected as a redox probe for the investigation of properties obtained from poly(His)/SPGE.

The electroactive surface areas of bare SPGE and poly(His)/SPGE were then measured using the CV technique at different scan rates with 5 mM $Ru(NH_3)_6^{3+}$(Figure 25). For a reversible process, the Randles–Sevcik equation was used to calculate the electroactive surface areas, as shown below (Charoenkitamorn et al., 2018):

$$I_{pa} = (2.69 \times 10^5)n^{3/2}AC_0^{*}D_0^{1/2}\nu^{1/2} \quad \text{..... equation 6}$$

where I_{pa} denotes the anodic peak current; n, the number of electron involved in the redox process; A, an electroactive surface area of electrode (cm^2); C_0^{*}, the concentration of $Ru(NH_3)_6^{3+}$(mol cm^{-3}); D_o (cm^2 s^{-1}), the diffusion coefficient; and ν (V s^{-1}), the scan rate. For 5 mM $Ru(NH_3)_6^{3+}$ in 0.1 M KCl as supporting electrolyte, the n and D_o values were 1 and 8.43×10^{-6} cm^2 s^{-1}, respectively (Wang et al., 2011). Therefore, the electroactive surface areas were found to be 0.066 and 0.074 cm^2 for the bare SPGE and poly(His)/SPGE, respectively. This indicates that the electroactive

surface area for the modified electrode is 1.12 times higher than that of the bare SPGE. Based on the findings, the polymer layer on the electrode's surface was responsible for the enhancement of active sites.

The total surface coverage (Γ) was derived from the charge concentration (Q) according to the relationship described in the equation to estimate the surface coverage of the bare electrode and polymer film on the modified electrode (Kumar et al., 2017):

$$\Gamma = \frac{Q}{nFA} \quad \text{..... equation 7}$$

where Γ is the total surface coverage (mol cm^{-2}); Q, the charge obtained from the anodic peak area of the supporting electrolyte (0.1 M PBS, pH 7.4); n, the number of involved electrons; F, Faraday's constant (96,485.34 C mol^{-1}); and A, the electroactive surface area. The calculated surface coverages of bare electrode and poly(His)/SPGE were found to be 1.55×10^{-10} and 7.84×10^{-10} mol cm^{-2}, respectively. The increased electroactive surface coverage can be attributed to the existence of a polymeric histidine film on the SPGE surface.

4.1.3 Electrochemical behavior of tyramine on poly(His)/SPGE

The electrochemical responses of tyramine detection were investigated using bare SPGE and poly(His)/SPGE *via* CV and DPV. The CV curves of 1 mM tyramine in 0.1 M PBS (pH 7.4) at the bare electrode and poly(His)/SPGE are presented in Figure 26A. It can be noticed that the electrooxidation of tyramine occurred at a potential of +0.51 V at an unmodified and a modified electrode. When compared with the bare SPGE (blue line), the characteristics of tyramine at poly(His)/SPGE (orange line) were sharper and had a higher peak current. Moreover, the occurrence of a single anodic peak indicated that the electrochemical reaction of tyramine was completely an irreversible process. The obtained results were consistent with those of the previous study (Erdogan et al., 2018). For the DPV measurements, as presented in Figure 26B, the electrooxidation peaks of tyramine were observed at potentials of +0.34 and +0.29 V for bare SPGE (blue line) and poly(His)/SPGE (orange line), respectively. Furthermore,

the peak current at poly(His)/SPGE was nearly three times that of bare SPGE. These results indicate that the polymeric film of L-histidine on SPGE exhibits electrocatalytic activity in terms of the improvement of the electron-transfer processes between the electrode surface and electroactive species in the solution. This enhancement in electron-transfer kinetics could be attributed to the high conductivity of poly(His)/SPGE, which contains the carboxyl groups on the polymeric L-histidine backbone (Wang & Huang, 2014).

To investigate the electron-transfer kinetics of tyramine, the effect of scan rate at poly(His)/SPGE was measured *via* CV, and the results are presented in Figure 26C. The electrooxidation current of tyramine was found to increase at a scan rate of 0.005 to 0.075 V s^{-1}. With an increased scan rate, the oxidation potential shifted to the positive direction, indicating that the electrooxidation of tyramine was an irreversible process. However, a linear relationship was observed between the oxidation currents and the square root of the scan rate ($\nu^{1/2}$) (presented in the inset in Figure 26C), which suggested a diffusion-controlled electrochemical process. A diffusion-controlled electrochemical process was also elucidated using the plot of log I_p versus log ν (Figure 27A). The slope of 0.5907 was consistent with the theoretically expected value of 0.5, confirming that the electrooxidation of tyramine was controlled by the diffusion process (Azizi et al., 2016). Furthermore, using the theoretical model described by Andrieux and Savèant, the information obtained from the relationship between I_{pa} and the $\nu^{1/2}$can be used to determine the diffusion coefficient (D_0) of tyramine.

$$I_{pa} = 0.496FACD_0^{\frac{1}{2}}\left(\frac{F}{RT}\right)^{1/2}\nu^{1/2} \quad \text{..... equation 8}$$

where I_{pa} denotes the anodic peak current of tyramine; F, Faraday's constant (96,485.34 C mol^{-1}); A, the electroactive surface area (0.074 cm^2); C, the concentration of tyramine (1×10^{-6} mol cm^{-3}); R, the gas constant (8.31447 J $mol^{-1}K^{-1}$); T, the absolute temperature (298 K); and ν, the scan rate. The plot of the electrooxidation current of tyramine versus $\nu^{1/2}$ (inset Figure 26C) provided the linear

regression of y = 183.57x –3.2432 (R^2 = 0.994). Hence, the calculated D_0 of Tyr was found to be 6.84 × 10^{-5} cm^2 s^{-1}.

$$E_{pa}=E^0+\frac{RT}{(1-\alpha)nF}\ln\frac{RTk_s}{(1-\alpha)nF}+\frac{RT}{(1-\alpha)nF}\ln\nu \quad \text{..... equation 9}$$

$$I_{pa} = (2.99 \times 10^5)\, n[(1-\alpha)n_\alpha]^{1/2}AC_sD_0^{1/2}\nu^{1/2} \quad \text{..... equation 10}$$

It is important to determine the factor of $(1-\alpha)n_\alpha$ before estimating the number of electrons in the irreversible process. As presented in Figure 27B, the calculation is based on a linear relationship between E_{pa} and ln ν (y = 0.0317x + 0.5967; R^2 = 0.9828). Hence, the calculated factor of $(1-\alpha)n_\alpha$ was found to be 0.81. As a result, the number of electrons involved in the electrooxidation of tyramine was calculated to be 1.11 (n ~ 1). The electrochemical behavior of tyramine under various pH conditions can be used to determine the number of protons involved in the electrooxidation process. In Figure 26D, the oxidation peak potentials (E_{pa}) of tyramine at poly(His)/SPGE in the pH range of 5.7–9.0 clearly shifted to the negative direction as the pH values increased. This is a consequence of the protonated form of tyramine involved in the oxidation process that could be facilitated the electron-transfer process at higher pH values (pK_a values of tyramine ~9.66 and ~10.41). Tyramine is fully protonated at a pH of around 7, indicating the existence of a positively charged amine group in the tyramine structure, since this pH value is lower than the actual pK_a for an amine group. As a result, the maximum peak current was observed at pH 7.4 for the tyramine detection. This phenomenon can be attributed to the protonated forms of tyramine at pH 7.4 fully interacted electrostatically with the carboxylic groups on the polymer backbone. Therefore, PBS at pH 7.4 was selected as the supporting electrolyte. Furthermore, the Nernst equation was used to characterize the linear relationship between the pH values and oxidation peak potentials (y = –0.0556x + 0.8397; R^2 = 0.9963). The numbers of electrons and protons at the electrode interface were denoted by m and n, respectively. The slope was found to be 0.0556, which was close to the theoretical value of 0.0591. This suggested that the numbers of electrons and protons

transferred at the electrode interface were equal, indicating that m = n = 1. Thus, one electron and one proton were involved in the electrooxidation of tyramine at poly(His)/SPGE, a finding consistent with those of previous studies (Sanu K. Anand et al., 2020).

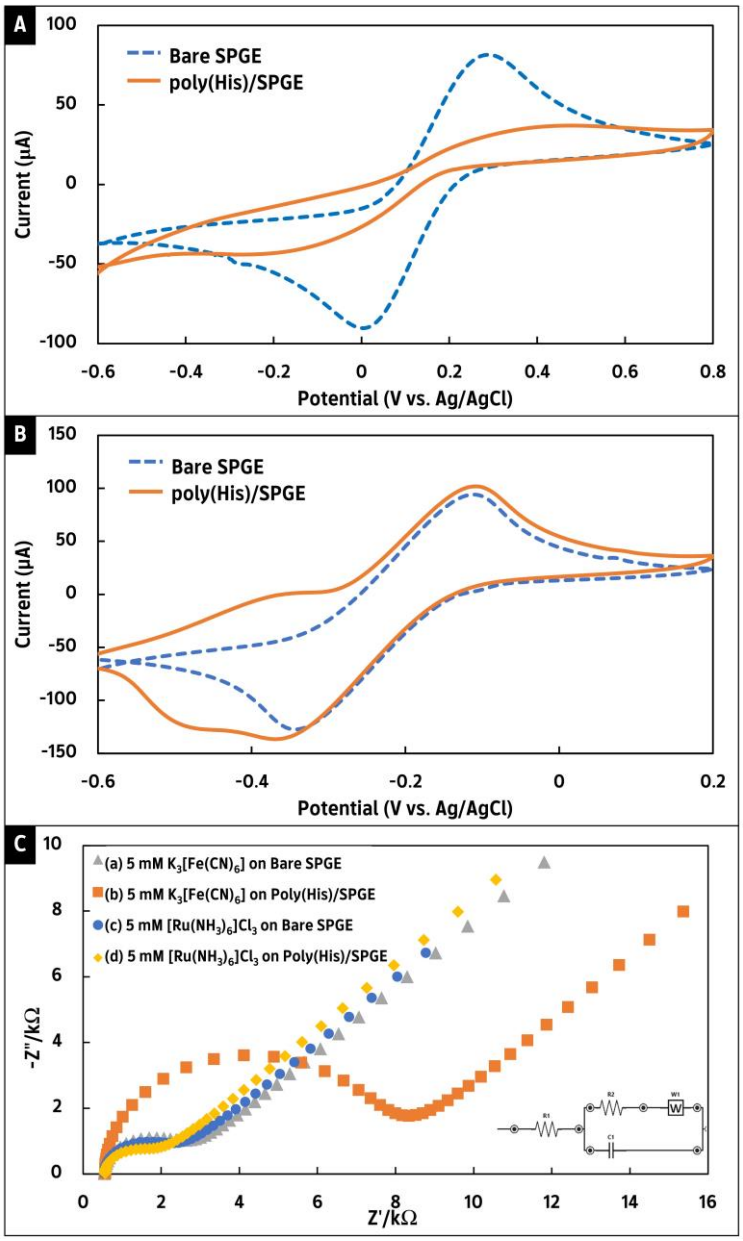

Figure 24 Cyclic voltammograms of both bare SPGE and poly(His)/SPGE in (A) 5 mM $Fe(CN)_6^{3-/4-}$ in 0.1 M KCl (potential ranges from –0.60 to +0.80 V, scan rate 0.075 V s^{-1}), (B) 5 mM $Ru(NH_3)_6^{3+}$ in 0.1M KCl (potential ranges from –0.60 to +0.20 V, scan rate

0.075 V s^{-1}), and (C) EIS curves of bare SPGE and poly(His)/SPGE in 5 mM $Fe(CN)_6^{3-/4-}$ (curve a and b) and 5 mM $Ru(NH_3)_6^{3+}$ (curve c and d)

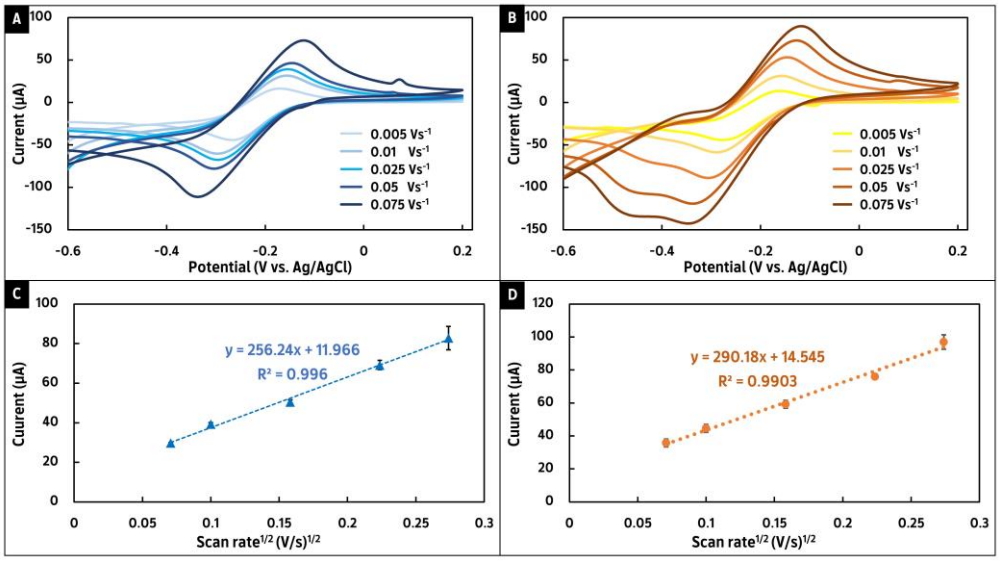

Figure 25 (A) and (B) represent CV curves for 5 mM $Ru(NH_3)_6^{3+}$ in 0.1 M KCl at bare SPGE and poly(His)/SPGE, respectively (Potential ranges from –0.65 to +2.0 V at different scan rates) and (C) and (D) show the plot of anodic peak current of 5 mM $Ru(NH_3)_6^{3+}$ vs. square root of scan rate at bare SPGE and poly(His)/SPGE, respectively

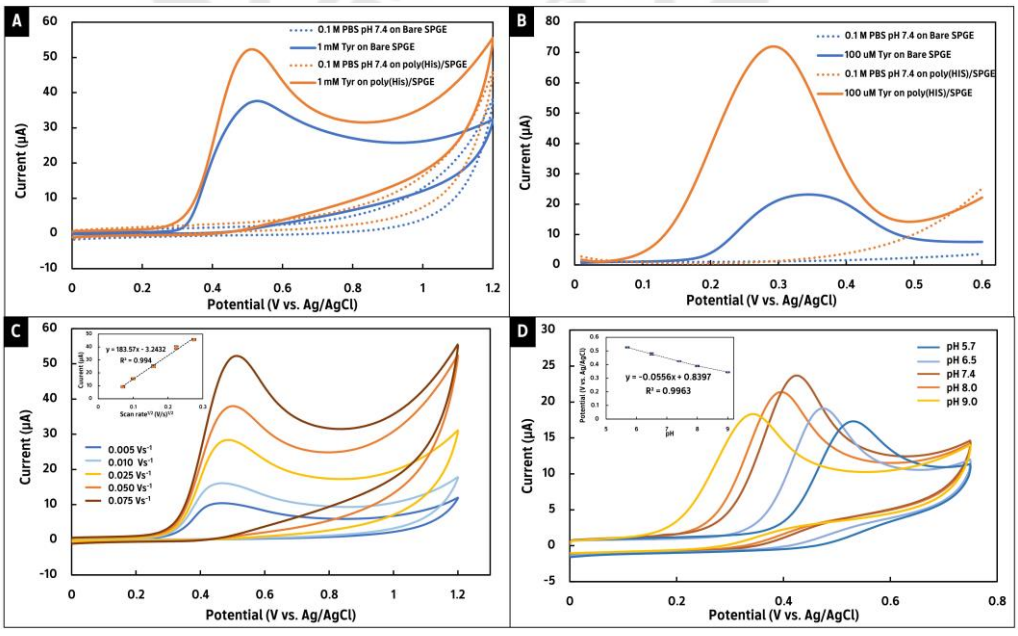

Figure 26 (A) CV curves of 1 mM tyramine in 0.1 M PBS (pH 7.4) at bare SPGE and poly(His)/SPGE (scan rate of 0.075 V s^{-1}), (B) DPV curves obtained for comparing both of bare SPGE and poly(His)/SPGE in 100 µM tyramine containing 0.1 M PBS (pH 7.4), (C) CV curves of 1 mM tyramine in 0.1 M PBS (pH 7.4) at different scans rate using poly(His)/SPGE (inset presents dependence of the anodic peak current on the square root of the scan rate), and (D) CV curves of 1 mM tyramine obtained for varying pH conditions

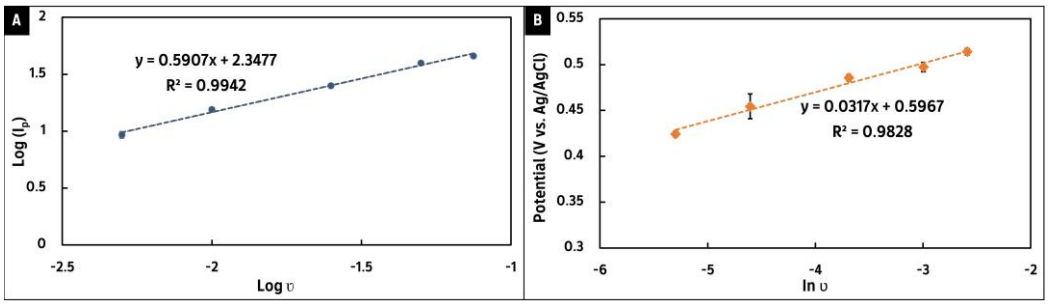

Figure 27 The linear relationship between (A) log (I_p) and log ν and (B) peak potential (E_p) and ln ν for 1 mM tyramine in 0.1 M PBS (pH 7.4) at poly(His)/SPGE (scan rate (ν); 0.005 to 0.075 V s^{-1})

4.1.4 Optimization of electropolymerization of L-histidine and electrochemical detection

To achieve excellent sensitivity and analytical performance for the detection of tyramine, several parameters in the electropolymerization process were examined. The electrochemical response of the target analyte was influenced by the thickness of the polymeric film. Consequently, the monomer concentration and the number of cycle scans were systematically investigated to obtain the optimal polymeric film thickness for the tyramine sensor. Figure. 28A and C illustrate the concentration of L-histidine and the number of cycle scans, respectively. For the monomer concentration, the peak current increased up to 40 mM and decreased thereafter. This might be due to the formation of a nonuniform polymeric layer. Meanwhile, a high electrochemical response was obtained when the number of cycle scans was set to 20. This means that a 20-cycle

scan is sufficient to generate a polymeric histidine film on the SPGE surface that could accelerate the electron-transfer at the electrode interface. Therefore, 40 mM of L-histidine and 20 cycles were selected as the optimized conditions for electropolymerization for further experiments.

The potential windows and scan rate affected the rates of the electrochemical reaction, film thickness, and dopant contents. Hence, the suitable applied potential windows and scan rate of the electropolymerization process were also investigated. The potential ranges (Figure 28B) were first fixed between –0.8 and +2.0 V; this finding could be used for the tyramine detection. However, this potential range resulted in a delay in the generation of a polymeric film onto the SPGE surface. Furthermore, an attempt was made to shift the final potential in a more negative direction. It was found that when the applied potentials were scanned from –0.8 to +1.5 V, the current for tyramine decreased. This implies that the final potential for the electropolymerization process must be higher than +1.5 V to ensure the oxidation of L-histidine. This phenomenon may be due to the fact that the imidazole groups of poly(His) can be overoxidized at higher anodic potentials, resulting in the introduction of carbonyl and carboxyl groups to the polymer skeleton, which can induce diffusion of the target analyte into the electrode interface (Chen et al., 2017). As a result, the final potential was set to +2.0 V, and the initial potential gradually shifted to a more positive direction. Surprisingly, when the initial potential was applied at –0.6 V, the signal current of tyramine was the highest. Therefore, an applied potential in the range of –0.6 to +2.0 V was selected for the electropolymerization process for further experiments. The tyramine responses for the formation of poly(His) film are presented in Figure 28D using a different scan rate. It was observed that a scan rate of 0.2 V s^{-1} exhibited a high sensitivity of the tyramine response due to the formation of a uniform polymeric layer. Therefore, the scan rate of 0.2 V s^{-1} was selected for the electropolymerization process because this condition offered the maximum current within a reasonable time duration for the modification process. Furthermore, the electrochemical conditions in DPV are a crucial parameter that can affect the tyramine peak shape and peak current.

All parameters of the DPV, including increment, amplitude, pulse width, and pulse period, were systematically examined *via* DPV using 100 µL of tyramine in 0.1 M PBS at pH 7.4. The optimum currents were detected at pulse width of 0.025 s, amplitude of 0.2 V, increment of 0.01 V, and pulse period of 0.5 s, which offered the best analytical performance for tyramine monitoring (Figure 29).

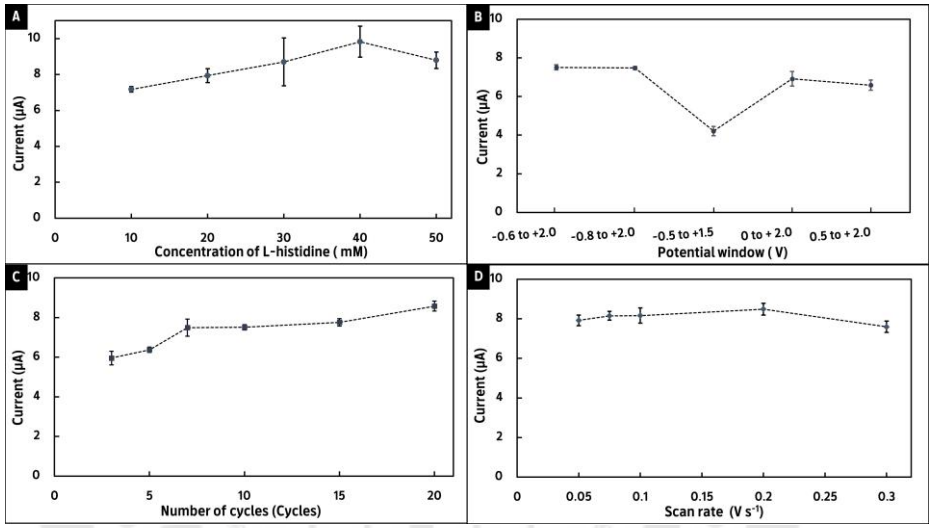

Figure 28 The influent of electropolymerization process included (A) concentration of L-histidine, (B) suitable potential windows, (C) number of cycle scans, and (D) scan rate

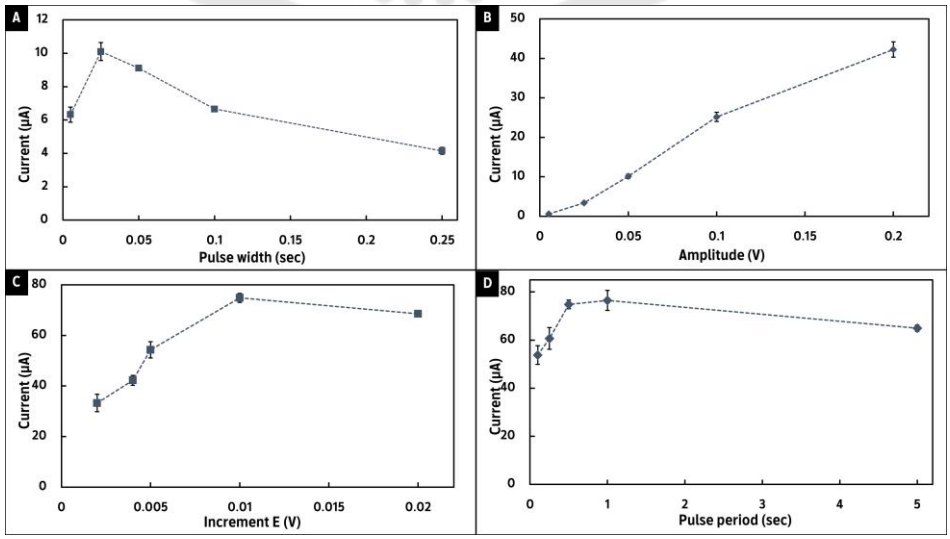

Figure 29 represents the crucial DPV parameters including (A) pulse width, (B) amplitude, (C) increment E, and (D) pulse period

4.1.5 Analytical performances

Under optimal conditions, the DPV technique was performed for the quantitation of tyramine, and the results are presented in Figure 30. The linear concentration ranges (Figure 30B) were found to be 0.5–20 and 50–300 μM with a linear regression equation of I_{pa} = 1.6069 $C_{tyramine}$ + 1.1467 (R^2 = 0.9933) and I_{pa} = 0.2455 $C_{tyramine}$ + 44.533 (R^2 = 0.9961), respectively. The limit of detection was estimated to be 0.065 μM based on 3SD/m, where SD denotes the standard deviation of 10 replicate measurements of a blank (0.1 M PBS, pH 7.4), and m denotes the slope of the calibration curve. The analytical performance of poly(His)/SPGE for tyramine determination was compared with other electrode characteristics listed in Table 3. The novel sensor based on the polymeric film of L-histidine exhibited better performance in some cases or was comparable with the other tyramine sensors reported so far, with a low LOD and a sufficiently wide linear range. Furthermore, when compared with other architectures that used complex materials, multiple and complicated processes, and/or enzyme immobilization, the proposed sensor proved its ease of fabrication by requiring only a single step of modification directly onto the electrode surface. Therefore, this produced sensor is not only sensitive enough for clinically significant tyramine monitoring in real samples; it also offers good potential for on-site and real-time analysis.

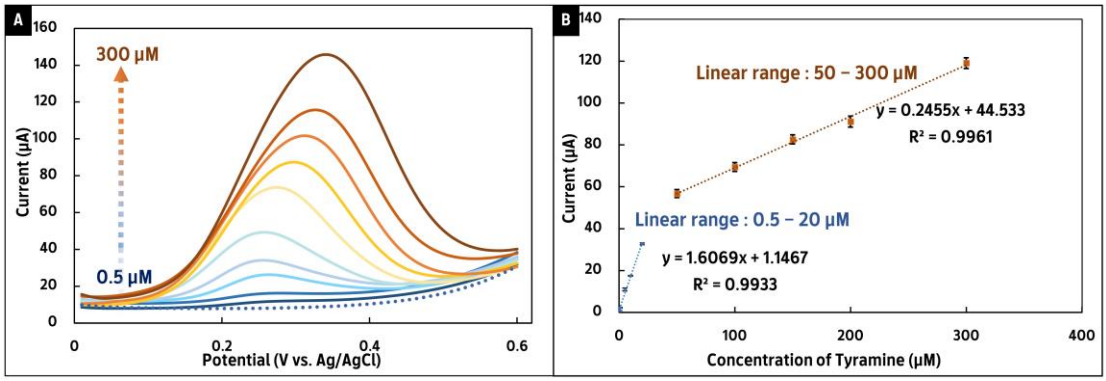

Figure 30 (A) DPV signals for different concentrations of tyramine at poly(His)/SPGE and (B) calibration plot between peak current and tyramine concentration

Table 3 Comparison of the tyramine determination performance at the different modified electrodes

Modification electrode	Technique	Real samples	Linear range (μM)	LOD (μM)	References
Pea seedling amine oxidase MnO_2/SPCE	Amp	Chicken meat	10–300	3.0	(Telsnig et al., 2013)
Q/fMWCNT/GCE	DPV	Yoghurt Urine	0.7 - 75	0.647	(Raoof, Ojani, Amiri-Aref, et al., 2012)
Tyr_{ase}/TiO_2/CMK-3/PDDA/Nafion/GE	CV	Camember cheese Sauerkraut Banana	6–130	1.5	(Kochana et al., 2016)
PO_4-Ppy/Pt	Amp	Sauerkrautt	4–80	0.547	(Apetrei & Apetrei, 2013)
P3MT/Pt	DPV	Moldy cheese	4.4 - 14000	1.32	(Küçük & Torul, 2018)
OPOAP/GCE	SWV	Rice vinegar	0.1-200	0.054	(Zhao et al., 2018)
TiO_2-Ag/PPy/GCE	CA	Cheese Sauerkraut	0.04 -3.07	0.02	(Erdogan et al., 2018)
AuNP-PANSA/AuE	EIS	Roquefort cheese, Yogurt Red wine Beer	0.8–80	0.04	(da Silva et al., 2019a)

Table 3 (Continued)

Modification electrode	Technique	Real samples	Linear range (μM)	LOD (μM)	References
P(LArg)/ERGO/GCE	DPV	Blood serum Urine	0.6 – 10 and 20 -70	0.145	(Sanu K Anand et al., 2020)
PCGE	DPV	Red wines	0.6–100	0.5	(da Silva et al., 2021)
Poly(His)/SPGE	DPV	Urine Serum Cheese samples	0.5- 20 and 50 -300	0.065	**This work**

MnO_2= manganese dioxide; Q/fMWCNT = quercetin on a functionalized multi-wall carbon nanotube; GCE = glassy carbon electrode; Tyr_{ase}= Tyrosinase; SPCE = screen-printed carbon electrode; TiO_2 = titania dioxide sol; PDDA = poly-(diallyl dimethyl ammonium chloride); GE = graphite electrode; PO_4-Ppy = phosphate-doped polypyrrole film; Pt = platinum electrode; P3MT = poly(3-methylthiophene); OPOAP = Overoxidized Poly(o-aminophenol); Ti_2O-Ag = titanium dioxide-silver nanocomposite; Ppy= polypyrrole; AuNP= gold nanoparticle; PANSA= poly-(8-anilino-1-napthalene sulphonic acid); AuE= gold electrode; P(L-Arg)= poly(L-Arginine); ERGO = electrochemically reduced graphene oxide; PCGE = pencil carbon graphite electrode; Amp= Amperometry; CV= Cyclic voltammetry; DPV= Differential pulse voltammetry; EIS = Electrochemical impedance spectroscopy; CA = Chronoamperometry.

To verify the performance of the proposed sensor, the precision in terms of reproducibility was investigated by determining the tyramine response at seven modified electrodes. The relative standard deviation (RSD) was calculated to be 1.23%, which indicated an excellent reproducibility. Furthermore, the long-term stability of poly(His)/SPGE was evaluated by measuring the response currents toward 100 μM of tyramine in 0.1 M PBS (pH 7.4) at 7-day intervals. The prepared poly(His)/SPGE were kept in a zip lock at room temperature before use. As presented in Figure 31, the

electrooxidation currents of tyramine could remain at 90.75% of their initial current response, after 35 days, indicating good stability of the fabricated sensor.

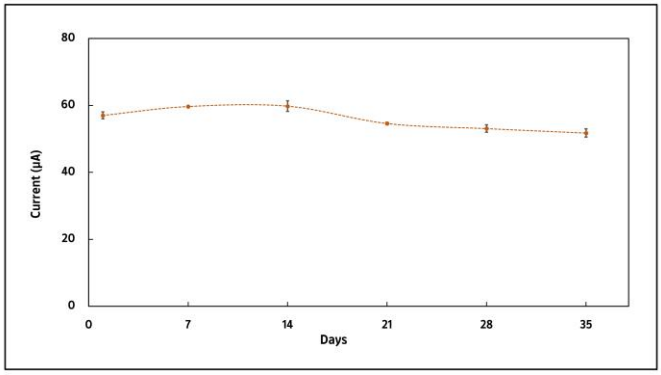

Figure 31 The study of long-term stability of poly(His)/SPGE

4.1.6 Interference study

To study the selectivity of the proposed sensor, the presence of tyramine in various concentration ratios of interfering substances was investigated *via* DPV. The possible interfering substances were Mg^{2+}, ascorbic acid (AA), glutathione (GSH), creatinine (Cr), bovine serum albumin (BSA), dopamine (DA), uric acid (UA), and cysteine (Cys), which are abundant in biological samples. Furthermore, some BAs such as cadaverine (Cad), histamine (Hist), and putrescine (Put), which are commonly found in cheese samples, were considered. The measurements were performed in 5 μM tyramine with co-existing concentrations of 1 mM for Mg^{2+}, AA, GSH, and Cr, 1% for BSA, 0.1 mM for DA, 50 μM for UA, 5 μM for Cys, and 0.5 mM for Cad, Hist, and Put. No significant change was observed in the current (less than ±5%), as presented in Figure 32. This indicated that poly(His)/SPGE has an excellent selectivity toward the determination of tyramine.

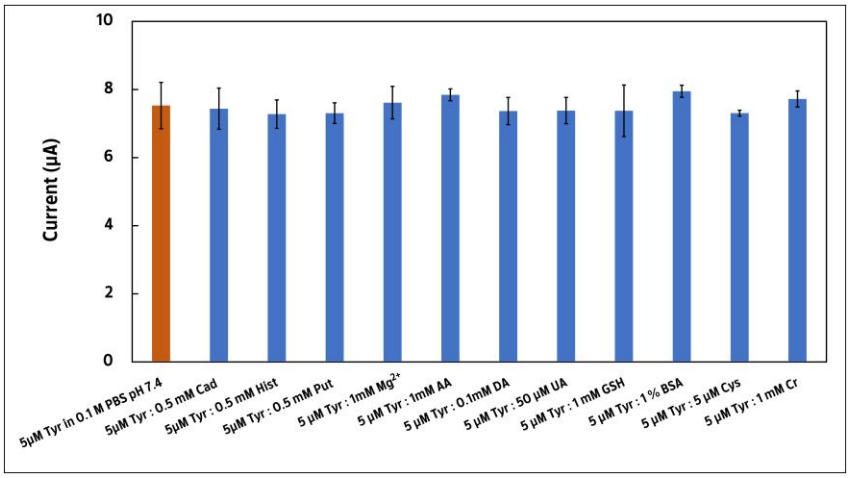

Figure 32 The effect of interferents on the anodic peak current of 5 μM tyramine at poly(His)/SPGE (n=3)

4.1.7 Practical applications in real samples

To illustrate its practical application in real-sample analysis, the tyramine sensor was used in human urine samples, serum samples, and three types of cheese samples. The analytical determination was performed using the standard addition method by spiking the standard tyramine (1, 5, 10, and 15 μM) in real samples. The values calculated based on the average of three replicates are presented in Table 4. The recovery and RSD values (%) were obtained in the acceptable value ranges of 82.58%–109.75% and 0.28%–8.03%, respectively. Moreover, the quantities of tyramine were found to be 7.03, 8.86, and 16.77 mg/kg in candy cheese plain, mozzarella cheese, and cheddar cheese, respectively. These findings indicate that poly(His)/SPGE has sufficient sensitivity, selectivity, and reliability for detecting the presence of tyramine in biological and food samples.

Table 4 The practical applications of poly(His)/SPGE for monitoring tyramine in real samples (n = 3)

Real Samples	Spiked (μM)	Found (μM)	Recovery (%)	RSD (%)
Human urine sample 1	1	0.95 ± 0.03	95.32	2.59
	5	5.48 ± 0.10	109.66	1.78
	10	10.74 ± 0.04	107.43	0.28
	15	14.36 ± 0.14	95.72	0.93
Human urine sample 2	1	1.04 ± 0.13	104.04	8.03
	5	5.49 ± 0.23	109.75	3.67
	10	10.48 ± 0.66	104.79	5.86
	15	14.52 ± 0.25	96.77	1.65
Human serum sample	1	1.06 ± 0.02	105.68	1.45
	5	5.26 ± 0.12	105.26	2.25
	10	10.23 ± 0.23	102.30	2.27
	15	15.37 ± 0.22	102.44	1.43
Candy cheese plain	1	1.34 ± 0.05	83.01	1.95
	5	5.42 ± 0.07	98.19	1.09
	10	9.82 ± 0.46	93.08	3.96
	15	14.96 ± 0.48	96.29	2.79
Mozzarella cheese	1	1.60 ± 0.11	95.61	2.94
	5	5.38 ± 0.09	94.75	1.13
	10	9.48 ± 0.08	88.37	0.70
	15	15.18 ± 0.41	96.86	2.34
Cheddar cheese	1	2.05 ± 0.12	82.58	3.13
	5	5.49 ± 0.33	85.27	4.59
	10	9.76 ± 0.40	85.34	3.52
	15	14.93 ± 0.42	91.37	2.55

4.2 The development of a new electrochemical platform using poly(L-proline)-linked nanodiamonds on a screen-printed graphene electrode for simultaneous detection of L-DOPA and L-Tyr

The details provided in this section are extracted from the original research article; see Appendix 2 for the full text.

4.2.1 Electrochemical performances of the modified electrodes with poly(L-Pro) and ND

The effect of different electrode preparation steps based on single, composite, layer-by-layer modification, and a bare SPGE on the electrochemical oxidation of L-DOPA and L-Tyr was first investigated. As shown in Figure 33A, the CV measurement at the bare SPGE (curve a) revealed weak anodic peak currents of L-DOPA and L-Tyr. In addition, a slight hump on the L-DOPA oxidation peak was noticed. After the ND layer was deposited on SPGE (curve b), a pair of obvious oxidation peaks of the target analyte was discovered, implying that the ND layer could eliminate a disturbance hump peak. While a single modification of poly(L-Pro) was present on SPGE (curve c), the oxidation peaks of L-DOPA and L-Tyr increased and showed sharp peaks at potentials of +0.049 V and +0.543 V, respectively. These findings may be a result of catalysis by poly(L-Pro). Therefore, the use of a combination of ND and poly(L-Pro) as modifiers was investigated using various modification approaches. At the composite ND-(L-Pro)/SPGE (curve d), the electrochemical signals of target analytes dramatically decreased compared with those of poly(L-Pro)/SPGE. Interestingly, better electrochemical responses and well-defined peaks of target analytes were observed at the layer-by-layer poly(L-Pro)/ND/SPGE (curve f).

The DPV technique is furthermore used to precisely confirm the electrochemical performances of various modified and unmodified electrodes. Figure 33B illustrates the DPV responses of 0.1 M PBS, pH 7.4 at the different electrodes. As expected, the disturbance peak was observed at the potential of –0.01 V at a bare SPGE (curve a). This phenomenon is attributed to the coexistence of screen-printing ink formulations, such as resins, solvents, and additives, that could be oxidized at the near

potential of L-DOPA oxidation. Interestingly, when the electrode surface is modified by ND or poly(L-Pro) with different modification steps, the disturbance peak is eliminated. This indicates that the integration of the ND layer with poly(L-Pro) is important for the suppression of background currents. From the obtained results, the poly(L-Pro)/ND/SPGE (curve f) provided a flat and lower signal of background currents. This could be beneficial for achieving a low detection limit. From the DPV responses in Figure 33C, it is clearly seen that the layer-by-layer poly(L-Pro)/ND/SPGE not only increased the oxidation peak current by 6- and 3-folds for L-DOPA and L-Tyr but also provided a lower detection potential for both target analytes. Therefore, it is logical to assume that poly(L-Pro)/ND/SPGE could be an appropriate electrode material for the simultaneous detection of L-DOPA and L-Tyr.

To study the changes in the impedance of modified electrodes, EIS was carried out in 5 mM $Fe(CN)_6^{3-/4-}$ in 0.1 M KNO_3 at the different electrodes. The charge transfer resistance (R_{ct}) is represented by the diameter of the semicircle (Bonanni et al., 2012) as shown in Figure 33D. The highest calculated R_{ct} is at the bare SPGE (11.83 kΩ) and is significantly reduced for ND/SPGE (9.39 kΩ), poly(L-Pro)/SPGE (3.24 kΩ), ND-(L-Pro)/SPGE (7.24 kΩ), ND/poly(L-Pro)/SPGE (4.84 kΩ), and poly(L-Pro)/ND/SPGE (1.98 kΩ). The decreased values indicated that the electron transfer process is more promoted at the modification layers. The poly(L-Pro)/ND/SPGE provided the lowest R_{ct}, confirming that both poly(L-Pro) and ND most facilitate the transfer process at the solution-electrode interface. It can be concluded that both modifiers have a synergistic effect due to the high electrical conductivity of the poly(L-Pro) film and the enlarged active surface area of ND.

Chronoamperometric experiments, as presented in Figure 34, were subsequently performed to confirm the electrocatalyst property of modifiers. The catalytic rate constant (k_{cat}) of both analytes on different electrodes was calculated by the following equation (Rotariu et al., 2010):

$$\frac{i_{cat}}{i_{buffer}} = \pi^{\frac{1}{2}}(k_{cat}Ct)^{1/2} \quad \text{..... equation 11}$$

where i_{cat} and i_{buffer} are the currents in the presence and absence of the target analyte, respectively, C represents the concentration of the target analyte, and t is the time at which the current values were taken. The catalytic rate constant was calculated from the slope of the linear relationship formed by plotting the i_{cat}/i_{buffer} vs. $t^{1/2}$ for 5 mM L-DOPA (Figure 34C) and 5 mM L-Tyr (Figure 34D). The catalytic rate constants of both target analytes at different strategies for electrode modification are summarized in Table 5. Table 5 shows the catalytical rate constant (k_{cat}) for both target analytes at different electrodes. It was found that k_{cat} significantly increased after modified electrodes with either or both poly(L-Pro) and ND. The poly(L-Pro)/ND/SPGE exhibits the highest k_{cat} for both target analytes. This confirmed that the layer-by-layer poly(L-Pro)/ND/SPGE has remarkable electrocatalytic capabilities toward the electrooxidation of L-DOPA and L-Tyr. According to all proving, poly(L-Pro)/ND/SPGE is the most suitable sensor for simultaneously determining L-DOPA and L-Tyr.

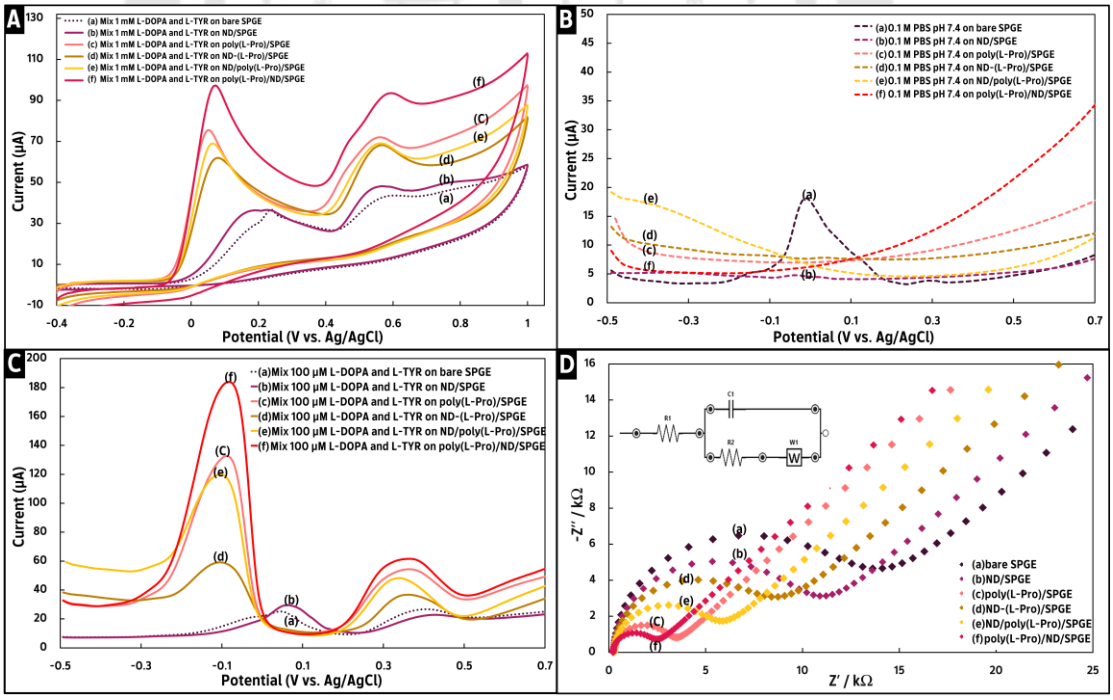

Figure 33 (A) CV responses of a mixture of 1 mM L-DOPA and 1 mM L-Tyr at the different electrodes, (B) DPV responses of 0.1 M PBS pH 7.4 at the different electrodes, (C) DPV responses of a mixture of 100 μM L-DOPA and 100 μM L-Tyr at the different

electrodes, and (D) EIS curves of 5 mM $Fe(CN)_6^{3-/4-}$ in 0.1 M KNO_3 at the different electrodes

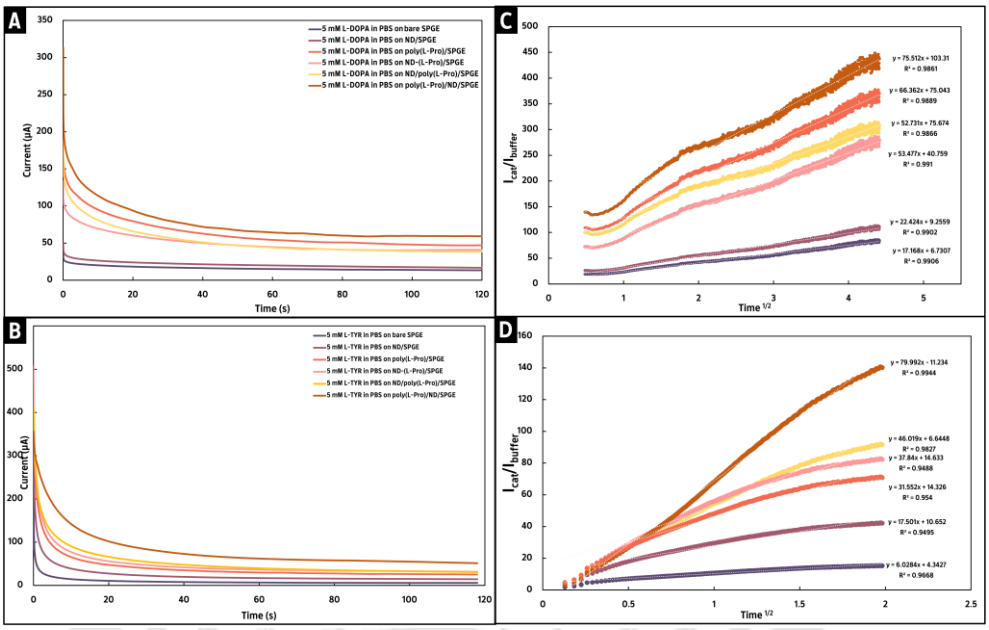

Figure 34 Chronoamperograms for (A) 5 mM L-DOPA and (B) 5 mM L-Tyr in 0.1 M PBS at different electrodes and linear segments of the plot I_{cat}/I_{buffer} vs. $t^{1/2}$ derived from chronoamperometric data for (C) 5 mM L-DOPA and (D) 5 mM L-Tyr

Table 5 The calculated catalytical rate constant toward L-DOPA and L-Tyr oxidation at six different electrodes.

Electrode	k_{cat} of L-DOPA (L mol^{-1} s^{-1})	k_{cat} of L-Tyr (L mol^{-1} s^{-1})
bare SPGE	1.88×10^4	2.31×10^3
ND/SPGE	3.20×10^4	1.95×10^4
poly(L-Pro)/SPGE	2.81×10^5	6.34×10^4
ND-(L-Pro)/SPGE	1.77×10^5	9.12×10^4
ND/poly(L-Pro)/SPGE	1.82×10^5	1.35×10^5
poly(L-Pro)/ND/SPGE	3.63×10^5	4.08×10^5

4.2.2 Characterization of the morphology and structure of the proposed electrode

To understand the surface morphology and structural features of different modified materials on SPGEs, various characterizations, including SEM-EDS analysis and Raman spectroscopy, were performed. The SEM images of a bare SPGE (Figure. 35A and B) showed the sheet-like structure's wrinkled edge. For the deposition of the ND layer on SPGE, it provided a relatively uniform size, but its aggregation revealed disparate shapes and sizes on the SPGE surface (Figure 35C and D). Hence, the surface roughness of ND/SPGE improved, indicating an increase in the surface-active site. While the poly(L-Pro) was distributed on SPGE, a smooth surface, and a thin film-like structure were observed (Figure 35E and F). Figure 35G and H showed the SEM images of SPGE after modifications of layer-by-layer via poly(L-Pro) and ND. Because of the ND's specific activity, it provides a good effective area for the growth of the poly(L-Pro) layer, and thus the poly(L-Pro) modified on the ND-deposited SPGE formed the three-dimensional smooth film that covered the clump-like morphology of ND particles on the stacking graphene sheet.

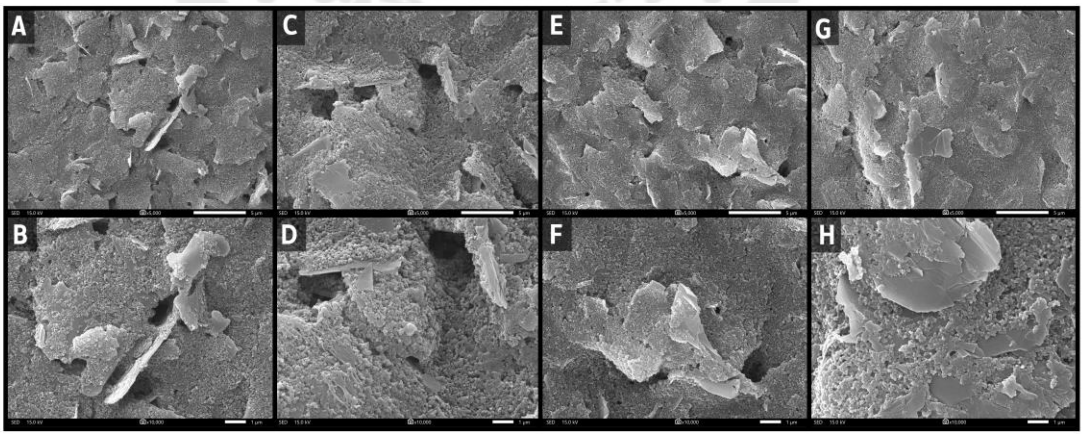

Figure 35 SEM images of (A and B) bare SPGE, (C and D) ND/SPGE, (E and F) poly(L-Pro)/SPGE, and (G and H) poly(L-Pro)/ND/SPGE at 5,000X (A, C, E, and G), and at 10,000X (B, D, F, and H)

A particle size distribution of ND on SPGE was determined from the SEM images using Image J processing. The particles are in the 30–100 nm range, with an average diameter size of 60.79 ± 15.38 nm (Figure 36), confirming that the agglomerated NDs retain their nanoscale size after the electrodeposition.

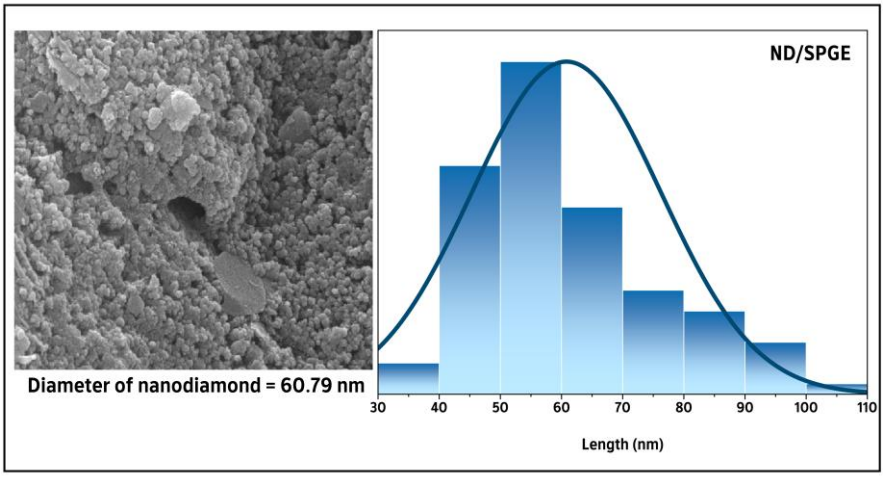

Figure 36 A particle size distribution of ND on SPGE

In addition, the SEM image is supported by EDS analysis to investigate the composition of different modified electrodes. It is proven that the surfaces of unmodified and modified electrodes consist mostly of carbon and oxygen (Figure 37). Slight nitrogen peaks in the EDS spectrogram were noted for both poly(L-Pro)/SPGE (Figure 37C) and poly(L-Pro)/ND/SPGE (Figure 37D). These results confirm the presence of a polymeric thin film of L-Pro. To prove the formation of poly(L-Pro)/ND/SPGE, the different electrodes based on either or both poly(L-Pro) and ND were characterized by Raman spectroscopy. The Raman spectra of the bare and modified SPGEs (in Figure 37E) showed the intense G band at ~1588 cm^{-1}, corresponding to in-plane vibration of the sp^2 bonded carbon structure, and the D band at ~1365 cm^{-1} mainly reflecting defects and disorders in the graphitic structure (Hajzus et al., 2022). Moreover, the presence of a more intense 2D band was observed at ~2726 cm^{-1} on bare SPGE, which can imply the number of graphene layers. The intensity ratio of the 2D and G bands (I_{2D}/I_G) of bare SPGE was found to be 0.17, indicating the multi-layered graphene grown

on the PVC substrate (Dong et al., 2011; Varga et al., 2017). In the case of ND/SPGE, the intensive D band was observed at ~1335 cm^{-1}, corresponding to the vibration of the sp^3 diamond lattice (Mochalin et al., 2012). The spectral region ranges at 826–930 cm^{-1} could be attributed to the ring stretching modes of the pyrrolidine ring and the variation of the COO^- group on L-Pro. The bands observed at ~1547 cm^{-1}, 2916 cm^{-1}, and 3174 cm^{-1} are assigned to the in-plane bending of NH, the symmetric stretch $\nu_s CH_2$, and the asymmetric stretch $\nu_{as} CH_2$ of L-Pro, respectively (Mary et al., 2009; Shimpi et al., 2014). The characteristic peaks for poly(L-Pro) and ND can be seen on the surface of the SPGE after layer-by-layer modification. The intensity ratios of the D and G bands in the Raman spectra (I_D/I_G) were calculated to be 0.93, 0.97, 0.99, and 1.08 for bare SPGE, ND/SPGE, poly(L-Pro)/SPGE, and poly(L-Pro)/ND/SPGE. These increased values indicated that a higher disordered level of the graphene structure was caused by the introduction of oxygen-containing functional groups from modifiers (Zhang et al., 2018).

4.2.3 Electrochemical characterization of poly(L-Pro)/ND/SPGE

As shown in Figure 38A, the cyclic voltammogram of the redox probe was significantly increased and sharpened after the layer-by-layer modification of poly(L-Pro) and ND to the SPGE surface. Moreover, it shifted the potential to be close to zero when compared with the bare SPGE. This suggests the increased transfer rate of $Fe(CN)_6^{3-/4-}$ to the electrode surface. These results were in good agreement with the EIS data in Figure 38B.

In addition, the electroactive surface areas were calculated to be 0.047 and 0.067 cm^2 for the bare SPGE and poly(L-Pro)/ND/SPGE, respectively. The electroactive surface area for the modified electrode was about 1.43 times larger than that of the bare SPGE. Furthermore, the calculated surface coverages of the bare electrode and poly(L-Pro)/ND/SPGE were found to be 1.60×10^{-10} and 7.92×10^{-10} mol cm^{-2}, respectively. The findings clearly demonstrated that the fabrication of layer-by-layer poly(L-Pro)/ND/SPGE is beneficial for improving active sites and surface coverage.

To evaluate the cycling stability of poly(L-Pro)/ND/SPGE, consecutive CV cycles of 5 mM $Fe(CN)_6^{3-/4-}$ in 0.1 M KNO_3 were performed at scan rates of 0.05 V s^{-1}. As shown in Figure 39, no change was observed from CV in the redox current after 15 cycles (about 89 % of the first cycle), which proved that the surface of this modified SPGE remained stable after functionalization and electrochemical process.

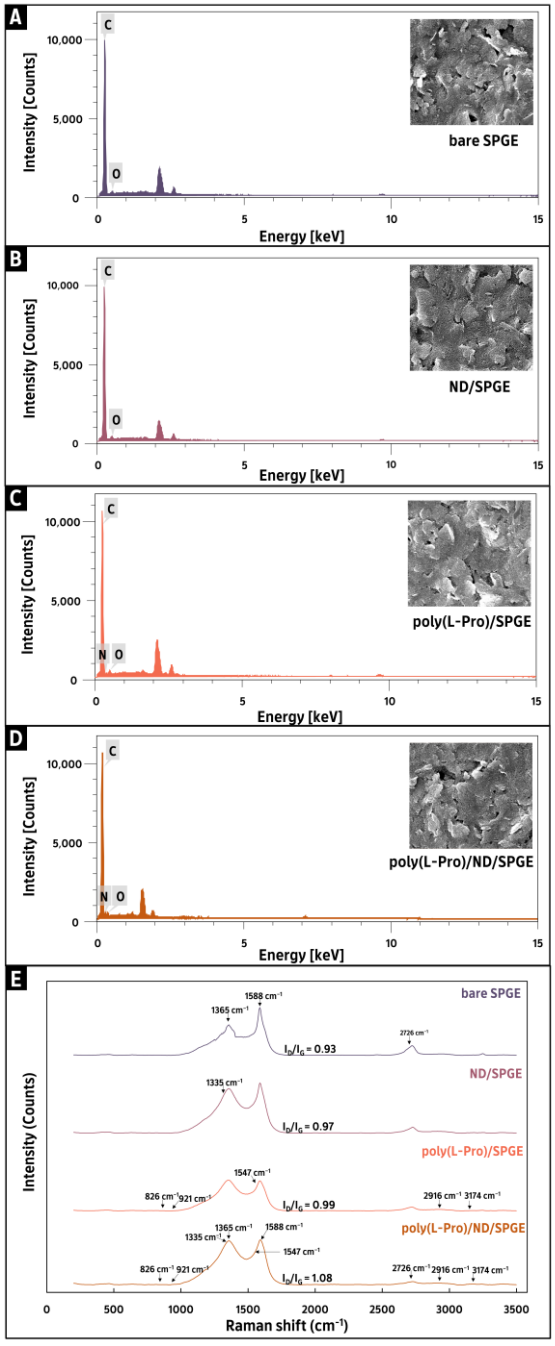

Figure 37 The SEM-EDS analysis for (A) bare SPGE, (B) ND/SPGE, (C) poly(L-Pro)/SPGE, (D) poly(L-Pro)/ND/SPGE, and (E) Raman spectra for the different electrodes

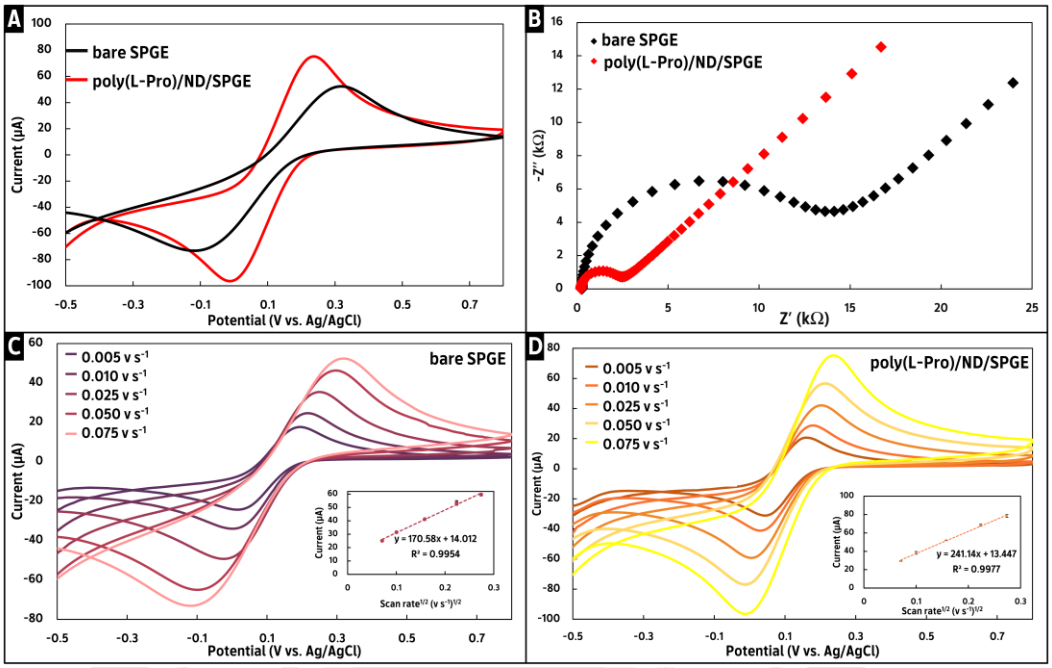

Figure 38 (A) Cyclic voltammograms, (B) EIS curves of 5 mM $Fe(CN)_6^{3-/4-}$ in 0.1 M KNO_3 at bare SPGE and poly(L-Pro)/ND/SPGE, and CV curves for 5 mM $Fe(CN)_6^{3-/4-}$ at (C) bare SPGE and (D) poly(L-Pro)/ND/SPGE with different scan rates (inset; the plot of I vs. $\nu^{1/2}$)

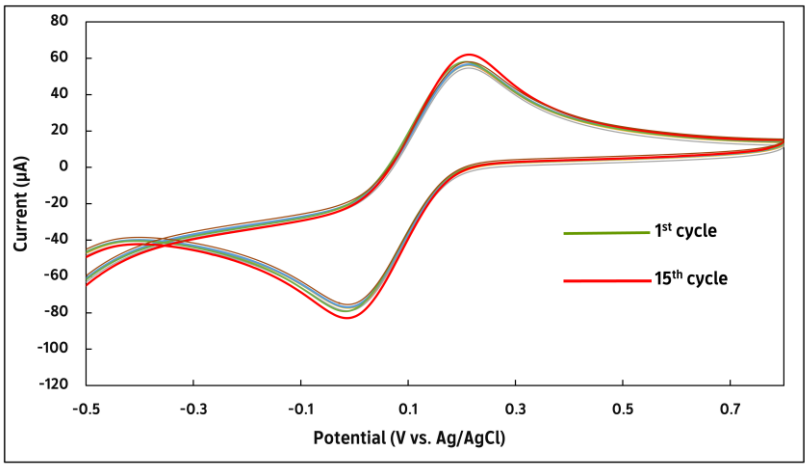

Figure 39 The cycling stability of poly(L-Pro)/ND/SPGE in the presence of 5 mM $Fe(CN)_6^{3-/4-}$ in 0.1 M KNO_3 at a scan rate of 0.05 V s^{-1}

4.2.4 Electrochemical behavior of L-DOPA and L-Tyr at poly(L-Pro)/ND/SPGE

The electrochemical responses for the simultaneous detection of L-DOPA and L-Tyr were investigated using bare SPGE and poly(L-Pro)/ND/SPGE via CV and DPV. As presented in Figure 40A, at the bare SPGE, the oxidation peaks are small and occur at potentials of +0.237 V for L-DOPA and +0.556 V for L-Tyr. On the other hand, at poly(L-Pro)/ND/SPGE, the oxidation peak currents of both target analytes increased significantly, and the peak potentials shifted to a negative potential of +0.071 V for L-DOPA and a slightly positive potential of +0.575 V for L-Tyr. Compared with bare SPGE, the peak potential difference (ΔEp) between L-DOPA and L-Tyr at poly(L-Pro)/ND/SPGE increased from 0.319 V to 0.504 V. The shift of peak potential and increase in ΔEp at layer-by-layer poly(L-Pro)/ND/SPGE can be attributed to the impact of hydroxyl (-OH) substitution in their aromatic rings: meta- and para-OH groups for L-DOPA and para-OH group for L-Tyr. Because of the higher OH group substituents, L-DOPA could be more chemically reactive than L-Tyr. As a result, L-DOPA can be easily oxidized at a more negative potential, further separating the response locations to L-Tyr and allowing for easier simultaneous detection. Moreover, the occurrence of a pair of anodic peaks indicated that the electrochemical reaction of L-DOPA and L-Tyr was a completely irreversible process. The DPV signals on bare SPGE were observed at potentials of +0.053 for L-DOPA and +0.396 V for L-Tyr, as shown in Figure 40B. Nevertheless, the anodic peak of L-DOPA at a bare SPGE showed an asymmetrical peak, caused by the disturbance substance in the screen-printing ink composition as mentioned before. This electrode material-induced disturbance resulted in complicated data interpretation and a lack of sensitivity. In contrast, at poly(L-Pro)/ND/SPGE, the background current is flat, and the electrooxidation of L-DOPA and L-Tyr increased dramatically with sharp and intense shapes at potentials of –0.087 and +0.347 V with peak currents of 6 and 3 times that of bare SPGE. According to all findings, the proposed electrode exhibits great electrocatalytic activity in terms of improving electron transfer kinetics at the electrode–solution interface. This enhancement could be attributed to a synergetic effect between

the high conductivity of poly(L-Pro) and the large surface-active area of ND, which enlarges the uniformity of poly(L-Pro) on the electrode surface.

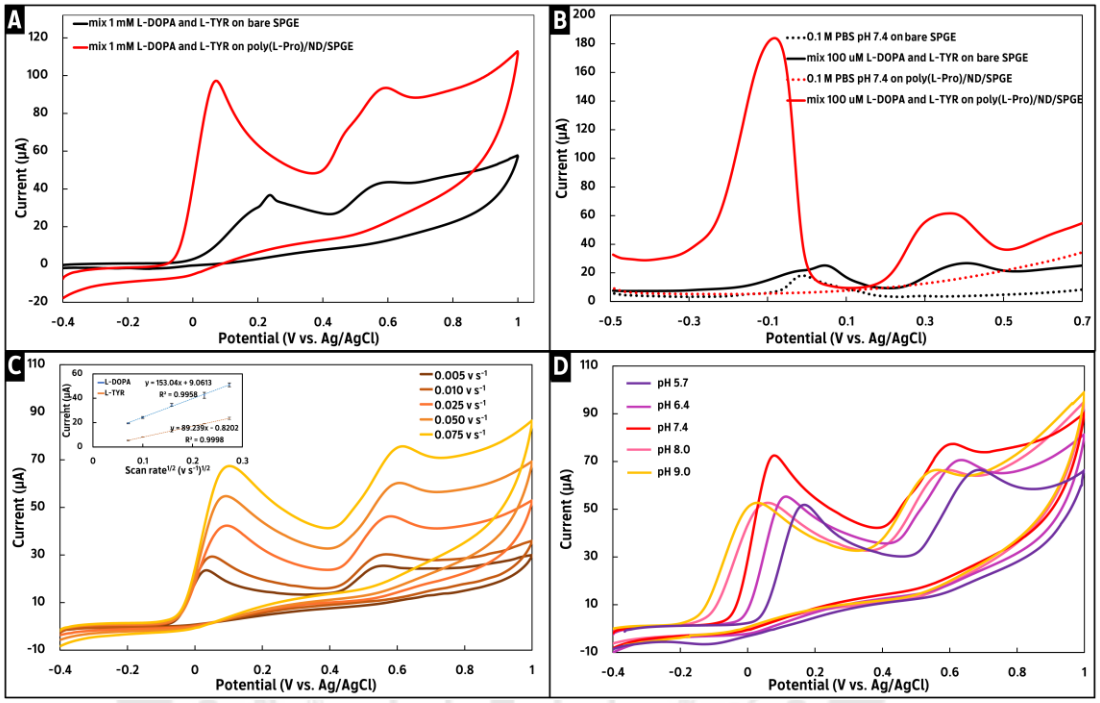

Figure 40 (A) CV curves of a mixture of 1mM L-DOPA and 1 mM L-Tyr at bare SPGE and poly(L-Pro)/ND/SPGE, (B) DPV curves obtained for comparing both of bare SPGE and poly(L-Pro)/ND/SPGE in a mixture of 100 µM L-DOPA and 100 µM L-Tyr, (C) CV curves of the mixture of 1 mM L-DOPA and 1 mM L-Tyr at different scan rate using poly(L-Pro)/ND/SPGE (inset; the plot of I vs. $\nu^{1/2}$), and (D) CV curves of the mixture of 1 mM L-DOPA and 1 mM L-Tyr with varying pH conditions

To gain an additional understanding of the sensing behavior of the poly(L-Pro)/ND/SPGE on both target analytes, computational chemistry calculations were performed by means of the density functional theory using the B3LYP/6-31G(d,p) level. According to the electrochemical results, electrodes with an upper layer of poly(L-Pro) significantly displayed a highly sensitive response to L-DOPA and L-Tyr. Therefore, the interaction between these analytes and the L-proline monomer was studied. The computational results proved that poly(L-Pro) has a stronger propensity to interact

with both target analytes via the electrostatic nature of the hydrogen bond (Figure 41A). Furthermore, an electron density map with an electrostatic potential for the interactions between both target analytes and L-Pro was also observed. The regions with the highest negative potential (high electron density) are highlighted in red, and the regions with the positive potential (low electron density) are indicated in green or blue color. As shown in Figure 41B, the electron density is located more on the aromatic rings and the hydroxyl and carbonyl groups of these analytes. The L-Pro monomer electron could be more localized at the carboxyl group. The presence of an electron cloud reveals the possibility of hydrogen bonding interactions between both target analytes and the poly(L-Pro) backbone, which induces the electron transfer process at the electrode–solution interface.

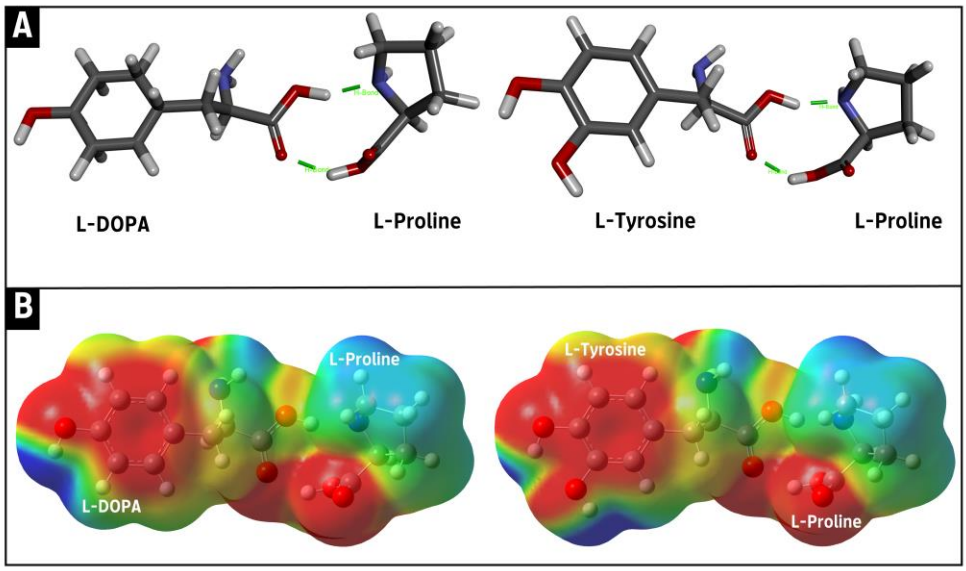

Figure 41 (A) Illustrates the optimized geometry of L-proline monomer—L-DOPA and L-Tyr complexes obtained by density functional theory and (B) the electron density mapped with ESP for the interactions between both target analytes and L-proline

Mass transport controlled by the electrooxidation of L-DOPA and L-Tyr was measured *via* CV. The effect of a scan rate of 0.005–0.075 V s^{-1} on poly(L-Pro)/ND/SPGE was shown in Figure 40C. The peak currents of L-DOPA and L-Tyr are proportional to

the square root of the scan rate (presented in the inset Figure 40C). Moreover, by plotting log I_p vs. log ν (Figure 42), the slopes of 0.5238 for L-DOPA and 0.5427 for L-Tyr were consistent with the theoretical value of 0.5, confirming that the electrooxidation of these analytes was controlled by the diffusion process (Velázquez-Palenzuela et al., 2011). Using the obtained information from the i-$\nu^{\frac{1}{2}}$ relationship (inset Figure 40C) together with the theoretic model described by Andrieux and Savèant (Andrieux & Savéant, 1980), the calculated diffusion coefficient (D_0) for L-DOPA and L-Tyr were found to be 5.93×10^{-5} cm^2 s^{-1} and 2.02×10^{-5} cm^2 s^{-1}).

For the irreversible process, the Randles–Sevcik relationship can be used to determine the number of electrons involved in the electrooxidation process (Boni et al., 2011). It was found that the number of electrons involved in the electrooxidation was calculated to be 1.31 (≈1) and 1.23 (≈1) for L-DOPA and L-Tyr, respectively.

Additionally, the effects of pH on the electrooxidation of both target analytes provide significant details about the mechanisms at the poly(L-Pro)/ND/SPGE interface. As the pH increased from 5.7 to 9.0, the oxidation peak potentials of L-DOPA and L-Tyr gradually shifted negatively, as presented in Figure 40D. The maximum peak currents of L-DOPA and L-Tyr were observed at pH 7.4. At this pH, they are in their zwitterionic forms due to the protonated amine and deprotonated carboxyl groups in their structures. These electrically neutral forms could be easily diffused from the bulk solution to the electrode interface via the electrostatic nature. Therefore, PBS at pH 7.4 was selected as the supporting electrolyte in further experiments. In addition, the slopes of a plot of E_p vs. pH as shown in Figure 42C, are –51.1 mV/pH for L-DOPA and –52.9 mV/pH for L-Tyr. Both are close to the theoretical value of –59.1 mV/pH, proving that there is an equal number of proton and electron transfers ($1e^-/1H^+$) involved in the electrooxidation of L-DOPA and L-Tyr at poly(L-Pro)/ND/SPGE.

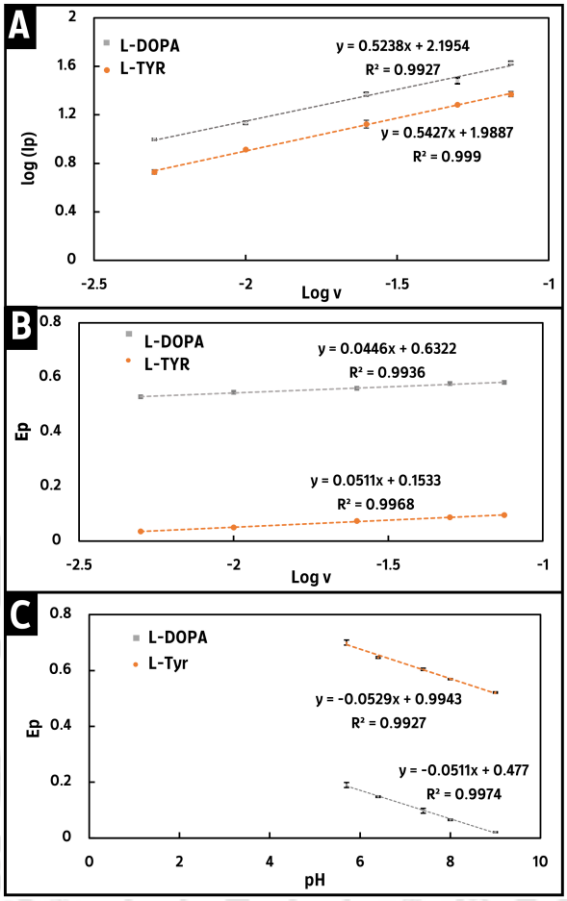

Figure 42 The linear relationship between (A) log (Ip) and log ν , (B) peak potential (E_p) and log ν (scan rate; 0.005 to 0.075 V s^{-1}), and (C) E_p and pH for 1 mM L-DOPA and L-Tyr in 0.1 M PBS (pH 7.4) at poly(L-Pro)/ND/SPGE

4.2.5 Optimization of the influence parameters for electrode modification and electrochemical detection

Because the parameters of ND deposition and poly(L-proline) manufacturing are critical for the electrochemical performance of L-DOPA and L-Tyr. The concentration of monomer, suitable potential window, and the number of cycles were investigated. The DPV technique was used to perform the simultaneous determination of L-DOPA and L-Tyr due to its low capacitive current, which results in high sensitivity. Therefore, all parameters of DPV were examined to obtain the best analytical performance.

Due to the enlarged surface area properties of ND, it is necessary to control the uniformity and thickness of ND. The concentration, the number of cycles, and the appropriate potential window for ND electrodeposition were systematically investigated, as shown in Figure 43. The potential range and number of cycling for ND formation represent the reaction time that ND is deposited on the electrode surface. The longer deposition time and more cycles might have contributed to the higher ND layer accumulation. As a result, the electrode became too dense, reducing its specific surface area and obstructing the growth of polymeric thin films as well as the electron transfer process. Consequently, the optimum potential range and cycles for ND growth were found to be from –0.8 to +0.8 V with 10 cycles. For the concentration of ND, the peak current of L-DOPA increased up to 0.1% w/v and then decreased, and the current signal for L-Tyr seemed to be slightly raised before decreasing after 0.1% w/v. Thus, 0.1% w/v of nanodiamonds resulted in a uniformly ND-based electrode with strong adhesion and good mechanical properties that could offer large surface-active sites, ultimately resulting in the thorough covering of polymeric L-proline film.

The quality and performance of polymeric L-proline film were also controlled by the parameters of CV experiments. The influences of the electropolymerization process were carried out on the electrooxidation responses of both target analytes as presented in Figure 44. The potential windows are expected to give rise to polymer films with unique morphologies and electronic properties. In general, the development of polymer produced by amino acid building blocks is required to extend the broad potential ranges to as much positive potential as possible. The final potential was therefore set at +2.0 V and then adjusted the initial potential to more positive directions (–0.8, –0.6, –0.2, and 0.0 V, respectively). It was observed that the potential windows between –0.6 and +0.2 V provided better electrochemical responses toward L-DOPA and L-Tyr oxidation. However, the final potential was shifted to a more negative direction for decreasing the manufacturing time of a polymeric film. Unfortunately, when the applied potentials were scanned from –0.6 to +1.5 V, the current responses for L-DOPA and L-Tyr dramatically decreased. This phenomenon may attribute to the

formation and adsorption of inactive polymeric L-proline film on the ND-based electrode, resulting in poor electrochemical responses. The polymerized of L-proline was carried out in the potential ranges between +0.98 and +1.65 V as shown in Figure 19B. Thus, the potential window ranges from –0.6 to +0.2 V were suitable for the activated polymeric L-proline growth. The concentration of monomer and the number of cycles is crucial for the formation and thickness of the film. As a result, 1 mM of L-proline with 15 cycling provided high electrochemical responses of both target analytes. Interestingly, the formation of the ND-based electrode increased the specific surface area of active materials, which was beneficial for effectively reducing the concentration of monomers. Therefore, 1 mM of L-proline and 15 cycles were selected as the optimized conditions for electropolymerization for further experiments.

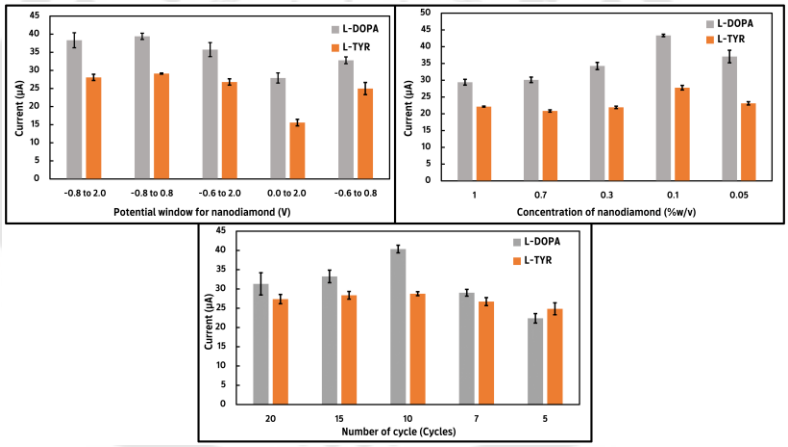

Figure 43 The influence of the electrodeposition process of ND

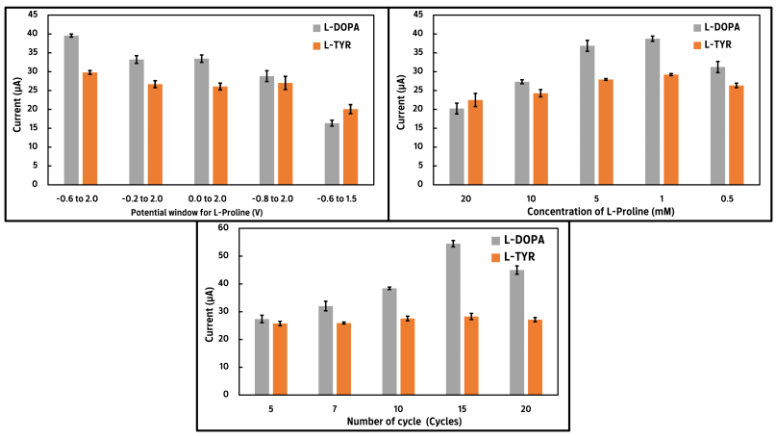

Figure 44 The influence of electropolymerization process of L-proline

4.2.6 Analytical performance

The simultaneous determination of L-DOPA and L-Tyr was carried out by containing the different concentrations of a mixture of target analytes in 0.1 M PBS pH 7.4. As shown in Figure 45A, two well-separated and distinct oxidation peaks of L-DOPA and L-Tyr were observed, and the peak currents for these analytes increased linearly with concentrations (Figure 45B) in the ranges from 0.075 μM to 50 μM for L-DOPA and 2.5–120 μM for L-Tyr. The detection limits (LODs) calculated using 3SD/slope are 0.021 μM and 0.74 μM, for L-DOPA and L-Tyr, respectively. To investigate the impact of the electrochemical response of these analytes on the individual system, the DPV analysis was performed using different concentrations for one analyte while maintaining the other at a fixed concentration. The obtained sensitivities in the simultaneous and individual systems were found to be statistically equivalent in terms of the slopes of linear ranges and detection limits (Figure 46). These demonstrate that the simultaneous measurement of these analytes was possible without interfering with one another.

In comparison to previous electrochemical sensors for the simultaneous determination of L-DOPA and L-Tyr (Table 6). It has been found that the performance of the proposed sensor is comparable to, and occasionally even worse or better than, that of the other sensing platforms. However, most previous reports used traditional-based electrodes, such as glassy carbon electrodes and carbon paste electrodes, which led to complicated pre-treatment and multi-modification steps. It is unsuitable for onsite analysis. Thus, the newly created sensor provided suitable linear ranges with acceptable LODs, material compatibility, an affordable price, and a portable platform, which are suitable for an alternative to simultaneously determine both analytes in a practical application. These findings could be beneficial for increasing scientific knowledge of sensor technology applications.

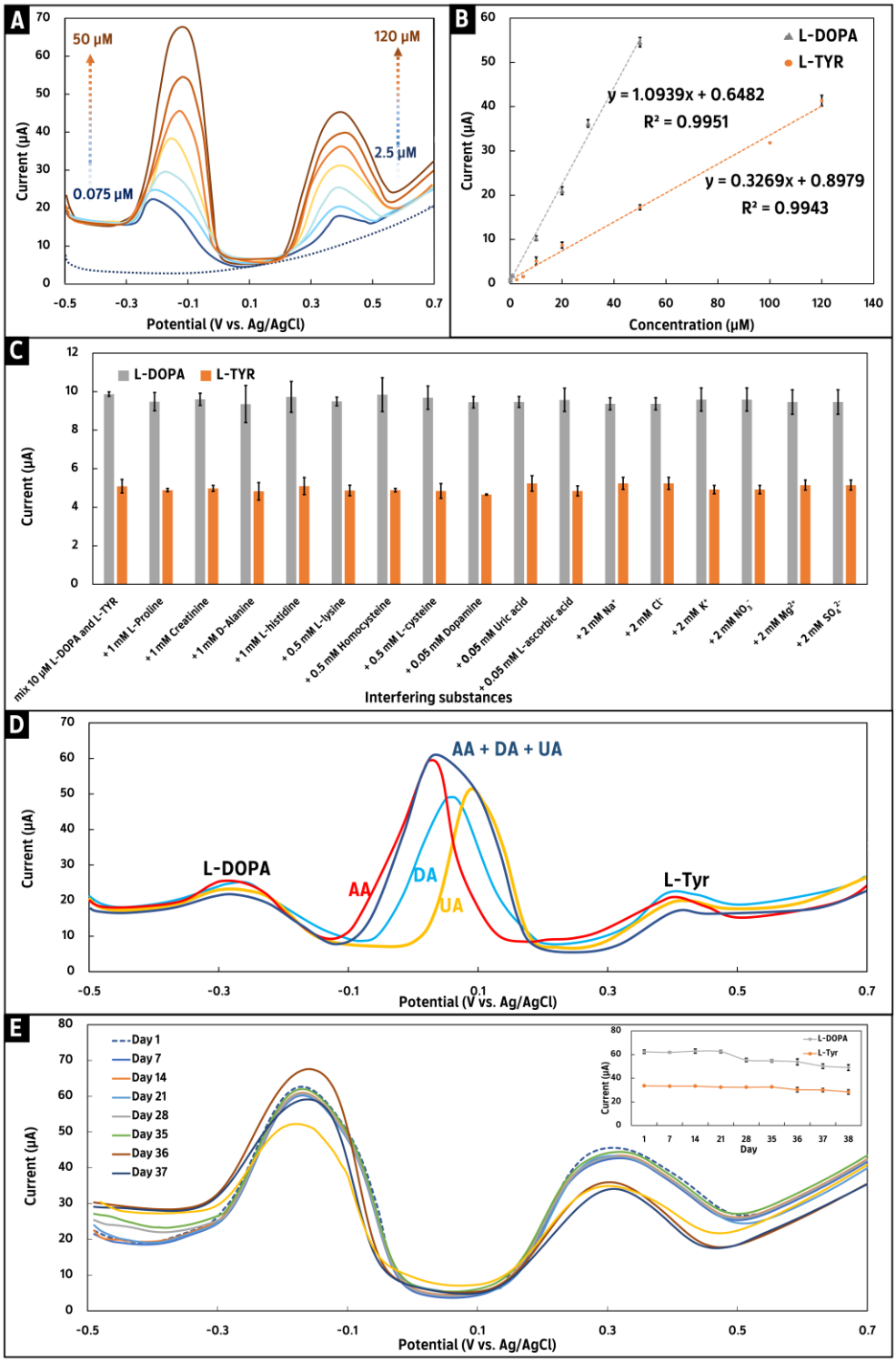

Figure 45 (A) DPV signals for different concentrations of a mixture of L-DOPA and L-Tyr at poly(L-Pro)/ND/SPGE, (B) calibration plot between anodic peak current and concentration of both target analytes, (C) the effect of interfering substances on the

anodic peak current of a mixture of 10 μM L-DOPA and 10 μM L-Tyr at poly(L-Pro)/ND/SPGE (n=3), (D) DPV curve of L-DOPA (10 μM) and L-Tyr (10 μM) in single and mixed ascorbic acid, dopamine, and uric acid (0.05 mM), and (E) the study of the stability of poly(L-Pro)/ND/SPGE

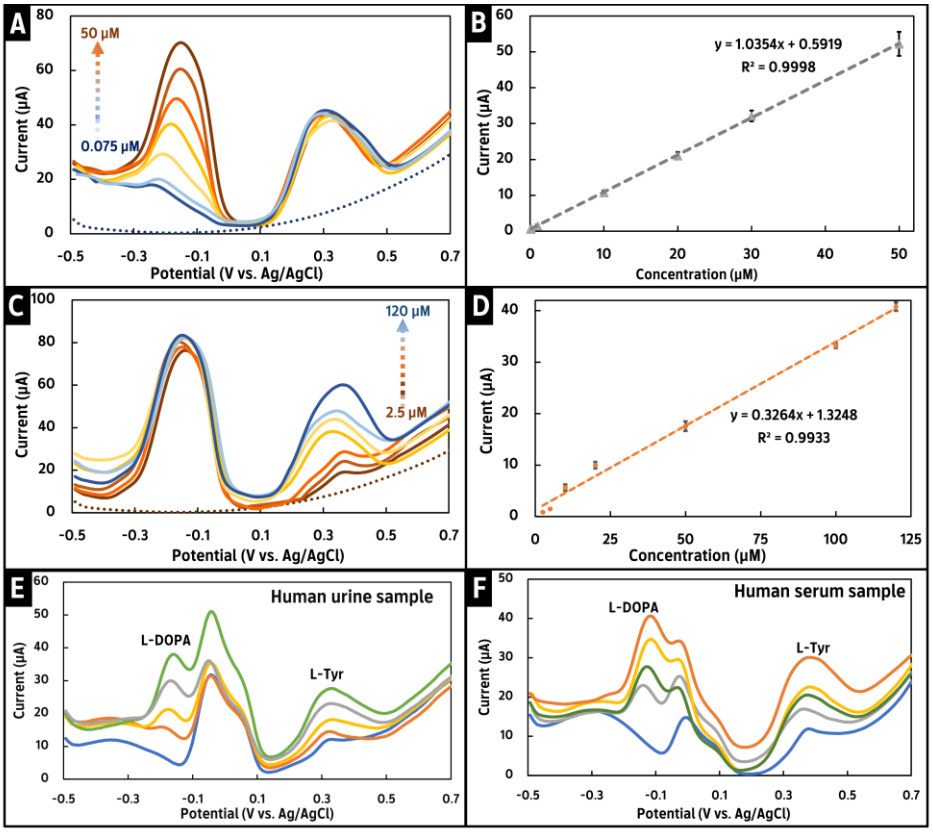

Figure 46 DPV signals for (A) varying concentrations of L-DOPA in the presence of 100 μM L-Tyr and (C) varying concentrations of L-Tyr in the presence of 100 μM L-DOPA at poly(L-Pro)/ND/SPGE, and calibration plot between anodic peak current and concentration of L-DOPA (B) and L-Tyr (D), and DPVs obtained for (E) human urine sample and (F) human serum sample, with increasing concentrations of L-DOPA (0, 2.5, 5, 10, and 20 μM) and L-Tyr (0, 5, 10, 20, and 40 μM)

Table 6 Analytical performance comparison of poly(L-Pro)/ND/SPGE and other electrochemical sensors for simultaneous determination of L-DOPA and L-Tyr

Electrode configuration	Technique	Real samples	Linear range (μM)		LOD (M)		References
			L-DOPA	L-Tyr	L-DOPA	L-Tyr	
p-AMTa/GCE	Amp	Human blood plasma	0.01–100	0.05–100	5.8×10^{-11}	1.9×10^{-11}	(Revin & John, 2013)
GR/ZnO/GSPE	SWV	Human blood serum and urine	1.0–1000	1.0–800	4.5×10^{-7}	3.4×10^{-7}	(Beitollahi & Garkani Nejad, 2016)
GR-EFTA/CPE	SWV	Human blood serum and urine	0.2–400	5.0–180	7.0×10^{-8}	2.0×10^{-6}	(Movlaee et al., 2017)
Cysteic acid/GCE	DPV	Human blood serum	0.35–4.0	1.7–50	1.1×10^{-7}	5.5×10^{-7}	(Hassanvand & Jalali, 2019)
CE/PHQ/CNT/GCE	DPV	Serum	0.005–20	0.03–170	2.2×10^{-10}	1.3×10^{-9}	(Atta et al., 2020)
pPTSA/GCE	SWV	Artificial blood serum and urine	1.0–90	1.0–70	1.2×10^{-7}	2.1×10^{-7}	(Sam et al., 2022)

Table 6 (Continued)

Electrode configuration	Technique	Real samples	Linear range (μM)		LOD (M)		References
			L-DOPA	L-Tyr	L-DOPA	L-Tyr	
poly(L-Pro)/ ND/SPGE	DPV	Human blood serum and urine	0.075–50	2.5–120	2.1×10^{-8}	7.4×10^{-7}	This work

p-AMTa = Poly(3-amino-5-mercapto-1,2,4-triazole); GCE = glassy carbon electrode; GR = graphene oxide; ZnO = zinc oxide; GSPE = graphite screen-printed electrode; GR = graphene; EFTA = ethyl 2-(4-ferrocenyl-[1,2,3]triazol-1-yl) acetate; CPE = carbon paste electrode; CE = benzo-12-crown-4, PHQ: Poly(hydroquinone); CNT = carbon nanotubes; pPTSA = poly(para-toluene sulphonic acid); Poly(L-Pro) = poly(L-proline); ND = nanodiamond; SPGE = screen-printed graphene electrode

4.2.7 Selectivity, stability, and reproducibility

To evaluate the selective applicability of the developed sensor, the influence of various substances potentially interfering was studied. The interfering substances were chosen from the group of substances commonly found in biological fluids. The tolerance limit was defined as the maximum concentration of the interfering substance that caused an error of < ±5%. The obtained results from Figure 45C show that there has no significant influence on the signal of L-DOPA and L-Tyr. Despite the fact that electrooxidation of ascorbic acid (AA), dopamine (DA), and uric acid (UA) occurs at a near-zero potential, this could potentially obstruct this detection. Therefore, the determination of 10 μM of L-DOPA and L-Tyr in single and mixed 0.05 mM of AA, DA, and UA were examined using poly(L-Pro)/ND/SPGE. As shown in Figure 45D, there is no interference observed even though the ratio of the concentration target analytes to those mentioned interfering species is up to 1:5. Therefore, poly(L-Pro)/ND/SPGE has good selectivity for the simultaneous determination of L-DOPA and L-Tyr in real samples.

For the stability investigation, the signals of L-DOPA and L-Tyr on the developed sensor were measured every 7 days for a sustained 5-week period. The developed sensor was kept in a plastic zip lock bag at room temperature throughout this evaluation. As seen in Figure 45E, the detection signals of L-DOPA and L-Tyr at day 35 remained at 87.8% and 97.2%, suggesting that the sensor's lifespan is about one month. Furthermore, the relative standard deviations for L-DOPA and L-Tyr were calculated to be 1.02% and 1.25% at seven independent electrodes (n =7), which suggested that the proposed sensing platform has good reproducibility. Therefore, poly(L-Pro)/ND/SPGE provides excellent selectivity, stability, and reproducibility that can be applied for practical use.

4.2.8 Real sample analysis

To verify the feasibility of the developed sensor and method for simultaneous determination of L-DOPA and L-Tyr, human blood serum and urine samples were tested using the standard addition method (Figure 46E and F). The values calculated based on the average of three replicates are presented in Table 7. It shows that the percentage recovery and RSD for L-DOPA ranged from 81.73% to 110.62% and 0.69% to 9.90%, respectively. In addition, the recovery of the spiked samples with L-Tyr ranged from 82.17% to 110.01%, with an RSD range of 0.40%–9.55%. These results were within recommended accuracy and precision as AOAC guidelines (AOAC, 1990). Therefore, poly(L-Pro)/ND/SPGE can be a promising analytical platform for the prognosis and metastatic monitoring of melanoma as well as the other abnormalities related to these biomarkers.

Table 7 Evaluation of the accuracy and precision of the proposed sensor for the simultaneous determination of L-DOPA and L-Tyr in real samples

Real sample	L-DOPA				L-Tyr			
	Spiked (μM)	Found (μM)	Recovery (%)	RSD (%)	Spiked (μM)	Found (μM)	Recovery (%)	RSD (%)
Serum 1	non-spike	n.d.	-	-	non-spike	1.62 ± 0.12	-	7.28
	2.5	2.47 ± 0.15	98.94	6.07	5	6.25 ± 0.37	92.45	5.96
	5	4.59 ± 0.31	91.84	6.73	10	10.71 ± 0.74	90.90	6.91
	10	10.01 ± 0.27	100.14	2.68	20	20.00 ± 1.91	91.87	9.53
	20	20.10 ± 1.30	100.50	6.44	40	39.67 ± 1.24	95.12	3.14
Serum 2	non-spike	n.d.	-	-	non-spike	1.03 ± 0.08	-	7.48
	2.5	2.40 ± 0.11	95.97	4.68	5	6.53 ± 0.08	110.01	1.15
	5	5.04 ± 0.11	100.78	2.21	10	10.75 ± 0.78	97.21	7.30
	10	10.57 ± 1.05	105.70	9.90	20	18.26 ± 1.03	86.18	5.62
	20	19.72 ± 0.69	98.59	3.50	40	40.49 ± 1.11	98.67	2.73
Serum 3	non-spike	n.d.	-	-	non-spike	1.84 ± 0.18	-	9.55
	2.5	2.29 ± 0.20	91.51	8.56	5	6.46 ± 0.38	92.38	5.86
	5	5.08 ± 0.29	101.59	5.80	10	10.06 ± 0.46	82.17	4.55
	10	10.43 ± 0.43	104.26	4.15	20	21.04 ± 0.08	96.00	0.40
	20	19.79 ± 0.18	98.96	0.93	40	39.28 ± 0.49	93.60	1.24
Serum 4	non-spike	n.d.	-	-	non-spike	1.15 ± 0.02	-	1.63
	2.5	2.20 ± 0.04	87.99	1.82	5	5.65 ± 0.37	82.76	6.55
	5	4.81 ± 0.03	96.23	0.69	10	11.01 ± 0.13	94.97	1.17
	10	11.06 ± 0.14	110.62	1.24	20	20.37 ± 1.05	94.28	5.17
	20	19.55 ± 0.61	97.76	3.10	40	39.48 ± 0.97	94.91	2.45
Urine 1	non-spike	0.85 ± 0.03	-	3.32	non-spike	0.33 ± 0.03	-	7.96
	2.5	3.42 ± 0.12	102.81	3.36	5	5.33 ± 0.48	100.19	8.94
	5	5.27 ± 0.29	88.30	5.58	10	11.26 ± 0.58	109.34	5.11
	10	9.69 ± 0.10	88.38	1.00	20	18.17 ± 1.31	89.24	7.23
	20	19.97 ± 0.30	95.61	1.49	40	40.55 ± 1.73	100.57	4.26

Table 7 (Continued)

Real sample	L-DOPA				L-Tyr			
	Spiked (μM)	Found (μM)	Recovery (%)	RSD (%)	Spiked (μM)	Found (μM)	Recovery (%)	RSD (%)
Urine 2	non-spike	0.88 ± 0.07	-	7.86	non-spike	0.22 ± 0.01	-	6.75
	2.5	3.40 ± 0.28	100.84	8.13	5	5.40 ± 0.16	103.51	2.98
	5	5.21 ± 0.27	86.52	5.14	10	10.97 ± 0.16	107.52	1.46
	10	9.87 ± 0.78	89.92	7.94	20	18.29 ± 0.25	90.36	1.36
	20	19.90 ± 1.00	95.09	5.05	40	40.56 ± 2.03	100.86	5.00
Urine 3	non-spike	0.85 ± 0.04	-	4.72	non-spike	0.23 ± 0.02	-	7.54
	2.5	3.29 ± 0.17	97.75	5.22	5	4.82 ± 0.39	91.85	8.03
	5	4.94 ± 0.31	81.73	6.37	10	9.74 ± 0.18	95.09	1.80
	10	10.40 ± 0.60	95.54	5.74	20	21.16 ± 1.95	104.66	9.21
	20	19.71 ± 0.60	94.31	3.03	40	39.50 ± 2.69	98.19	6.82

4.3 The development of an amperometric sensor based on hemin-entrapped polyethyleneimine assembled short-thin multi-walled carbon nanotubes on screen-printed graphene electrode for measuring H_2O_2 levels

4.3.1 Electrochemical reduction of H_2O_2 by hemin-PEI/ST-MWCNTs/SPGE

CV measurements were carried out to verify the performance of hemin stabilization and activation by PEI modified ST-MWCNTs/SPGE. Figure 47A shows CV voltammograms of modified SPGEs in 20 mM PBS, pH 7 under aerated and deaerated conditions. The cathodic curves in aerated condition (red line) were observed at ca. –0.3 V vs. Ag/AgCl, implying the reduction of oxygen mediated by hemin. Also, the additional cathodic peak at –0.75 V was attributed to the direct reduction of O_2 in DMSO (Tieman et al., 1990). This phenomenon confirmed that the O_2 reduction did not interfere with the electrocatalytic reduction of H_2O_2, which started at a potential of 0.2 V. The characteristic peaks of an electron transfer process of Fe^{2+}/Fe^{3+} couple at the core

of hemin were clearly seen in the potential range from –0.1 to –1.0 V. (Sosna et al., 2014). In contrast with previous studies, it was discovered that these characteristic peak potentials of hemin had shifted in a positive direction (Palanisamy et al., 2020). This shift could be caused by the matrix effects of positively charged PEI and modified multi-MWCNTs (Lopes et al., 2024).

To evaluate the electrocatalytic activity of hemin entrapped PEI towards H_2O_2 reduction, the CV curves of hemin-PEI/ST-MWCNTs/SPGE are measured with a H_2O_2 concentration range of 0 to 5 mM. As shown in Figure 47B, the reduction currents increase gradually with increasing concentrations of H_2O_2. The redox reaction of hemin is initially oxidized ferric hemin into the higher oxidation state Compound I ($Fe^{(IV)}$ =O $Porph^{+\bullet}$) by H_2O_2. This compound is subsequently reduced by two protons provided from the electrolyte and two electrons supplied from the ST-MWCNTs modified electrode, resulting in a transition to the ferric state of hemin (Chung et al., 2019; Zhang et al., 2013).

$$\text{Hemin } (Fe^{(III)}) + H_2O_2 \longrightarrow \text{Compound I } (Fe^{(IV)}\text{=O } Porph^{+\bullet}) + H_2O$$

$$\text{Compound I } (Fe^{(IV)}\text{=O } Porph^{+\bullet}) + H^+ + e^- \longrightarrow \text{Compound II } (H^{+-}Fe^{(IV)}\text{=O})$$

$$\text{Compound II } (H^{+-}Fe^{(IV)}\text{=O}) + H^+ + e^- \longrightarrow \text{Hemin } (Fe^{(III)}) + H_2O$$

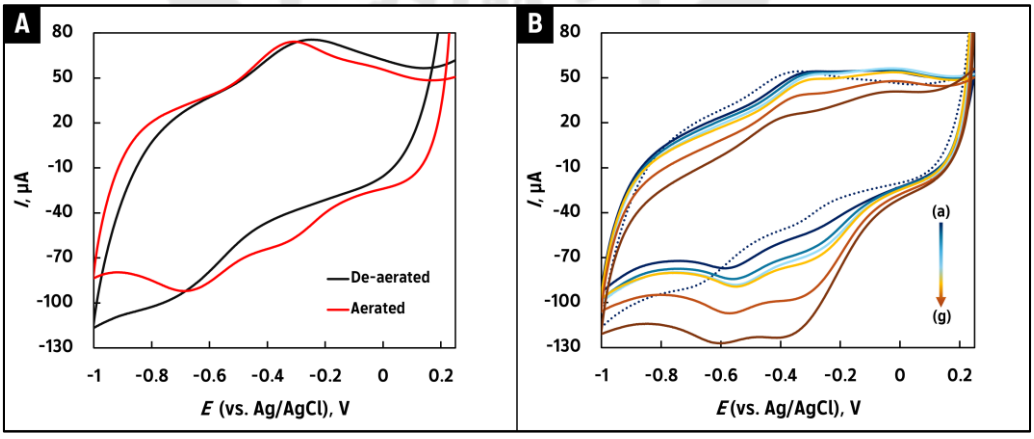

Figure 47 (A) Representative cyclic voltammograms recorded with hemin-PEI/ST-MWCNTs/SPGE in 20 mM PBS, pH 7, in the presence of 0.26 mM O_2(red lines) and in the absence of O_2, under N_2 atmosphere (black lines) and (B) hemin-PEI/ST-

MWCNTs/SPGE in aerated 20 mM PS, pH 7, containing: (a) 0, (b) 0.1, (c) 0.3, (d) 0.5, (e) 1, (f) 3, (g) 5 mM H_2O_2. Potential scan rate: 0.02 V s^{-1}

4.3.2 Amperometric sensing of H_2O_2 using hemin-PEI/ST-MWCNTs/SPGE

A chronoamperometric approach was used to determine the quantitative amount of H_2O_2. Figure 48A displays a typical chronoamperometric response at –0.2 V after adding an aliquot of H_2O_2 to the buffer solution. The reductive current reached a stable baseline within 10 s, suggesting a fast process. A well-defined chronoamperometric response change was linearly increased with two dynamic concentration ranges (Figure 48B). The linear equations are I_p (μA) = –2.2799 $C_{H_2O_2}$(μM) + 15.947 (R^2 = 0.9936) and I_p (μA) = –0.0231 $C_{H_2O_2}$(μM) + 36.642 (R^2 = 0.9913) for the concentrations ranging from 1 μM to 10 μM and 30 μM to 1 mM. The limit of detection was calculated to be 0.11 μM using the equation of 3SD/m, where SD is the standard deviation of 10 repeated measurements of a blank solution (20 mM PBS, pH 7), and m is the slope of the calibration curve. The results demonstrated that the developed H_2O_2 sensing has wide linear working ranges and a low LOD, making it sufficient for EBC analysis. The comparative performances of non-enzymatic H_2O_2 sensing platforms are listed in Table 8. The newly developed sensor exhibited better analytical performance compared to screen-printed electrode platforms, however, it occasionally performed worse than some conventional electrodes. Many previous studies nevertheless require a complex and multi-fabrication procedure and/or alterations to the experimental conditions, making them unsuitable for real-time and on-site analysis. It is worth noting that the unique features of hemin-PEI/ST-MWCNTs modified SPGE make it an attractive analytical tool with broad potential applications in H_2O_2 sensors and advanced sensor technologies.

Table 8 Comparison of performances of developed sensor for the detection of H_2O_2 with those of sensors based on different architectures.

Modified electrode	Detection technique	E_{app} (V)	Linear Range (μM)	LOD (μM)	Long term stability	References
H-GNs/ PEDOT/GCE	Amp	–0.2 [a]	0.5–70.0	0.08	21 days	(Lei et al., 2014)
PPY-He-RGO/GCE	Amp	–0.15[b]	0.5–80.0	0.13	21 days	(Huang et al., 2014)
rGO-H-Au /GCE	Amp	–0.18[b]	0.1–40.0	0.03	30 days	(Gu et al., 2016)
GrMWCNTs/ GCE	Amp	–0.4[b]	20.0–2100.0	9.4	N/A	(Woo et al., 2012)
H-GO-CNTs/GCE	Amp	–0.15[a]	0.6–7200.0	0.2	7 days	(Zhang et al., 2013)
Cu-hemin MOFs/CS-rGO/GCE	Amp	–0.175[a]	0.065–410.0	0.019	15 days	(Wang et al., 2016)
PB/SPCE	Amp	–0.05[b]	0.4–100.0	0.4	N/A	(O'Halloran et al., 2001)
PtNP/ MWCNTC/ SPGFE	Amp	–0.4[b]	5.0–2000.0	1.23	N/A	(Niu et al., 2012)
PtNp-CNF-PDDA/SPCE	Amp	0.5[b]	25.0–1500.0	11.0	N/A	(Lamas-Ardisana et al., 2014)
AgNP–PVA/SPGlE	CV	–1.0 to 0.0[b]	1.0–500.0	0.3	80 days	(Ghosale et al., 2018)

Table 8 (Continued)

Modified electrode	Detection technique	E_{app} (V)	Linear Range (μM)	LOD (μM)	Long term stability	References
PEDOT: PSS/SPE	Amp	–1.0[b]	1.0–100.0	0.97	N/A	(Campos-Arias et al., 2023)
Hemin-PEI/ST-MWCNTs/ SPGE	Amp	–0.2[b]	1.0–10.0 and 30.0–1000.0	0.11	****	**This work**

[a] V vs. SCE; [b] V vs. Ag/AgCl; Amp = amperometry; CV = cyclic voltammetry; GCE = glassy carbon electrode; H–GNs/PEDOT = ternary nanocomposite hemin–graphene sheets modified poly(3,4-ethylenedioxythiophene);PPY-He-RGO = polypyrrole-hemin-reduced graphene oxide composites; rGO-H-Au = reduced graphene oxide-Hemin-Au nanohybrids; GrMWCNTs = graphene-multi-walled carbon nanotube composites; H-GO-CNTs = hemin-graphene oxide-pristine carbon nanotubes complexes; Cu-hemin MOFs/CS-rGO = copper-hemin-metal organic frameworks - reduced graphene oxide nanocomposite; PB/SPCE = prussian blue bulk modified carbon screen-printed electrode; PtNP/ MWCNTC/ SPGFE = platinum nanoparticle-decorated multi-walled carbon nanotube clusters vertically aligned on a screen-printed gold nanofilm electrode; PtNp-CNF-PDDA/SPCEs = a dispersion of platinum nanoparticle decorated carbon nanofibers in poly(diallyldimethylammonium) chloride modified screen-printed carbon electrode; AgNP–PVA/SPGIE = silver nanoparticles modified with poly(vinyl alcohol) coated on screen-printed glass electrode; PEDOT:PSS/SPE = poly(3,4-ethylenedioxythiophene)-polystyrene sulfonate modified screen-printed electrode; hemin-PEI/ST-MWCNTs/SPGE = hemin-entrapped polyethyleneimine modified short thin multiwalled carbon nanotubes coated screen-printed graphene electrode.

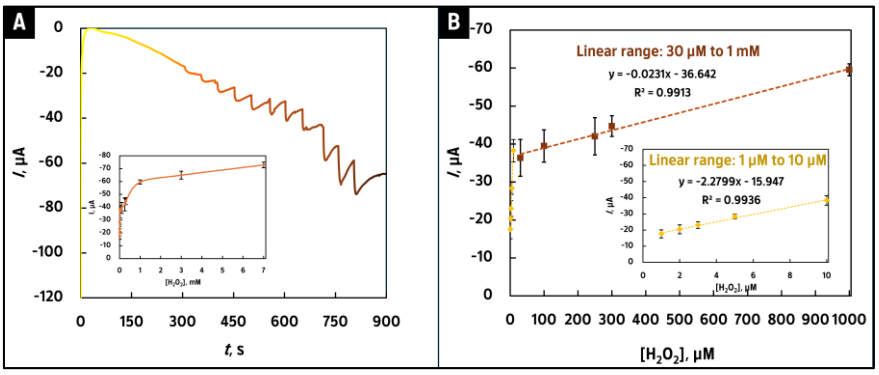

Figure 48 (A) Real-time chronoamperometric curve of hemin-PEI/ST-MWCNTs/SPGE for successive addition of H_2O_2 into PBS solution; inset shows the current response versus different concentrations of H_2O_2 ranging from 0.001 to 7 mM and (B) calibration plot between peak current and H_2O_2 concentration.

4.3.3 Selectivity

The selectivity of the proposed sensor towards H_2O_2 was investigated with the interfering substances of some commonly found in breath samples, such as ascorbic acid, uric acid, urea, glucose (Glc), glycine (Gly), NH_4^+ Ca^{2+}, SO_4^{2-}, Na^+, Cl^-, and SO_3^{2-}. The tolerance limit was taken as the maximum concentration of foreign substances that caused a relative error of approximately ±5% for the determination of the H_2O_2 containing 1 mM of those above-mentioned species. Figure 49 demonstrates that adding competitive substances does not result in noticeable changes in H_2O_2 current responses. This confirmed that this non-enzymatic sensor exhibited good selectivity and could be applied for the detection of H_2O_2 in practical use.

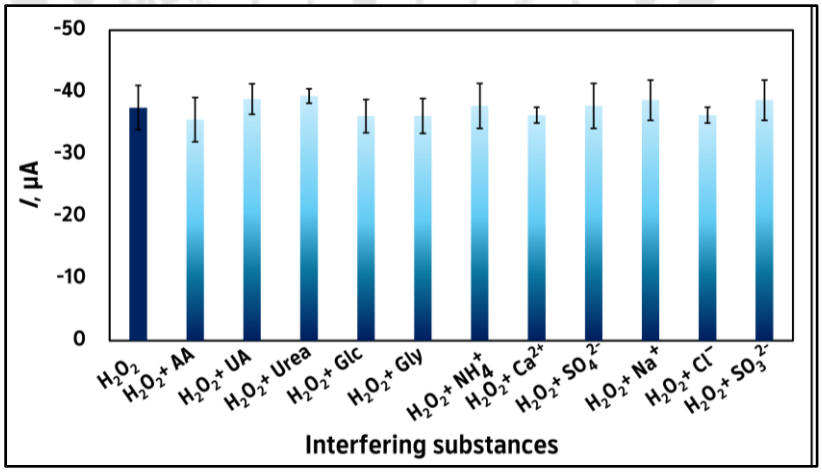

Figure 49 Selectivity of hemin-PEI/ST-MWCNTs/SPGE towards H_2O_2 (10 µM) over interfering substances (the concentrations were all 1 mM)

4.3.4 Real sample analysis

To evaluate practical feasibility of the proposed sensor, exhaled breath condensate samples were examined using the standard addition method. All samples were diluted twice in supporting electrolyte before analysis. The values calculated from the average of three repeated measurements are displayed in Table 9. The recovery and relative standard deviation (RSD) values were within the AOAC acceptable ranges of 80.96%–106.73% and 4.24%–10.03%, respectively (AOAC, 1990). Moreover, the levels of H_2O_2 in EBC samples from healthy volunteers were found to be 0.18, 0.33, 0.87, 0.39, and 0.13 μM. This indicated that hemin-PEI/ST-MWCNTs/SPGE can put forward into the real-time monitoring of H_2O_2 in practical applications.

Table 9 Determination of H_2O_2 in real exhaled breath samples

Real samples	Added (μM)	Found (μM)	Recovery (%)	RSD (%)
EBC sample 1	4.0	4.19 ± 0.83	100.22	8.26
	8.5	8.94 ± 1.70	103.59	9.52
EBC sample 2	4.0	4.60 ± 0.63	106.73	8.55
	8.5	8.55 ± 1.07	96.73	9.40
EBC sample 3	4.0	4.90 ± 0.50	100.70	4.85
	8.5	7.86 ± 0.63	82.23	4.24
EBC sample 4	4.0	4.35 ± 0.41	98.97	7.31
	8.5	7.28 ± 0.59	80.96	7.34
EBC sample 5	4.0	4.03 ± 0.28	97.48	5.31
	8.5	7.17 ± 0.92	82.75	10.03

CHAPTER 5
CONCLUSIONS AND FUTURE WORKS

5.1 Conclusions

This dissertation involved the development of electrochemical sensing systems for monitoring significant biological indicators, including tyramine, L-DOPA, L-Tyr, and H_2O_2. These innovations focus mainly on their use in practical application and field analysis. Thanks to their lightweight and compact design, sensing platforms have moved from complex materials to simpler and more affordable electrode platforms. Additionally, they can be used for the analysis of a single drop sample, enabling rapid detection at the patient's location or another related area for point-of-care testing and on-site analysis. The remarkable approaches of electrochemical sensing platforms for the detection of significant analytes were summarized as follows:

5.1.1 The development of a novel tyramine sensor using poly (histidine) assembled on a screen-printed graphene electrode

A novel poly(His)/SPGE was successfully prepared by a simple electropolymerization process. According to the literature reviews, no published works have addressed the use of poly(His) modified SPGE in the development of tyramine sensors. Thus, the measurement of this vasoactive amine using Poly(His)/SPGE was performed for the first time. The utilization of a poly(His)- modified electrode resulted in a significant enhancement of the electrocatalytic activity towards the electrooxidation of tyramine, leading to an approximately three-fold increase in the peak currents. The improved electron-transfer kinetics at poly(His)/SPGE can be attributed to its negatively charged behavior on the electrode surface, which effectively induces the positively charged form of tyramine at the optimal pH of 7.4 through electrostatic forces. The as-proposed electrochemical sensing platform provides two wide working ranges along with a low limit of detection (0.065 μM). Furthermore, this novel sensor was effectively utilized to quantify the amounts of Tyr in various biological fluids and cheese samples, yielding satisfactory results. The benefits of this approach

include its cost-effectiveness, easy fabrication, and user-friendliness, rendering it a highly promising tool for food quality and safety control and healthcare applications.

5.1.2 The development of a new electrochemical platform using poly(L-proline)-linked nanodiamonds on a screen-printed graphene electrode for simultaneous detection of L-DOPA and L-Tyr

The first use of poy(L-Pro) coated nanodiamond on printed graphene electrodes as a sensitive sensing platform for the simultaneous detection of L-DOPA and L-Tyr was performed. Here, ND is the ability to remove coexisting interfering materials from ink composition, which leads to increased sensitivity and expanded applications. In addition, the coupling between the good conductivity of poly(L-Pro) and the high surface area of ND offers fast electron transfer and shows excellent electrocatalytic properties for L-DOPA and L-Tyr oxidation. In an effort to prove any presence of the proposed materials on the electrode surface, a scanning electron microscope, an energy-dispersive X-ray spectrometer, and Raman spectroscopy were used to explain the surface morphologies and chemical compositions. Furthermore, a computational chemistry calculation was carried out to enhance comprehension of the interaction between poly(L-Pro)/ND/SPGE and the target analytes. The sensor offered broad linear ranges (0.075–50 μM for L-DOPA and 2.5–120 μM for L-Tyr), remarkable sensitivity, robust anti-interference capability, and notable stability, which can be directly compared to the other platforms. Ultimately, the developed sensor was used to simultaneously determine these specific substances in urine and serum samples, yielding acceptable results. These findings possess the potential to offer significant information to scientists pursuing materials with advantageous features for electrocatalysis, chemical sensor and bio sensing technology.

5.1.3 The development of an amperometric sensor based on hemin-entrapped polyethyleneimine assembled short-thin multi-walled carbon nanotubes on screen-printed graphene electrode for measuring H_2O_2 levels

Through the synergistic combination of unique features of hemin, the effective characteristics of PEI, and the enlarged active area supplied by ST-MWCNTs layers on printed graphene electrodes can open new horizons for H_2O_2 monitoring. The developed sensing platform was accomplished through step-by-step drop casting methods. By utilizing the aforementioned components, it exhibits enhanced electrocatalytic activity for the reduction of H_2O_2, with a starting potential of approximately 0.2 V. An amperometric approach was employed, resulting in a rapid response time of less than 5 s. The current response of the sensor was proportional to the H_2O_2 concentration in ranges of 1–10 μM and 30–1000 μM with a detection limit of 0.11 μM. The rapid response time, low detection limit, good selectivity, wide linear range, cost-effectiveness, and high sensitivity of this sensor make it highly desirable as a non-enzymatic H_2O_2 sensor. Moreover, this recently developed sensing platform was applied to determine the levels of H_2O_2 in samples of human exhaled breath. The obtained recoveries and RSD were in accordance with the guidelines set by AOAC. Regardless, the proof-of-concept device paves the way to a point-of-care hydrogen peroxide sensing platform, enabling its potential in clinical applications.

5.2 Future works

All the proposed electrochemical sensing platforms showed effective performance, facile fabrication, user-friendliness, and remarkable stable features. Nevertheless, there will be a development of extremely sensitive sensing approaches capable of detecting significant markers at the sub-nanomolar level. This advancement aims to overcome the challenge of accurately and precisely monitoring clinical conditions at an early stage. Thus, considering the perspectives gained from this dissertation, subsequent attempts will emphasize the use of proper and ecologically friendly materials while preserving the ideas of simple fabrication and superior catalytic efficiency. To achieve and comply with rapid test turnarounds and field testing, a new

generation of miniaturized sensing platforms should be integrated with Internet of Things (IoT) technologies, such as wireless sensor nodes and smart applications, allowing for a wide range of applications. These frameworks offer an innovative opportunity to unlock practical use in the future.

REFERENCES

Anand, S. K., Mathew, M. R., Radecki, J., Radecka, H., & Kumar, K. G. (2020). Individual and simultaneous voltammetric sensing of norepinephrine and tyramine based on poly(L-arginine)/reduced graphene oxide composite film modified glassy carbon electrode. *Journal of Electroanalytical Chemistry*, *878*, 114531. https://doi.org/10.1016/j.jelechem.2020.114531

Andrieux, C. P., & Savéant, J. M. (1980). Electron transfer through redox polymer films. *Journal of Electroanalytical Chemistry and Interfacial Electrochemistry*, *111*(2), 377-381. https://doi.org/10.1016/S0022-0728(80)80058-1

AOAC. (1990). Official methods of analysis. In: Aoac Washington, DC.

Apetrei, I. M., & Apetrei, C. (2013). Amperometric biosensor based on polypyrrole and tyrosinase for the detection of tyramine in food samples. *Sensors and Actuators B: Chemical*, *178*, 40-46.

Atta, N. F., Galal, A., & El-Gohary, A. R. (2020). Crown ether modified poly (hydroquinone)/carbon nanotubes based electrochemical sensor for simultaneous determination of levodopa, uric acid, tyrosine and ascorbic acid in biological fluids. *Journal of Electroanalytical Chemistry*, *863*, 114032.

Ayerdurai, V., Cieplak, M., Noworyta, K. R., Gajda, M., Ziminska, A., Sosnowska, M., . . . Kutner, W. (2021). Electrochemical sensor for selective tyramine determination, amplified by a molecularly imprinted polymer film. *Bioelectrochemistry*, *138*, 107695. https://doi.org/10.1016/j.bioelechem.2020.107695

Azizi, S. N., Ghasemi, S., & Amiripour, F. (2016). Nickel/P nanozeolite modified electrode: A new sensor for the detection of formaldehyde. *Sensors and Actuators B: Chemical*, *227*, 1-10. https://doi.org/10.1016/j.snb.2015.11.142

Baghayeri, M., & Namadchian, M. (2013). Fabrication of a nanostructured luteolin biosensor for simultaneous determination of levodopa in the presence of acetaminophen and tyramine: application to the analysis of some real samples. *Electrochimica Acta*, *108*, 22-31.

Bahulekar, R., Ayyangar, N. R., & Ponrathnam, S. (1991). Polyethyleneimine in immobilization of biocatalysts. *Enzyme and microbial technology*, *13*(11), 858-868. https://doi.org/10.1016/0141-0229(91)90101-F

Banga, I., Paul, A., Muthukumar, S., & Prasad, S. (2022). HELP (Hydrogen peroxide electrochemical profiling): A novel biosensor for measuring hydrogen peroxide levels expressed in breath for monitoring airway inflammation using electrochemical methods. *Biosensors and Bioelectronics: X*, *10*, 100139. https://doi.org/10.1016/j.biosx.2022.100139

Bard, A. J., & Faulkner, L. R. (2001). *Electrochemical Methods: Fundamentals and Applications* (2nd ed.). Wiley.

Bauri, K., Nandi, M., & De, P. (2018). Amino acid-derived stimuli-responsive polymers and their applications. *Polymer Chemistry*, *9*(11), 1257-1287. https://doi.org/10.1039/C7PY02014G

Beitollahi, H., & Garkani Nejad, F. (2016). Graphene oxide/ZnO nano composite for sensitive and selective electrochemical sensing of levodopa and tyrosine using modified graphite screen printed electrode. *Electroanalysis*, *28*(9), 2237-2244.

Benkerroum, N. (2016). Biogenic amines in dairy products: origin, incidence, and control means. *Comprehensive Reviews in Food Science and Food Safety*, *15*(4), 801-826.

Bianchetti, M. G., Minder, I., Beretta-Piccoli, C., Meier, A., & Weidmann, P. (1982). Effects of tyramine on blood pressure and plasma catecholamines in normal and hypertensive subjects. *Klin Wochenschr*, *60*(9), 465-470. https://doi.org/10.1007/bf01720361

Biji, K., Ravishankar, C., Venkateswarlu, R., Mohan, C., & Gopal, T. S. (2016). Biogenic amines in seafood: a review. *Journal of food science and technology*, *53*(5), 2210-2218.

Bonanni, A., Loo, A. H., & Pumera, M. (2012). Graphene for impedimetric biosensing. *TrAC Trends in Analytical Chemistry*, *37*, 12-21. https://doi.org/10.1016/j.trac.2012.02.011

Boni, A. C., Wong, A., Dutra, R. A. F., & Sotomayor, M. D. P. T. (2011). Cobalt phthalocyanine as a biomimetic catalyst in the amperometric quantification of dipyrone using FIA. *Talanta*, *85*(4), 2067-2073. https://doi.org/10.1016/j.talanta.2011.07.038

Calvo-Pérez, A., Domínguez-Renedo, O., Alonso-Lomillo, M. A., & Arcos-Martínez, M. J. (2013). Disposable amperometric biosensor for the determination of tyramine using plasma amino oxidase. *Microchimica Acta*, *180*(3), 253-259.

Campos-Arias, L., del Olmo, R., Peřinka, N., Casado, N., Vilas-Vilela, J. L., Mecerreyes, D., . . . Lanceros-Méndez, S. (2023). PEDOT:PSS-based screen-printable inks for H_2O_2 electrochemical detection. *Electrochimica Acta*, *439*, 141615. https://doi.org/10.1016/j.electacta.2022.141615

Cao, Y., Shi, H., Zheng, Y., Tan, Z., Xie, Z., Zhang, C., & Chen, Z. (2023). Polyaniline/Prussian blue nanolayer enhanced electrochemical sensing of H_2O_2 in EBC using an integrated condensation facemask. *Sensors and Actuators B: Chemical*, *393*, 134189. https://doi.org/10.1016/j.snb.2023.134189

Capuron, L., Schroecksnadel, S., Féart, C., Aubert, A., Higueret, D., Barberger-Gateau, P., . . . Fuchs, D. (2011). Chronic low-grade inflammation in elderly persons is associated with altered tryptophan and tyrosine metabolism: role in neuropsychiatric symptoms. *Biological psychiatry*, *70*(2), 175-182.

Carelli, D., Centonze, D., Palermo, C., Quinto, M., & Rotunno, T. (2007). An interference free amperometric biosensor for the detection of biogenic amines in food products. *Biosensors and Bioelectronics*, *23*(5), 640-647.

Charoenkitamorn, K., Chaiyo, S., Chailapakul, O., & Siangproh, W. (2018). Low-cost and disposable sensors for the simultaneous determination of coenzyme Q10 and α-lipoic acid using manganese (IV) oxide-modified screen-printed graphene electrodes. *Analytica Chimica Acta*, *1004*, 22-31. https://doi.org/10.1016/j.aca.2017.12.026

Chaudhuri, K. R., Healy, D. G., & Schapira, A. H. (2006). Non-motor symptoms of Parkinson's disease: diagnosis and management. *The Lancet Neurology*, *5*(3),

235-245.

Chen, S., Yuan, R., Chai, Y., Zhang, L., Wang, N., & Li, X. (2007). Amperometric third-generation hydrogen peroxide biosensor based on the immobilization of hemoglobin on multiwall carbon nanotubes and gold colloidal nanoparticles. *Biosensors and Bioelectronics*, *22*(7), 1268-1274. https://doi.org/10.1016/j.bios.2006.05.022

Chen, Y., Liu, X.-M., Wu, X., Liu, X.-C., Dong, W.-H., Han, B.-K., . . . Chen, Q. (2017). An array of poly-l-histidine functionalized multi-walled carbon nanotubes on 4-aminothiophenol self-assembled monolayer and the application for sensitively glucose sensing. *Electrochimica Acta*, *258*, 988-997. https://doi.org/10.1016/j.electacta.2017.11.150

Chen, Z., Lv, Z., Sun, Y., Chi, Z., & Qing, G. (2020). Recent advancements in polyethyleneimine-based materials and their biomedical, biotechnology, and biomaterial applications. *Journal of Materials Chemistry B*, *8*(15), 2951-2973. https://doi.org/10.1039/C9TB02271F

Chitravathi, S., Kumara Swamy, B. E., Mamatha, G. P., & Chandrashekar, B. N. (2012). Electrocatalytic oxidation of tyrosine at poly(threonine)-film modified carbon paste electrode and its voltammetric determination in real samples. *Journal of Molecular Liquids*, *172*, 130-135. https://doi.org/10.1016/j.molliq.2012.03.022

Chung, Y., Ji, J., & Kwon, Y. (2019). Performance evaluation of enzymatic biofuel cells using a new cathodic catalyst containing hemin and poly acrylic acid promoting the oxygen reduction reaction. *Journal of Materials Chemistry C*, *7*(37), 11597-11605.

da Silva, A. G., Franco, D. L., & Santos, L. D. (2021). A simple, fast, and direct electrochemical determination of tyramine in Brazilian wines using low-cost electrodes. *Food Control*, *130*, 108369.

da Silva, W., Ghica, M. E., Ajayi, R. F., Iwuoha, E. I., & Brett, C. M. (2019a). Impedimetric sensor for tyramine based on gold nanoparticle doped-poly (8-anilino-1-naphthalene sulphonic acid) modified gold electrodes. *Talanta*, *195*, 604-612.

da Silva, W., Ghica, M. E., Ajayi, R. F., Iwuoha, E. I., & Brett, C. M. (2019b). Tyrosinase based amperometric biosensor for determination of tyramine in fermented food and beverages with gold nanoparticle doped poly (8-anilino-1-naphthalene sulphonic acid) modified electrode. *Food chemistry*, *282*, 18-26.

Dalkıran, B., Erden, P. E., Kaçar, C., & Kılıç, E. (2019). Disposable Amperometric Biosensor Based on Poly-L-lysine and Fe_3O_4 NPs-chitosan Composite for the Detection of Tyramine in Cheese. *Electroanalysis*, *31*(7), 1324-1333.

Dalmasso, P. R., Pedano, M. L., & Rivas, G. A. (2015). Electrochemical determination of Cu (II) using a glassy carbon electrode modified with multiwall carbon nanotubes dispersed in polyhistidine. *Electroanalysis*, *27*(9), 2164-2170.

Datta, D., Das, K. P., Deepak, K., & Das, B. (2022). Candidates of functionalized nanomaterial-based membranes. In *Membranes with Functionalized Nanomaterials* (81-127). Elsevier.

Dong, X., Wang, P., Fang, W., Su, C.-Y., Chen, Y.-H., Li, L.-J., . . . Chen, P. (2011). Growth of large-sized graphene thin-films by liquid precursor-based chemical vapor deposition under atmospheric pressure. *Carbon*, *49*(11), 3672-3678. https://doi.org/10.1016/j.carbon.2011.04.069

Emelyanov, A., Fedoseev, G., Abulimity, A., Rudinski, K., Fedoulov, A., Karabanov, A., & Barnes, P. J. (2001). Elevated Concentrations of Exhaled Hydrogen Peroxide in Asthmatic Patients. *Chest*, *120*(4), 1136-1139. https://doi.org/10.1378/chest.120.4.1136

Erdogan, Z. O., Akin, I., & Kucukkolbasi, S. (2018). A new non-enzymatic sensor based on TiO_2-Ag/polypyrrole for electrochemical detection of tyramine. *Synthetic Metals*, *246*, 96-100.

Evans, S. A. G., Elliott, J. M., Andrews, L. M., Bartlett, P. N., Doyle, P. J., & Denuault, G. (2002). Detection of Hydrogen Peroxide at Mesoporous Platinum Microelectrodes. *Analytical chemistry*, *74*(6), 1322-1326. https://doi.org/10.1021/ac011052p

Gao, W., Tjiu, W. W., Wei, J., & Liu, T. (2014). Highly sensitive nonenzymatic glucose and H_2O_2 sensor based on $Ni(OH)_2$/electroreduced graphene oxide−Multiwalled

carbon nanotube film modified glass carbon electrode. *Talanta*, *120*, 484-490. https://doi.org/10.1016/j.talanta.2013.12.012

Garnier, J.-P., Letellier, S., Cassinat, B., Lebbé, C., Kerob, D., Baccard, M., . . . Bousquet, B. (2007). Clinical value of combined determination of plasma L-DOPA/tyrosine ratio, S100B, MIA and LDH in melanoma. *European Journal of Cancer*, *43*(4), 816-821.

Ghosale, A., Shrivas, K., Deb, M. K., Ganesan, V., Karbhal, I., Bajpai, P. K., & Shankar, R. (2018). A low-cost screen printed glass electrode with silver nano-ink for electrochemical detection of H_2O_2. *Analytical methods*, *10*(26), 3248-3255. https://doi.org/10.1039/C8AY00652K

Gohil, S. V., Suhail, S., Rose, J., Vella, T., & Nair, L. S. (2017). Chapter 8 - Polymers and Composites for Orthopedic Applications. In S. Bose & A. Bandyopadhyay, *Materials for Bone Disorders* (349-403). Academic Press. https://doi.org/10.1016/B978-0-12-802792-9.00008-2

Gonçalves da Silva, A., Franco, D. L., & Santos, L. D. (2021). A simple, fast, and direct electrochemical determination of tyramine in Brazilian wines using low-cost electrodes. *Food Control*, *130*, 108369. https://doi.org/10.1016/j.foodcont.2021.108369

Gu, C.-J., Kong, F.-Y., Chen, Z.-D., Fan, D.-H., Fang, H.-L., & Wang, W. (2016). Reduced graphene oxide-Hemin-Au nanohybrids: Facile one-pot synthesis and enhanced electrocatalytic activity towards the reduction of hydrogen peroxide. *Biosensors and Bioelectronics*, *78*, 300-307.

Guo, Y., Deng, L., Li, J., Guo, S., Wang, E., & Dong, S. (2011). Hemin−Graphene Hybrid Nanosheets with Intrinsic Peroxidase-like Activity for Label-free Colorimetric Detection of Single-Nucleotide Polymorphism. *ACS Nano*, *5*(2), 1282-1290. https://doi.org/10.1021/nn1029586

Hadjiconstantinou, M., & Neff, N. H. (2008). Enhancing aromatic L-amino acid decarboxylase activity: implications for L-DOPA treatment in Parkinson's disease. *CNS neuroscience & therapeutics*, *14*(4), 340-351.

Hajzus, J. R., Shriver-Lake, L. C., Dean, S. N., Erickson, J. S., Zabetakis, D., Golden, J., . . . Trammell, S. A. (2022). Modifications of epitaxial graphene on SiC for the electrochemical detection and identification of heavy metal salts in seawater. *Sensors*, *22*(14), 5367.

Halliwell, B., Clement, M. V., & Long, L. H. (2000). Hydrogen peroxide in the human body. *FEBS Letters*, *486*(1), 10-13. https://doi.org/10.1016/S0014-5793(00)02197-9

Hasan, M. R., Ahommed, M. S., Daizy, M., Bacchu, M. S., Ali, M. R., Al-Mamun, M. R., . . . Hossain, S. I. (2021). Recent development in electrochemical biosensors for cancer biomarkers detection. *Biosensors and Bioelectronics: X*, *8*, 100075. https://doi.org/10.1016/j.biosx.2021.100075

Hasanzadeh, M., Hassanpour, S., Nahr, A. S., Shadjou, N., Mokhtarzadeh, A., & Mahboob, S. (2018). Electropolymerization of proline supported beta cyclodextrin inside amino functionalized magnetic mesoporous silica nanomaterial: one step preparation, characterization and electrochemical application. *Anal. Bioanal. Electrochem*, *10*(1), 77-97.

Hasanzadeh, M., Nahar, A. S., Hassanpour, S., Shadjou, N., Mokhtarzadeh, A., & Mohammadi, J. (2017). Proline dehydrogenase-entrapped mesoporous magnetic silica nanomaterial for electrochemical biosensing of L-proline in biological fluids. *Enzyme and microbial technology*, *105*, 64-76.

Hassanvand, Z., & Jalali, F. (2019). Simultaneous determination of l-DOPA, l-tyrosine and uric acid by cysteic acid-modified glassy carbon electrode. *Materials Science and Engineering: C*, *98*, 496-502.

Hazards, E. P. o. B. (2011). Scientific opinion on risk based control of biogenic amine formation in fermented foods. *Efsa Journal*, *9*(10), 2393.

Heli, H., & Pishahang, J. (2014). Cobalt oxide nanoparticles anchored to multiwalled carbon nanotubes: Synthesis and application for enhanced electrocatalytic reaction and highly sensitive nonenzymatic detection of hydrogen peroxide. *Electrochimica Acta*, *123*, 518-526. https://doi.org/10.1016/j.electacta.2014.01.032

Ho, L., Faccenda, J., Innes, J., & Greening, A. (1999). Expired hydrogen peroxide in

breath condensate of cystic fibrosis patients. *European Respiratory Journal*, *13*(1), 103-106.

Holguin, F. (2013). Oxidative stress in airway diseases. *Annals of the American Thoracic Society*, *10*(Supplement), S150-S157.

Holt, K. B., Ziegler, C., Caruana, D. J., Zang, J., Millán-Barrios, E. J., Hu, J., & Foord, J. S. (2008). Redox properties of undoped 5 nm diamond nanoparticles. *Physical Chemistry Chemical Physics*, *10*(2), 303-310.

Huang, J., Xing, X., Zhang, X., He, X., Lin, Q., Lian, W., & Zhu, H. (2011). A molecularly imprinted electrochemical sensor based on multiwalled carbon nanotube-gold nanoparticle composites and chitosan for the detection of tyramine. *Food Research International*, *44*(1), 276-281.

Huang, W., Hao, Q., Lei, W., Wu, L., & Xia, X. (2014). Polypyrrole-hemin-reduce graphene oxide: rapid synthesis and enhanced electrocatalytic activity towards the reduction of hydrogen peroxide. *Materials Research Express*, *1*(4), 045601.

Hushcha, Y., Blo, I., Oton-Gonzalez, L., Mauro, G. D., Martini, F., Tognon, M., & Mattei, M. D. (2021). microRNAs in the Regulation of Melanogenesis. *International journal of molecular sciences*, *22*(11), 6104.

Jadon, N., Jain, R., Sharma, S., & Singh, K. (2016). Recent trends in electrochemical sensors for multianalyte detection–A review. *Talanta*, *161*, 894-916.

Jiang, T., Sun, X., Wei, L., & Li, M. (2020). Determination of hydrogen peroxide released from cancer cells by a Fe-Organic framework/horseradish peroxidase-modified electrode. *Analytica Chimica Acta*, *1135*, 132-141. https://doi.org/10.1016/j.aca.2020.09.040

Jin, X., Geng, C., Zhao, D., Liu, Y., Wang, X., Liu, X., & Wong, D. K. Y. (2023). Peroxidase-encapsulated Zn/Co-zeolite imidazole framework nanosheets on ZnCoO nanowire array for detecting H_2O_2 derived from mitochondrial superoxide anion. *Biosensors and Bioelectronics*, *237*, 115547. https://doi.org/10.1016/j.bios.2023.115547

Johra, F. T., Lee, J.-W., & Jung, W.-G. (2014). Facile and safe graphene preparation on solution based platform. *Journal of Industrial and Engineering Chemistry*, *20*(5),

2883-2887.

Kaewjua, K., & Siangproh, W. (2022). A novel tyramine sensing-based polymeric L-histidine film-coated screen-printed graphene electrode: Capability for practical applications. *Electrochimica Acta*, *419*, 140388.

Kaewjua, K., & Siangproh, W. (2023). Innovative electrochemical platform for the simultaneous determination of l-DOPA and l-tyrosine using layer-by-layer assembled L-proline-linked nanodiamonds on printed graphene. *Microchimica Acta*, *190*(10), 398.

Khan, M., Liu, X., Zhu, J., Ma, F., Hu, W., & Liu, X. (2018). Electrochemical detection of tyramine with ITO/APTES/ErGO electrode and its application in real sample analysis. *Biosensors and Bioelectronics*, *108*, 76-81.

Kim, H. R., Ingram, J. L., & Que, L. G. (2023). Effects of oxidative stress on airway epithelium permeability in asthma and potential implications for patients with comorbid obesity. *Journal of asthma and allergy*, 481-499.

Kissinger, P., & Heineman, W. R. (2018). *Laboratory Techniques in Electroanalytical Chemistry, revised and expanded*. CRC press.

Kochana, J., Wapiennik, K., Knihnicki, P., Pollap, A., Janus, P., Oszajca, M., & Kuśtrowski, P. (2016). Mesoporous carbon-containing voltammetric biosensor for determination of tyramine in food products. *Analytical and bioanalytical chemistry*, *408*(19), 5199-5210.

Kolpin, C., & Swofford, H. (1978). Heme catalyzed reduction of oxygen and hydrogen peroxide at a mercury electrode surface. *Analytical chemistry*, *50*(7), 920-929.

Kordasht, H. K., Hasanzadeh, M., Seidi, F., & Alizadeh, P. M. (2021). Poly (amino acids) towards sensing: Recent progress and challenges. *TrAC Trends in Analytical Chemistry*, *140*, 116279.

Krishnamoorthy, K., Veerapandian, M., Kim, G.-S., & Jae Kim, S. (2012). A one step hydrothermal approach for the improved synthesis of graphene nanosheets. *Current Nanoscience*, *8*(6), 934-938.

Küçük, A., & Torul, O. (2018). Voltammetric sensor based on poly (3-methylthiophene)

synthesized in dichloromethane for tyramine determination in moldy cheese. *Synthetic Metals*, *237*, 23-28.

Kukovecz, Á., Kozma, G., & Kónya, Z. (2013). Multi-Walled Carbon Nanotubes. In R. Vajtai, *Springer Handbook of Nanomaterials* (147-188). Springer Berlin Heidelberg. https://doi.org/10.1007/978-3-642-20595-8_5

Kumar, D. R., Kesavan, S., Nguyen, T. T., Hwang, J., Lamiel, C., & Shim, J.-J. (2017). Polydopamine@electrochemically reduced graphene oxide-modified electrode for electrochemical detection of free-chlorine. *Sensors and Actuators B: Chemical*, *240*, 818-828. https://doi.org/10.1016/j.snb.2016.09.025

Ladero, V., Calles-Enríquez, M., Fernández, M., & A Alvarez, M. (2010). Toxicological effects of dietary biogenic amines. *Current Nutrition & Food Science*, *6*(2), 145-156.

Lamas-Ardisana, P. J., Loaiza, O. A., Añorga, L., Jubete, E., Borghei, M., Ruiz, V., . . . Grande, H. J. (2014). Disposable amperometric biosensor based on lactate oxidase immobilised on platinum nanoparticle-decorated carbon nanofiber and poly(diallyldimethylammonium chloride) films. *Biosensors and Bioelectronics*, *56*, 345-351. https://doi.org/10.1016/j.bios.2014.01.047

Lases, E. C., Duurkens, V. A., Gerritsen, W. B., & Haas, F. J. (2000). Oxidative stress after lung resection therapy: a pilot study. *Chest*, *117*(4), 999-1003.

Lasia, A. (2002). Electrochemical impedance spectroscopy and its applications. In *Modern aspects of electrochemistry* (143-248). Springer.

Lei, W., Wu, L., Huang, W., Hao, Q., Zhang, Y., & Xia, X. (2014). Microwave-assisted synthesis of hemin–graphene/poly(3,4-ethylenedioxythiophene) nanocomposite for a biomimetic hydrogen peroxide biosensor. *Journal of Materials Chemistry B*, *2*(27), 4324-4330. https://doi.org/10.1039/C4TB00313F

Letellier, S., Garnier, J., Spy, J., Stoitchkov, K., Le Bricon, T., Baccard, M., . . . Bousquet, B. (1999). Development of metastases in malignant melanoma is associated with an increase in the plasma L-dopa/L-tyrosine ratio. *Melanoma research*, *9*(4), 389-394.

Letellier, S., Garnier, J. P., Spy, J., & Bousquet, B. (1997). Determination of the L-dopa/L-tyrosine ratio in human plasma by high-performance liquid chromatography: usefulness as a marker in metastatic malignant melanoma. *Journal of Chromatography B: Biomedical Sciences and Applications*, *696*(1), 9-17.

Li, Q., Zhang, Y., Li, P., Xue, H., & Jia, N. (2020). A nanocomposite prepared from hemin and reduced graphene oxide foam for voltammetric sensing of hydrogen peroxide. *Microchimica Acta*, *187*, 1-8.

Li, Y., Hsieh, C.-H., Lai, C.-W., Chang, Y.-F., Chan, H.-Y., Tsai, C.-F., . . . Wu, L.-c. (2017). Tyramine detection using PEDOT: PSS/AuNPs/1-methyl-4-mercaptopyridine modified screen-printed carbon electrode with molecularly imprinted polymer solid phase extraction. *Biosensors and Bioelectronics*, *87*, 142-149.

Linares, D. M., del Rio, B., Redruello, B., Ladero, V., Martin, M. C., Fernandez, M., . . . Alvarez, M. A. (2016). Comparative analysis of the in vitro cytotoxicity of the dietary biogenic amines tyramine and histamine. *Food Chemistry*, *197*, 658-663. https://doi.org/10.1016/j.foodchem.2015.11.013

Liu, C., Du, P., Zhao, H., & Wang, L. (2018). Synthesis of l-Histidine-Attached Graphene Nanomaterials and Their Application for Steel Protection. *ACS Applied Nano Materials*, *1*(3), 1385-1395. https://doi.org/10.1021/acsanm.8b00149

Liu, X., Zhang, L., Wei, S., Chen, S., Ou, X., & Lu, Q. (2014). Overoxidized polyimidazole/graphene oxide copolymer modified electrode for the simultaneous determination of ascorbic acid, dopamine, uric acid, guanine and adenine. *Biosensors and Bioelectronics*, *57*, 232-238. https://doi.org/10.1016/j.bios.2014.02.017

Liu, Z., Xing, Z., Zu, Y., Tan, S., Zhao, L., Zhou, Z., & Sun, T. (2012). Synthesis and characterization of L-histidine capped silver nanoparticles. *Materials Science and Engineering: C*, *32*(4), 811-816. https://doi.org/10.1016/j.msec.2012.01.031

Lopes, P., Kaewjua, K., Shipovskov, S., & Ferapontova, E. E. (2024). Glucose and Glutamate Detection by Oxidase/Hemin Peroxidase Mimic Cascades Assembled on Macro‐and Microelectrodes. *ChemElectroChem*, e202300682.

Luo, M., Song, Y., Ali Khan, N., Wei, W., Lu, Y., Zhao, Q., . . . Wang, D. (2024). Facile fabrication of HRP-$Cu_3(PO_4)_2$ hybrid nanoflowers on screen-printed electrode for electrochemical detection of H_2O_2. *Microchemical Journal*, *197*, 109845. https://doi.org/10.1016/j.microc.2023.109845

MacNee, W. (2001). Oxidative stress and lung inflammation in airways disease. *European journal of pharmacology*, *429*(1-3), 195-207.

Mary, Y. S., Ushakumari, L., Harikumar, B., Varghese, H. T., & Panicker, C. Y. (2009). FT-IR, FT-raman and SERS spectra of L-proline. *Journal of the Iranian Chemical Society*, *6*(1), 138-144. https://doi.org/10.1007/BF03246512

Mavrogiorgis, D., Bilalis, P., Karatzas, A., Skoulas, D., Fotinogiannopoulou, G., & Iatrou, H. (2014). Controlled polymerization of histidine and synthesis of well-defined stimuli responsive polymers. Elucidation of the structure–aggregation relationship of this highly multifunctional material. *Polymer Chemistry*, *5*(21), 6256-6278.

McCabe-Sellers, B. J., Staggs, C. G., & Bogle, M. L. (2006). Tyramine in foods and monoamine oxidase inhibitor drugs: a crossroad where medicine, nutrition, pharmacy, and food industry converge. *Journal of Food Composition and Analysis*, *19*, S58-S65.

Melgarejo-Torres, R., Pérez-Vega, S. B., Rivera-Arredondo, V. M., & Che-Galicia, G. (2019). Chapter Six - Multiphase bioreactors in the pharmaceutical industry. In S. Huerta-Ochoa, C. O. Castillo-Araiza, & G. Quijano, *Advances in Chemical Engineering* (Vol. 54, 195-237). Academic Press. https://doi.org/10.1016/bs.ache.2019.01.005

Mesu, J. G., Visser, T., Soulimani, F., & Weckhuysen, B. M. (2005). Infrared and Raman spectroscopic study of pH-induced structural changes of l-histidine in aqueous environment. *Vibrational Spectroscopy*, *39*(1), 114-125. https://doi.org/10.1016/j.vibspec.2005.01.003

Mochalin, V. N., Shenderova, O., Ho, D., & Gogotsi, Y. (2012). The properties and applications of nanodiamonds. *Nature Nanotechnology*, *7*(1), 11-23. https://doi.org/10.1038/nnano.2011.209

Movlaee, K., Beitollahi, H., Ganjali, M. R., & Norouzi, P. (2017). Electrochemical platform for simultaneous determination of levodopa, acetaminophen and tyrosine using a graphene and ferrocene modified carbon paste electrode. *Microchimica Acta*, *184*, 3281-3289.

Nagaraja, C., Shashibhushan, B. L., Sagar, Asif, M., & Manjunath, P. H. (2012). Hydrogen peroxide in exhaled breath condensate: A clinical study. *Lung India*, *29*(2), 123-127. https://doi.org/10.4103/0970-2113.95303

Niu, X., Zhao, H., Chen, C., & Lan, M. (2012). Platinum nanoparticle-decorated carbon nanotube clusters on screen-printed gold nanofilm electrode for enhanced electrocatalytic reduction of hydrogen peroxide. *Electrochimica Acta*, *65*, 97-103. https://doi.org/10.1016/j.electacta.2012.01.030

Núñez-Bajo, E., & Fernández Abedul, M. T. (2020). Chapter 8 - Chronoamperometric determination of ascorbic acid on paper-based devices. In M. T. Fernandez Abedul, *Laboratory Methods in Dynamic Electroanalysis* (75-83). Elsevier. https://doi.org/10.1016/B978-0-12-815932-3.00008-5

O'Halloran, M. P., Pravda, M., & Guilbault, G. G. (2001). Prussian Blue bulk modified screen-printed electrodes for H_2O_2 detection and for biosensors. *Talanta*, *55*(3), 605-611. https://doi.org/10.1016/S0039-9140(01)00469-6

Özogul, Y., & Özogul, F. (2019). Biogenic amines formation, toxicity, regulations in food.

Palanisamy, S., Velusamy, V., Balu, S., Velmurugan, S., Yang, T. C. K., & Chen, S.-W. (2020). Sonochemical synthesis and anchoring of zinc oxide on hemin-mediated multiwalled carbon nanotubes-cellulose nanocomposite for ultra-sensitive biosensing of H_2O_2. *Ultrasonics Sonochemistry*, *63*, 104917. https://doi.org/10.1016/j.ultsonch.2019.104917

Patel, B. A. (2020). Chapter 2 - Amperometry and potential step techniques. In B. Patel, *Electrochemistry for Bioanalysis* (9-26). Elsevier. https://doi.org/10.1016/B978-0-12-821203-5.00009-9

Paulsen, P., Grossgut, R., Bauer, F., & Rauscher-Gabernig, E. (2012). Estimates of maximum tolerable levels of tyramine content in foods in Austria. *Journal of Food &*

Nutrition Research, *51*(1).

Pourhajghanbar, M., Arvand, M., & Habibi, M. F. (2023). Surface imprinting by using bi-functional monomers on spherical template magnetite for selective detection of levodopa in biological fluids. *Talanta*, *254*, 124136. https://doi.org/10.1016/j.talanta.2022.124136

Qiao, Y., Yang, G., Jian, F., Qin, Y., & Yang, L. (2009). Hydrogen peroxide electrochemical detection for the development of protein film-modified sensor. *Sensors and Actuators B: Chemical*, *141*(1), 205-209. https://doi.org/10.1016/j.snb.2009.05.015

Rand, M., & Trinker, F. R. (1968). The mechanism of the augmentation of responses to indirectly acting sympathomimetic amines by monoamine oxidase inhibitors. *British journal of pharmacology and chemotherapy*, *33*(2), 287.

Raoof, J. B., Ojani, R., Amiri-Aref, M., & Baghayeri, M. (2012). Electrodeposition of quercetin at a multi-walled carbon nanotubes modified glassy carbon electrode as a novel and efficient voltammetric sensor for simultaneous determination of levodopa, uric acid and tyramine. *Sensors and Actuators B: Chemical*, *166*, 508-518.

Raoof, J. B., Ojani, R., Baghayeri, M., & Amiri-Aref, M. (2012). Application of a glassy carbon electrode modified with functionalized multi-walled carbon nanotubes as a sensor device for simultaneous determination of acetaminophen and tyramine. *Analytical methods*, *4*(6), 1579-1587.

Revin, S. B., & John, S. A. (2013). Electrochemical marker for metastatic malignant melanoma based on the determination of l-dopa/l-tyrosine ratio. *Sensors and Actuators B: Chemical*, *188*, 1026-1032. https://doi.org/10.1016/j.snb.2013.08.019

Rotariu, L., Zamfir, L.-G., & Bala, C. (2010). Low potential thiocholine oxidation at carbon nanotube-ionic liquid gel sensor. *Sensors and Actuators B: Chemical*, *150*(1), 73-79.

Sam, S., Mathew, M. R., & Kumar, K. G. (2022). A Simple electropolymer based voltammetric sensor for the simultaneous determination of melanoma biomarkers–L-dopa and L-tyrosine. *Journal of The Electrochemical Society*, *169*(2), 027511.

Santos, M. S. (1996). Biogenic amines: their importance in foods. *International journal of food microbiology*, *29*(2-3), 213-231.

Scholz, F. (2010). *Electroanalytical methods* (Vol. 1). Springer.

Schrand, A. M., Hens, S. A. C., & Shenderova, O. A. (2009). Nanodiamond particles: properties and perspectives for bioapplications. *Critical reviews in solid state and materials sciences*, *34*(1-2), 18-74.

Shaidarova, L., Chelnokova, I., Leksina, Y. A., Il'ina, M., Gedmina, A., & Budnikov, H. (2018). Flow-injection amperometric determination of DOPA and tyrosine at a dual electrode modified with the gold–cobalt binary system. *Journal of analytical chemistry*, *73*, 176-182.

Shalaby, A. R. (1996). Significance of biogenic amines to food safety and human health. *Food Research International*, *29*(7), 675-690.

Shimpi, M. R., Childs, S. L., Boström, D., & Velaga, S. P. (2014). New cocrystals of ezetimibe with l-proline and imidazole. *CrystEngComm*, *16*(38), 8984-8993. https://doi.org/10.1039/C4CE01127A

Sies, H. (2017). Hydrogen peroxide as a central redox signaling molecule in physiological oxidative stress: Oxidative eustress. *Redox Biology*, *11*, 613-619. https://doi.org/10.1016/j.redox.2016.12.035

Simoska, O., Lee, Y. S., & Minteer, S. D. (2023). 7.15 - Fundamentals and applications of enzymatic bioelectrocatalysis. In J. Reedijk & K. R. Poeppelmeier, *Comprehensive Inorganic Chemistry III (Third Edition)* (456-491). Elsevier. https://doi.org/10.1016/B978-0-12-823144-9.00057-1

Slominski, A., Zmijewski, M. A., & Pawelek, J. (2012). L-tyrosine and L-dihydroxyphenylalanine as hormone-like regulators of melanocyte functions. *Pigment cell & melanoma research*, *25*(1), 14-27.

Smith, T. (1981). Amines in food. *Food chemistry*, *6*(3), 169-200.

Song, H., Ni, Y., & Kokot, S. (2014). Investigations of an electrochemical platform based on the layered MoS_2–graphene and horseradish peroxidase nanocomposite for direct electrochemistry and electrocatalysis. *Biosensors and Bioelectronics*, *56*, 137-143.

https://doi.org/10.1016/j.bios.2014.01.014

Sosna, M., Fapyane, D., & Ferapontova, E. E. (2014). Reconstitution of peroxidase onto hemin-terminated alkanethiol self-assembled monolayers on gold. *Journal of Electroanalytical Chemistry*, *728*, 18-25. https://doi.org/10.1016/j.jelechem.2014.06.012

Stoitchkov, K., Letellier, S., Garnier, J.-P., Bousquet, B., Tsankov, N., Morel, P., . . . Le Bricon, T. (2003). Evaluation of the serum L-dopa/L-tyrosine ratio as a melanoma marker. *Melanoma Research*, *13*(6), 587-593.

Stoitchkov, K., Letellier, S., Garnier, J., Bousquet, B., Tsankov, N., Morel, P., . . . Le Bricon, T. (2002). Melanoma progression and serum L-dopa/L-tyrosine ratio: a comparison with S100B. *Melanoma Research*, *12*(3), 255-262.

Stone, J. R., & Yang, S. (2006). Hydrogen peroxide: a signaling messenger. *Antioxidants & redox signaling*, *8*(3-4), 243-270.

Sveinbjornsdottir, S. (2016). The clinical symptoms of Parkinson's disease. *Journal of neurochemistry*, *139*, 318-324.

Telsnig, D., Kalcher, K., Leitner, A., & Ortner, A. (2013). Design of an amperometric biosensor for the determination of biogenic amines using screen printed carbon working electrodes. *Electroanalysis*, *25*(1), 47-50.

Tieman, R. S., Coury, L. A., Kirchhoff, J. R., & Heineman, W. R. (1990). The electrochemistry of hemin in dimethylsulfoxide. *Journal of Electroanalytical Chemistry and Interfacial Electrochemistry*, *281*(1), 133-145. https://doi.org/10.1016/0022-0728(90)87035-I

Upadhyay, A., Chen, S.-M., Ting, T.-W., & Peng, Y.-Y. (2011). A biosensor for hydrogen peroxide based on single walled carbon nanotube and metal oxide modified indium tin oxide electrode. *International Journal of Electrochemical Science*, *6*(8), 3466-3482.

Varga, M., Izak, T., Vretenar, V., Kozak, H., Holovsky, J., Artemenko, A., . . . Kromka, A. (2017). Diamond/carbon nanotube composites: Raman, FTIR and XPS spectroscopic studies. *Carbon*, *111*, 54-61.

https://doi.org/10.1016/j.carbon.2016.09.064

Veal, E. A., Day, A. M., & Morgan, B. A. (2007). Hydrogen peroxide sensing and signaling. *Molecular cell*, *26*(1), 1-14.

Velázquez-Palenzuela, A., Centellas, F., Garrido, J. A., Arias, C., Rodríguez, R. M., Brillas, E., & Cabot, P.-L. (2011). Kinetic analysis of carbon monoxide and methanol oxidation on high performance carbon-supported Pt–Ru electrocatalyst for direct methanol fuel cells. *Journal of Power Sources*, *196*(7), 3503-3512. https://doi.org/10.1016/j.jpowsour.2010.12.044

Wang, B., & Huang, J. S. (2014). Using poly-L-histidine modified glassy carbon electrode to trace hydroquinone in the sewage water. *International Journal of Electrochemistry*, *2014*.

Wang, B., Zhang, J.-J., Pan, Z.-Y., Tao, X.-Q., & Wang, H.-S. (2009). A novel hydrogen peroxide sensor based on the direct electron transfer of horseradish peroxidase immobilized on silica–hydroxyapatite hybrid film. *Biosensors and Bioelectronics*, *24*(5), 1141-1145. https://doi.org/10.1016/j.bios.2008.06.053

Wang, J. (2006). *Analytical Electrochemistry* (3rd ed.). John Wiley & Sons, Inc.

Wang, L., Yang, H., He, J., Zhang, Y., Yu, J., & Song, Y. (2016). Cu-Hemin Metal-Organic-Frameworks/Chitosan-Reduced Graphene Oxide Nanocomposites with Peroxidase-Like Bioactivity for Electrochemical Sensing. *Electrochimica Acta*, *213*, 691-697. https://doi.org/10.1016/j.electacta.2016.07.162

Wang, Y., Limon-Petersen, J. G., & Compton, R. G. (2011). Measurement of the diffusion coefficients of $[Ru(NH_3)_6]^{3+}$ and $[Ru(NH_3)_6]^{2+}$ in aqueous solution using microelectrode double potential step chronoamperometry. *Journal of Electroanalytical Chemistry*, *652*(1), 13-17. https://doi.org/10.1016/j.jelechem.2010.12.011

Wang, Y., Wang, Z., Rui, Y., & Li, M. (2015). Horseradish peroxidase immobilization on carbon nanodots/CoFe layered double hydroxides: Direct electrochemistry and hydrogen peroxide sensing. *Biosensors and Bioelectronics*, *64*, 57-62. https://doi.org/10.1016/j.bios.2014.08.054

Weber, F. L., & Reiser, B. J. (1982). Relationship of plasma amino acids to nitrogen balance and portal-systemic encephalopathy in alcoholic liver disease. *Digestive Diseases and Sciences*, *27*, 103-110.

Wittmann, C., Chockley, P., Singh, S. K., Pase, L., Lieschke, G. J., & Grabher, C. (2012). Hydrogen Peroxide in Inflammation: Messenger, Guide, and Assassin. *Advances in Hematology*, *2012*, 541471. https://doi.org/10.1155/2012/541471

Woo, S., Kim, Y.-R., Chung, T. D., Piao, Y., & Kim, H. (2012). Synthesis of a graphene–carbon nanotube composite and its electrochemical sensing of hydrogen peroxide. *Electrochimica Acta*, *59*, 509-514. https://doi.org/10.1016/j.electacta.2011.11.012

Xin, X., Gong, T., & Hong, Y. (2022). Hydrogen peroxide initiates oxidative stress and proteomic alterations in meningothelial cells. *Scientific Reports*, *12*(1), 14519. https://doi.org/10.1038/s41598-022-18548-3

Xu, F., Sun, Y., Zhang, Y., Shi, Y., Wen, Z., & Li, Z. (2011). Graphene–Pt nanocomposite for nonenzymatic detection of hydrogen peroxide with enhanced sensitivity. *Electrochemistry communications*, *13*(10), 1131-1134. https://doi.org/10.1016/j.elecom.2011.07.017

Xue, T., Jiang, S., Qu, Y., Su, Q., Cheng, R., Dubin, S., . . . Duan, X. (2012). Graphene-supported hemin as a highly active biomimetic oxidation catalyst. *Angew Chem Int Ed Engl*, *51*(16), 3822-3825. https://doi.org/10.1002/anie.201108400

Yang, J.-H., Kim, H. T., & Kim, H. (2014). A cyclodextrin-based approach for selective detection of catecholamine hormone mixtures. *Micro and Nano Systems Letters*, *2*(1), 1. https://doi.org/10.1186/s40486-014-0001-z

Yang, L., Xu, C., Ye, W., & Liu, W. (2015). An electrochemical sensor for H_2O_2 based on a new Co-metal-organic framework modified electrode. *Sensors and Actuators B: Chemical*, *215*, 489-496. https://doi.org/10.1016/j.snb.2015.03.104

Yigit, M., & Ersoy, L. (2003). Determination of tyramine in cheese by LC–UV. *Journal of pharmaceutical and biomedical analysis*, *31*(6), 1223-1228.

Youdim, M. B., Edmondson, D., & Tipton, K. F. (2006). The therapeutic potential of

monoamine oxidase inhibitors. *Nature reviews neuroscience*, *7*(4), 295-309.

Zhang, G., & Dasgupta, P. K. (1992). Hematin as a peroxidase substitute in hydrogen peroxide determinations. *Analytical chemistry*, *64*(5), 517-522. https://doi.org/10.1021/ac00029a013

Zhang, W., Jia, B., & Furumai, H. (2018). Fabrication of graphene film composite electrochemical biosensor as a pre-screening algal toxin detection tool in the event of water contamination. *Scientific Reports*, *8*(1), 10686. https://doi.org/10.1038/s41598-018-28959-w

Zhang, Y., Xia, Z., Liu, H., Yang, M., Lin, L., & Li, Q. (2013). Hemin-graphene oxide-pristine carbon nanotubes complexes with intrinsic peroxidase-like activity for the detection of H_2O_2 and simultaneous determination for Trp, AA, DA, and UA. *Sensors and Actuators B: Chemical*, *188*, 496-501. https://doi.org/10.1016/j.snb.2013.07.010

Zhang, Y., Zhang, M., Wei, Q., Gao, Y., Guo, L., Al-Ghanim, K. A., . . . Zhang, X. (2016). An easily fabricated electrochemical sensor based on a graphene-modified glassy carbon electrode for determination of octopamine and tyramine. *Sensors*, *16*(4), 535.

Zhao, X., Yi, L., Wang, C., Xian, Y., Zeng, X., & Bai, W. (2018). Simple and sensitive electrochemical sensor for tyramine determination based on overoxidized poly (o-aminophenol) film modified electrode. *Int. J. Electrochem. Sci*, *13*, 10289-10301.

Zhu, X., Niu, X., Zhao, H., & Lan, M. (2014). Doping ionic liquid into Prussian blue-multiwalled carbon nanotubes modified screen-printed electrode to enhance the nonenzymatic H_2O_2 sensing performance. *Sensors and Actuators B: Chemical*, *195*, 274-280. https://doi.org/10.1016/j.snb.2014.01.052

Zhu, X., & Shi, L. (2019). Electrochemistry. In *Nano-inspired Biosensors for Protein Assay with Clinical Applications* (209-236). Elsevier.

Appendix

Appendix 1

Electrochimica Acta 419 (2022) 140388

Contents lists available at ScienceDirect

Electrochimica Acta

journal homepage: www.journals.elsevier.com/electrochimica-acta

A novel tyramine sensing-based polymeric L-histidine film-coated screen-printed graphene electrode: Capability for practical applications

Kantima Kaewjua, Weena Siangproh *

Department of Chemistry, Faculty of Science, Srinakharinwirot University, Sukhumvit 23, Wattana, Bangkok 10110, Thailand

ARTICLE INFO

Keywords:
Tyramine
Poly(histidine)
Screen-printed graphene electrode
Electrochemical detection

ABSTRACT

A novel electrochemical sensor for the determination of tyramine (Tyr) based on a polymeric film of L-histidine coated on a screen-printed graphene electrode (poly(His)/SPGE) is presented for the first time. This developed sensor was constructed through a single modification step via an electropolymerization process. The poly(His) feature exhibited an outstanding electrocatalytic activity in the electrooxidation of Tyr. Under optimal conditions, the Tyr sensor revealed relatively broad two linear ranges of 0.5–20 μM and 50–300 μM with a limit of detection and limit of quantification of 0.065 μM (3SD/slope) and 0.22 μM (10SD/slope), respectively. Furthermore, the reliability of this proposed sensor was successfully investigated by detecting Tyr in both biological fluids and cheese samples, with satisfactory recovery ranges (82.58%–109.75%) and relative standard deviations (0.28%–8.03%). Therefore, the proposed sensor has distinct advantages, such as low cost, easy operation, disposable, high sensitivity, and good selectivity.

On the merits of the aforementioned benefits, the newly developed electrochemical sensor could be a promising alternative approach for Tyr assessment in food quality and safety control, as well as a better understanding of clinical function associated with migraine triggers.

1. Introduction

Biogenic amines (BAs) are basic nitrogenous compounds mainly produced by microbial decarboxylation of amino acids [1]. Various BAs have been found in food, either naturally or as a result of contamination during food processing and storage [2]. Therefore, these compounds can be used as chemical freshness indicators for protein-rich foods, microbial contamination, hygienic status, and food quality [3]. Tyramine (Tyr) is one of the most significant BAs that originated from the decarboxylation of tyrosine. This BA is mainly found in a variety of foods and beverages, such as meat, fish products, alcoholic beverages, and fermented dairy products, especially cheese [4–6].

Normally, the ingestion of Tyr-containing foods does not have adverse effects on the human health as it is readily detoxified by the action of monoamine oxidase (MAO) in the intestinal wall and liver. On the other hand, it cannot be properly detoxified when consumed in large quantities in food and in patients treated with monoamine oxidase inhibitor drugs (MAOI), which results in an indirect stimulation of the noradrenaline release from the sympathetic nerve terminals [7]. An excessive amount of Tyr has not only been proposed as the cause of hypertensive crises in certain patients and dietary-induced migraines; it can also cause toxicological effects and diseases, such as brain hemorrhage, palpitations, nausea, and diarrhea [6,8,9]. In addition, it was reported that Tyr was more cytotoxic than other BAs in an *in vitro* model of the human intestinal epithelium at concentrations commonly found in certain foods [10]. Hence, Tyr needs to be controlled to ensure the level of food quality and safety of consumers.

Several analytical techniques have been developed to detect Tyr in food products, such as high-performance liquid chromatography (HPLC) with different types of detection [11–13], gas chromatography (GC) [14], ion chromatography [15], capillary electrophoresis (CE) [16], and immunoassays [17,18]. Even though the techniques mentioned exhibit high accuracy and precision, in most cases, they require tedious sample preparation and derivatization steps, as well as expensive and complex instruments. Consequently, these techniques have been limited to routine and on-site monitoring. The electroanalytical method offers the practical benefits of ease of operation, cost-effectiveness, suitability for real-time detection, less sensitivity to matrix effects, and sample volume reduction while maintaining high sensitivity and selectivity. Therefore, electroanalytical approach is widely used for the detection of target

* Corresponding author.
E-mail address: weena@g.swu.ac.th (W. Siangproh).

https://doi.org/10.1016/j.electacta.2022.140388
Received 15 February 2022; Received in revised form 10 April 2022; Accepted 13 April 2022
Available online 14 April 2022

analytes in numerous fields, such as food contaminants analysis [19–21], clinical analysis [22,23] and environmental monitoring [24]. Tyr can be investigated using electrochemical techniques owing to its electroactive nature. However, its poor sensitivity and selectivity become the bottleneck in the electrochemical detection of Tyr at the bare electrode without any modification. Chemical modification of such electrodes with single molecular, multi-molecular, ionic, and polymeric components provides electrocatalytic properties in terms of increasing active surface area and accelerating electron transfer kinetics, which is beneficial for electrochemical sensing applications [25,26]. Hence, chemically modified electrodes (CME) have gained increasing attention in the field of electroanalysis for achieving acceptable sensitivity and selectivity.

Recently, various materials, such as the nanostructured luteolin immobilized functionalized multiwall carbon nanotube-modified glassy carbon electrode [27], gold nanoparticle-doped conducting polymer on gold electrodes [28], reduced graphene oxide-based indium tin oxide electrode [29], and molecularly imprinted polymers derived from derivatized polythiophene film [30], have been used to develop electrochemical sensors for Tyr determination in food products and biological samples. Furthermore, the use of enzyme immobilization on various materials is another attractive choice for improving the electrochemical response and the limit of quantitative detection for Tyr. Some of the immobilizations of tyrosinase enzyme onto various substrates have been reported, including, glassy carbon electrode modified by both gold nanoparticles and poly(8-anilino-1-naphthalene sulphonic acid) [31], functionalized polymeric film of 4-mercaptophenylacetic acid on carbon graphite lead electrode [32]. In addition, the different amine oxidases, including plasma amine oxidase enzyme [33] and pea seedling amine oxidase enzyme [34], were immobilized on the surface of diverse working electrodes to improve the performance of the electrochemical biosensors for Tyr determination. The application of previous modified electrodes has been limited for in-field and real-time analysis due to the numerous modification procedures and the use of complicated materials. To overcome the aforementioned limitations, the preparation of modified electrodes and user-friendly materials has been simplified and focused on.

Amino acid-based polymer-modified electrodes have attracted a considerable amount of interest for use in electrochemical sensing applications owing to their environmental stability, non-toxicity, ease of manufacturing, biocompatibility, low cost, adjustable physicochemical properties, and a wide number of side functional groups [35–37]. Poly (histidine) (poly(His)) is a biocompatible material that has gained a lot of attention in electrochemical platforms. Poly(His) film facilitates electron-transfer at the electrode–solution interface and increases the electrocatalytic activity of target analytes due to the variety of functional groups formed after electrode surface modification, which includes carboxylic groups, amine groups, and imidazole rings [38]. Ease of operation, rapid response, and portability were the features considered in the attempts to develop an electrochemical sensor for the detection of Tyr in practical applications. Screen-printed electrodes (SPEs) can be manufactured in a variety of designs and materials, depending on the application and willingness to be easily modified electrode surface to improve the sensitivity and selectivity of measurement in electroanalytical applications [39]. Furthermore, SPEs combined with electrochemical approaches have demonstrated the capability of being capable sensors for transitioning traditional benchtop techniques into field analysis, as well as low cost, robust, and rapid sensing devices [40]. Graphene, a typical nanocarbon material, has been extensively used as a promising electrode material for electrochemical sensor applications owing to its superior electrical conductivity, good mechanical strength, high mobility of charge carriers, and large surface area [41]. Thus, graphene-based substrates could be used to improve the electrochemical efficiency in electroanalytical sensing applications.

The advantages of amino acid-based polymers and graphene-based substrates inspired us to develop a novel, simple, and highly sensitive electrochemical sensor for Tyr monitoring based on a poly(His)-modified screen-printed graphene electrode (poly(His)/SPGE). As mentioned in this paper, the proposed sensor has been fabricated through a single modification step that is directly generated at the electrode surface *via* electropolymerization. The use of a poly(His)-modified electrode exerted an electrocatalytic effect on the electrooxidation of Tyr by nearly tripling the peak currents. All the concerned parameters were systematically optimized to obtain the optimal conditions. The promising results indicated that the developed Tyr sensor could potentially be an alternative tool for practical use to analyze the Tyr levels in food and biological samples.

2. Experimental

2.1. Chemicals, materials, and instruments

Tyramine hydrochloride, L-histidine monohydrochloride monohydrate, cadaverine dihydrochloride, histamine dihydrochloride, 1,4-diaminobutane dihydrochloride, L-ascorbic acid, dopamine hydrochloride, uric acid, bovine serum albumin, creatinine, potassium ferricyanide $K_3[Fe(CN)_6]$, and hexaammine ruthenium(III) chloride $[Ru(NH_3)_6]Cl_3$ were purchased from Sigma-Aldrich (St. Louis, MO, USA). 0.1 M Phosphate buffer solution (PBS) was prepared by mixing sodium dihydrogen orthophosphate ($NaH_2PO_4.2H_2O$) and disodium hydrogen orthophosphate ($Na_2HPO_4.2H_2O$), which were obtained from Ajax (Australia). All aqueous solutions were prepared in deionized (DI) water produced by the Milli-Q system ($R = 18.2\ M\Omega$ cm at 25 °C).

The morphology and chemical composition of the electrode materials were examined using a scanning electron microscope (SEM, SU3500) (Hitachi High-Tech., Japan) and a SEM and energy-dispersive X-ray spectrometer (IT300) (JEOL Ltd., Japan), respectively. The electrochemical measurements, *via* cyclic voltammetry (CV) and differential pulse voltammetry (DPV), were performed at room temperature on a CHI 1200C potentiostat (Austin, TX, USA). Electrochemical impedance spectroscopy (EIS) measurements were performed using Sensit smart (Houten, the Netherlands).

2.2. Fabrication of poly(histidine)-modified SPGE

The patterned SPGE was designed using Adobe Illustrator CC, and the template block screen was constructed using the designed pattern by Chaiyaboon Brothers Co., Ltd. (Bangkok, Thailand). The SPGE, consisting of a working electrode (WE), counter electrode (CE), and reference electrode (RE), was fabricated onto the transparency film substrate using an in-house screen-printing technique. First, the WE and CE were manually screened onto the substrate using graphene ink from Serve Science Co., Ltd. (product code: SSG-1760A, Bangkok, Thailand) and placed into a hot air oven at a temperature of 55 °C for 30 min. Then, the RE and conducting pad were screened onto the same substrate using silver/silver chloride (Ag/AgCl) ink obtained from Sun Chemical (product code: C2130809D5, Slough, United Kingdom) for the complement of an electrochemical cell and heated again at 55 °C for 30 min for solvent drying. Before use, the prepared SPGE was attached with adhesive tape to each electrode strip under the detection area for the confinement of the electrode surface area.

A single step electropolymerization was employed for electrode modification. Electropolymerization of L-histidine was directly performed onto the prepared SPGE surface using the CV technique. This procedure was accomplished by dropping 100 μL of 40 mM L-histidine monomer in 0.1 M PBS (pH 7.4) onto the electrode surface area and applying the potential from −0.6 to +2.0 V for 20 cycles at a scan rate of 0.2 Vs^{-1}. The electropolymerization of L-histidine can be explained by the anodic peak of L-histidine, which was first observed around +1.5 V (Fig. S1), which is the oxidized form of the imidazole ring on the side chain. As observed in the second cycle of scans at a potential of +1.2 V, the His radicals were then coupled to form poly(His). Interestingly, as

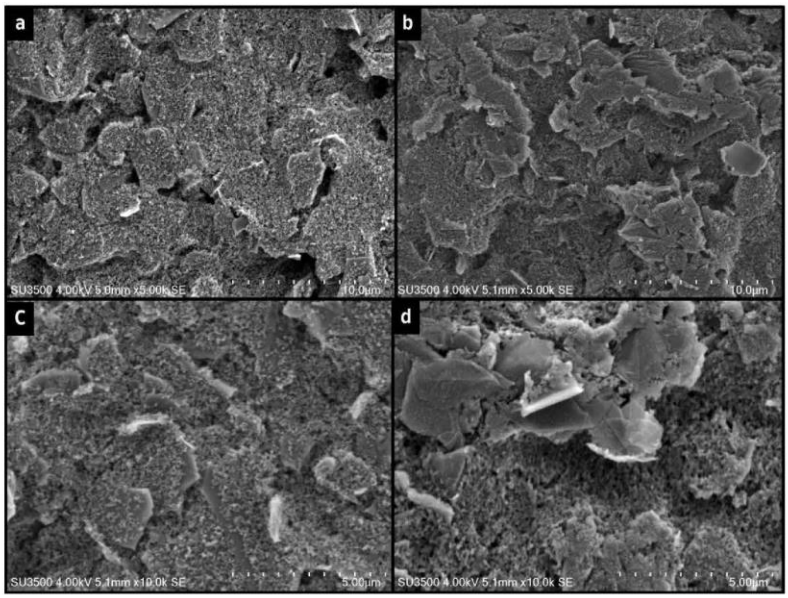

Fig. 1. SEM images of bare SPGE (a and c), and poly(His)/SPGE (b, d) at 5,000X (a, b), and 10,000X (c, d).

the number of cycles scans increased, this defined-peak current gradually decreased, indicating the formation of a polymer coating at the electrode surface. After the modification step, the modified electrode was rinsed with DI water and allowed to dry at room temperature. Finally, poly(His)/SPGE was obtained and kept in a ziplock bag in a dark and dry location. The overall fabrication and electrochemical measurement processes of the proposed sensor are presented in Scheme 1.

2.3. Electrochemical measurement

All measurements were performed using a three-electrode system with poly(His)/SPGE as the WE, graphene ink as the CE, and Ag/AgCl as the RE and were repeated at least three times at room temperature. For the electrochemical measurement, 100 μL of standard Tyr solution in 0.1 M PBS (pH 7.4) was dropped onto the electrode surface area. CV was employed for the study of the electrochemical behavior of Tyr. The potential range of 0.0 to +1.2 V vs. Ag/AgCl at a scan rate of 0.075 Vs^{-1} was set. DPV was optimized and used for the determination of Tyr. All parameters of DPV were successfully achieved by scanning the potential in the range of 0.0 to +0.6 V vs Ag/AgCl with a pulse width of 0.025 s, an amplitude of 0.2 V, an increment of 0.01 V, and a pulse period of 0.5 s.

The EIS measurements were performed in 5 mM $K_3[Fe(CN)_6]$ with a potential range of 0.0–0.1 V, a frequency range of 0.01 Hz to100 kHz, and an amplitude of 0.1 V, as well as 5 mM $[Ru(NH_3)_6]Cl_3$ in 0.1 M KCl with a potential range from −0.1 to 0.1 V, a frequency range of 0.01 Hz to 100 kHz, and an amplitude of 0.1 V.

2.4. Real-sample preparation

The practical applications of the proposed poly(His)/SPGE were investigated using three different types of real samples, namely, urine, serum, and cheese samples.

All biological samples were well received by volunteers who gave their consent to participate in the trial. Urine samples were obtained from healthy human volunteers in our laboratory, and serum samples were obtained from healthy patients. To eliminate particulates, urine sample solutions were filtered through a 0.45 μm Millipore membrane. On the other hand, serum sample was utilized without any purification process. Different concentrations of standard Tyr with an appropriate calibration curve were separately spiked into biological samples and then diluted 50 and 100 times (1000 μL) with supporting electrolyte (0.1 M PBS, pH 7.4) for the urine and serum samples, respectively.

Cheese samples (candy cheese pain, mozzarella cheese, and cheddar cheese) were obtained from local supermarkets in Thailand. Cheese samples were performed according to the published literature [42]. The aliquots of each homogenized sample (2.5 g) were transferred into 15-mL plastic centrifuge tubes, and 5 mL of PBS (0.1 M, pH 7.4) was added and mixed for 2 min using a vortex. The mixture was placed in an ultrasonic bath for 20 min and centrifuged for 10 min at 3000 rpm. The supernatant was collected, and the process was performed two more times. Finally, the extracts were collected and made up to volume in a 25-mL volumetric flask with PBS. Before analysis, different concentrations of standard Tyr with an appropriate calibration curve were spiked into 100 μL cheese sample solution and diluted to 1000 μL with supporting electrolyte (0.1 M PBS, pH 7.4).

3. Results and discussion

3.1. Characterization of bare SPGE and poly(His)/SPGE

As illustrated in Fig. 1, the surface morphologies of bare SPGE and poly(His)/SPGE were investigated using a SEM. The SEM images of bare SPGE, as presented in Fig. 1a and c (at 5,000X and 10,000X magnification, respectively), exhibited a rough and wrinkled surface, uniformly

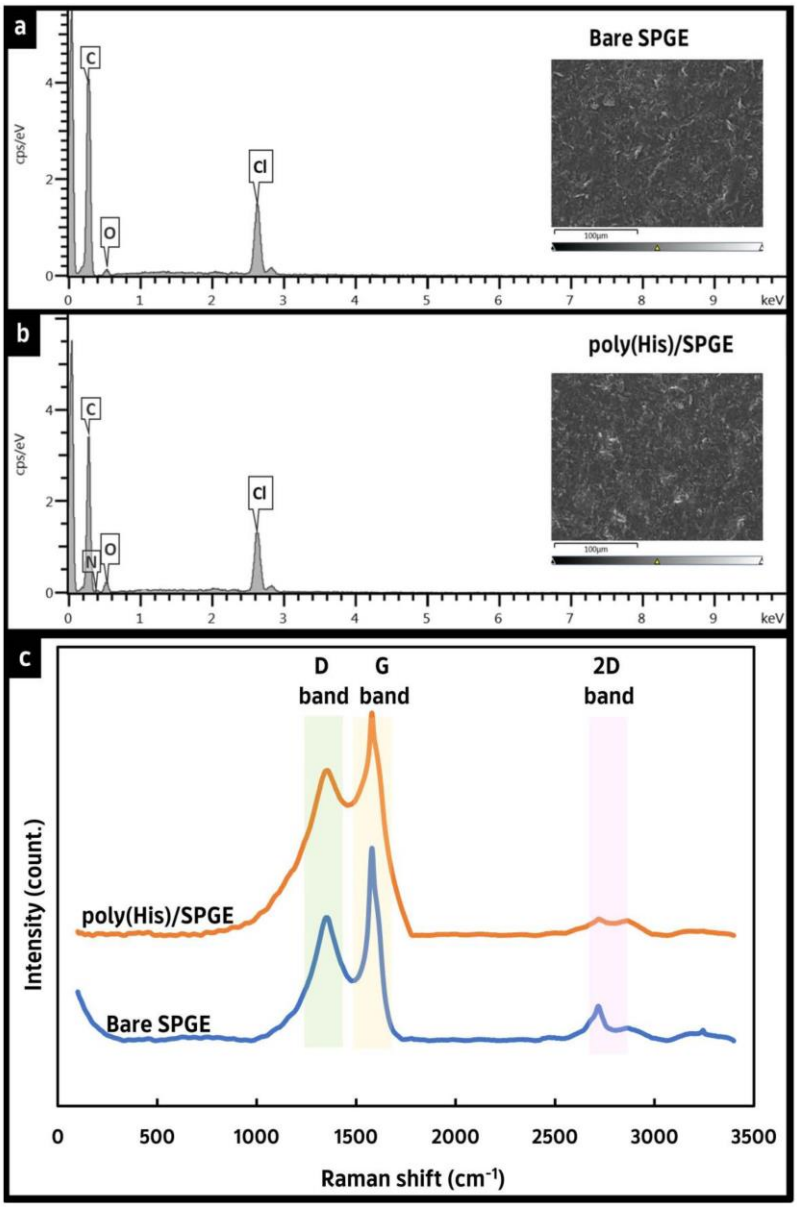

Fig. 2. The SEM-EDS analysis of bare SPGE (a) and poly(His)/SPGE (b) and Raman spectra of both unmodified and modified SPGE (c).

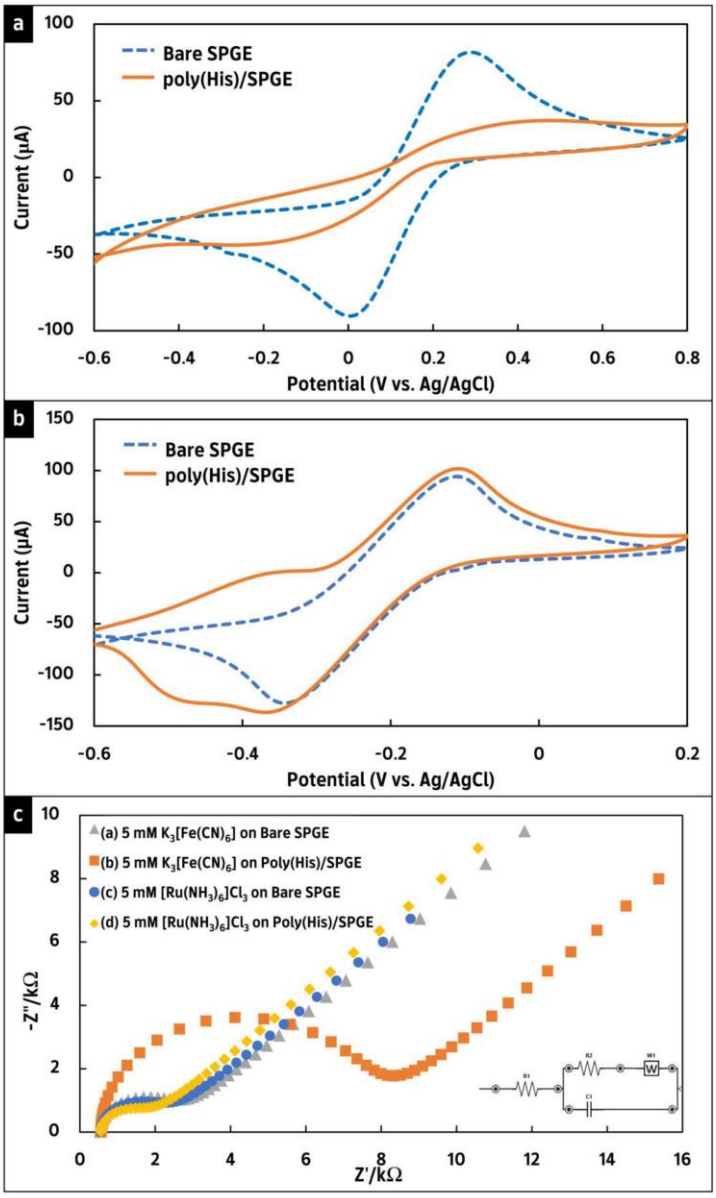

Fig. 3. Cyclic voltammograms of both bare SPGE and poly(His)/SPGE in (a) 5 mM $Fe(CN)_6^{3-/4-}$ in 0.1 M KCl (potential ranges from −0.60 to +0.80 V, scan rate 0.075 V s^{-1}), (b) 5 mM $Ru(NH_3)_6^{3+}$ in 0.1 M KCl (potential ranges from −0.60 to +0.20 V, scan rate 0.075 V s^{-1}) and (c) EIS curves of bare SPGE and poly(His)/SPGE in 5 mM $Fe(CN)_6^{3-/4-}$ (curve a and b) and 5 mM $Ru(NH_3)_6^{3+}$ (curve c and d).

distributed particles, and a stack of graphene layers. After the modification of poly(His) onto SPGE, the electrode surface (Fig. 1b and d at 5000X and 10,000X magnification, respectively) displayed a relatively smooth surface and a more film-like texture than the bare SPGE surface. This phenomenon indicated that the bare SPGE surface is completely covered by the polymeric thin film of poly(His).

Scanning electron microscopy and energy-dispersive X-ray spectrometry (SEM-EDS) as well as Raman spectroscopy were employed to confirm the presence of poly(His) on the SPGE surface, as presented in Fig. 2. The constituent elements of bare SPGE and poly(His)/SPGE were identified using the SEM-EDS technique, as presented in Fig. 2a and b, respectively. The C, O, and Cl elements, which are related to the composition of graphene ink, were present in the bare SPGE. Meanwhile, the SEM-EDS analysis of modified poly(His) onto SPGE was similar to that of bare SPGE, with the exception that the distinguishing peak due to the N atom significantly increased when the histidine molecule was used as a monomer. This indicated that a poly(His) layer had indeed been applied to the SPGE surface. Furthermore, the Raman spectra in Fig. 2c indicated the characteristic G (~1582.39 cm^{-1}) and 2D (~2718.76 cm^{-1}) bands and a D peak at 1350 cm^{-1} for bare SPGE (blue line). The appearance of the D band could be due to the low defect content of the graphene layers during the manufacturing process of graphene ink [43,44]. Interestingly, poly(His)-modified SPGE (orange line) revealed not only increased intensities of two characteristic bands but also a sharp, intense peak at 1579.44 cm^{-1}, corresponding to the C=C stretching vibration of the imidazole ring at pH ~ 7 [45,46]. The disordered level of the graphene structure was calculated using the intensity ratio of D and G bands (I_D/I_G). The intensity ratio value was found to increase from 0.63 to 0.74 after modification with poly(His), indicating the higher disorder level of modified graphene [47]. The results clearly indicated that the electropolymerization of L-histidine was successfully modified on the SPGE surface.

In addition, we have focused on the use of different amino acid-based polymers to develop highly sensitive and selective detection of Tyr. Based on the variable functional group on the side chain, we selected some amino acids in each category: electrically side chain, polar side chain, and non-polar side chain to modify the SPGE. As shown in Fig. S2, the SPGE modified with poly(histidine) was found to provide the highest current compared to the other amino acid-based polymer modified electrodes. As a result, we believe that the histidine monomer is a potential amino acid for fabricating the polymer in order to improve the sensitivity and selectivity of Tyr detection.

3.2. Electrochemical characterization of poly(His)/SPGE

To investigate the electrochemical performance of bare SPGE and poly(His)-modified SPGE, the CV and EIS measurements were performed by using both an anionic ($Fe(CN)_6^{3-/4}$) redox probe and a cationic ($Ru(NH_3)_6^{3+}$) redox probe. The cyclic voltammogram of 5-mM $Fe(CN)_6^{3-/4}$ in 0.1 M KCl exhibited two well-defined peaks at potentials of +0.280 and +0.004 V at bare electrode, as presented in Fig. 3a (dash line). On the other hand, the redox behaviors of $Fe(CN)_6^{3-/4}$ were significantly reduced and broadened after the modification of electropolymerization of L-histidine on the SPGE surface. In addition, the peak currents decreased while the peak potential increased up to +0.357 V (straight line). This poor electrochemical response of $Fe(CN)_6^{3-/4}$ derived from poly(His)/SPGE suggested that an electrostatic repulsion force existed between the negatively charged carboxylic group in the poly(His) thin film and the anionic redox probe. Meanwhile, a cyclic voltammogram of bare and modified SPGE using 5 mM $Ru(NH_3)_6^{3+}$ in 0.1 M KCl provided a pair of redox peaks at potentials of −0.327 and −0.125 V, correlating with the redox reaction of this electroactive probe. When the electrochemical properties of the bare (dash line) and modified electrodes (straight line) were compared, the poly(His)/SPGE electrode demonstrated minor changes in the peak current and an ΔE shift to a more positive potential (from +0.202 to +0.256 V), as presented in Fig. 3b. This phenomenon can be explained by the electrostatic interaction between negatively charged carboxyl groups on the surface of the poly(His) film and the cationic redox probe. The anionic behavior of L-histidine polymeric film may be attributed to the most abundant carboxyl groups on the polymer backbone, which are derived from both the L-histidine monomer's characteristics and the over-oxidized imidazole side chain [48]. As a result, the electrochemical behavior of $Ru(NH_3)_6^{3+}$ on poly(His)/SPGE improved the electron-transfer process at the electrode–solution interface.

To gain a better understanding of electron-transfer processes, EIS was employed to characterize unmodified and modified poly(His) on SPGE using both $Fe(CN)_6^{3-/4}$ and $Ru(NH_3)_6^{3+}$ as electroactive probes. In the Nyquist plot, the length of the semicircle diameter corresponds to the electron-transfer resistance (R_{et}) at the electrode–solution interface. The calculated R_{et} values for bare SPGE and poly(His)/SPGE using 5 mM $Fe(CN)_6^{3-/4}$ as a redox probe were 1.60 and 11.5 kΩ, respectively. On the other hand, the calculated R_{et} values of 5 mM $Ru(NH_3)_6^{3+}$ at the bare electrode and modified electrode were found to be 1.85 and 1.15 kΩ, respectively. As presented in Fig. 3c, the bare SPGE when using anion (curve a) and cation (curve c) redox probes exhibited a similar behavior as a small length of semicircle diameter, indicating good graphene conductivity. When comparing the bare electrode with the modified polymer of L-histidine on SPGE, the length of the semicircle diameter of $Fe(CN)_6^{3-/4}$ was significantly increased (curve b), whereas the semicircle diameter of $Ru(NH_3)_6^{3+}$ was slightly decreased (curve d). The increased impedance at the modified electrode when using $Fe(CN)_6^{3-/4}$ arises from the electron-transfer process at the interface was hindered. This was attributed to the strong electrostatic repulsion between the carboxyl groups of the poly(His) film and the negatively charged redox indicator ferricyanide, which was in good agreement with the CV data presented in Fig. 3a. On the other hand, the R_{et} value when using the cationic electroactive probe at the modified electrode was smaller than that of a bare SPGE, indicating that the polymeric film of L-histidine has a higher electroactive surface coverage and excellent electrocatalytic activities, which improves the electron-transfer process at the electrode interface. As a result, $Ru(NH_3)_6^{3+}$ was selected as a redox probe for the investigation of properties obtained from poly(His)/SPGE.

The electroactive surface areas of bare SPGE and poly(His)/SPGE were then measured using the CV technique at different scan rates with 5-mM $Ru(NH_3)_6^{3+}$(Fig. S3). For a reversible process, the Randles–Sevcik equation was used to calculate the electroactive surface areas, as shown below [49]:

$$I_{pa} = \left(2.69 \times 10^5\right) n^{3/2} A C_0^* D_0^{1/2} \upsilon^{1/2}$$

where I_{pa} denotes the anodic peak current; n, the number of electron involved in the redox process; A, an electroactive surface area of electrode (cm^2); C_0^*, the concentration of $Ru(NH_3)_6^{3+}$(mol cm^{-3}); D_o (cm^2 s^{-1}), the diffusion coefficient; and υ (V s^{-1}), the scan rate.

For 5 mM $Ru(NH_3)_6^{3+}$ in 0.1 M KCl as supporting electrolyte, the n and D_o values were 1 and 8.43×10^{-6} cm^2 s^{-1}, respectively [50]. Therefore, the electroactive surface areas were found to be 0.066 and 0.074 cm^2 for the bare SPGE and poly(His)/SPGE, respectively. This indicates that the electroactive surface area for the modified electrode is 1.12 times higher than that of the bare SPGE. Based on the findings, we believe that the polymer layer on the electrode's surface was responsible for the enhancement of active sites.

The total surface coverage (Γ) was derived from the charge concentration (Q) according to the relationship described in the equation to estimate the surface coverage of the bare electrode and polymer film on the modified electrode [51]:

$$\Gamma = \frac{Q}{nFA}$$

where Γ is the total surface coverage (mol cm^{-2}); Q, the charge obtained from the anodic peak area of the supporting electrolyte (0.1 M PBS, pH

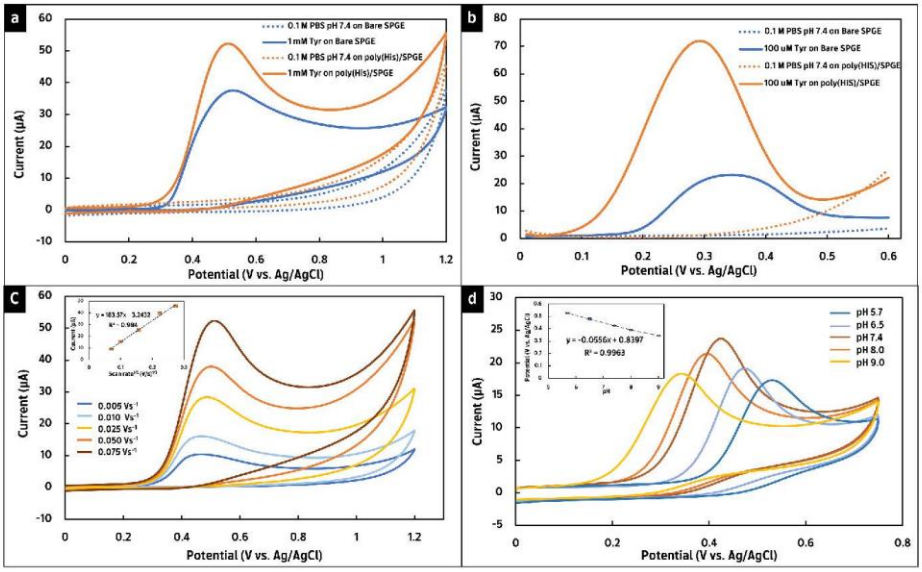

Fig. 4. (a) CV curves of 1-mM Tyr in 0.1 M PBS (pH 7.4) at bare SPGE and poly(His)/SPGE (scan rate of 0.075 Vs^{-1}), (b) DPV curves obtained for comparing both of bare SPGE and poly(His)/SPGE in 100 µM Tyr containing 0.1 M PBS (pH 7.4), (c) CV curves of 1 mM Tyr in 0.1 M PBS (pH 7.4) at different scans rate using poly(His)/SPGE (inset presents dependence of the anodic peak current on the square root of the scan rate). and (d) CV curves of 1 mM Tyr obtained for varying pH conditions.

7.4); *n*, the number of involved electrons; *F*, Faraday's constant (96,485.34 C mol ^{1}); and A, the electroactive surface area. The calculated surface coverages of bare electrode and poly(His)/SPGE were found to be 1.55×10^{10} and 7.84×10^{10} mol cm ^{2}, respectively. The increased electroactive surface coverage can be attributed to the existence of a polymeric histidine film on the SPGE surface.

3.3. *Electrochemical behavior of Tyr on poly(His)/SPGE*

The electrochemical responses of Tyr detection were investigated using bare SPGE and poly(His)/SPGE *via* CV and DPV. The CV curves of 1-mM Tyr in 0.1 M PBS (pH 7.4) at the bare electrode and poly(His)/SPGE are presented in Fig. 4a. It can be noticed that the electrooxidation of Tyr occurred at a potential of +0.51 V at an unmodified and a modified electrode. When compared with the bare SPGE (blue line), the characteristics of Tyr at poly(His)/SPGE (orange line) were sharper and had a higher peak current. Moreover, the occurrence of a single anodic peak indicated that the electrochemical reaction of Tyr was completely an irreversible process. The obtained results were consistent with those of the previous study [52]. For the DPV measurements, as presented in Fig. 4b, the electrooxidation peaks of Tyr were observed at potentials of +0.34 and +0.29 V for bare SPGE (blue line) and poly(His)/SPGE (orange line), respectively. Furthermore, the peak current at poly (His)/SPGE was nearly three times that of bare SPGE. These results indicate that the polymeric film of L-histidine on SPGE exhibits electrocatalytic activity in terms of the improvement of the electron-transfer processes between the electrode surface and electroactive species in the solution. This enhancement in electron-transfer kinetics could be attributed to the high conductivity of poly(His)/SPGE, which contains the carboxyl groups on the polymeric L-histidine backbone [53].

To investigate the electron-transfer kinetics of Tyr, the effect of scan rate at poly(His)/SPGE was measured *via* CV, and the results are presented in Fig. 4c. The electrooxidation current of Tyr was found to increase at a scan rate of 0.005 to 0.075 Vs ^{1}. With an increased scan rate, the oxidation potential shifted to the positive direction, indicating that the electrooxidation of Tyr was an irreversible process. However, a linear relationship was observed between the oxidation currents and the square root of the scan rate ($\upsilon^{1/2}$) (presented in the inset in Fig. 4c), which suggested a diffusion-controlled electrochemical process. A diffusion-controlled electrochemical process was also elucidated using the plot of log Ip versus log υ (Fig. S4(a)). The slope of 0.5907 was consistent with the theoretically expected value of 0.5, confirming that the electrooxidation of Tyr was controlled by the diffusion process [54]. Furthermore, using the theoretical model described by Andrieux and Savèant, the information obtained from the relationship between I_{pa} and the $\upsilon^{1/2}$can be used to determine the diffusion coefficient (D_0) of Tyr.

$$I_{pa} = 0.496FAC_0^{*}\left(\frac{F}{RT}\right)^{1/2}\upsilon^{1/2}$$

where I_{pa} denotes the anodic peak current of Tyr; F, Faraday's constant (96,485.34 C mol ^{1}); A, the electroactive surface area (0.074 cm^2); C, the concentration of Tyr (1×10^{6} mol cm ^{3}); R, the gas constant (8.31447 J mol ^{1}K ^{1}); T, the absolute temperature (298 K); and υ, the scan rate. The plot of the electrooxidation current of Tyr versus $\upsilon^{1/2}$ (inset Fig. 4c) provided the linear regression of $y = 183.57x - 3.2432$ ($R^2 = 0.994$). Hence, the calculated D_0 of Tyr was found to be 6.84×10^{5} cm^2 s ^{1}.

$$E_{pa} = E^{0} + \frac{RT}{(1-\alpha)nF}\ln\frac{RTk_s}{(1-\alpha)nF} + \frac{RT}{(1-\alpha)nF}\ln\upsilon$$

$$I_{pa} = \left(2.99 \times 10^{5}\right) n[(1-\alpha)n_{\alpha}]^{1/2}AC_sD_0^{1/2}\upsilon^{1/2}$$

It is important to determine the factor of $(1\text{-}\alpha)n_{\alpha}$ before estimating

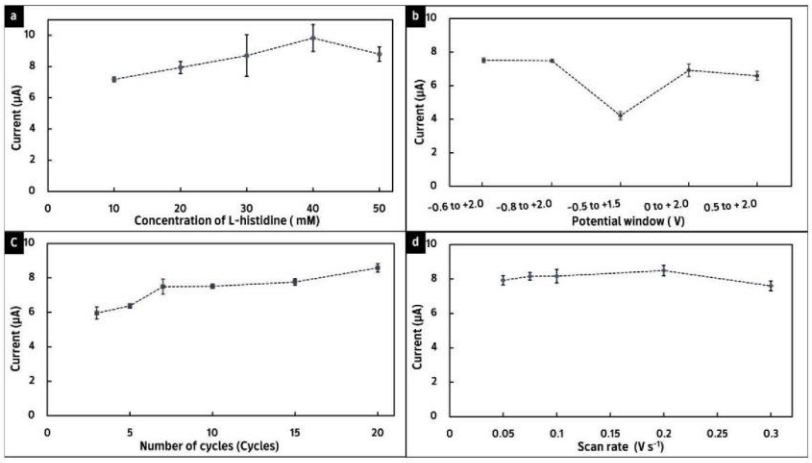

Fig. 5. The influent of electro-polymerization process included (a) concentration of L-histidine, (b) suitable potential windows, (c) number of cycle scans and (d) scan rate.

the number of electrons in the irreversible process. As presented in Fig. S4 (b), the calculation is based on a linear relationship between E_{pa} and ln υ ($y = 0.0317x + 0.5967$; $R^2 = 0.9828$). Hence, the calculated factor of $(1\text{-}\alpha)n_\alpha$ was found to be 0.81. As a result, the number of electrons involved in the electrooxidation of Tyr was calculated to be 1.11 (n ~ 1). The electrochemical behavior of Tyr under various pH conditions can be used to determine the number of protons involved in the electrooxidation process. In Fig. 4d, the oxidation peak potentials (E_{pa}) of Tyr at poly(His)/SPGE in the pH range of 5.7−9.0 clearly shifted to the negative direction as the pH values increased. This is a consequence of the protonated form of Tyr involved in the oxidation process that could be facilitated the electron-transfer process at higher pH values (pK_a values of Tyr ~9.66 and ~10.41). Tyr is fully protonated at a pH of around 7, indicating the existence of a positively charged amine group in the Tyr structure, since this pH value is lower than the actual pK_a for an amine group. As a result, the maximum peak current was observed at pH 7.4 for the Tyr detection. We believe that the protonated forms of Tyr at pH 7.4 fully interacted electrostatically with the carboxylic groups on the polymer backbone. Therefore, PBS at pH 7.4 was selected as the supporting electrolyte. Furthermore, the Nernst equation was used to characterize the linear relationship between the pH values and oxidation peak potentials ($y = -0.0556x + 0.8397$; $R^2 = 0.9963$). The numbers of electrons and protons at the electrode interface were denoted by m and n, respectively. The slope was found to be 0.0556, which was close to the theoretical value of 0.0591. This suggested that the numbers of electrons and protons transferred at the electrode interface were equal, indicating that $m = n = 1$. Thus, one electron and one proton were involved in the electrooxidation of Tyr at poly(His)/SPGE, a finding consistent with those of previous studies [55].

3.4. Optimization of electropolymerization of L-histidine and electrochemical detection

To achieve excellent sensitivity and analytical performance for the detection of Tyr, several parameters in the electropolymerization process were examined. The electrochemical response of the target analyte was influenced by the thickness of the polymeric film. Consequently, the monomer concentration and the number of cycle scans were systematically investigated to obtain the optimal polymeric film thickness for the Tyr sensor. Fig. 5a and c illustrate the concentration of L-histidine and the number of cycle scans, respectively. For the monomer concentration, the peak current increased up to 40 mM and decreased thereafter. This might be due to the formation of a nonuniform polymeric layer. Meanwhile, a high electrochemical response was obtained when the number of cycle scans was set to 20. This means that a 20-cycle scan is sufficient to generate a polymeric histidine film on the SPGE surface that could accelerate the electron-transfer at the electrode interface. Therefore, 40 mM of L-histidine and 20 cycles were selected as the optimized conditions for electropolymerization for further experiments.

The potential windows and scan rate affected the rates of the electrochemical reaction, film thickness, and dopant contents. Hence, the suitable applied potential windows and scan rate of the electropolymerization process were also investigated. The potential ranges (Fig. 5b) were first fixed between −0.8 and +2.0 V; this finding could be used for the Tyr detection. However, this potential range resulted in a delay in the generation of a polymeric film onto the SPGE surface. We also attempted to shift the final potential to a more negative direction. It was found that when the applied potentials were scanned from −0.8 to +1.5 V, the current for Tyr decreased. This implies that the final potential for the electropolymerization process must be higher than +1.5 V to ensure the oxidation of L-histidine. This phenomenon may be due to the fact that the imidazole groups of poly(His) can be overoxidized at higher anodic potentials, resulting in the introduction of carbonyl and carboxyl groups to the polymer skeleton, which can induce diffusion of the target analyte into the electrode interface [56]. As a result, the final potential was set to +2.0 V, and the initial potential gradually shifted to a more positive direction. Surprisingly, when the initial potential was applied at −0.6 V, the signal current of Tyr was the highest. Therefore, an applied potential in the range of −0.6 to +2.0 V was selected for the electropolymerization process for further experiments. The Tyr responses for the formation of poly(His) film are presented in Fig. 5d using a different scan rate. It was observed that a scan rate of 0.2 Vs^{-1} exhibited a high sensitivity of the Tyr response due to the formation of a uniform polymeric layer. Therefore, the scan rate of 0.2 Vs^{-1} was selected for the electropolymerization process because this condition

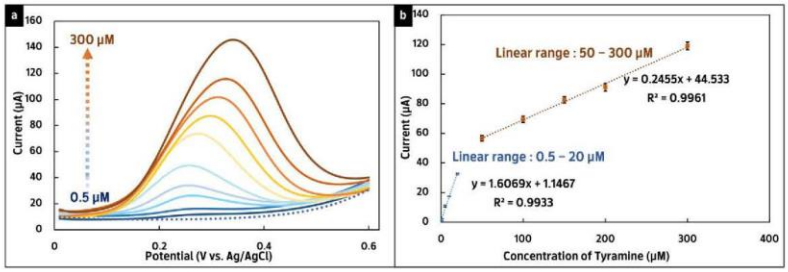

Fig. 6. (a) DPV signals for different concentrations of Tyr at poly(His)/SPGE. (b) calibration plot between peak current and Tyr concentration.

offered the maximum current within a reasonable time duration for the modification process.

Furthermore, the electrochemical conditions in DPV are a crucial parameter that can affect the Tyr peak shape and peak current. All parameters of the DPV, including increment, amplitude, pulse width, and pulse period, were systematically examined *via* DPV using 100 µL of Tyr in 0.1 M PBS at pH 7.4. The optimum currents were detected at pulse width of 0.025 s, amplitude of 0.2 V, increment of 0.01 V, and pulse period of 0.5 s, which offered the best analytical performance for Tyr monitoring (Fig. S5).

3.5. Analytical performances

Under optimal conditions, the DPV technique was performed for the quantitation of Tyr, and the results are presented in Fig. 6. The linear concentration ranges (Fig. 6 (b)) were found to be 0.5–20 and 50–300 µM with a linear regression equation of $I_{pa} = 1.6069\ C_{Tyr} + 1.1467$ ($R^2 = 0.9933$) and $I_{pa} = 0.2455\ C_{Tyr} + 44.533$ ($R^2 = 0.9961$), respectively. The limit of detection (LOD) was estimated to be 0.065 µM based on 3SD/m, where SD denotes the standard deviation of 10 replicate measurements of a blank (0.1 M PBS, pH 7.4), and m denotes the slope of the calibration curve. The analytical performance of poly(His)/SPGE for Tyr determination was compared with other electrode characteristics listed in Table S1. The novel sensor based on the polymeric film of L-histidine exhibited better performance in some cases or was comparable with the other Tyr sensors reported so far, with a low LOD and a sufficiently wide linear range. Furthermore, when compared with other architectures that used complex materials, multiple and complicated processes, and/or enzyme immobilization, the proposed sensor proved its ease of fabrication by requiring only a single step of modification directly onto the electrode surface. Therefore, this produced sensor is not only sensitive enough for clinically significant Tyr monitoring in real samples; it also offers good potential for on-site and real-time analysis.

To verify the performance of the proposed sensor, the precision in terms of reproducibility was investigated by determining the Tyr response at seven modified electrodes. The relative standard deviation (RSD) was calculated to be 1.23%, which indicated an excellent reproducibility. Furthermore, the long-term stability of poly(His)/SPGE was evaluated by measuring the response currents toward 100 µM of Tyr in 0.1 M PBS (pH 7.4) at 7-day intervals. The prepared poly(His)/SPGE were kept in a ziplock at room temperature before use. As presented in Fig. S6, the electrooxidation currents of Tyr could remain at 90.75% of their initial current response, after 35 days, indicating good stability of the fabricated sensor.

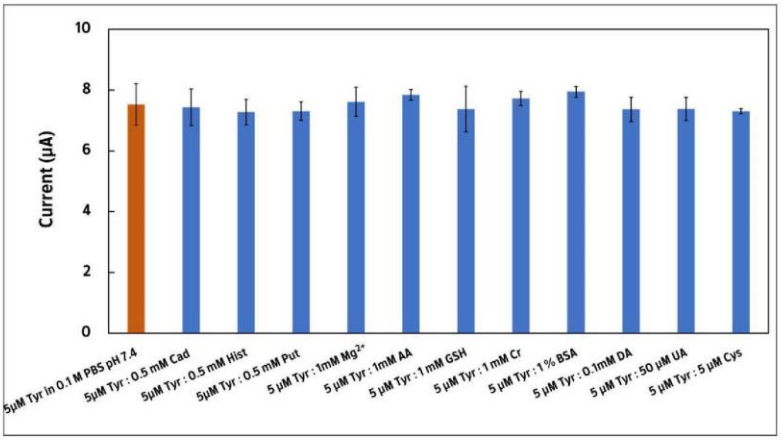

Fig. 7. The effect of interferents on the anodic peak current of 5 µM Tyr at poly(His)/SPGE (n 3).

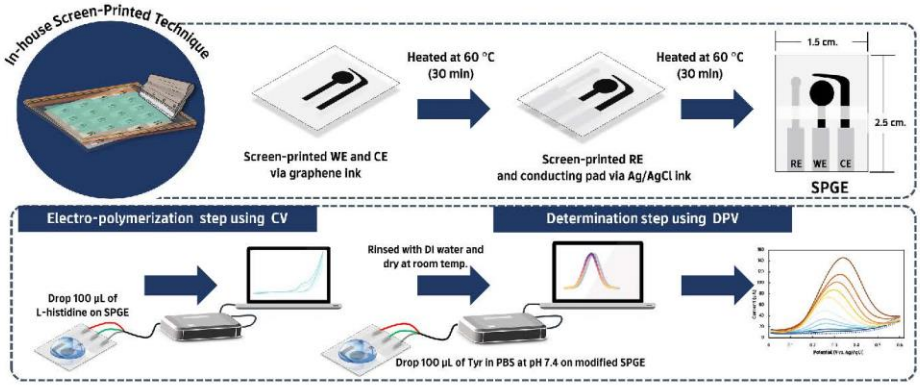

Scheme 1. Schematic representation of the fabrication and electrochemical detection procedures for the Tyr quantification using poly(His)/SPGE.

Table 1
The practical applications of poly(His)/SPGE for monitoring Tyr in real samples (n 3).

Real Samples	Spiked (µM)	Found (µM)	Recovery (%)	RSD (%)
Human urine sample 1	1	0.95 ± 0.03	95.32	2.59
	5	5.48 ± 0.10	109.66	1.78
	10	10.74 ± 0.04	107.43	0.28
	15	14.36 ± 0.14	95.72	0.93
Human urine sample 2	1	1.04 ± 0.13	104.04	8.03
	5	5.49 ± 0.23	109.75	3.67
	10	10.48 ± 0.66	104.79	5.86
	15	14.52 ± 0.25	96.77	1.65
Human serum sample	1	1.06 ± 0.02	105.68	1.45
	5	5.26 ± 0.12	105.26	2.25
	10	10.23 ± 0.23	102.30	2.27
	15	15.37 ± 0.22	102.44	1.43
Candy cheese plain	1	1.34 ± 0.05	83.01	1.95
	5	5.42 ± 0.07	98.19	1.09
	10	9.82 ± 0.46	93.08	3.96
	15	14.96 ± 0.48	96.29	2.79
Mozzarella cheese	1	1.60 ± 0.11	95.61	2.94
	5	5.38 ± 0.09	94.75	1.13
	10	9.48 ± 0.08	88.37	0.70
	15	15.18 ± 0.41	96.86	2.34
Cheddar cheese	1	2.05 ± 0.12	82.58	3.13
	5	5.49 ± 0.33	85.27	4.59
	10	9.76 ± 0.40	85.34	3.52
	15	14.93 ± 0.42	91.37	2.55

3.6. Interference study

To study the selectivity of the proposed sensor, the presence of Tyr in various concentration ratios of interfering substances was investigated *via* DPV. The possible interfering substances were Mg^{2+}, ascorbic acid (AA), glutathione (GSH), creatinine (Cr), bovine serum albumin (BSA), dopamine (DA), uric acid (UA), cysteine (Cys), which are abundant in biological samples. Furthermore, some BAs such as cadaverine (Cad), histamine (Hist) and putrescine (Put), which are commonly found in cheese samples, were considered. The measurements were performed in 5 µM Tyr with co-existing concentrations of 1 mM for Mg^{2+}, AA, GSH, and Cr, 1% for BSA, 0.1 mM for DA, 50 µM for UA, 5 µM for Cys, and 0.5 mM for Cad, Hist, and Put. No significant change was observed in the current (less than ±5%), as presented in Fig. 7. This indicated that poly (His)/SPGE has an excellent selectivity toward the determination of Tyr.

3.7. Practical applications in real samples

To illustrate its practical application in real-sample analysis, the Tyr sensor was used in human urine samples, serum samples, and three types of cheese samples. The analytical determination was performed using the standard addition method by spiking the standard Tyr (1, 5, 10, and 15 µM) in real samples. The values calculated based on the average of three replicates are presented in Table 1. The recovery and RSD values (%) were obtained in the acceptable value ranges of 82.58%–109.75% and 0.28%–8.03%, respectively. Moreover, the quantities of Tyr were found to be 7.03, 8.86, and 16.77 mg/kg in candy cheese plain, mozzarella cheese, and cheddar cheese, respectively. These findings indicate that poly(His)/SPGE has sufficient sensitivity, selectivity, and reliability for detecting the presence of Tyr in biological and food samples.

4. Conclusion

For the first time, a novel electrochemical sensor based on poly(His)-modified SPGE was proposed to sensitively and selectively detect the Tyr content. The polymeric film based on L-histidine was simply synthesized and deposited onto the SPGE surface through a single step of electro-polymerization. This poly(His) exhibited a remarkable electrocatalytic performance by promoting the electron-transfer process at the electrode–solution interface, which in turn allowed better sensitivity and selectivity. Under optimal conditions, the proposed electrochemical sensing offers a broad linear range with a low LOD. Furthermore, this developed sensor was successfully used to determine the Tyr levels in both biological fluids and cheese samples with acceptable recoveries, showing promise for application in clinical functions as well as food quality and safety control. Its advantages include cost-effectiveness, simple fabrication, ease of use, fast response, and suitability for on-field and routine detections, making it a promising alternative tool for Tyr analysis in practical applications.

CRediT authorship contribution statement

Kantima Kaewjua: Conceptualization, Methodology, Validation, Investigation, Formal analysis, Writing – original draft, Visualization. **Weena Siangproh:** Conceptualization, Investigation, Resources, Writing – review & editing, Supervision, Project administration, Funding acquisition.

Declaration of Competing Interest

The authors declare that they have no known competing financial interest or personal relationship that could have appeared to influence the work reported in this paper.

Acknowledgments

KK would like to thank the financial support from the National Research Council of Thailand (NRCT) through the Royal Golden Jubilee PhD program (NRCT5-RGJ63017–151) and WS would like to acknowledge the financial support from the National Research Council of Thailand (NRCT) and Srinakharinwirot University through Research Grants for Talented Mid-Career Researchers (N41A640098). The authors would like to thank Enago (www.enago.com) for the English language review.

Supplementary materials

Supplementary material associated with this article can be found, in the online version, at doi:10.1016/j.electacta.2022.140388.

References

[1] A. Naila, S. Flint, G. Fletcher, P. Bremer, G. Meerdink, Control of biogenic amines in food – existing and emerging approaches, J. Food Sci. 75 (2010) R139–R150.
[2] J.M. Lorenzo, S. Martínez, I. Franco, J. Carballo, Biogenic amine content during the manufacture of dry-cured lacón, a Spanish traditional meat product: effect of some additives, Meat Sci. 77 (2007) 287–293.
[3] E.P.O.B. Hazards, Scientific opinion on risk based control of biogenic amine formation in fermented foods, Efsa J. 9 (2011) 2393.
[4] A. Halász, A. Baráth, L. Simon-Sarkadi, W. Holzapfel, Biogenic amines and their production by microorganisms in food, Trends Food Sci. Technol. 5 (1994) 42–49.
[5] M.S. Santos, Biogenic amines: their importance in foods, Int. J. Food Microbiol. 29 (1996) 213–231.
[6] T. Smith, Amines in food, Food Chem. 6 (1981) 169–200.
[7] V. Ladero, M. Calles-Enríquez, M. Fernández, M.A. Alvarez, Toxicological effects of dietary biogenic amines, Curr. Nutr. Food Sci. 6 (2010) 145–156.
[8] B.J. McCabe-Sellers, C.G. Staggs, M.L. Bogle, Tyramine in foods and monoamine oxidase inhibitor drugs: a crossroad where medicine, nutrition, pharmacy, and food industry converge, J. Food Compos. Anal. 19 (2006) S58–S65.
[9] Y. Özogul, F. Özogul, Biogenic amines formation, toxicity, regulations in food, Biogenic Amines in Food, Analysis, Occurrence and Toxicity (2019) 1–17.
[10] D.M. Linares, B. del Río, B. Redruello, V. Ladero, M.C. Martin, M. Fernandez, P. Ruas-Madiedo, M.A. Alvarez, Comparative analysis of the *in vitro* cytotoxicity of the dietary biogenic amines tyramine and histamine, Food Chem. 197 (2016) 658–663.
[11] M. Yigit, L. Ersoy, Determination of tyramine in cheese by LC–UV, J. Pharm. Biomed. Anal. 31 (2003) 1223–1228.
[12] R. Preti, M.L. Antonelli, R. Bernacchia, G. Vinci, Fast determination of biogenic amines in beverages by a core–shell particle column, Food Chem. 187 (2015) 555–562.
[13] H. Dong, K. Xiao, Modified QuEChERS combined with ultra high performance liquid chromatography tandem mass spectrometry to determine seven biogenic amines in Chinese traditional condiment soy sauce, Food Chem. 229 (2017) 502–508.
[14] C. Almeida, J. Fernandes, S. Cunha, A novel dispersive liquid–liquid microextraction (DLLME) gas chromatography-mass spectrometry (GC–MS) method for the determination of eighteen biogenic amines in beer, Food Control 25 (2012) 380–388.
[15] A. Jastrzębska, A. Piasta, E. Szłyk, Application of ion chromatography for the determination of biogenic amines in food samples, J. Anal. Chem. 70 (2015) 1131–1138.
[16] M.S. Steiner, R.J. Meier, C. Spangler, A. Duerkop, O.S. Wolfbeis, Determination of biogenic amines by capillary electrophoresis using a chameleon type of fluorescent stain, Microchim. Acta 167 (2009) 259.
[17] W. Sheng, C. Sun, G. Fang, X. Wu, G. Hu, Y. Zhang, S. Wang, Development of an enzyme-linked immunosorbent assay for the detection of tyramine as an index of freshness in meat and seafood, J. Agric. Food Chem. 64 (2016) 8944–8949.
[18] B. Zhang, W. Sheng, Y. Liu, N. Huang, W. Zhang, S. Wang, Multiplexed fluorescence immunoassay combined with magnetic separation using upconversion nanoparticles as multicolor labels for the simultaneous detection of tyramine and histamine in food samples, Anal. Chim. Acta 1130 (2020) 117–125.
[19] S. Tajik, A. Lohrasbi-Nejad, P. Mohammadzadeh Jahani, M.B. Askari, P. Salarizadeh, H. Beitollahi, Co-detection of carmoisine and tartrazine by carbon paste electrode modified with ionic liquid and MoO_3/WO_3 nanocomposite, J. Food Meas. Charact. 16 (2022) 722–730.
[20] H. Beitollahi, M. Shahsavari, I. Sheikhshoaie, S. Tajik, P.M. Jahani, S. Z. Mohammadi, A.A. Afshar, Amplified electrochemical sensor employing screen-printed electrode modified with Ni-ZIF-67 nanocomposite for high sensitive analysis of Sudan I in present bisphenol A, Food Chem. Toxicol. 161 (2022), 112824.
[21] F.G. Nejad, I. Sheikhshoaie, H. Beitollahi, Simultaneous detection of carmoisine and tartrazine in food samples using GO-Fe_3O_4-PAMAM and ionic liquid based electrochemical sensor, Food Chem. Toxicol. 162 (2022), 112864.
[22] M. Shahsavari, M. Mortazavi, S. Tajik, I. Sheikhshoaie, H. Beitollahi, Synthesis and characterization of GO/ZIF-67 nanocomposite: investigation of catalytic activity for the determination of epinine in the presence of dobutamine, Micromachines 13 (2022) 88 (Basel).
[23] M. Shahsavari, S. Tajik, I. Sheikhshoaie, F.G. Nejad, H. Beitollahi, Synthesis of Fe_3O_4@ copper (II) imidazolate nanoparticles: catalytic activity of modified graphite screen printed electrode for the determination of levodopa in presence of melatonin, Microchem. J. 170 (2021), 106637.
[24] S. Tajik, M.B. Askari, S.A. Ahmadi, F.G. Nejad, Z. Dourandish, R. Razavi, H. Beitollahi, A. Di Bartolomeo, Electrochemical sensor based on $ZnFe_2O_4$/RGO nanocomposite for ultrasensitive detection of hydrazine in real samples, Nanomaterials 12 (2022) 491.
[25] S. Tajik, H. Beitollahi, S.a. Ahmadi, M.B. Askari, A. Di Bartolomeo, Screen-printed electrode surface modification with $NiCo_2O_4$/RGO nanocomposite for hydroxylamine detection, Nanomaterials 11 (2021) 3208.
[26] S. Tajik, Y. Orooji, Z. Ghazanfari, F. Karimi, H. Beitollahi, R.S. Varma, H.W. Jang, M. Shokouhimehr, Nanomaterials modified electrodes for electrochemical detection of Sudan I in food, J. Food Meas. Charact. 15 (2021) 3837–3852.
[27] M. Baghayeri, M. Namadchian, Fabrication of a nanostructured luteolin biosensor for simultaneous determination of levodopa in the presence of acetaminophen and tyramine: application to the analysis of some real samples, Electrochim. Acta 108 (2013) 22–31.
[28] M. Khan, X. Liu, J. Zhu, F. Ma, W. Hu, X. Liu, Electrochemical detection of tyramine with ITO/APTES/ErGO electrode and its application in real sample analysis, Biosens. Bioelectron. 108 (2018) 76–81.
[29] W. da Silva, M.E. Ghica, R.F. Ajayi, E.I. Iwuoha, C.M. Brett, Impedimetric sensor for tyramine based on gold nanoparticle doped-poly (8-anilino-1-naphthalene sulphonic acid) modified gold electrodes, Talanta 195 (2019) 604–612.
[30] V. Ayerdurai, M. Cieplak, K.R. Noworyta, M. Gajda, A. Ziminska, M. Sosnowska, J. Piechowska, P. Borowicz, W. Lisowski, S. Shao, Electrochemical sensor for selective tyramine determination, amplified by a molecularly imprinted polymer film, Bioelectrochemistry 138 (2021), 107695.
[31] W. da Silva, M.E. Ghica, R.F. Ajayi, E.I. Iwuoha, C.M. Brett, Tyrosinase based amperometric biosensor for determination of tyramine in fermented food and beverages with gold nanoparticle doped poly (8-anilino-1-naphthalene sulphonic acid) modified electrode, Food Chem. 282 (2019) 18–26.
[32] I.P. Soares, A.G. da Silva, R. da Fonseca Alves, R.A.M. de Souza Corrêa, L. F. Ferreira, D.L. Franco, Electrochemical enzymatic biosensor for tyramine based on polymeric matrix derived from 4-mercaptophenylacetic acid, J. Solid State Electrochem. 23 (2019) 985–995.
[33] A. Calvo-Pérez, O. Domínguez-Renedo, M.A. Alonso-Lomillo, M.J. Arcos-Martínez, Disposable amperometric biosensor for the determination of tyramine using plasma amino oxidase, Microchim. Acta 180 (2013) 253–259.
[34] D. Telsnig, K. Kalcher, A. Leitner, A. Ortner, Design of an amperometric biosensor for the determination of biogenic amines using screen printed carbon working electrodes, Electroanalysis 25 (2013) 47–50.
[35] S. He, P. He, X. Zhang, X. Zhang, K. Liu, L. Jia, F. Dong, Poly (glycine)/graphene oxide modified glassy carbon electrode: preparation, characterization and simultaneous electrochemical determination of dopamine, uric acid, guanine and adenine, Anal. Chim. Acta 1031 (2018) 75–82.
[36] E.S. Gomes, F.R. Leite, B.R. Ferraz, H.A. Mourão, A.R. Malagutti, Voltammetric sensor based on cobalt-poly (methionine)-modified glassy carbon electrode for determination of estriol hormone in pharmaceuticals and urine, J. Pharm. Anal. 9 (2019) 347–357.
[37] W. Khamcharoen, C.S. Henry, W. Siangproh, A novel L-cysteine sensor using in-situ electropolymerization of L-cysteine: potential to simple and selective detection, Talanta 237 (2022), 122983.
[38] M.F. Bergamini, D.P. Santos, M.V.B. Zanoni, Electrochemical behavior and voltammetric determination of pyrazinamide using a poly-histidine modified electrode, J. Electroanal. Chem. 690 (2013) 47–52.
[39] S. Tajik, Y. Orooji, F. Karimi, Z. Ghazanfari, H. Beitollahi, M. Shokouhimehr, R. S. Varma, H.W. Jang, High performance of screen-printed graphite electrode modified with Ni–Mo-MOF for voltammetric determination of amaranth, J. Food Meas. Charact. 15 (2021) 4617–4622.
[40] A.G.M. Ferrari, S.J. Rowley-Neale, C.E. Banks, Screen-printed electrodes: transitioning the laboratory in-to-the field, Talanta Open (2021), 100032.

[41] C. Cheng, S. Li, A. Thomas, N.A. Kotov, R. Haag, Functional graphene nanomaterials based architectures: biointeractions, fabrications, and emerging biological applications, Chem. Rev. 117 (2017) 1826–1914.
[42] D. Carelli, D. Centonze, C. Palermo, M. Quinto, T. Rotunno, An interference free amperometric biosensor for the detection of biogenic amines in food products, Biosens. Bioelectron. 23 (2007) 640–647.
[43] K. Krishnamoorthy, M. Veerapandian, G.S. Kim, S.J. Kim, A one step hydrothermal approach for the improved synthesis of graphene nanosheets, Curr. Nanosci. 8 (2012) 934–938.
[44] F.T. Johra, J.W. Lee, W.G. Jung, Facile and safe graphene preparation on solution based platform, J. Ind. Eng. Chem. 20 (2014) 2883–2887.
[45] J.G. Mesu, T. Visser, F. Soulimani, B.M. Weckhuysen, Infrared and Raman spectroscopic study of pH-induced structural changes of L-histidine in aqueous environment, Vib. Spectrosc. 39 (2005) 114–125.
[46] Z. Liu, Z. Xing, Y. Zu, S. Tan, L. Zhao, Z. Zhou, T. Sun, Synthesis and characterization of L-histidine capped silver nanoparticles, Mater. Sci. Eng. C 32 (2012) 811–816.
[47] C. Liu, P. Du, H. Zhao, L. Wang, Synthesis of L-histidine-attached graphene nanomaterials and their application for steel protection, ACS Appl. Nano Mater. 1 (2018) 1385–1395.
[48] X. Liu, L. Zhang, S. Wei, S. Chen, X. Ou, Q. Lu, Overoxidized polyimidazole/graphene oxide copolymer modified electrode for the simultaneous determination of ascorbic acid, dopamine, uric acid, guanine and adenine, Biosens. Bioelectron. 57 (2014) 232–238.
[49] K. Charoenkitamorn, S. Chaiyo, O. Chailapakul, W. Siangproh, Low-cost and disposable sensors for the simultaneous determination of coenzyme Q10 and α-lipoic acid using manganese (IV) oxide-modified screen-printed graphene electrodes, Anal. Chim. Acta 1004 (2018) 22–31.
[50] Y. Wang, J.G. Limon-Petersen, R.G. Compton, Measurement of the diffusion coefficients of $[Ru(NH_3)_6]^{3+}$ and $[Ru(NH_3)_6]^{2+}$ in aqueous solution using microelectrode double potential step chronoamperometry, J. Electroanal. Chem. 652 (2011) 13–17.
[51] D.R. Kumar, S. Kesavan, T.T. Nguyen, J. Hwang, C. Lamiel, J.J. Shim, Polydopamine@ electrochemically reduced graphene oxide-modified electrode for electrochemical detection of free-chlorine, Sens. Actuators B 240 (2017) 818–828.
[52] Z.O. Erdogan, I. Akin, S. Kucukkolbasi, A new non-enzymatic sensor based on TiO_2-Ag/polypyrrole for electrochemical detection of tyramine, Synth. Met. 246 (2018) 96–100.
[53] B. Wang, J.S. Huang, Using poly-L-histidine modified glassy carbon electrode to trace hydroquinone in the sewage water, Int. J. Electrochem. 2014 (2014).
[54] S.N. Azizi, S. Ghasemi, F. Amiripour, Nickel/P nanozeolite modified electrode: a new sensor for the detection of formaldehyde, Sens. Actuators B 227 (2016) 1–10.
[55] S.K. Anand, M.R. Mathew, J. Radecki, H. Radecka, K.G. Kumar, Individual and simultaneous voltammetric sensing of norepinephrine and tyramine based on poly (L-arginine)/reduced graphene oxide composite film modified glassy carbon electrode, J. Electroanal. Chem. 878 (2020), 114531.
[56] Y. Chen, X.M. Liu, X. Wu, X.C. Liu, W.H. Dong, B.K. Han, X. Du, C. Zhang, Y. Y. Zhang, H.T. Wang, Q. Chen, An array of poly-L-histidine functionalized multi-walled carbon nanotubes on 4-aminothiophenol self-assembled monolayer and the application for sensitively glucose sensing, Electrochim. Acta 258 (2017) 988–997.

Supplementary Information

A novel tyramine sensing-based polymeric L-histidine film-coated screen-printed graphene electrode: Capability for practical applications

Kantima Kaewjua, and Weena Siangproh*

Department of Chemistry, Faculty of Science, Srinakharinwirot University, Sukhumvit 23, Wattana, Bangkok 10110, Thailand

*Corresponding author:

E-mail address: weenasi@hotmail.com, weena@g.swu.ac.th

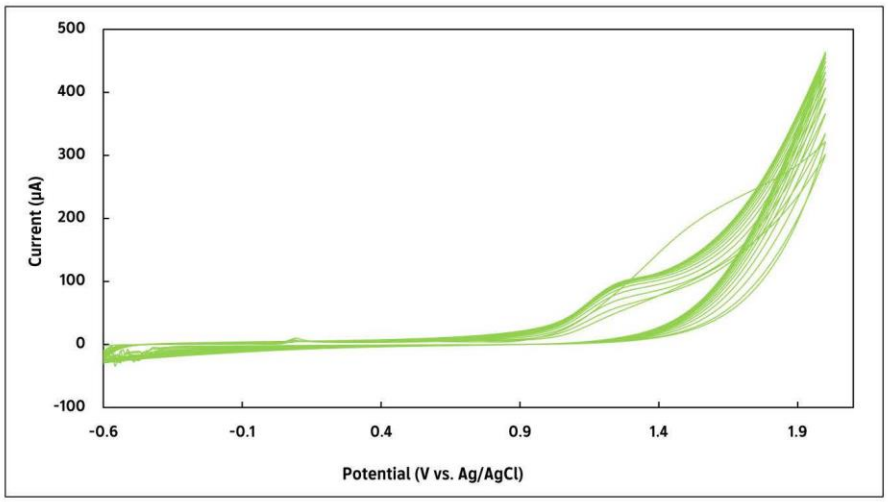

Fig. S1 Cyclic voltammogram of electropolymerization of 40 mM L-histidine in 0.1 M PBS at pH 7.4 (potential ranges from −0.6 to +2.0 V for 20 cycles, scan rate at 0.2 Vs^{-1})

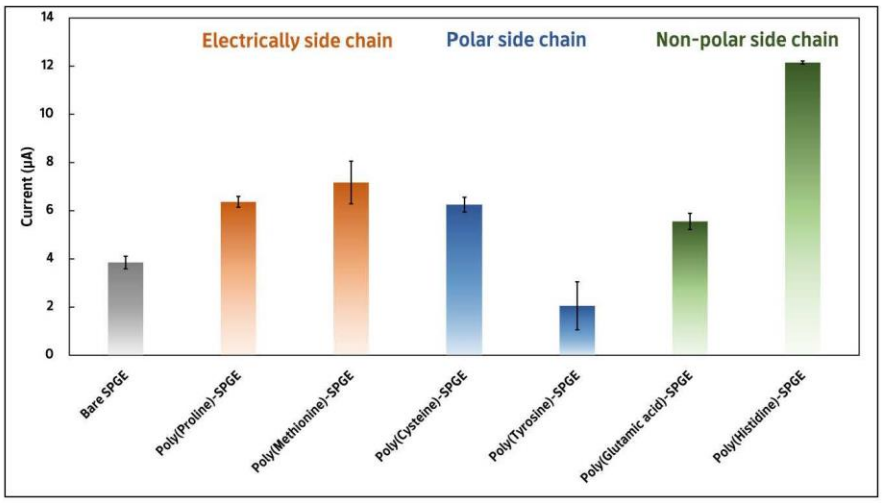

Fig. S2 Preliminary results of DPV signals for 100 µM of Tyr in 0.1 M PBS (pH 7.4) at different amino acids-based polymers modified SPGE (n=3)

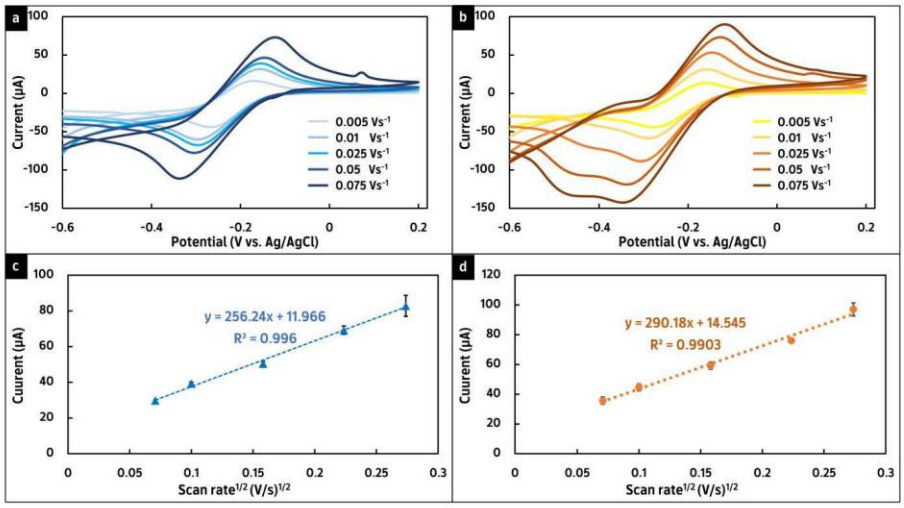

Fig. S3 (a) and (b) represent CV curves for 5-mM $Ru(NH_3)_6^{3+}$ in 0.1 M KCl at bare SPGE and poly(His)/SPGE, respectively. (Potential ranges from −0.65 to +2.0 V at different scan rates). (c) and (d) show the plot of anodic peak current of 5-mM $Ru(NH_3)_6^{3+}$ vs. square root of scan rate at bare SPGE and poly(His)/SPGE, respectively.

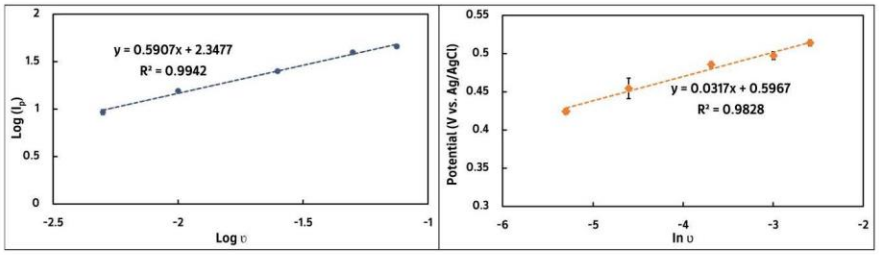

Fig. S4 The linear relationship between (a) log (I_p) and log υ, (b) peak potential (Ep) and ln υ for 1 mM Tyr in 0.1 M PBS (pH 7.4) at poly(His)/SPGE (scan rate (υ); 0.005 to 0.075 Vs^{-1})

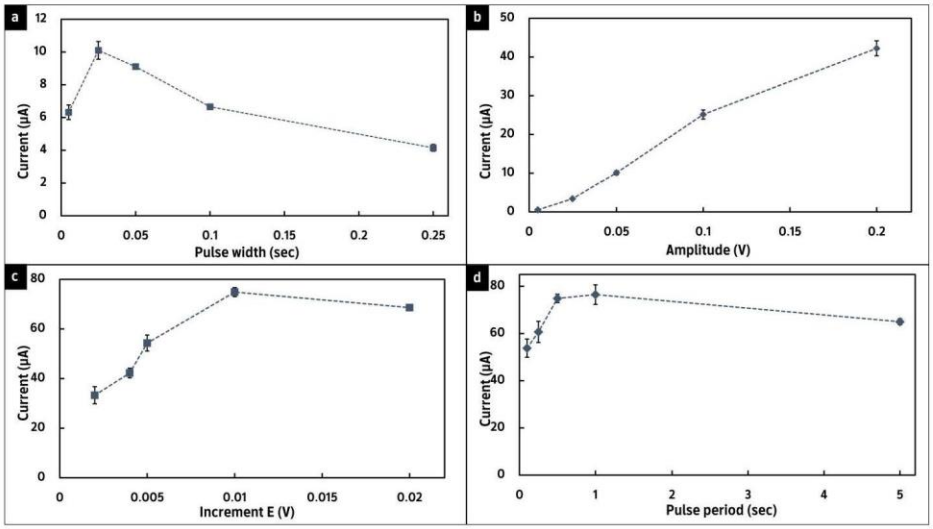

Fig. S5 represents the crucial DPV parameters including (a) pulse width, (b) amplitude, (c) increment E, and (d) pulse period.

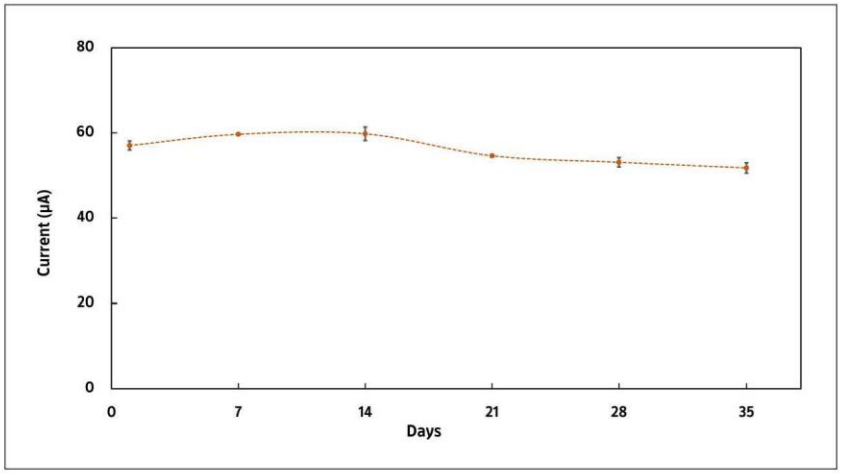

Fig. S6 The study of long-term stability of poly(His)/SPGE

Table S1 Comparison of the tyramine determination performance at the different modified electrodes.

Modification electrode	Technique	Real Samples	Linear range (μM)	LOD (μM)	Ref.
Pea seedling amine oxidase MnO_2/SPCE	Amp	Chicken meat	10–300	3.0	[1]
Q/fMWCNT/GCE	DPV	Yoghurt Urine	0.7 - 75	0.647	[2]
Tyr_{ase}/TiO_2/CMK3/PDDA/Nafion/GE	CV	Camember cheese Sauerkraut Banana	6–130	1.5	[3]
PO_4-Ppy/Pt	Amp	Sauerkrautt	4 -80	0.57	[4]
P3MT/Pt	DPV	Moldy cheese	4.4 - 14000	1.32	[5]
OPOAP/GCE	SWV	Rice vinegar	0.1-200	0.054	[6]
TiO_2-Ag/PPy/GCE	CA	Cheese Sauerkraut	0.04 -3.07	0.02	[7]
AuNP-PANSA/AuE	EIS	Roquefort cheese, Yogurt Red wine Beer	0.8–80	0.04	[8]
P(L-Arg)/ERGO/GCE	DPV	Blood serum Urine	0.6 – 10 and 20 -70	0.145	[9]
PCGE	DPV	Red wines	0.6–100	0.5	[10]

Poly(His)/SPGE	DPV	Urine Serum Cheese samples	0.5- 20 and 50 -300	0.065	**This work**

MnO_2= manganese dioxide; Q/fMWCNT = quercetin on a functionalized multi-wall carbon nanotube; GCE = glassy carbon electrode; Tyr_{ase}= Tyrosinase; SPCE = screen-printed carbon electrode; TiO_2 = titania dioxide sol; PDDA = poly-(diallyl dimethyl ammonium chloride); GE = graphite electrode; PO_4-Ppy = phosphate-doped polypyrrole film;Pt = platinum electrode; P3MT = poly(3-methylthiophene); OPOAP = Overoxidized Poly(o-aminophenol); Ti_2O-Ag = titanium dioxide-silver nanocomposite; Ppy= polypyrrole; AuNP= gold nanoparticle; PANSA= poly-(8-anilino-1-napthalene sulphonic acid); AuE= gold electrode; P(L-Arg)= poly(L-Arginine); ERGO = electrochemically reduced graphene oxide; PCGE = pencil carbon graphite electrode; Amp= Amperometry; CV= Cyclic voltammetry; DPV= Differential pulse voltammetry; EIS = Electrochemical impedance spectroscopy; CA = Chronoamperometry.

References

[1] D. Telsnig, K. Kalcher, A. Leitner, A. Ortner, Design of an Amperometric Biosensor for the Determination of Biogenic Amines Using Screen Printed Carbon Working Electrodes, Electroanalysis, 25 (2013) 47-50.

[2] J.B. Raoof, R. Ojani, M. Amiri-Aref, M. Baghayeri, Electrodeposition of quercetin at a multi-walled carbon nanotubes modified glassy carbon electrode as a novel and efficient voltammetric sensor for simultaneous determination of levodopa, uric acid and tyramine, Sensors and Actuators B: Chemical, 166-167 (2012) 508-518.

[3] J. Kochana, K. Wapiennik, P. Knihnicki, A. Pollap, P. Janus, M. Oszajca, P. Kuśtrowski, Mesoporous carbon-containing voltammetric biosensor for determination of tyramine in food products, Analytical and Bioanalytical Chemistry, 408 (2016) 5199-5210.

[4] I.M. Apetrei, C. Apetrei, Amperometric biosensor based on polypyrrole and tyrosinase for the detection of tyramine in food samples, Sensors and Actuators B: Chemical, 178 (2013) 40-46.

[5] A. Küçük, O. Torul, Voltammetric sensor based on poly(3-methylthiophene) synthesized in dichloromethane for tyramine determination in moldy cheese, Synthetic Metals, 237 (2018) 23-28.

[6] X. Zhao, Simple and Sensitive Electrochemical Sensor for Tyramine Determination Based on Overoxidized Poly(o-aminophenol) Film Modified Electrode, International Journal of Electrochemical Science, (2018).

[7] Z.O. Erdogan, I. Akin, S. Kucukkolbasi, A new non-enzymatic sensor based on TiO2-Ag/polypyrrole for electrochemical detection of tyramine, Synthetic Metals, 246 (2018) 96-100.

[8] W. da Silva, M.E. Ghica, R.F. Ajayi, E.I. Iwuoha, C.M.A. Brett, Impedimetric sensor for tyramine based on gold nanoparticle doped-poly(8-anilino-1-naphthalene sulphonic acid) modified gold electrodes, Talanta, 195 (2019) 604-612.

[9] S.K. Anand, M.R. Mathew, J. Radecki, H. Radecka, K.G. Kumar, Individual and simultaneous voltammetric sensing of norepinephrine and tyramine based on poly(L-arginine)/reduced graphene oxide composite film modified glassy carbon electrode, Journal of Electroanalytical Chemistry, 878 (2020) 114531.

[10] A. Gonçalves da Silva, D.L. Franco, L.D. Santos, A simple, fast, and direct electrochemical determination of tyramine in Brazilian wines using low-cost electrodes, Food Control, 130 (2021) 108369.

Appendix 2

Microchimica Acta (2023) 190:398
https://doi.org/10.1007/s00604-023-05970-1

ORIGINAL PAPER

Innovative electrochemical platform for the simultaneous determination of L-DOPA and L-tyrosine using layer-by-layer assembled L-proline-linked nanodiamonds on printed graphene

Kantima Kaewjua[1] · Weena Siangproh[1]

Received: 11 July 2023 / Accepted: 27 August 2023

Abstract
Discovering alternative analytical techniques is crucial for practical applications; thus, this work aims to develop an innovative and simple electrochemical sensor for melanoma and the clinical diagnosis of related disorders by the simultaneous determination of 3,4-dihydroxy-L-phenylalanine (L-DOPA) and L-tyrosine (L-Tyr). The fabrication is based on the layer-by-layer electrodeposition of poly L-proline (poly(L-pro)) and nanodiamond (ND) onto a screen-printed graphene electrode (SPGE). The poly(L-pro)/ND/SPGEs were morphologically characterized by scanning electron microscopy, energy-dispersive X-ray spectrometry, and Raman spectroscopy followed by electrochemical investigation using cyclic voltammetry, differential pulse voltammetry, chronoamperometry, and electrochemical impedance spectroscopy. These modifier-based electrodes pave a feasible way to unlock the coexisting interfering substances from screen-printing ink composition and improve the sensitivity. Additionally, computational chemistry calculations were performed to fully comprehend the sensing behavior on both target analytes. Under optimal conditions, the developed sensor provided linear concentration ranges of 0.075–50 μM, with a detection limit of 0.021 μM for L-DOPA, and 2.5–120 μM with a detection limit of 0.74 μM for L-Tyr. To demonstrate the reliability of the poly(L-pro)/ND/SPGE in practical application, it was successfully applied to the determination of these analytes in human urine and blood serum samples, with satisfactory recovery ranges (81.73–110.62% for L-DOPA and 82.17–110.01% for L-Tyr) and relative standard deviations (0.69–9.90% for L-DOPA and 0.40–9.55% for L-Tyr). Due to its simplicity, long-term stability (> 87.8% of their initial currents after 35 days), and portability, the developed sensor is a promising alternative analytical method for on-site clinical monitoring.

Keywords L-DOPA · L-Tyrosine · Nanodiamond · Poly(L-proline) · Electrochemical sensor · Differential pulse voltammetry

Introduction

It is now widely acknowledged that climate change affects both human and environmental health. As a result of these changes, continued global warming and overexposure to ultraviolet radiation are of great concern because they might have an impact on the increasing incidence of skin cancer [1–3]. Melanoma is one of the most life-threatening skin cancers, with an unpredictable pattern of dissemination, a high risk of recurrence, and a high mortality rate [4]. It is brought on by abnormal and excessive melanocyte proliferation in the skin, mucous membranes, eyes, nerve centers, and meninges [5, 6]. Even though the traditional and contemporary methods for early melanoma diagnosis—clinical observation, skin biopsy, and histopathology—provide information on the histological type and biological behavior of the disease [7–9], they have drawbacks that limit their use in point-of-care applications. Therefore, the development of a novel analytical approach for detecting new biomarkers related to melanoma diagnosis is crucial for staging, prognosis, and therapeutic efficacy, resulting in reducing cancer mortality, saving lives, and decreasing therapy costs.

From the literature review, the measurement of tyrosinase activity by quantifying melanin precursors, which are 3,4-dihydroxy-L-phenylalanine (L-DOPA) and L-tyrosine (L-Tyr), could provide additional information on melanoma prognosis and metastatic spread [10, 11] because tyrosinase

✉ Weena Siangproh
weena@g.swu.ac.th

[1] Department of Chemistry, Faculty of Science, Srinakharinwirot University, Sukhumvit 23, Bangkok 10110, Wattana, Thailand

Published online: 18 September 2023

can catalyze the conversion of L-Tyr to L-DOPA [12, 13]. It was reported that during melanoma metastases, in biological fluids, the concentration of L-DOPA increases while the concentration of L-Tyr decreases. Thus, the L-DOPA/L-Tyr ratio can be used as an index of tyrosinase activity to identify the stage of melanoma in human blood plasma or serum. In healthy individuals, the normal blood serum levels of L-DOPA and L-Tyr concentrations, and the L-DOPA/L-tyrosine ratio, are approximately 6.48 nM, 60.0 μM, and 16.0×10^{-5}, respectively. Melanoma patients can be identified by monitoring a blood serum L-DOPA/L-Tyr ratio that exceeds 20×10^{-5} [14, 15]. Besides being mentioned, the abnormal concentration of these biomolecules is useful for other clinical diagnoses such as progressive neurological disorders [16] as well as neuropsychiatric and eating disorders [17].

Only a few techniques, including high-performance liquid chromatography (HPLC) [18, 19] and capillary electrophoresis (CE) [20, 21] in combination with various detectors, have been developed so far for the simultaneous determination of L-DOPA and L-Tyr. However, HPLC and CE are not ideal for onsite analysis due to the high cost and size of equipment, the requirement for highly trained personnel, the need for analyte derivatization, and the production of massive amounts of chemical waste. The electrochemical technique has gained considerable attention to overcome the above limitations owing to its attractive features, including rapid detection, affordability, high sensitivity, portability, and applicability as a point-of-care test [22]. However, there are only a few reports that use electroanalytical methods to simultaneously determine L-DOPA and L-Tyr, such as triazole derivatives modified on glassy carbon electrodes, chemically cyclodextrin on microelectrodes, bimetallic Au–Co-coated screen-printed electrodes, and carbon nanomaterial-based electrodes [23–27], although these sensors demonstrated robust performance, their lack long-term stability, and time-consuming modification processes, making them inappropriate for real point-of-need applications. Therefore, the development of a sensitive, selective, and simple electroanalytical method for the determination of L-DOPA and L-Tyr is challenging and important for practical applications.

Nowadays, the transition from laboratory benchtop to point-of-care detection using screen-printed electrodes has gained attention in the field of sensor technology. Graphene-based screen-printed electrodes (SPGEs) have attracted interest as portable electrochemical sensors that are more practical and accessible in a variety of applications. To improve electrochemical responsiveness and selectivity, however, modification using the proper electrocatalyst modifiers is sometimes still necessary. Nanodiamond (ND) has been becoming one of the most attractive carbon nanomaterials for modifying electrode surfaces due to its excellent chemical stability, mechanical modulus, and electronic properties, as well as its lower toxicity and ability to provide a larger specific surface area [28–32]. Therefore, these unique characteristics inspired us to apply them as part of a modifier to improve the performance of the electrochemical sensors. Another modifier is amino acid (AA)–based polymers, which have been used to improve conductivity and tremendously expand application prospects in the electrochemical field due to their excellent biocompatibility and functional groups with diverse side chain structures [33, 34]. L-Proline (L-pro) is AA with a secondary amine group in the alpha position of carboxyl group [35], attracting attention as a building block for AA-based polymer fabrication in various sensors [36–38].

To the best of our knowledge, there is no report on the combination of an AA-based polymer and ND being an electrochemical sensor. Therefore, we proposed a layer-by-layer electrodeposition of poly(L-pro) and ND on SPGE for the simultaneous detection of L-DOPA and L-Tyr to obtain their ratio. Poly(L-pro) and ND on graphene-based substrates exhibit remarkably improved electrocatalytic properties of L-DOPA and L-Tyr. These came from the benefit of the synergistic effect between high-conductive poly(L-pro) film and the enlarged surface area of ND. The promising results obtained indicated that the developed sensor could potentially be an alternative tool for the determination of L-DOPA and L-Tyr in practical applications.

Experimental

Chemicals, reagents, materials, and apparatus

Details of chemicals, reagents, materials, and apparatus are described in SI Section 1.1.

Fabrication of poly(L-pro)/ND/SPGE

The details on the fabrication of homemade SPGE are described in SI Section 1.2. The SPGE device consists typically of three electrodes: the counter electrode (CE), the working electrode (WE), and the reference electrode (RE) on the polyvinyl chloride (PVC) substrate. Layer-by-layer poly(L-pro)/ND/SPGE was fabricated as follows: First, 100 μL of 0.1% w/v ND suspension was dropped on the surface of a graphene-based substrate and then deposited by sweeping a potential window from − 0.8 V to + 0.8 V for 10 repetitive cycles at a scan rate of 0.1 V s^{-1} (Fig. S1A). The obtained ND/SPGE was carefully washed with DI water and left for about 10 s to dry in the air. In the second step, a poly(L-pro) layer was polymerized over ND/SPGE surface from 1 mM L-proline in 0.1 M PBS pH 7.4 by cycling in a potential window from − 0.6 to + 2.0 V for 15 cycles at a scan rate of

0.1 V s^{-1} (Fig. S1B). The different electrodes, ND/SPGE, poly(L-pro)/SPGE, and ND/poly(L-pro)/SPGE, were prepared as described above, with the exception that ND-(L-pro)/SPGE was prepared by mixing ND and L-pro in the solution and performed under the same conditions for electropolymerization of L-pro. The overall fabrication steps of homemade SPGE and poly(L-pro)/ND/SPGE are presented in Fig. 1.

Electrochemical measurements

All measurements were performed using a three-electrode system with poly(L-pro)/ND/SPGE as the WE, graphene ink as the CE, and Ag/AgCl as the RE, and were carried out at least three times at room temperature. For the electrochemical measurement, 100 µL of a mixture of L-DOPA and L-Tyr solution in 0.1 M PBS (pH 7.4) was dropped onto the electrode surface area. Additional information on electrochemical measurements is presented in SI Section 1.1.

Real-sample preparation

Details of real-sample preparation are presented in SI Section 1.1.

Results and discussion

Electrochemical performances of the modified electrodes with poly(L-pro) and ND

The effect of different electrode preparation steps based on single, composite, layer-by-layer modification, and a bare SPGE on the electrochemical oxidation of L-DOPA and L-Tyr was first investigated. As shown in Fig. 2A, the CV measurement at the bare SPGE (curve a) revealed weak anodic peak currents of L-DOPA and L-Tyr. In addition, a slight hump on the L-DOPA oxidation peak was noticed. After the ND layer was deposited on SPGE (curve b), a pair of obvious oxidation peaks of the target analyte was discovered, implying that the ND layer could eliminate a disturbance hump peak. While a single modification of poly(L-pro) was present on SPGE (curve c), the oxidation peaks of L-DOPA and L-Tyr increased and showed sharp peaks at potentials of + 0.049 V and + 0.543 V, respectively. These findings may be a result of catalysis by poly(L-pro). Therefore, we are inspired to combine ND and poly(L-pro) as modifiers using various modification approaches. At the composite ND-(L-pro)/SPGE (curve d), the electrochemical signals of target analytes dramatically decreased compared with those of poly(L-pro)/SPGE. Interestingly, better electrochemical responses and well-defined peaks of target analytes were observed at the layer-by-layer poly(L-pro)/ND/SPGE (curve f).

The DPV technique is furthermore used to precisely confirm the electrochemical performances of various modified and unmodified electrodes. Figure 2B illustrates the DPV responses of 0.1 M PBS, pH 7.4 at the different electrodes. As expected, the disturbance peak was observed at the potential of − 0.01 V at a bare SPGE (curve a). We strongly believe that this phenomenon is attributed to the coexistence of screen-printing ink formulations, such as resins, solvents, and additives, that could be oxidized at the near potential of L-DOPA oxidation. Interestingly, when the electrode surface is modified by ND or poly(L-pro) with different modification steps, the disturbance peak is eliminated. This indicates that the integration of the ND layer with poly(L-pro) is important for the suppression of background currents. From the obtained results, the poly(L-pro)/ND/SPGE (curve f) provided a flat and lower signal of background currents. This could be beneficial for achieving a low detection limit. From the DPV responses in Fig. 2C, it is clearly seen that the layer-by-layer poly(L-pro)/ND/SPGE not only increased the oxidation peak current by 6- and 3-fold for L-DOPA and L-Tyr but also provided a lower detection potential for both target analytes. Therefore, it is logical to assume that poly(L-pro)/ND/SPGE could be an appropriate electrode material for the simultaneous detection of L-DOPA and L-Tyr.

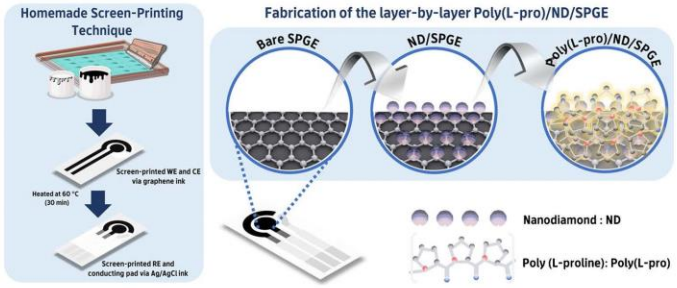

Fig. 1 Schematic representation of the fabrication processes for the poly(L-pro)/ND/SPGE

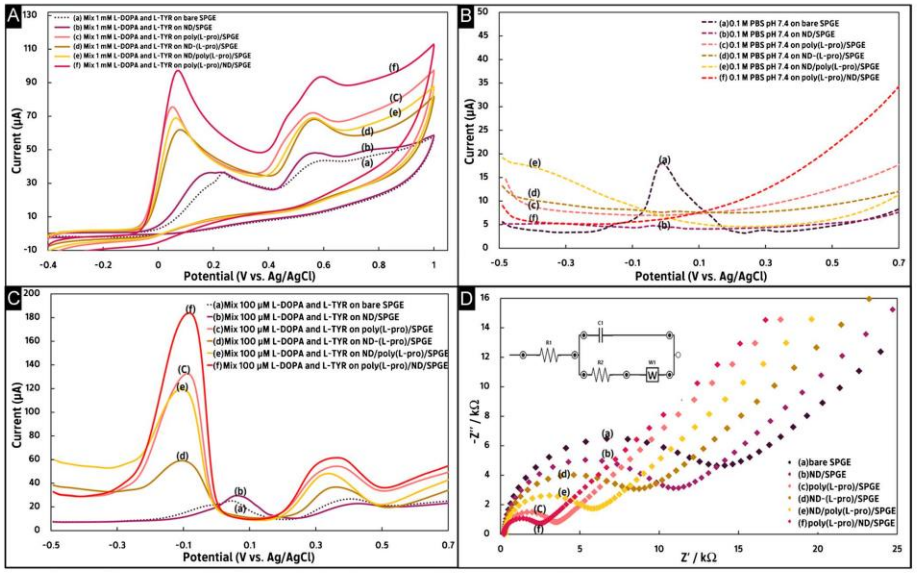

Fig. 2 **A** CV responses of a mixture of 1 mM L-DOPA and 1 mM L-Tyr at the different electrodes, **B** DPV responses of 0.1 M PBS pH 7.4 at the different electrode, **C** DPV responses of a mixture of 100 μM L-DOPA and 100 μM L-Tyr at the different electrodes, and **D** EIS curves of 5 mM $Fe(CN)_6^{3-/4-}$ in 0.1 M KNO_3 at the different electrodes

To study the changes in the impedance of modified electrodes, EIS was carried out in 5 mM $Fe(CN)_6^{3-/4-}$ in 0.1 M KNO_3 at the different electrodes. The charge transfer resistance (R_{ct}) is represented by the diameter of the semicircle [39] as shown in Fig. 2D. The highest calculated R_{ct} is at the bare SPGE (11.83 kΩ) and is significantly reduced for ND/SPGE (9.39 kΩ), poly(L-pro)/SPGE (3.24 kΩ), ND-(L-pro)/SPGE (7.24 kΩ), ND/poly(L-pro)/SPGE (4.84 kΩ), and poly(L-pro)/ND/SPGE (1.98 kΩ). The decreased values indicated that the electron transfer process is more promoted at the modification layers. The poly(L-pro)/ND/SPGE provided the lowest R_{ct}, confirming that both poly(L-pro) and ND most facilitate the transfer process at the solution-electrode interface. It can be concluded that both modifiers have a synergistic effect due to the high electrical conductivity of the poly(L-pro) film and the enlarged active surface area of ND.

Chronoamperometric experiments, as presented in Fig. S2, were subsequently performed to confirm the electrocatalyst property of modifiers. Table S1 shows the catalytical rate constant (k_{cat}) for both target analytes at different electrodes. It was found that k_{cat} significantly increased after modified electrodes with either or both poly(L-pro) and ND. The poly(L-pro)/ND/SPGE exhibits the highest k_{cat} for both target analytes. This confirmed that the layer-by-layer poly(L-pro)/ND/SPGE has remarkable electrocatalytic capabilities toward the electrooxidation of L-DOPA and L-Tyr. According to all proving, we strongly confirmed that poly(L-pro)/ND/SPGE is the most suitable sensor for simultaneously determining L-DOPA and L-Tyr.

Characterization of the morphology and structure of the proposed electrode

To understand the surface morphology and structural features of different modified materials on SPGEs, various characterizations, including SEM–EDS analysis and Raman spectroscopy, were performed. The SEM images of a bare SPGE (Fig. 3A, B) showed the sheet-like structure's wrinkled edge. For the deposition of the ND layer on SPGE, it provided a relatively uniform size, but its aggregation revealed disparate shapes and sizes on the SPGE surface (Fig. 3C, D). Hence, the surface roughness of ND/SPGE improved, indicating an increase in the surface-active site,

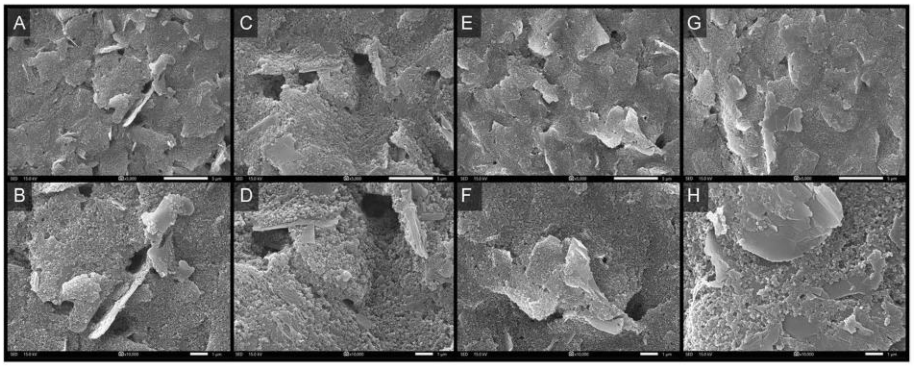

Fig. 3 SEM images of bare SPGE (**A**, **B**), ND/SPGE (**C**, **D**), poly(L-pro)/SPGE (**E**, **F**), and poly(L-pro)/ND/SPGE (**G**, **H**) at 5000× (**A**, **C**, **E**, **G**), and 10,000× (**B**, **D**, **F**, **H**)

while the poly(L-pro) was distributed on SPGE, a smooth surface and a thin film-like structure were observed (Fig. 3E, F). Figure 3G and H show the SEM images of SPGE after modifications of layer-by-layer via poly(L-pro) and ND. Because of the ND's specific activity, it provides a good effective area for the growth of the poly(L-pro) layer, and thus the poly(L-pro) modified on the ND-deposited SPGE formed the three-dimensional smooth film that covered the clump-like morphology of ND particles on the stacking graphene sheet.

A particle size distribution of ND on SPGE was determined from the SEM images using Image J processing. The particles are in the 30–100 nm range, with an average diameter size of 60.79 ± 15.38 nm (in SI Section 1.4, Fig. S3), confirming that the agglomerated NDs retain their nanoscale size after the electrodeposition. In addition, the SEM image is supported by EDS analysis to investigate the composition of different modified electrodes. It is proven that the surfaces of unmodified and modified electrodes consist mostly of carbon and oxygen (Fig. 4). Slight nitrogen peaks in the EDS spectrogram were noted for both poly(L-pro)/SPGE (Fig. 4C) and poly(L-pro)/ND/SPGE (Fig. 4D). These results confirm the presence of a polymeric thin film of L-pro. To prove the formation of poly(L-pro)/ND/SPGE, the different electrodes based on either or both poly(L-pro) and ND were characterized by Raman spectroscopy. The Raman spectra of the bare and modified SPGEs (in Fig. 4E) showed the intense G band at ~ 1588 cm^{-1}, corresponding to in-plane vibration of the sp^2 bonded carbon structure, and the D band at ~ 1365 cm^{-1} mainly reflecting defects and disorders in the graphitic structure [40]. Moreover, the presence of a more intense 2D band was observed at ~ 2726 cm^{-1} on bare SPGE, which can imply the number of graphene layers. The intensity ratio of the 2D and G bands (I_{2D}/I_G) of bare SPGE was found to be 0.17, indicating the multi-layered graphene grown on the PVC substrate [41, 42]. In the case of ND/SPGE, the intensive D band was observed at ~1335 cm^{-1}, corresponding to the vibration of the sp^3 diamond lattice [43]. The spectral region ranges at 826–930 cm^{-1} could be attributed to the ring stretching modes of the pyrrolidine ring and the variation of the COO^- group on L-pro. The bands observed at ~1547 cm^{-1}, 2916 cm^{-1}, and 3174 cm^{-1} are assigned to the in-plane bending of NH, the symmetric stretch $\upsilon_s CH_2$, and the asymmetric stretch $\upsilon_{as} CH_2$ of L-pro, respectively [44, 45]. The characteristic peaks for poly(L-pro) and ND can be seen on the surface of the SPGE after layer-by-layer modification. The intensity ratios of the D and G bands in the Raman spectra (I_D/I_G) were calculated to be 0.93, 0.97, 0.99, and 1.08 for bare SPGE, ND/SPGE, poly(L-pro)/SPGE, and poly(L-pro)/ND/SPGE. These increased values indicated that a higher disordered level of the graphene structure was caused by the introduction of oxygen-containing functional groups from modifiers [46].

Electrochemical characterization of poly(L-pro)/ND/SPGE

As shown in Fig. 5A, the cyclic voltammogram of the redox probe was significantly increased and sharpened after the layer-by-layer modification of poly(L-pro) and ND to the SPGE surface. Moreover, it shifted the potential to be close to zero when compared with the bare SPGE. This suggests the increased

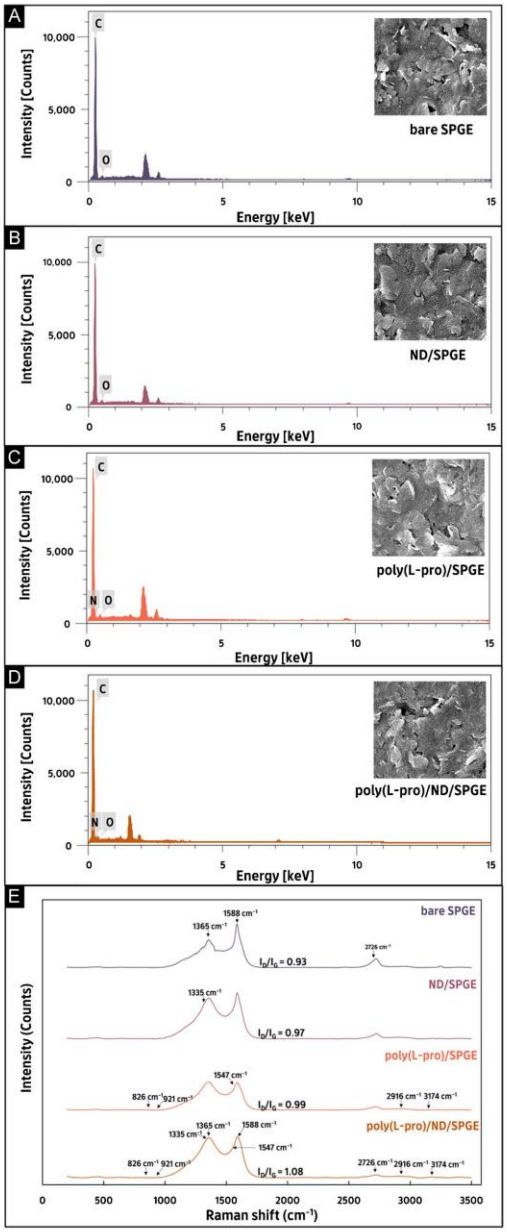

Fig. 4 The SEM–EDS analysis for bare SPGE (**A**), ND/SPGE (**B**), poly(L-pro)/SPGE (**C**) and poly(L-pro)/ND/SPGE (**D**), Raman spectra for the different electrodes (**E**)

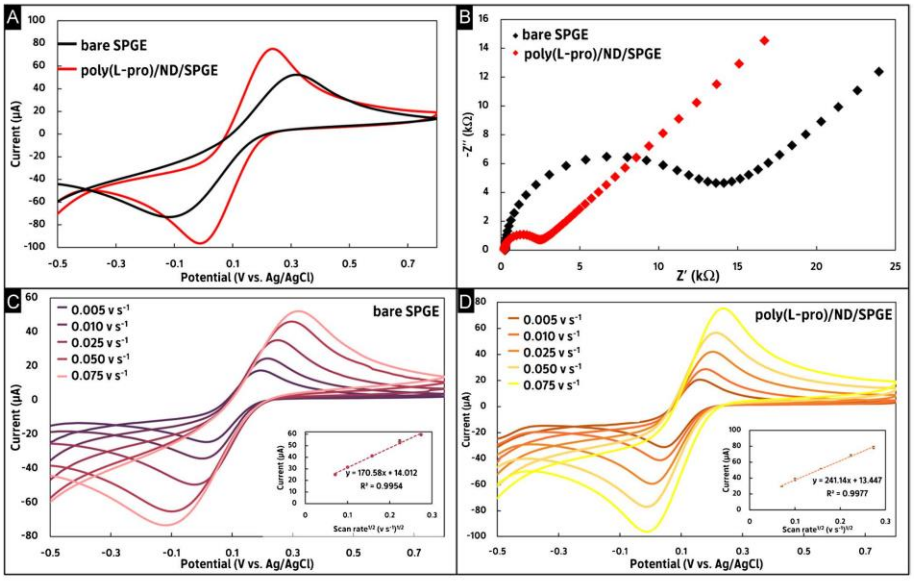

Fig. 5 **A** Cyclic voltammograms, **B** EIS curves of 5 mM $Fe(CN)_6^{3-/4-}$ in 0.1 M KNO_3 at bare SPGE and poly(L-pro)/ND/SPGE, CV curves for 5 mM $Fe(CN)_6^{3-/4-}$ at bare SPGE (**C**), and poly(L-pro)/ND/SPGE (**D**) with different scan rate (inset; the plot of I vs. $\upsilon^{1/2}$)

transfer rate of $Fe(CN)_6^{3-/4-}$ to the electrode surface. These results were in good agreement with the EIS data in Fig. 5B.

In addition, the electroactive surface areas were calculated to be 0.047 and 0.067 cm^2 for the bare SPGE and poly(L-pro)/ND/SPGE, respectively. The electroactive surface area for the modified electrode was about 1.43 times larger than that of the bare SPGE. Furthermore, the calculated surface coverages of the bare electrode and poly(L-pro)/ND/SPGE were found to be 1.60×10^{-10} and 7.92×10^{-10} mol cm^{-2}, respectively. The findings clearly demonstrated that the fabrication of layer-by-layer poly(L-pro)/ND/SPGE is beneficial for improving active sites and surface coverage. Detailed information for all calculations of electroactive surface areas and surface coverages is available in SI Section 1.5.

To evaluate the cycling stability of poly(L-pro)/ND/SPGE, consecutive CV cycles of 5 mM $Fe(CN)_6^{3-/4-}$ in 0.1 M KNO_3 were performed at scan rates of 50 mVs^{-1}. As shown in Fig. S4, no change was observed in the redox current after 15 CV cycles (about 89% of the first cycle) at a scan rate of 50 mV s^{-1}, which proved that the surface of this modified SPGE remained stable after functionalization and electrochemical process.

Electrochemical behavior of L-DOPA and L-Tyr at poly(L-pro)/ND/SPGE

The electrochemical responses for the simultaneous detection of L-DOPA and L-Tyr were investigated using bare SPGE and poly(L-pro)/ND/SPGE via CV and DPV. As presented in Fig. 6A, at the bare SPGE, the oxidation peaks are small and occur at potentials of + 0.237 V for L-DOPA and + 0.556 V for L-Tyr. On the other hand, at poly(L-pro)/ND/SPGE, the oxidation peak currents of both target analytes increased significantly, and the peak potentials shifted to a negative potential of + 0.071 V for L-DOPA and a slightly positive potential of + 0.575 V for L-Tyr. Compared with bare SPGE, the peak potential difference (ΔE_p) between L-DOPA and L-Tyr at poly(L-pro)/ND/SPGE increased from 0.319 to 0.504 V. The shift of peak potential and increase in ΔEp at layer-by-layer poly(L-pro)/ND/SPGE can be attributed to the impact of hydroxyl (–OH) substitution in their aromatic rings: meta- and para-OH groups for L-DOPA and para-OH group for L-Tyr. Because of the higher OH group substituents, L-DOPA could be more chemically reactive than

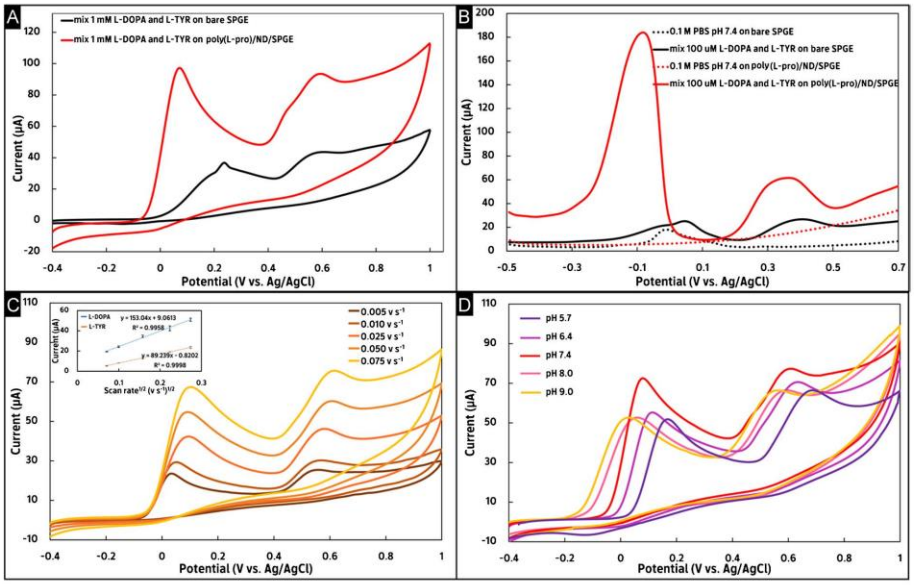

Fig. 6 **A** CV curves of a mixture of 1 mM L-DOPA and 1 mM L-Tyr at bare SPGE and poly(L-pro)/ND/SPGE, **B** DPV curves obtained for comparing both of bare SPGE and poly(L-pro)/ND/SPGE in a mixture of 100 μM L-DOPA and 100 μM L-Tyr, **C** CV curves of the mixture of 1 mM L-DOPA and 1 mM L-Tyr at different scan rate using poly(L-pro)/ND/SPGE (inset; the plot of **I** vs. $\upsilon^{1/2}$), and **D** CV curves of the mixture of 1 mM L-DOPA and 1 mM L-Tyr with varying pH conditions

L-Tyr. As a result, L-DOPA can be easily oxidized at a more negative potential, further separating the response locations to L-Tyr and allowing for easier simultaneous detection. Moreover, the occurrence of a pair of anodic peaks indicated that the electrochemical reaction of L-DOPA and L-Tyr was a completely irreversible process. The DPV signals on bare SPGE were observed at potentials of + 0.053 V for L-DOPA and + 0.396 V for L-Tyr, as shown in Fig. 6B. Nevertheless, the anodic peak of L-DOPA at a bare SPGE showed an asymmetrical peak, caused by the disturbance substance in the screen-printing ink composition as mentioned before. This electrode material-induced disturbance resulted in complicated data interpretation and a lack of sensitivity. In contrast, at poly(L-pro)/ND/SPGE, the background current is flat, and the electrooxidation of L-DOPA and L-Tyr increased dramatically with sharp and intense shapes at potentials of − 0.087 and + 0.347 V with peak currents of 6 and 3 times that of bare SPGE. According to our findings, the proposed electrode exhibits great electrocatalytic activity in terms of improving electron transfer kinetics at the electrode–solution interface. This enhancement could be attributed to a synergetic effect between the high conductivity of poly(L-pro) and the large surface-active area of ND, which enlarges the uniformity of poly(L-pro) on the electrode surface.

To gain an additional understanding of the sensing behavior of the poly(L-pro)/ND/SPGE on both target analytes, computational chemistry calculations were performed by means of the density functional theory using the B3LYP/6-31G(d,p) level. According to the electrochemical results, electrodes with an upper layer of poly(L-pro) significantly displayed a highly sensitive response to L-DOPA and L-Tyr. We will therefore focus on the interaction between these analytes and the L-proline monomer. The computational results proved that poly(L-pro) has a stronger propensity to interact with both target analytes via the electrostatic nature of the hydrogen bond (SI Section 1.6, Fig. S5A). Furthermore, an electron density map with an electrostatic potential for the interactions between both target analytes and L-pro was also observed. The regions with the highest

negative potential (high electron density) are highlighted in red, and the regions with the positive potential (low electron density) are indicated in green or blue color. As shown in Fig. S5B, the electron density is located more on the aromatic rings and the hydroxyl and carbonyl groups of these analytes. The L-pro monomer electron could be more localized at the carboxyl group. The presence of an electron cloud reveals the possibility of hydrogen bonding interactions between both target analytes and the poly(L-pro) backbone, which induces the electron transfer process at the electrode–solution interface.

Mass transport controlled by the electrooxidation of L-DOPA and L-Tyr was measured via CV. The effect of a scan rate of 0.005–0.075 Vs^{-1}on poly(L-pro)/ND/SPGE is shown in Fig. 6C. The peak currents of L-DOPA and L-Tyr are proportional to the square root of the scan rate (presented in the inset Fig. 6C). Moreover, by plotting log Ip vs. log υ (as shown in SI Section 1.7, Fig. S6A), the slopes of 0.5238 for L-DOPA and 0.5427 for L-Tyr were consistent with the theoretical value of 0.5, confirming that the electrooxidation of these analytes was controlled by the diffusion process [47]. Using the obtained information from the i-$\nu^{\frac{1}{2}}$ relationship (inset Fig. 6C) together with the theoretic model described by Andrieux and Savèant [48], the calculated diffusion coefficient (D_0) for L-DOPA and L-Tyr were found to be 5.93×10^{-5} cm^2 s^{-1} and 2.02×10^{-5} cm^2 s^{-1}, respectively, which is explained in SI Section 1.8.

For the irreversible process, the Randles–Sevcik relationship (see SI Section 1.8) can be used to determine the number of electrons involved in the electrooxidation process [49]. It was found that the number of electrons involved in the electrooxidation was calculated to be 1.31 (≈1) and 1.23 (≈1) for L-DOPA and L-Tyr, respectively.

Additionally, the effects of pH on the electrooxidation of both target analytes provide significant details about the mechanisms at the poly(L-pro)/ND/SPGE interface. As the pH increased from 5.7 to 9.0, the oxidation peak potentials of L-DOPA and L-Tyr gradually shifted negatively, as presented in Fig. 6D. The maximum peak currents of L-DOPA and L-Tyr were observed at pH 7.4. At this pH, they are in their zwitterionic forms due to the protonated amine and deprotonated carboxyl groups in their structures. These electrically neutral forms could be easily diffused from the bulk solution to the electrode interface via the electrostatic nature. Therefore, PBS at pH 7.4 was selected as the supporting electrolyte in further experiments. In addition, the slopes of a plot of Ep vs. pH as provided in SI Section 1.7, Fig. S6C, are – 51.1 mV/pH for L-DOPA and – 52.9 mV/pH for L-Tyr. Both are close to the theoretical value of – 59.1 mV/pH, proving that there is an equal number of proton and electron transfers ($1e^-/1H^+$) involved in the electrooxidation of L-DOPA and L-Tyr at poly(L-pro)/ND/SPGE.

Optimization of the influence parameters for electrode modification and electrochemical detection

Because the parameters of ND deposition and poly(L-proline) manufacturing are critical for the electrochemical performance of L-DOPA and L-Tyr, the concentration of monomer, suitable potential window, and the number of cycles were investigated. The DPV technique was used to perform the simultaneous determination of L-DOPA and L-Tyr due to its low capacitive current, which results in high sensitivity. Therefore, all parameters of DPV were examined to obtain the best analytical performance. More details on the optimization of electrode modification and electrochemical detection are provided in SI Section 1.9, Figs. S7, S8, and S9.

Analytical performance

The simultaneous determination of L-DOPA and L-Tyr was carried out by containing the different concentrations of a mixture of target analytes in 0.1 M PBS pH 7.4. As shown in Fig. 7A, two well-separated and distinct oxidation peaks of L-DOPA and L-Tyr were observed, and the peak currents for these analytes increased linearly with concentrations (Fig. 7B) in the ranges from 0.075 to 50 μM for L-DOPA and 2.5–120 μM for L-Tyr. The detection limits (LODs) calculated using 3SD/slope are 0.021 μM and 0.74 μM, for L-DOPA and L-Tyr, respectively. To investigate the impact of the electrochemical response of these analytes on the individual system, the DPV analysis was performed using different concentrations for one analyte while maintaining the other at a fixed concentration. The obtained sensitivities in the simultaneous and individual systems were found to be statistically equivalent in terms of the slopes of linear ranges and detection limits (SI Section 1.10, Fig. S10). These demonstrate that the simultaneous measurement of these analytes was possible without interfering with one another.

In comparison to previous electrochemical sensors for the simultaneous determination of L-DOPA and L-Tyr (Table S2), it has been found that the performance of the proposed sensor is comparable to, and occasionally even worse or better than, that of the other sensing platforms. However, most previous reports used traditional-based electrodes, such as glassy carbon electrodes and carbon

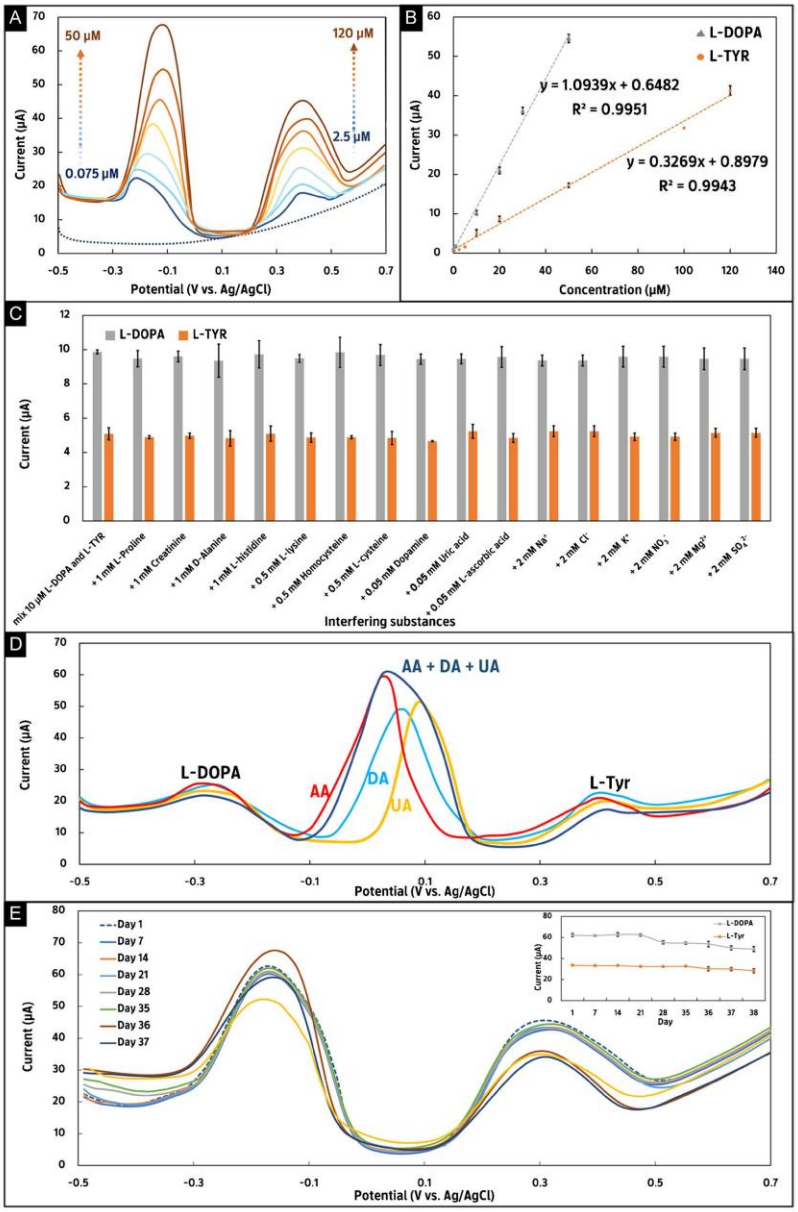
A
50 μM
120 μM
2.5 μM
0.075 μM
Current (μA)
Potential (V vs. Ag/AgCl)
B
L-DOPA
L-TYR
y = 1.0939x + 0.6482
R² = 0.9951
y = 0.3269x + 0.8979
R² = 0.9943
Current (μA)
Concentration (μM)
C
L-DOPA
L-TYR
Current (μA)
mix 10 μM L-DOPA and L-TYR
+ 1 mM L-Proline
+ 1 mM Creatinine
+ 1 mM D-Alanine
+ 1 mM L-Histidine
+ 0.5 mM L-lysine
+ 0.5 mM Homocysteine
+ 0.5 mM L-cysteine
+ 0.05 mM Dopamine
+ 0.05 mM Uric acid
+ 0.05 mM L-ascorbic acid
+ 2 mM Na+
+ 2 mM Cl-
+ 2 mM K+
+ 2 mM NO3-
+ 2 mM Mg2+
+ 2 mM SO4 2-
Interfering substances
D
AA + DA + UA
L-DOPA
AA
DA
UA
L-Tyr
Current (μA)
Potential (V vs. Ag/AgCl)
E
Day 1
Day 7
Day 14
Day 21
Day 28
Day 35
Day 36
Day 37
L-DOPA
L-Tyr
Current (μA)
Day
Current (μA)
Potential (V vs. Ag/AgCl)

◂**Fig. 7** **A** DPV signals for different concentrations of a mixture of L-DOPA and L-Tyr at poly(L-pro)/ND/SPGE. **B** Calibration plot between anodic peak current and concentration of both target analytes. **C** The effect of interfering substances on the anodic peak current of a mixture of 10 µM L-DOPA and 10 µM L-Tyr at poly(L-pro)/ND/SPGE ($n = 3$), **D** DPV curve of L-DOPA (10 µM) and L-Tyr (10 µM) in single and mixed ascorbic acid, dopamine, and uric acid (0.05 mM), and **E** The study of the stability of poly(L-pro)/ND/SPGE

paste electrodes, which led to complicated pre-treatment and multi-modification steps. It is unsuitable for onsite analysis. Thus, our newly created sensor provided suitable linear ranges with acceptable LODs, material compatibility, an affordable price, and a portable platform, which are suitable for an alternative to simultaneously determine both analytes in a practical application. We believe that our findings could be beneficial for increasing scientific knowledge of sensor technology applications.

Selectivity, stability, and reproducibility

To evaluate the selective applicability of the developed sensor, the influence of various substances potentially interfering was studied. The interfering substances were chosen from the group of substances commonly found in biological fluids. The tolerance limit was defined as the maximum concentration of the interfering substance that caused an error of $< \pm 5\%$. The obtained results from Fig. 7C show that there was no significant influence on the signal of L-DOPA and L-Tyr. Despite the fact that electrooxidation of ascorbic acid (AA), dopamine (DA), and uric acid (UA) occurs at a near-zero potential, this could potentially obstruct this detection. Therefore, the determination of 10 µM of L-DOPA and L-Tyr in single and mixed 0.05 mM of AA, DA, and UA were examined using poly(L-pro)/ND/SPGE. As shown in Fig. 7D, there is no interference observed even though the ratio of the concentration target analytes to those mentioned interfering species is up to 1:5. Therefore, poly(L-pro)/ND/SPGE has good selectivity for the simultaneous determination of L-DOPA and L-Tyr in real samples.

For the stability investigation, the signals of L-DOPA and L-Tyr on the developed sensor were measured every 7 days for a sustained 5-week period. The developed sensor was kept in a plastic zip lock bag at room temperature throughout this evaluation. As seen in Fig. 7E, the detection signals of L-DOPA and L-Tyr at day 35 remained at 87.8% and 97.2%, suggesting that the sensor's lifespan is about 1 month. Furthermore, the relative standard deviations (%RSD) for L-DOPA and L-Tyr were calculated to be 1.02% and 1.25% at seven independent electrodes ($n = 7$), which suggested that the proposed sensing platform has good reproducibility. Therefore, poly(L-pro)/ND/SPGE provides excellent selectivity, stability, and reproducibility that can be applied for practical use.

Real sample analysis

To verify the feasibility of the developed sensor and method for simultaneous determination of L-DOPA and L-Tyr, human blood serum and urine samples were tested using the standard addition method (SI Section 1.10, Fig. S10E and F). The values calculated based on the average of three replicates are presented in Table 1. It shows that the percentage recovery and RSD for L-DOPA ranged from 81.73 to 110.62% and 0.69 to 9.90%, respectively. In addition, the recovery of the spiked samples with L-Tyr ranged from 82.17 to 110.01%, with an RSD range of 0.40–9.55%. These results were within recommended accuracy and precision as AOAC guidelines [50]. Therefore, poly(L-pro)/ND/SPGE can be a promising analytical platform for the prognosis and metastatic monitoring of melanoma as well as the other abnormalities related to these biomarkers.

Conclusion

In this work, we have established an innovative and sensitive electrochemical sensor-based layer-by-layer poly(L-pro)/ND/SPGE for the simultaneous determination of L-DOPA and L-Tyr for the first time. In comparison, the use of bare SPGE failed to discriminate L-DOPA signals from the co-existence of screen-printing ink formula and lacked sensitivity for both target analytes. In contrast, the proposed modified electrode successfully resolved electrode material-induced disturbances also while improving electrochemical response. Furthermore, the proposed sensor was easily fabricated in only two steps, first electrodeposition of ND and then electropolymerization of L-proline, all in 8 min. The capability of coupling the good conductivity of poly(L-pro) with the high surface area of ND benefits electron transfer and shows excellent electrocatalytic activity toward the oxidation of L-DOPA and L-Tyr. In addition to offering a wide linear detection range for L-DOPA and L-Tyr, poly(L-pro)/ND/SPGE also demonstrated outstanding differentiation between the two target analytes with high sensitivity and selectivity. For real-world applications, the proposed sensor was applied to quantify these target biomarkers in human blood serum and urine samples. The obtained recovery and %RSDs were acceptable, showing great potential

Table 1 Evaluation of the accuracy and precision of the proposed sensor for the simultaneous determination of L-DOPA and L-Tyr in real samples

Real sample	L-DOPA				L-Tyr			
	Spiked (μM)	Found (μM)	Recovery (%)	RSD (%)	Spiked (μM)	Found (μM)	Recovery (%)	RSD (%)
Serum 1	Non-spike	n.d	–	–	Non-spike	1.62 ± 0.12	–	7.28
	2.5	2.47 ± 0.15	98.94	6.07	5	6.25 ± 0.37	92.45	5.96
	5	4.59 ± 0.31	91.84	6.73	10	10.71 ± 0.74	90.90	6.91
	10	10.01 ± 0.27	100.14	2.68	20	20.00 ± 1.91	91.87	9.53
	20	20.10 ± 1.30	100.50	6.44	40	39.67 ± 1.24	95.12	3.14
Serum 2	Non-spike	n.d	–	–	Non-spike	1.03 ± 0.08	–	7.48
	2.5	2.40 ± 0.11	95.97	4.68	5	6.53 ± 0.08	110.01	1.15
	5	5.04 ± 0.11	100.78	2.21	10	10.75 ± 0.78	97.21	7.30
	10	10.57 ± 1.05	105.70	9.90	20	18.26 ± 1.03	86.18	5.62
	20	19.72 ± 0.69	98.59	3.50	40	40.49 ± 1.11	98.67	2.73
Serum 3	Non-spike	n.d	–	–	Non-spike	1.84 ± 0.18	–	9.55
	2.5	2.29 ± 0.20	91.51	8.56	5	6.46 ± 0.38	92.38	5.86
	5	5.08 ± 0.29	101.59	5.80	10	10.06 ± 0.46	82.17	4.55
	10	10.43 ± 0.43	104.26	4.15	20	21.04 ± 0.08	96.00	0.40
	20	19.79 ± 0.18	98.96	0.93	40	39.28 ± 0.49	93.60	1.24
Serum 4	Non-spike	n.d	–	–	Non-spike	1.15 ± 0.02	–	1.63
	2.5	2.20 ± 0.04	87.99	1.82	5	5.65 ± 0.37	82.76	6.55
	5	4.81 ± 0.03	96.23	0.69	10	11.01 ± 0.13	94.97	1.17
	10	11.06 ± 0.14	110.62	1.24	20	20.37 ± 1.05	94.28	5.17
	20	19.55 ± 0.61	97.76	3.10	40	39.48 ± 0.97	94.91	2.45
Urine 1	Non-spike	0.85 ± 0.03	–	3.32	Non-spike	0.33 ± 0.03	–	7.96
	2.5	3.42 ± 0.12	102.81	3.36	5	5.33 ± 0.48	100.19	8.94
	5	5.27 ± 0.29	88.30	5.58	10	11.26 ± 0.58	109.34	5.11
	10	9.69 ± 0.10	88.38	1.00	20	18.17 ± 1.31	89.24	7.23
	20	19.97 ± 0.30	95.61	1.49	40	40.55 ± 1.73	100.57	4.26
Urine 2	Non-spike	0.88 ± 0.07	–	7.86	Non-spike	0.22 ± 0.01	–	6.75
	2.5	3.40 ± 0.28	100.84	8.13	5	5.40 ± 0.16	103.51	2.98
	5	5.21 ± 0.27	86.52	5.14	10	10.97 ± 0.16	107.52	1.46
	10	9.87 ± 0.78	89.92	7.94	20	18.29 ± 0.25	90.36	1.36
	20	19.90 ± 1.00	95.09	5.05	40	40.56 ± 2.03	100.86	5.00
Urine 3	Non-spike	0.85 ± 0.04	–	4.72	Non-spike	0.23 ± 0.02	–	7.54
	2.5	3.29 ± 0.17	97.75	5.22	5	4.82 ± 0.39	91.85	8.03
	5	4.94 ± 0.31	81.73	6.37	10	9.74 ± 0.18	95.09	1.80
	10	10.40 ± 0.60	95.54	5.74	20	21.16 ± 1.95	104.66	9.21
	20	19.71 ± 0.60	94.31	3.03	40	39.50 ± 2.69	98.19	6.82

in clinical monitoring. All the findings could provide crucial information to scientists looking for improved materials with useful properties for electrocatalysis, chemical sensors, and biosensing. Taking advantage of catalytic materials and manufacturing electrochemical sensors, extremely sensitive L-DOPA and L-Tyr sensing at the nanomolar level will be developed to unlock the bottleneck of accurately and precisely monitoring early-stage melanoma.

Supplementary Information The online version contains supplementary material available at https://doi.org/10.1007/s00604-023-05970-1.

Acknowledgements KK gratefully acknowledges the financial support from the National Research Council of Thailand (NRCT) through the Royal Golden Jubilee PhD program (NRCT5-RGJ63017-151) and WS would like to acknowledge the financial support from the National Research Council of Thailand (NRCT) and Srinakharinwirot University through Research Grants for Talented Mid-Career Researchers (N41A640098). The authors would like to thank Enago (www.enago.com) for the English language review.

Data Availability All data underlying this study are available in the article itself and its supplementary material.

Declarations

Conflict of Interest The authors declare no competing interests.

References

1. Siegel RL, Miller KD, Fuchs HE (2021) Jemal A (2021) Cancer statistics. CA Cancer J Clin 71(1):7–33. https://doi.org/10.3322/caac.21669
2. Sung H, Ferlay J, Siegel RL, Laversanne M, Soerjomataram I, Jemal A, Bray F (2021) Global cancer statistics 2020: GLOBOCAN estimates of incidence and mortality worldwide for 36 cancers in 185 countries. CA Cancer J Clin 71(3):209–249. https://doi.org/10.3322/caac.21660
3. Parker ER (2021) The influence of climate change on skin cancer incidence–a review of the evidence. Int J Womens Dermatol 7(1):17–27. https://doi.org/10.1016/j.ijwd.2020.07.003
4. Lo JA, Fisher DE (2014) The melanoma revolution: from UV carcinogenesis to a new era in therapeutics. Science 346(6212): 945–949. https://doi.org/10.1126/science.1253735
5. Cichorek M, Wachulska M, Stasiewicz A, Tymińska A (2013) Skin melanocytes: biology and development. Postep Derm Alergol 30(1):30–41. https://doi.org/10.5114/pdia.2013.33376
6. Carr S, Smith C, Wernberg J (2020) Epidemiology and risk factors of melanoma. Surg Clin North Am 100(1):1–12. https://doi.org/10.1016/j.suc.2019.09.005
7. Gheoca Mutu DE, Avino A, Balcangiu-Stroescu AE, Mehedințu M, Bălan DG, Brînduşe LA, Popescu AM, Ionescu D, Cristea BM, Tomescu LF, Jecan CR, Răducu L (2022) Histopathological evaluation of cutaneous malignant melanoma: a retrospective study. Exp Ther Med 23(6):1–7. https://doi.org/10.3892/etm.2022.11329
8. Berwick M, Wiggins C (2006) The current epidemiology of cutaneous malignant melanoma. Front Biosci 11(2):1244–1254. https://doi.org/10.2741/1877
9. Heerfordt IM, Andersen JD, Philipsen PA, Langhans L, Tvedebrink T, Schmidt G, Poulsen T, Lerche CM, Morling N, Wulf HC (2022) Detection of cutaneous malignant melanoma using RNA sampled by tape strips: a study protocol. PLoS One 17(9):e0274413. https://doi.org/10.1371/journal.pone.0274413
10. Davis LE, Shalin SC, Tackett AJ (2019) Current state of melanoma diagnosis and treatment. Cancer Biol Ther 20(11):1366–1379. https://doi.org/10.1080/15384047.2019.1640032
11. Deacon DC, Smith EA, Judson-Torres RL (2021) Molecular biomarkers for melanoma screening, diagnosis and prognosis: current state and future prospects. Front Med 8:642380. https://doi.org/10.3389/fmed.2021.642380
12. Rzepka Z, Buszman E, Beberok A, Wrześniok D (2016) From tyrosine to melanin: signaling pathways and factors regulating melanogenesis. Postepy Hig Med Dosw 70:695–708. https://doi.org/10.5604/17322693.1208033
13. Körner A, Pawelek J (1982) Mammalian tyrosinase catalyzes three reactions in the biosynthesis of melanin. Science 217(4565):1163–1165. https://doi.org/10.1126/science.6810464
14. Stoitchkov K, Letellier S, Garnier JP, Bousquet B, Tsankov N, Morel P, Ghanem G, Le Bricon T (2003) Evaluation of the serum L-dopa/L-tyrosine ratio as a melanoma marker. Melanoma Res 13(6):587–593
15. Garnier JP, Letellier S, Cassinat B, Lebbé C, Kerob D, Baccard M, Morel P, Basset-Seguin N, Dubertret L, Bousquet B, Stoitchkov K, Le Bricon T (2007) Clinical value of combined determination of plasma L-DOPA/tyrosine ratio, S100B, MIA and LDH in melanoma. Eur J Cancer 43(4):816–821. https://doi.org/10.1016/j.ejca.2006.11.022
16. Sabens LEA, Steller KM, Mieyal JJ (2011) Levodopa activates apoptosis signaling kinase 1 (ASK1) and promotes apoptosis in a neuronal model: implications for the treatment of Parkinson's disease. Chem Res Toxicol 24(10):1644–1652. https://doi.org/10.1021/tx200082h
17. Capuron L, Schroecksnadel S, Féart C, Aubert A, Higueret D, Barberger-Gateau P, Layé S, Fuchs D (2011) Chronic low-grade inflammation in elderly persons is associated with altered tryptophan and tyrosine metabolism: role in neuropsychiatric symptoms. Biol Psychiatry 70(2):175–182. https://doi.org/10.1016/j.biopsych.2010.12.006
18. Olšovská J, Novotná J, Flieger M, Spížek J (2007) Assay of tyrosine hydroxylase based on high-performance liquid chromatography separation and quantification of L-dopa and L-tyrosine. Biomed Chromatogr 21(12):1252–1258. https://doi.org/10.1002/bmc.880
19. Tufi S, Lamoree M, de Boer J, Leonards P (2015) Simultaneous analysis of multiple neurotransmitters by hydrophilic interaction liquid chromatography coupled to tandem mass spectrometry. J Chromatogr A 1395:79–87. https://doi.org/10.1016/j.chroma.2015.03.056
20. Sánchez-López E, Marcos A, Ambrosio E, Marina ML, Crego AL (2016) Enantioseparation of the constituents involved in the phenylalanine-tyrosine metabolic pathway by capillary electrophoresis tandem mass spectrometry. J Chromatogr A 1467:372–382. https://doi.org/10.1016/j.chroma.2016.06.053
21. Robinson G, Smyth M (1997) Simultaneous determination of products and intermediates of l-DOPA oxidation using capillary electrophoresis with diode-array detection. Analyst 122(8):797–802. https://doi.org/10.1039/A701844D
22. Shakeel F, Asad M, Zafar F, Abdelwahab AA, Akhtar N, Ahmad HB, Shafiq Z, Shenashen MA (2023) Bioinspired NC coated BM-ZIF for electrochemical monitoring of adrenaline from blood and pharmaceutical samples. Electroanalysis 35(4):e202200128. https://doi.org/10.1002/elan.202200128
23. Revin SB, John SA (2013) Electrochemical marker for metastatic malignant melanoma based on the determination of l-DOPA/l-tyrosine ratio. Sens Actuators B Chem 188:1026–1032. https://doi.org/10.1016/j.snb.2013.08.019
24. Yang JH, Kim HT, Kim H (2014) A cyclodextrin-based approach for selective detection of catecholamine hormone mixtures. Micro Nano Syst Lett 2(1):1–10. https://doi.org/10.1186/s40486-014-0001-z
25. Shaidarova LG, Chelnokova IA, Leksina YA, Il'ina MA, Gedmina AV, Budnikov HC (2018) Flow-injection amperometric determination of DOPA and tyrosine at a dual electrode modified with the gold–cobalt binary system. J Anal Chem 73:176–182. https://doi.org/10.1134/S1061934818020119
26. Hassanvand Z, Jalali F (2019) Simultaneous determination of l-DOPA, l-tyrosine and uric acid by cysteic acid-modified glassy carbon electrode. Mater Sci Eng C 98:496–502. https://doi.org/10.1016/j.msec.2018.12.131
27. Atta NF, Galal A, El-Gohary AR (2020) Crown ether modified poly(hydroquinone)/carbon nanotubes based electrochemical sensor for simultaneous determination of levodopa, uric acid, tyrosine and ascorbic acid in biological fluids. J Electroanal Chem 863:114032. https://doi.org/10.1016/j.jelechem.2020.114032
28. Yu X, Chen X, Ding X, Yu X, Zhao X, Chen X (2020) Facile fabrication of flower-like MoS2/nanodiamond nanocomposite toward high-performance humidity detection. Sens Actuators B Chem 317:128168. https://doi.org/10.1016/j.snb.2020.128168

29. Zang JB, Wang YH, Zhao SZ, Bian LY, Lu J (2007) Electrochemical properties of nanodiamond powder electrodes. Diam Relat Mater 16(1):16–20. https://doi.org/10.1016/j.diamond.2006.03.010
30. Jiang L, Santiago I, Foord J (2021) A comparative study of fouling-free nanodiamond and nanocarbon electrochemical sensors for sensitive bisphenol A detection. Carbon 174:390–395. https://doi.org/10.1016/j.carbon.2020.11.073
31. Pandey K, Dwivedi MM, Sanjay SS (2022) A brief review on synthesis and application of polymer–nanodiamond composite. Mater Today: Proc 68:2772–2780. https://doi.org/10.1016/j.matpr.2022.09.032
32. Emran MY, Khalifa H, Gomaa H, Shenashen MA, Akhtar N, Mekawy M, Faheem A, El-Safty SA (2017) Hierarchical C-N doped NiO with dual-head echinop flowers for ultrasensitive monitoring of epinephrine in human blood serum. Microchim Acta 184:4553–4562. https://doi.org/10.1007/s00604-017-2498-3
33. Kordasht HK, Hasanzadeh M, Seidi F, Alizadeh PM (2021) Poly (amino acids) towards sensing: recent progress and challenges. TrAC Trends Anal Chem 140:116279. https://doi.org/10.1016/j.trac.2021.116279
34. Moulaee K, Neri G (2021) Electrochemical amino acid sensing: a review on challenges and achievements. Biosensors 11(12):502. https://doi.org/10.3390/bios11120502
35. Cowan PM, McGAVIN S (1955) Structure of poly-L-proline. Nature 176:501–503. https://doi.org/10.1038/176501a0
36. Arslan E, Çakır S (2014) A novel palladium nanoparticles-poly-proline-modified graphite electrode and its application for determination of curcumin. J Solid State Electrochem 18:1611–1620. https://doi.org/10.1007/s10008-014-2382-6
37. Hasanzadeh M, Hassanpour S, Nahr AS, Shadjou N, Mokhtarzadeh A, Mahboob S (2018) Electropolymerization of proline supported beta cyclodextrin inside amino functionalized magnetic mesoporous silica nanomaterial: one step preparation, characterization and electrochemical application. Anal Bioanal Electrochem 10(1):77–97
38. Mu X, Qi L, Dong P, Qiao J, Hou J, Nie Z, Ma H (2013) Facile one-pot synthesis of L-proline-stabilized fluorescent gold nanoclusters and its application as sensing probes for serum iron. Biosens Bioelectron 49:249–255. https://doi.org/10.1016/j.bios.2013.05.019
39. Bonanni A, Loo AH, Pumera M (2012) Graphene for impedimetric biosensing. TrAC Trends Anal Chem 37:12–21. https://doi.org/10.1016/j.trac.2012.02.011
40. Hajzus JR, Shriver-Lake LC, Dean SN, Erickson JS, Zabetakis D, Golden J, Pennachio DJ, Myers-Ward RL, Trammell SA (2022) Modifications of epitaxial graphene on SiC for the electrochemical detection and identification of heavy metal salts in seawater. Sensors 22(14):5367. https://doi.org/10.3390/s22145367
41. Varga M, Izak T, Vretenar V, Kozak H, Holovsky J, Artemenko A, Hulman M, Skakalova V, Lee DS, Kromka A (2017) Diamond/carbon nanotube composites: Raman, FTIR and XPS spectroscopic studies. Carbon 111:54–61. https://doi.org/10.1016/j.carbon.2016.09.064
42. Dong X, Wang P, Fang W, Su CY, Chen YH, Li LJ, Huang W, Chen P (2011) Growth of large-sized graphene thin-films by liquid precursor-based chemical vapor deposition under atmospheric pressure. Carbon 49(11):3672–3678. https://doi.org/10.1016/j.carbon.2011.04.069
43. Mochalin V, Shenderova O, Ho D, Gogotsi Y (2012) The properties and applications of nanodiamonds. Nature Nanotech 7:11–23. https://doi.org/10.1038/nnano.2011.209
44. Mary YS, Ushakumari L, Harikumar B, Varghese HT, Panicker CY (2009) FT-IR, FT-raman and SERS spectra of L-proline. J Iran Chem Soc 6:138–144. https://doi.org/10.1007/BF03246512
45. Shimpi MR, Childs SL, Boström D, Velaga SP (2014) New cocrystals of ezetimibe with L-proline and imidazole. CrystEngComm 16(38):8984–8993. https://doi.org/10.1039/C4CE01127A
46. Zhang W, Jia B, Furumai H (2018) Fabrication of graphene film composite electrochemical biosensor as a pre-screening algal toxin detection tool in the event of water contamination. Sci Rep 8(1):10686. https://doi.org/10.1038/s41598-018-28959-w
47. Velázquez-Palenzuela A, Centellas F, Garrido JA, Arias C, Rodríguez RM, Brillas E, Cabot PL (2011) Kinetic analysis of carbon monoxide and methanol oxidation on high performance carbon-supported Pt–Ru electrocatalyst for direct methanol fuel cells. J Power Sources 196(7):3503–3512. https://doi.org/10.1016/j.jpowsour.2010.12.044
48. Andrieux CP, Savéant JM (1980) Electron transfer through redox polymer films. J Electroanal Chem Interfacial Electrochem 111(2–3):377–381. https://doi.org/10.1016/S0022-0728(80)80058-1
49. Boni AC, Wong A, Dutra RAF, Sotomayor MDPT (2011) Cobalt phthalocyanine as a biomimetic catalyst in the amperometric quantification of dipyrone using FIA. Talanta 85(4):2067–2073. https://doi.org/10.1016/j.talanta.2011.07.038
50 Analysis AOM (2016) Appendix F: guidelines for standard method performance requirements. AOAC International, Gaithersburg, MD

Electronic Supplementary Material

Innovative electrochemical platform for the simultaneous determination of L-DOPA and L-tyrosine using layer-by-layer assembled L-proline-linked nanodiamonds on printed graphene

Kantima Kaewjua, and Weena Siangproh*

Department of Chemistry, Faculty of Science, Srinakharinwirot University, Sukhumvit 23, Wattana, Bangkok 10110, Thailand

*Corresponding author:

E-mail address: weena@g.swu.ac.th, weenasi@hotmail.com (W. Siangproh)

1.1 Experimental

Chemicals, reagents, materials, and apparatus

All reagents were of analytical grade and used without further purification. 1% ND dispersions in water (10 nM) were obtained from Adámas Technologies (Raleigh, NC). L-DOPA and L-Tyr were purchased from Merck (Darmstadt, Germany). L-pro, D-alanine, L-ascorbic acid, dopamine hydrochloride, uric acid, L-histidine, creatinine, homocysteine, L-cysteine, and potassium ferricyanide ($K_3[Fe(CN)_6]$) were supplied by Sigma-Aldrich (St. Louis, MO, USA). The 0.1-M phosphate buffer solution (PBS) was prepared by mixing sodium dihydrogen orthophosphate ($NaH_2PO_4.2H_2O$) and disodium hydrogen orthophosphate ($Na_2HPO_4.2H_2O$), which were obtained from Ajax (Australia). Deionized water, produced by the Milli-Q system (R = 18.2 MΩ cm at 25°C), was used throughout the experiments.

The morphology and element composition of the electrode surface were investigated using a scanning electron microscope (SEM) and an energy-dispersive X-ray spectrometer (EDS) (JSM-IT500HR) (JEOL Ltd., Japan). The bare and modified electrodes were analyzed utilizing Fourier transform Raman spectroscopy (Perkin Elmer model Spectrum GX) (Shelton, Connecticut, USA). The Raman results identified the existence of chemical bindings after each step of electrode functionalization at the excitation wavelength of 532 nm. Electrochemical measurements, via cyclic voltammetry (CV) and differential pulse voltammetry (DPV), were performed using a laptop controlled by a CHI 1200C potentiostat (Austin, TX, USA), and electrochemical impedance spectroscopy (EIS) was performed using Sensit Smart (Houten, the Netherlands).

Electrochemical measurements

CV was employed for the study of the electrochemical behaviors of both L-DOPA and L-Tyr. The potential range of −0.4 to +1.0 V vs. Ag/AgCl at a scan rate of 0.075 Vs^{-1} was set. Differential pulse voltammetry (DPV) was optimized and used for the determination of L-DOPA and L-Tyr. All DPV parameters were successfully achieved by scanning the potential in the range of −0.5 to +0.7 V vs. Ag/AgCl with a pulse width of 0.025 s, an amplitude of 0.2 V, a pulse period of 0.5 s, and an increment of 0.007 V. The EIS measurements were performed in a solution of 5 mM $Fe(CN)_6^{3-/4-}$ in 0.1 M KNO_3 with a potential range of 0.0–0.1 V, a frequency range of 0.01 Hz–100 kHz, and an amplitude of 0.1 V.

Real-sample preparation

Biological fluids have been utilized to evaluate the applicability of the proposed sensor for monitoring the target analytes in real samples. All biological samples were well received by healthy volunteers in our laboratory, and serum samples were obtained from healthy patients. Informed consent was obtained from all human subjects, and they already knew what would happen to the human subjects in a trial. There was no purification process used on any of the samples. Different concentrations of the standard mixture L-DOPA and L-Tyr with an adequate standard calibration were spiked into biological samples and then diluted 50 and 100 times (1000 µL) with supporting electrolyte (0.1 M PBS, pH 7.4) for the serum and urine samples, respectively. The electrochemical measurement was performed via DPV under the optimized conditions. Lastly, accuracy and precision were subsequently evaluated and compared to spiked values.

1.2 The fabrication procedures of homemade SPGE and layer-by-layer poly(L-pro)/ND/SPGE

Homemade SPGE was fabricated by stepwise ink deposition using screen-printing technology. The templates for homemade SPGE were designed using Adobe Illustrator CC. The template patterns were constructed by Chaiyaboon Brothers Co., Ltd. (Bangkok, Thailand). Initially, the PVC paper substrate was cleaned with ethanol before use. Then, the template of the SPGE was attached on top of the PVC paper substrate. Graphene ink from Serve Science Co., Ltd. (product code: SSG-1760A, Bangkok, Thailand) was applied onto the template of the SPGE and then screened with a rubber squeegee. This step was repeated twice to obtain a homogeneous surface of WE and CE and placed into a hot air oven at a temperature of 60°C for 30 min. Next, silver/silver chloride (Ag/AgCl) ink obtained from Sun Chemical (product code: C2130809D5, Slough, United Kingdom) was applied to form the RE and conducting pad onto the same substrate and heated again at 60°C for 30 min for solvent drying to obtain good adhesion between the ink and the PVC substrate. Finally, insulator ink was then screened on top of the homemade SPGE to fix the area of the electrode surface.

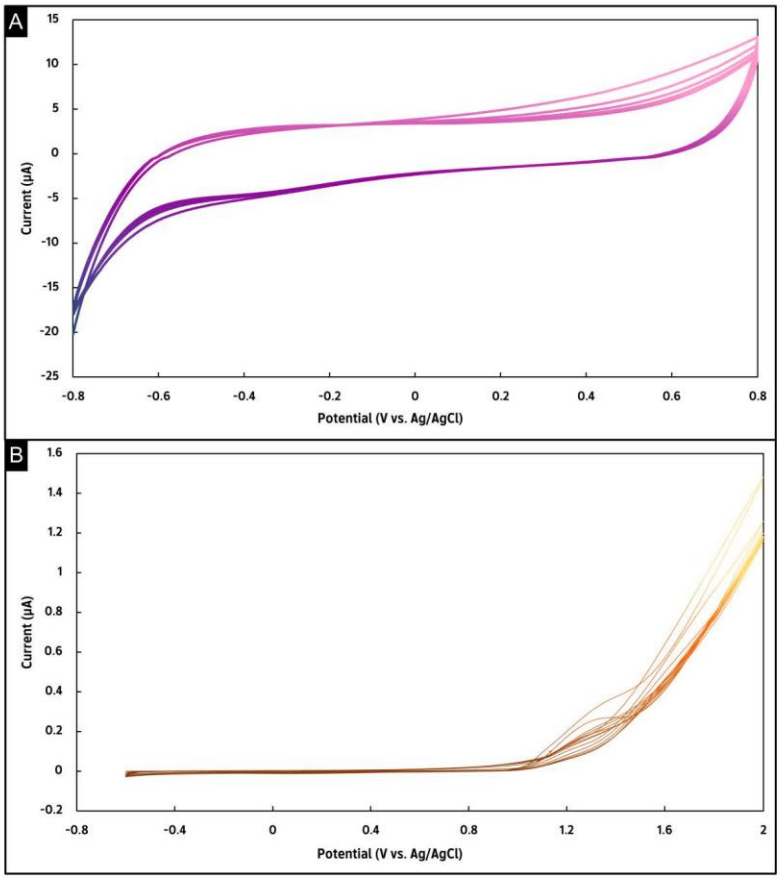

Fig. S1 A The signals of electrodeposition of 0.1% w/v ND (potential ranges from −0.8 to +0.8 V for 10 cycles, scan rate at 0.1 Vs^{-1}). **B** Cyclic voltammogram of electropolymerization of 1 mM L-proline in 0.1 M PBS at pH 7.4 (potential ranges from −0.6 to +2.0 V for 15 cycles, scan rate at 0.1 Vs^{-1}).

1.3 Chronoamperometric experiments

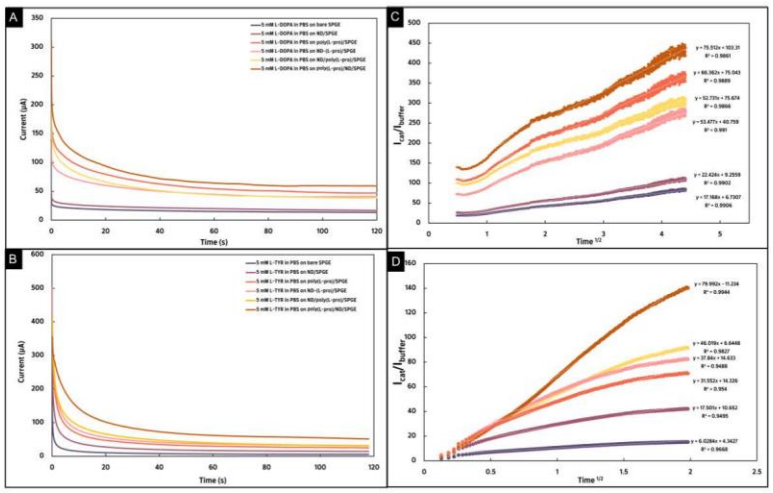

Fig. S2 Chronoamperograms for 5 mM L-DOPA (**A**) and 5 mM L-Tyr (**B**) in 0.1 M PBS at different electrodes. Linear segments of the plot I_{cat}/I_{buffer} vs. $t^{1/2}$ derived from chronoamperometric data for 5 mM L-DOPA (**C**) and 5 mM L-Tyr (**D**).

The catalytic rate constant (k_{cat}) of both analytes on different electrodes was calculated by the following equation [1]:

$$\frac{i_{cat}}{i_{buffer}} = \pi^{\frac{1}{2}}(k_{cat}Ct)^{1/2} \qquad (1)$$

where i_{cat} and i_{buffer} are the currents in the presence and absence of the target analyte, respectively, C represents the concentration of the target analyte, and t is the time at which the current values were taken. The catalytic rate constant was calculated from the slope of the linear relationship formed by plotting the i_{cat}/i_{buffer} vs. $t^{1/2}$ for 5 mM L-DOPA (Fig. S2C) and 5 mM L-Tyr (Fig. S2D).

The catalytic rate constants of both target analytes at different strategies for electrode modification are summarized in Table S1.

Table S1 The calculated catalytical rate constant toward L-DOPA and L-Tyr oxidation at six different electrodes.

Electrode	k_{cat} of L-DOPA (L mol^{-1} s^{-1})	k_{cat} of L-Tyr (L mol^{-1} s^{-1})
bare SPGE	1.88 x 10^4	2.31 x 10^3
ND/SPGE	3.20 x 10^4	1.95 x 10^4
poly(L-pro)/SPGE	2.81 x 10^5	6.34 x 10^4
ND-(L-pro)/SPGE	1.77 x 10^5	9.12 x 10^4
ND/poly(L-pro)/SPGE	1.82 x 10^5	1.35 x 10^5
poly(L-pro)/ND/SPGE	3.63 x 10^5	4.08 x 10^5

1.4 The particle size distribution of nanodiamond

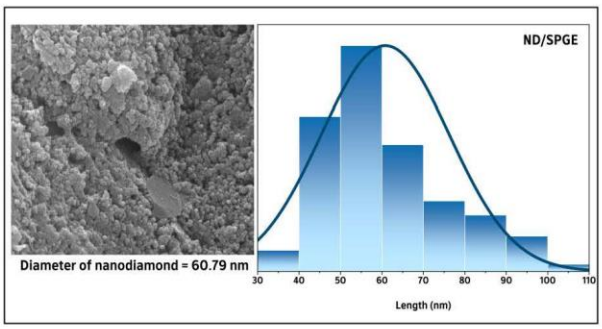

Fig. S3 A particle size distribution of ND on SPGE

1.5 Electrochemical characterization of poly(L-pro)/ND/SPGE

Based on the reversible process, the calculation of the active surface areas of both bare and modified SPGEs was evaluated using the Randles–Sevcik equation [2]:

$$I_{pa} = (2.69 \times 10^5)\, n^{3/2} A C_0^{*} D_0^{1/2} \upsilon^{1/2} \qquad (2)$$

where I_{pa} is the anodic peak current (μA), n is the number of electrons involved in the redox reaction (number of electrons of $Fe(CN)_6^{3-/4-}$ is equal to 1), A refers to the effective surface area (cm^2), D is the diffusion coefficient, which is 7.26×10^{-6} cm^2 s^{-1}, υ is the scan rate (V s^{-1}), and C is the concentration of the redox reactant (5×10^{-6} mol cm^{-3}). Using the linear relationship between the anodic peak current and the square root of scan rate (inset in Figs. 5C and D).

The surface coverage of the polymeric thin film on the poly(L-pro)/ND/SPGE was calculated using the following equation [3]:

$$\Gamma = \frac{Q}{nFA} \qquad (3)$$

where Γ is the total surface coverage (mol cm^{-2}), Q refers to the charge obtained from the anodic peak area of the supporting electrolyte (0.1 M PBS, pH 7.4), n is the number of involved electrons, F is Faraday's constant (96,485.34 C mol^{-1}), and A is the electroactive surface area.

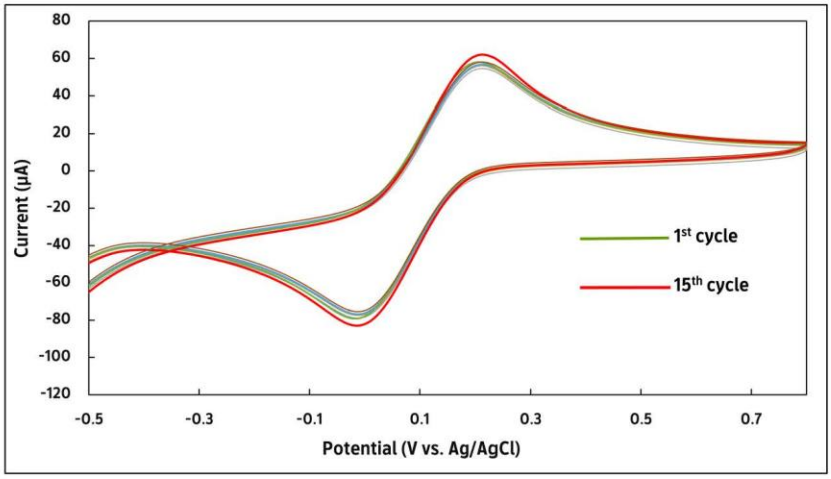

Fig. S4 The cycling stability of poly(L-pro)/ND/SPGE in the presence of 5 mM $Fe(CN)_6^{3-/4-}$ in 0.1 M KNO_3 at a scan rate of 50 mVs^{-1}

1.6 Computational calculations

All computational calculations are performed using Gaussian 16 programs.

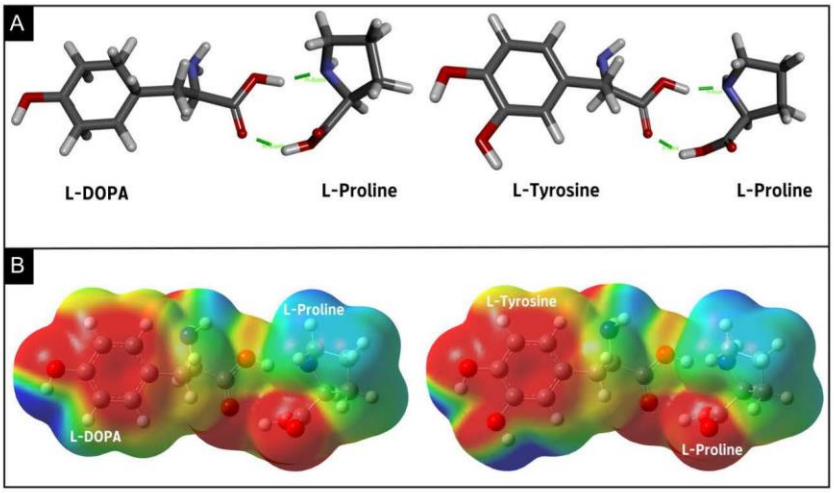

Fig. S5 A illustrates the optimized geometry of L-proline monomer–L-DOPA and L-Tyr complexes obtained by density functional theory. **B** The electron density mapped with ESP for the interactions between both target analytes and L-proline.

1.7 The different linear relationship on electrochemical behavior of L-DOPA and L-Tyr

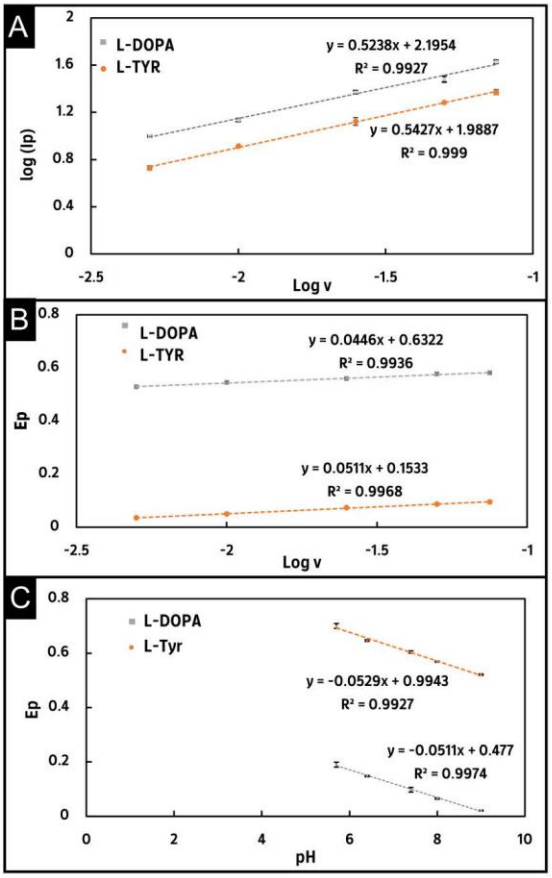

Fig. S6 The linear relationship between **A** log (Ip_a) and log υ, **B** peak potential (Ep) and log υ (scan rate (υ); 0.005 to 0.075 Vs^{-1}), and **C** Ep and pH for 1 mM L-DOPA and L-Tyr in 0.1 M PBS (pH 7.4) at poly(L-pro)/ND/SPGE.

1.8 Calculation of diffusion coefficient and the number of electrons

The diffusion coefficient (D_0)

$$I_{pa} = 0.496FACD_0^{\frac{1}{2}}\left(\frac{F}{RT}\right)^{1/2}\upsilon^{1/2} \quad (4)$$

where I_{pa} denotes the anodic peak current of L-DOPA and L-Tyr; F is Faraday's constant (96,485.34 C mol^{-1}), A denotes the electroactive surface area (0.067 cm^2), C is the concentration of both target analytes (1×10^{-6} mol cm^{-3}); R is the gas constant (8.31447 J $mol^{-1}K^{-1}$); T is the absolute temperature (298 K), and υ is the scan rate. The L-DOPA and L-Tyr diffusion coefficient could therefore be obtained from the slope of the linear regression of i-$v^{\frac{1}{2}}$ shown in the inset of Fig. 6C in the main text.

The Randles–Sevcik relationship for irreversible process

The Randles–Sevcik relationship (eq. 5) can be used to calculate the number of electrons in the irreversible electrooxidation process at the electrode–solution interface [4]:

$$I_{pa} = (2.99 \times 10^5)\, n[(1-\alpha)n_\alpha]^{1/2}AC_sD_0^{1/2}\upsilon^{1/2} \quad (5)$$

$$\text{Slope} = \frac{1.15RT}{(1-\alpha)nF} \quad (6)$$

The factor of $(1-\alpha)n_\alpha$ was firstly calculated from eq. 6 [5], which is described by the linear relationship between the anodic peak potential (Ep) and log υ (as shown in Fig. S6B). Hence, the calculated factors of $(1-\alpha)n_\alpha$ for L-DOPA and L-Tyr were found to be 0.58 and 0.66, respectively.

1.9 The optimization of the layer-by-layer electrode modifications and electrochemical detection

Due to the enlarged surface area properties of ND, it is necessary to control the uniformity and thickness of ND. The concentration, the number of cycles as well as the appropriate potential window for ND electrodeposition were systematically investigated as shown in Fig. S7. The potential range and number of cycling for ND formation represent the reaction time that ND is deposited on the electrode surface. The longer deposition time and more cycles might have contributed to the higher ND layer accumulation. As a result, the electrode became

too dense, reducing its specific surface area and obstructing the growth of polymeric thin films as well as the electron transfer process. Consequently, the optimum potential range and cycles for ND growth were found to be from –0.8 to +0.8 V with 10 cycles. For the concentration of ND, the peak current of L-DOPA increased up to 0.1% w/v and then decreased, and the current signal for L-Tyr seemed to be slightly raised before decreasing after 0.1% w/v. Thus, 0.1% w/v of nanodiamonds resulted in a uniformly ND-based electrode with strong adhesion and good mechanical properties that could offer large surface-active sites, ultimately resulting in the thorough covering of polymeric L-proline film.

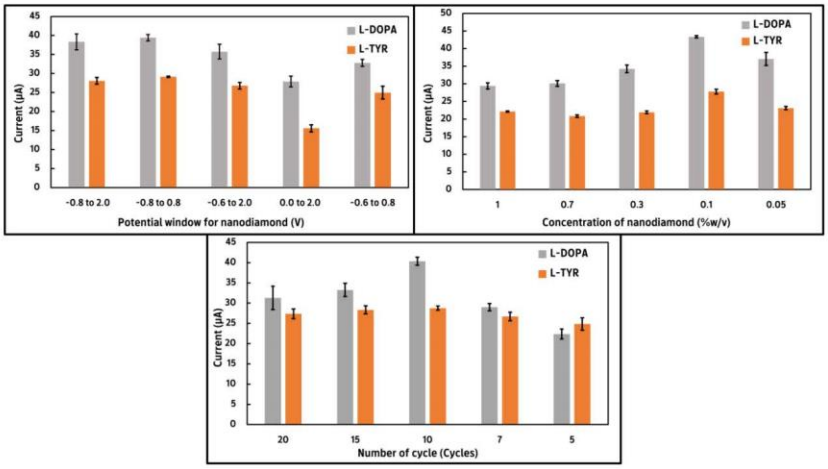

Fig. S7 The influence of the electrodeposition process of ND.

The quality and performance of polymeric L-proline film were also controlled by the parameters of CV experiments. The influences of the electropolymerization process were carried out on the electrooxidation responses of both target analytes as presented in Fig. S8. The potential windows are expected to give rise to polymer films with unique morphologies and electronic properties. Based on our knowledge, the development of polymer produced by amino acid building blocks is required to extend the broad potential ranges to as much positive potential as possible. The final potential was therefore set at +2.0 V and then adjusted the initial potential to more positive directions (−0.8, −0.6, −0.2, and 0.0 V, respectively). It was

observed that the potential windows between −0.6 and +0.2 V provided better electrochemical responses toward L-DOPA and L-Tyr oxidation. However, we attempted to shift the final potential to a more negative direction for decreasing the manufacturing time of a polymeric film. Unfortunately, when the applied potentials were scanned from −0.6 to +1.5 V, the current responses for L-DOPA and L-Tyr dramatically decreased. This phenomenon may attribute to the formation and adsorption of inactive polymeric L-proline film on the ND-based electrode, resulting in poor electrochemical responses. The polymerized of L-proline was carried out in the potential ranges between +0.98 and +1.65 V as shown in Fig. S1B. Thus, the potential window ranges from –0.6 to +0.2 V were suitable for the activated polymeric L-proline growth. The concentration of monomer and the number of cycles is crucial for the formation and thickness of the film. As a result, 1 mM of L-proline with 15 cycling provided high electrochemical responses of both target analytes. Interestingly, the formation of the ND-based electrode increased the specific surface area of active materials, which was beneficial for effectively reducing the concentration of monomers. Therefore, 1 mM of L-proline and 15 cycles were selected as the optimized conditions for electropolymerization for further experiments.

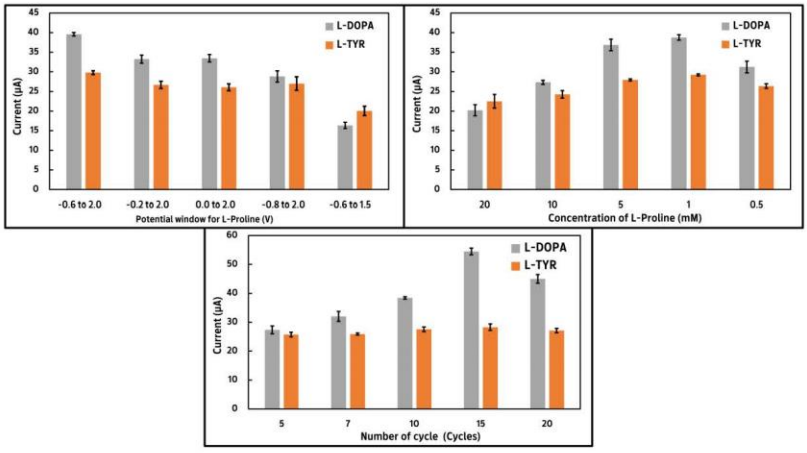

Fig. S8 The influence of electropolymerization process of L-proline.

All parameters of the DPV, including increment, amplitude, pulse width, and pulse period, were systematically examined. Fig. S9 represents DPV responses of 100 µL of L-DOPA and L-Tyr in 0.1 M PBS at pH 7.4. The optimum currents were detected at a pulse width of 0.025 s, amplitude of 0.2 V, pulse period of 0.5 s, and increment of 0.007 V, which offered the best analytical performance for the simultaneous detection of L-DOPA and L-Tyr. Following these investigations, the sharp and symmetrical peaks of both analytes appeared.

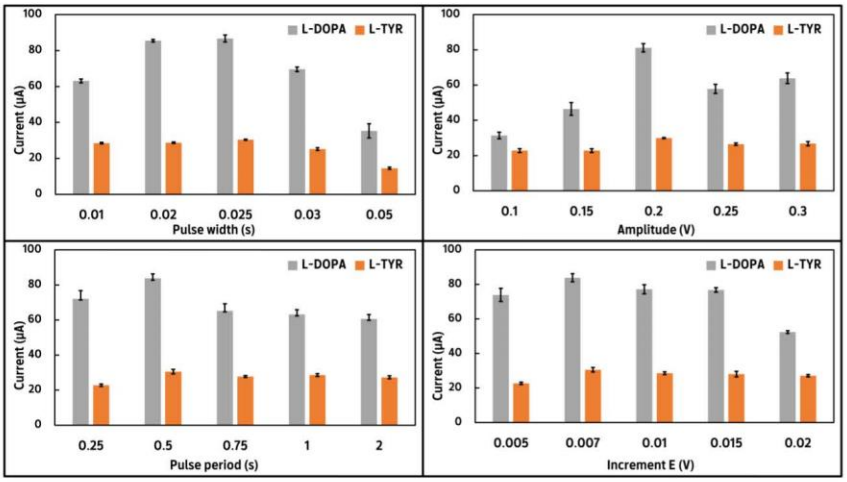

Fig. S9 represents the crucial DPV parameters including pulse width, amplitude, pulse period, and increment E.

1.10 The individual detection of L-DOPA and L-Tyr and real sample analysis

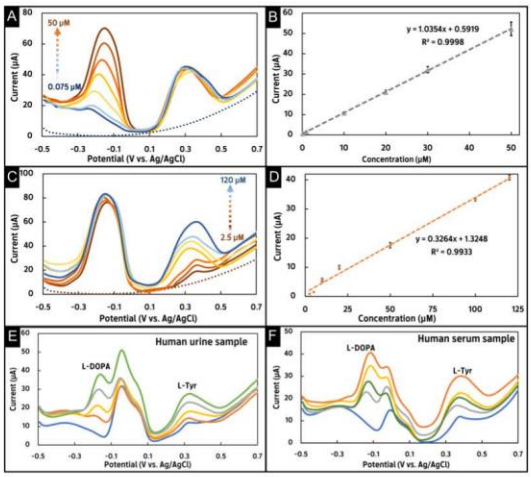

Fig. S10 DPV signals for varying concentrations of L-DOPA in the presence of 100 µM L-Tyr (**A**) and varying concentrations of L-Tyr in the presence of 100 µM L-DOPA (**C**) at poly(L-pro)/ND/SPGE, and Calibration plot between anodic peak current and concentration of L-DOPA (**B**), and L-Tyr (**D**). DPVs obtained for human urine sample and (**E**) and human serum sample (**F**), with increasing concentrations of L-DOPA (0, 2.5, 5, 10, and 20 µM), L-Tyr (0, 5, 10, 20,40 µM).

1.11 The analytical performance comparison between the different electrode configurations and the proposed electrode for simultaneous determination of L-DOPA and L-Tyr.

Table S2 Analytical performance comparison of poly(L-pro)/ND/SPGE and other electrochemical sensors for simultaneous determination of L-DOPA and L-Tyr.

Electrode configuration	Techniques	Real sample	Linear range (µM)		LOD (M)		Ref.
			L-DOPA	L-Tyr	L-DOPA	L-Tyr	
p-AMTa/GCE	Amp	Human blood plasma	0.01–100	0.05–100	5.8×10^{-11}	1.9×10^{-11}	[6]
GR/ZnO/GSPE	SWV	Human blood serum and urine samples	1.0–1000	1.0–800	4.5×10^{-7}	3.4×10^{-7}	[7]
GR and EFTA/CPE	SWV	Human blood serum and urine samples	0.2–400	5.0–180	7.0×10^{-8}	2.0×10^{-6}	[8]
Cysteic acid/GCE	DPV	Human blood serum	0.35–4.0	1.7–50	1.1×10^{-7}	5.5×10^{-7}	[9]
CE/PHQ/CNT/ GCE	DPV	Serum samples	0.005–20	0.03–170	2.2×10^{-10}	1.3×10^{-9}	[10]
pPTSA/GCE	SWV	Artificial blood serum and urine samples	1.0–90	1.0–70	1.2×10^{-7}	2.1×10^{-7}	[11]
poly(L-pro)/ ND/SPGE	DPV	Human blood serum and urine samples	0.075–50	2.5–120	2.1×10^{-8}	7.4×10^{-7}	This work

p-AMTa: Poly(3-amino-5-mercapto-1,2,4-triazole), GCE: glassy carbon electrode, GR: graphene oxide, ZnO: zinc oxide, GSPE: graphite screen-printed electrode, GR: graphene, EFTA: ethyl 2-(4-ferrocenyl-[1,2,3]triazol-1-yl) acetate, CPE: carbon paste electrode, CE: benzo-12-crown-4, PHQ:

Poly(hydroquinone), CNT: carbon nanotubes, pPTSA: poly(para-toluene sulphonic acid), Poly(L-pro): poly(L-proline), ND: nanodiamond, SPGE: screen-printed graphene electrode.

References:

[1] Rotariu L, Zamfir LG, Bala C (2010) Low potential thiocholine oxidation at carbon nanotube-ionic liquid gel sensor. Sens Actuators B Chem 150(1): 73-79. https://doi.org/10.1016/j.snb.2010.07.040

[2] Shahrokhian S, Ghalkhani M (2010) Glassy carbon electrodes modified with a film of nanodiamond–graphite/chitosan: Application to the highly sensitive electrochemical determination of Azathioprine. Electrochim Acta: 55(11): 3621-3627. https://doi.org/10.1016/j.electacta.2010.01.099

[3] Kumar DR, Kesavan S, Nguyen TT, Hwang J, Lamiel C, Shim JJ (2017) Polydopamine@ electrochemically reduced graphene oxide-modified electrode for electrochemical detection of free-chlorine. Sens Actuators B Chem 240: 818-828. https://doi.org/10.1016/j.snb.2016.09.025

[4] Boni AC, Wong A, Dutra RAF, Sotomayor MDPT (2011) Cobalt phthalocyanine as a biomimetic catalyst in the amperometric quantification of dipyrone using FIA. Talanta 85(4): 2067-2073. https://doi.org/10.1016/j.talanta.2011.07.038

[5] Yilmaz S, Baltaoglu E, Saglikoglu G, Yagmur S, Polat K, Sadikoglu M (2013) Electroanalytical determination of metronidazole in tablet dosage form. J Serb Chem Soc 78(2): 295-302. https://doi.org/10.2298/JSC120111069Y

[6] Revin SB, John SA (2013) Electrochemical marker for metastatic malignant melanoma based on the determination of l-dopa/l-tyrosine ratio. Sens Actuators B Chem 188: 1026-1032. https://doi.org/10.1016/j.snb.2013.08.019

[7] Beitollahi H, Garkani Nejad F (2016) Graphene oxide/ZnO nano composite for sensitive and selective electrochemical sensing of levodopa and tyrosine using modified graphite

screen printed electrode. Electroanalysis 28(9): 2237-2244. https://doi.org/10.1002/elan.201600143

[8] Movlaee K, Beitollahi H, Ganjali MR, Norouzi P (2017) Electrochemical platform for simultaneous determination of levodopa, acetaminophen and tyrosine using a graphene and ferrocene modified carbon paste electrode. Microchim Acta 184(9): 3281-3289. https://doi.org/10.1007/s00604-017-2291-3

[9] Hassanvand Z, Jalali F (2019) Simultaneous determination of l-DOPA, l-tyrosine and uric acid by cysteic acid-modified glassy carbon electrode. Mater Sci Eng C 98: 496-502. https://doi.org/10.1016/j.msec.2018.12.131

[10] Atta NF, Galal A, El-Gohary AR (2020) Crown ether modified poly(hydroquinone)/carbon nanotubes based electrochemical sensor for simultaneous determination of levodopa, uric acid, tyrosine and ascorbic acid in biological fluids. J Electroanal Chem 863: 114032. https://doi.org/10.1016/j.jelechem.2020.114032

[11] Sam S, Mathew MR, Kumar KG (2022). A Simple Electropolymer Based Voltammetric Sensor for the Simultaneous Determination of Melanoma Biomarkers–L-Dopa and L-Tyrosine. J Electrochem Soc 169(2): 027511. https://doi.org/10.1149/1945-7111/ac51a1

VITA